



ISSN 2518-7198 (Print)
ISSN 2663-5089 (Online)

BULLETIN **OF THE KARAGANDA UNIVERSITY**

PHYSICS Series

2025 • Volume 30 • Issue 2(118)

ISSN 2663-5089 (Online)
ISSN-L 2518-7198 (Print)
Индексі 74616
Индекс 74616

**ҚАРАҒАНДЫ
УНИВЕРСИТЕТІНІҢ
ХАБАРШЫСЫ**

ВЕСТНИК
КАРАГАНДИНСКОГО
УНИВЕРСИТЕТА

BULLETIN
OF THE KARAGANDA
UNIVERSITY

ФИЗИКА сериясы

Серия ФИЗИКА

PHYSICS Series

2025

30-том • 2(118)-шығарылым
Том 30 • Выпуск 2(118)
Volume 30 • Issue 2(118)

1996 жылдан бастап шығады
Издается с 1996 года
Founded in 1996

Жылына 4 рет шығады
Выходит 4 раза в год
Published 4 times a year

Қарағанды / Караганда / Karaganda
2025

Бас редакторы
PhD, проф. **Н.Қ. Танашева**

Жауапты хатишы
PhD, қауымд. проф. **Д.Ж. Қарабекова**

Редакция алқасы

Н.Х. Ибраев,	физ.-мат. ғыл. д-ры, проф., акад. Е.А. Бөкетов атындағы Қарағанды университеті (Қазақстан);
Б.Р. Нүсіпбеков,	техн. ғыл. канд., проф., Әбілқас Сағынов атындағы Қарағанды техникалық университеті, Қарағанды (Қазақстан);
А.О. Сәулебеков,	физ.-мат. ғыл. д-ры, проф., М.В. Ломоносов атындағы Мәскеу мемлекеттік университетінің Қазақстан филиалы, Астана (Қазақстан);
Б.Р. Ильясов,	PhD, қауымд. проф., Astana IT University, Астана (Қазақстан);
А.Д. Погребняк,	физ.-мат. ғыл. д-ры, проф., Сумы мемлекеттік университеті (Украина);
А.П. Суржиков,	физ.-мат. ғыл. д-ры, проф., Томск политехникалық университеті (Ресей);
И.П. Курытник,	техн. ғыл. д-ры, проф., Освенцимдегі В. Пилецкий атындағы Мемлекеттік жоғары кәсіптік мектебі (Польша);
М. Стоев,	PhD, инженерия д-ры, «Неофит Рильский» Оңтүстік-Батыс университеті, Благоевград (Болгария);
В.Ю. Кучерук,	техн. ғыл. д-ры, проф., Винница ұлттық техникалық университеті (Украина);
В.А. Кульбачинский,	физ.-мат. ғыл. д-ры, проф., М.В. Ломоносов атындағы Мәскеу мемлекеттік университеті (Ресей);
Bisquert Juan,	проф., физика проф., Хайме I университеті, Кастельо-де-ла-Плана (Испания);
Chun Li,	PhD, Чанчунь ғылым және технология университеті (Қытай);
Д.Т. Валиев,	физ.-мат. ғыл. канд., доц., Томск ұлттық политехникалық зерттеу университеті (Ресей)

Редакцияның мекенжайы: 100024, Қазақстан, Қарағанды қ., Университет к-сі, 28
E-mail: vestnikku@gmail.com; karabekova71@mail.ru
Сайты: physics-vestnik.ksu.kz

Атқарушы редактор
PhD **Г.Б. Саржанова**

Корректорлары
С.С. Балкеева, И.Н. Муртазина

Компьютерде беттеген
В.В. Бутякин

Қарағанды университетінің хабаршысы. «Физика» сериясы. — 2025. — 30-т., 2(118)-шығ. — 106 б. — ISSN-L 2518-7198 (Print). ISSN 2663-5089 (Online).

Меншік иесі: «Академик Е.А. Бөкетов атындағы Қарағанды университеті» КЕАҚ.

Қазақстан Республикасы Ақпарат және қоғамдық даму министрлігімен тіркелген. 30.09.2020 ж. № KZ38VPY00027378 қайта есепке қою туралы куәлігі.

Басуға 30.06.2025 ж. қол қойылды. Пішімі 60×84 1/8. Қағазы офсеттік. Көлемі 13,25 б.т. Таралымы 200 дана. Бағасы келісім бойынша. Тапсырыс № 58.

«Акад. Е.А. Бөкетов ат. Қарағанды ун-ті» КЕАҚ баспасының баспаханасында басылып шықты.
100024, Қазақстан, Қарағанды қ., Университет к-сі, 28. Тел. (7212) 35-63-16. E-mail: izd_karu@mail.kz

© Академик Е.А. Бөкетов атындағы Қарағанды университеті, 2025

Главный редактор

PhD, проф. **Н.К. Танашева**

Ответственный секретарь

PhD, ассоц. проф. **Д.Ж. Карабекова**

Редакционная коллегия

Н.Х. Ибраев,	д-р физ.-мат. наук, проф., Карагандинский университет им. акад. Е.А. Букетова (Казахстан);
Б.Р. Нусупбеков,	канд. техн. наук, проф., Карагандинский технический университет им. А. Сагинова, Караганда (Казахстан);
А.О. Саулебеков,	д-р физ.-мат. наук, проф., Казахстанский филиал Московского государственного университета им. М.В. Ломоносова, Астана (Казахстан);
Б.Р. Ильясов,	PhD, ассоц. проф., Astana IT University, Астана (Казахстан);
А.Д. Погребняк,	д-р физ.-мат. наук, проф., Сумской государственный университет (Украина);
А.П. Суржиков,	д-р физ.-мат. наук, проф., Томский политехнический университет (Россия);
И.П. Курытник,	д-р техн. наук, проф., Государственная высшая профессиональная школа им. В. Пилецкого в Освенциме (Польша);
М. Стоев,	PhD, д-р инженерии, Юго-Западный университет «Неофит Рильский», Благоевград (Болгария);
В.Ю. Кучерук,	д-р техн. наук, проф., Винницкий национальный технический университет (Украина);
В.А. Кульбачинский,	д-р физ.-мат. наук, проф., Московский государственный университет им. М.В. Ломоносова (Россия);
Bisquert Juan,	проф., проф. физики, Университет Хайме I, Кастельо-де-ла-Плана (Испания);
Chun Li,	PhD, Чанчуньский университет науки и технологии (Китай);
Д.Т. Валиев,	канд. физ.-мат. наук, доц., Национальный исследовательский Томский политехнический университет (Россия)

Адрес редакции: 100024, Казахстан, г. Караганда, ул. Университетская, 28

E-mail: vestnikku@gmail.com; karabekova71@mail.ru

Сайт: physics-vestnik.ksu.kz

Исполнительный редактор

PhD **Г.Б. Саржанова**

Корректоры

С.С. Балкеева, И.Н. Муртазина

Компьютерная верстка

В.В. Бутяйкин

Вестник Карагандинского университета. Серия «Физика». — 2025. — Т. 30, вып. 2(118). — 106 с. — ISSN-L 2518-7198 (Print). ISSN 2663-5089 (Online).

Собственник: НАО «Карагандинский университет имени академика Е.А. Букетова».

Зарегистрирован Министерством информации и общественного развития Республики Казахстан. Свидетельство о постановке на переучет № KZ38VPY00027378 от 30.09.2020 г.

Подписано в печать 30.06.2025 г. Формат 60×84 1/8. Бумага офсетная. Объем 13,25 п.л. Тираж 200 экз. Цена договорная. Заказ № 58.

Отпечатано в типографии издательства НАО «Карагандинский университет им. акад. Е.А. Букетова». 100024, Казахстан, г. Караганда, ул. Университетская, 28. Тел.(7212) 35-63-16. E-mail: izd_kagu@mail.kz

© Карагандинский университет им. акад. Е.А. Букетова, 2025

Chief Editor

PhD, Professor **N.K. Tanasheva**

Responsible secretary

Associate Professor, PhD **D.Zh. Karabekova**

Editorial board

N.Kh. Ibrayev,	Prof., Doctor of phys.-math. sciences, Karagandy University of the name of acad. E.A. Buketov (Kazakhstan);
B.R. Nussupbekov,	Prof., Cand. of techn. sciences, Abylkas Saginov Karaganda Technical University, Karaganda (Kazakhstan);
A.O. Saulebekov,	Prof., Doctor of phys.-math. sciences, Kazakhstan branch of Lomonosov Moscow State University, Astana (Kazakhstan);
B.R. Ilyassov,	PhD, Assoc. Prof., Astana IT University (Kazakhstan);
A.D. Pogrebnjak,	Prof., Doctor of phys.-math. sciences, Sumy State University (Ukraine);
A.P. Surzhikov,	Prof., Doctor of phys.-math. sciences, Tomsk Polytechnic University (Russia);
I.P. Kurytnik,	Prof., Doctor of techn. sciences, The State School of Higher Education in Oświęcim (Auschwitz) (Poland);
M. Stoev,	PhD, Doctor of engineering, South-West University “Neofit Rilski”, Blagoevgrad (Bulgaria);
V.Yu. Kucheruk,	Prof., Doctor of techn. sciences, Vinnytsia National Technical University, Vinnitsia (Ukraine);
V.A. Kulbachinskii,	Prof., Doctor of phys.-math. sciences, Lomonosov Moscow State University (Russia);
Bisquert Juan,	Prof. of phys., Prof. (Full), Universitat Jaume I, Castellon de la Plana (Spain);
Chun Li,	PhD, Changchun University of Science and Technology (China);
D.T. Valiev,	Assoc. Prof., Cand. of phys.-math. sciences, National Research Tomsk Polytechnic University (Russia)

Postal address: 28, University Str., 100024, Karaganda, Kazakhstan

E-mail: vestnikku@gmail.com; karabekova71@mail.ru

Web-site: physics-vestnik.ksu.kz

Executive Editor

PhD **G.B. Sarzhanova**

Proofreaders

S.S. Balkeyeva, I.N. Murtazina

Computer layout

V.V. Butyaikin

Bulletin of the Karaganda University. “Physics” Series. — 2025. — Vol. 30, Iss. 2(118). — 106 p. — ISSN-L 2518-7198 (Print). ISSN 2663-5089 (Online).

Proprietary: NLC “Karagandy University of the name of academician E.A. Buketov”.

Registered by the Ministry of Information and Social Development of the Republic of Kazakhstan. Rediscount certificate No. KZ38VPY00027378 dated 30.09.2020.

Signed in print 30.06.2025. Format 60×84 1/8. Offset paper. Volume 13,25 p.sh. Circulation 200 copies. Price upon request. Order № 58.

Printed in the Publishing house of NLC “Karagandy University of the name of acad. E.A. Buketov”.
28, University Str., Karaganda, 100024, Kazakhstan. Tel. (7212) 35-63-16. E-mail: izd_karu@mail.kz

© Karagandy University of the name of academician E.A. Buketov, 2025

МАЗМҰНЫ – СОДЕРЖАНИЕ – CONTENTS

КОНДЕНСАЦИЯ ЛАНҒАН КҮЙДІҢ ФИЗИКАСЫ ФИЗИКА КОНДЕНСИРОВАННОГО СОСТОЯНИЯ PHYSICS OF THE CONDENSED MATTER

<i>Adyrbekova G., Saidakhmetov P., Burganova R., Piyanzina I., Baiman G., Baubekova G., Tayurskii D.</i> Density functional theory study of azobenzene derivatives as potential materials for wettability switching	6
<i>Seisembekova T.E., Aimukhanov A.K., Zeinidenov A.K., Alexeev A.M., Abeuov D.R.</i> The effect of MoSe ₂ nanoparticles on the properties ZnO electron transport layer of organic solar cell	19

ТЕХНИКАЛЫҚ ФИЗИКА ТЕХНИЧЕСКАЯ ФИЗИКА TECHNICAL PHYSICS

<i>Igamov B.D., Kamardin A.I., Nabiev D.Kh., Imanova G.T., Bekpulatov I.R., Turapov I.Kh., Norbutaev N.E.</i> Study of Mn ₄ Si ₇ Silicide Alloys Produced Under Different Conditions Using an X-ray Diffractometer	27
<i>Akhatova Zh.Zh., Ilyassov B.R., Seisenbayeva G.S., Kambar D.S., Aimukhanov A.K., Aldasheva L.S., Zavgorodniy A.V.</i> Electrochemical rectifying device based on polymer thin films.....	35
<i>Goldstein A.E., Stryapchev K.A.</i> Measurement of ferromagnetic pipe wall thickness by magnetic flux leakage method	47

ЖЫЛУФИЗИКАСЫ ЖӘНЕ ТЕОРИЯЛЫҚ ЖЫЛУТЕХНИКАСЫ ТЕПЛОФИЗИКА И ТЕОРЕТИЧЕСКАЯ ТЕПЛОТЕХНИКА THERMOPHYSICS AND THEORETICAL THERMOENGINEERING

<i>Sabdenov K.O., Smagulov Zh.K., Erzada M., Zhakatayev T.A.</i> Simulation of a Stirling Engine with a Reversible Reaction $\text{CO} + 2\text{H}_2 \leftrightarrow \text{CH}_3\text{OH}$	55
<i>Zhapbasbayev U.K., Bossinov D.Zh., Pahomov M.A., Sattinova Z.</i> Modeling of Turbulent Non-Isothermal Flow in a Heating Network Pipe	67
<i>Rakhadilov B.K., Kengesbekov A.B., Magazov N.M., Kusainov A.A., Kairbaeva L.S., Molbosynov Y.S.</i> Study of the Effect of Thermomechanical Treatments on the Property of Beryllium Bronze in Order to Expand Its Application	75
<i>Katsyv S., Kukharchuk V., Madyarov V., Kucheruk V., Kulakov P., Hribov M.</i> Non-standard analysis in electrical engineering. Ideal DC inductive circuits with infinitesimal parameters of different orders	87
<i>Tanasheva N.K., Minkov L.L., Bakhtybekova A.R., Kyzdarbekova Sh.S., Potapova A.A., Botpaev N.K.</i> Aerodynamic optimization of Magnus wind turbine blades using an active deflector	97

Article

UDC 536.4:519.688

 <https://doi.org/10.31489/2025PH2/6-18>

Received: 27.11.2024

Accepted: 28.02.2025

G. Adyrbekova¹, P. Saidakhmetov¹, R. Burganova², I. Piyanzina²,
G. Baiman¹, G. Baubekova¹, D. Tayurskii²


¹Department of Physics, M. Auezov South Kazakhstan University, Tauke Khan Ave 5, Shymkent, 160012, Kazakhstan;

²Institute of Physics, Kazan Federal University, Kremlyovskaya St. 18, Kazan, 420008, Tatarstan, Russia

**Density functional theory study of azobenzene derivatives
as potential materials for wettability switching**

In this study, density functional theory (DFT) is employed to analyze the properties of 16 azobenzene derivatives, assessing their potential as wettability switching materials. Inspired by K. Ichimura's 2001 report on azobenzene-modified surface wettability, we explore the impact of photoisomerization-induced changes in molecular dipole moments between *cis* and *trans* configurations of different azobenzene derivatives. In parent azobenzene molecule this process transforms non-polar molecule into a more hydrophilic *cis* form. The control of surface wettability holds immense potential across diverse domains, such as industry, medicine, microbiology, electronics, and materials science. By harnessing this control, we can unlock the potential to create innovative materials, elevate functionality, and boost efficiency. It enables to enhance product performance, improve adhesion, and achieve precision in liquid handling. Our investigation delves into the structural, electronic, and molecular aspects of all studied molecules utilizing the hybrid B3LYP functional with DFT-D3 dispersion correction and a 6-31++G(d, p) basis set, presenting promising azo-type structures for surface wettability manipulation. Two azobenzene derivatives emerge as potential candidates, exhibiting transformations during *cis-trans* photoisomerization — one towards increased hydrophilicity and the other in the opposite direction.

Keywords: azobenzene derivative, wettability switching, photoisomerization, dipole moments, *cis-trans* configurations, DFT, B3LYP functional, 6-31++G(d, p) basis set, photoswitchable materials, hydrophilicity

 Corresponding author: Saidakhmetov Pulat, timpf_ukgu@mail.ru

Introduction

Wettability is a significant property of solids, governing the spreading behavior of liquid drops on a solid surface. This phenomenon is quantified through the measurement of contact angle (CA), classifying surfaces as either hydrophilic or hydrophobic. Superhydrophobic surfaces, of particular interest, are intricately connected to both fundamental science and practical applications.

Examples of superhydrophobic surfaces can be found in nature, namely are observed in various plants and insects. Lotus leaves, for instance, are characterized by their ability to repel water, resulting in a self-cleaning effect, while water striders feature hydrophobic legs to stay above the water surface [1]. This has spurred significant interest in constructing novel bio-inspired hydrophilic or hydrophobic surfaces. The applications of such surfaces are diverse, with notable uses in antifogging, self-cleaning glasses (lotus effect), transparent electronics and nanomedicine [2, 3].

Various methods exist for manipulating wettability of solid surfaces, encompassing temperature gradients, electric fields, chemical surface modification, pH alterations, solvent influences, and light irradiation [1, 4, 5]. Benefiting from a non-contact mode and acting as a precise stimulus, light can be accurately directed to the target region for the controlled manipulation of chemical reactions and physical properties, providing a more elegant design and intelligent control. Materials suitable for light-induced wettability control exhibit two fundamental properties under irradiation: a switch between bistable states and a change in surface energy [6]. Among inorganic compounds, titanium dioxide (TiO_2) stands out, transitioning to a highly hydrophilic state (0° contact angle for water) under ultraviolet irradiation (UV) [2]. Within the realm of organic compounds, azobenzenes, spiropyrans, and cinnamates are notable, showcasing a typical change in chemical configurations between two states. The advantages of organic compounds over inorganic ones include their amenability to chemical modification, adaptability, and greater reaction diversity [6].

The pioneering work on wettability control of a surface modified with azobenzene was introduced by K. Ichimura [7]. The concept revolves around the photoisomerization of azobenzene during irradiation, transforming the nonpolar *trans*-azobenzene into the polar and more hydrophilic *cis*-azobenzene. Following this discovery, azobenzene and its derivatives underwent extensive examination as the base for molecular switches, developing fabrication of the light-responsive surfaces [8–11]. Subsequent investigations focused on the fundamental aspects of *cis-trans* isomerization, including solvatochromic behavior [12–14], solvent-dependent kinetics, intermolecular and surface interactions, and their effect on wettability switching [15–17].

The present research aims to facilitate the fast and simple design of molecules suitable for creating monolayers and functionalized surfaces with controlled wetting properties, responsive to external light irradiation. Through the analysis of structural, electronic, and molecular properties of 16 azobenzene derivatives using the density functional theory (DFT), we evaluate their potential as materials capable of wettability switching. This endeavor is consistent with the broader goal of improving the understanding and application of photosensitive surfaces to control wetting characteristics individually and effectively.

Methods

For the properties characterization the *ab-initio* calculations were carried out using the Gaussian 16 [18] program within DFT and hybrid B3LYP30 functional with DFT-D3 dispersion corrections. Additionally, water solvent effect was estimated using polarizable continuum model (PCM). The energies of the structures were calculated with a self-consistent field (SCF) convergence of 10^{-8} a.u. for the density matrix. All structures were optimized using the Berny algorithm [19] with the convergence criteria being a maximum force less than 45×10^{-5} and a rms force less than 3×10^{-4} . We used a 6-31++G(d, p) basis set which is the most appropriate in terms of accuracy and computational time for the determination of electronic properties [20]. Geometry parameters for each structure were free of constraints and allowed to relax during the optimization process.

In contrast, our previous research [21] utilized an older computational scheme, focusing on only seven molecules, several of which are reexamined in this study. This shift not only allows for a more comprehensive understanding of molecular interactions but also highlights the advancements made in computational methodologies. The incorporation of these modern techniques provides a clearer insight into the molecular behaviours in aqueous environments, underscoring the significance and originality of the current findings.

The common structure of studied molecules is presented in Figure and includes the following azobenzene derivatives:

1. Azobenzene as a parent molecule;
2. Azobenzene substituted with electron donating groups NH_2 , $\text{SO}_2\text{-NH}_2$, $\text{N}(\text{CH}_3)_2$, known as aminoazobenzenes;
3. Azobenzene substituted with electron acceptor groups OH , NO_2 , $\text{CH}_2\text{-CH}_2\text{-OH}$, F , CF_3 , C_6H_5 ;
4. Azobenzene substituted with electron acceptor groups in more, than one positions of hydrogen atoms of a phenyl ring;
5. Azobenzene derivatives of the pseudostilbene type.

These derivatives are essentially modified with an electron acceptor at one end of a phenyl ring and an electron-donating group at the other end of another phenyl ring. This type is commonly referred to as push-pull azobenzene, owing to the intriguing charge transfer that occurs within the molecule.

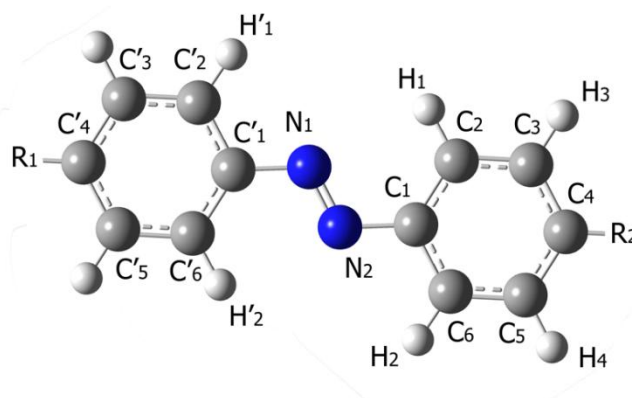


Figure. Structure of *trans* configuration of studied molecules.
Blue atoms are nitrogen, dark gray atoms are carbon, white atoms are hydrogen

The full list of considered molecules is itemized in Table 1.

Table 1

Short names, functional groups R1 and R2, corresponding SMILES specificities and structural forms of the studied azobenzene derivatives

Short name	R ₁	R ₂	SMILES	The structural formulas of studied compounds
AB	H	H	<chem>c1ccc(cc1)/N=N/c1ccccc1</chem>	
HOAB	OH	H	<chem>Oc1ccc(cc1)/N=N/c1ccccc1</chem>	
FHOAB	OH	F	<chem>Oc1ccc(cc1)/N=N/c1ccc(F)c1</chem>	
CH ₃ HOAB	OH	CH ₃	<chem>Cc1cccc(c1)/N=N/c1ccc(O)cc1</chem>	
CH ₃ OHOAB	OH	O-CH ₃	<chem>COc1cccc(c1)/N=N/c1ccc(O)cc1</chem>	
CF ₃ HOAB	OH	CF ₃	<chem>Oc1ccc(-n:n-c2ccc(cc2)C(F)(F)F)cc1</chem>	
C ₆ H ₅ HOAB	OH	C ₆ H ₅	<chem>Oc1ccc(cc1)/N=N/c1cccc(c1)-c1ccccc1</chem>	
CH ₂ CH ₂ HOAB	H	CH ₂ -CH ₂ -OH	<chem>OCCc1ccc(cc1)/N=N/c1ccccc1</chem>	

Continuation of Table 1

Short name	R ₁	R ₂	SMILES	The structural formulas of studied compounds
MY	H	N-(CH ₃) ₂	C[n](C):c1ccc(-n:n-c2ccccc2)cc1	
DO3	NO ₂	NH ₂	[nH2]:c1ccc(-n:n-c2ccc(cc2)-n(:o):o)cc1	
AAB	NH ₂	H	Nc1ccc(-n:n-c2ccccc2)cc1	
SO ₂ NH ₂ AB	NH ₂	SO ₂ NH ₂	NS(=O)(=O)c1ccc(-n:n-2ccc(:[nH2])cc2)cc1	
ADAB	NH ₂	N(CH ₃) ₂	CN(C)c1ccc(-n:n-c2ccc(N)cc2)cc1	
DR1	NO ₂	N(CH ₂ CH ₃) (CH ₂ CH ₂ OH)	CC[n](CCO):c1ccc(-n:n-c2ccc(cc2)-n(:o):o)cc1	

Short name	R ₁	R ₂	Hi	SMILES	The structural formulas of studied compounds
F(HO) ₃ AB	F	OH	H' ₁ , H' ₂ →OH	Oc1ccc(cc1)/N=N/c1cc(O)c(F)c(O)c1	
F ₅ HOAB	OH	F	H ₁ , H ₂ , H ₃ , H ₄ →F	Oc1ccc(-n:n-c2c(F)c(F)c(F)c(F)c2F)cc1	
HO ₃ AB	OH	OH	H' ₁ , H' ₂ →OH	Oc1cc(O)c(-n:n-c2ccccc2)c(O)c1	

We analyzed both *trans* and *cis* forms, along with all potential arrangements of functional groups for each molecule. Verified stationary configurations were determined through vibrational frequency analysis, exclusively using configurations with real frequencies for calculations. In the case of multiple options, the most stable configuration was chosen for subsequent analysis. Boltzmann statistics were applied to determine the probability and, subsequently, the average value of the desired property for each configuration.

The chemical potential (μ), absolute hardness (η), and electronegativity (χ) were determined through the finite-difference approximation based on the ionization potential (I) and electron affinity (A). The energy of the last occupied Kohn-Sham orbital corresponds to the highest occupied molecular orbital (HOMO) associated with $-I$. Similarly, the energy of the first unoccupied Kohn-Sham orbital is often used as an approximation for the energy of the lowest unoccupied molecular orbital (LUMO) and can be equated with $-A$, despite the crude nature of this approximation due to DFT being a ground state theory.

Results and discussion

Optimized structures

The characteristic lengths of bonds, distances, torsion angles, and dihedral angles describing the optimized molecules in their *trans* and *cis* configurations are presented in Table 2.

Table 2

Optimized geometrical parameters (angles in degrees, bond length in Å) for the *trans* and *cis* configurations of studied molecules obtained from B3LYP-D3 6-31++G(d, p) calculations in the gas phase and water solvent

Molecule	<i>trans</i>						<i>cis</i>								
	N1C1	N1N2	N2C1	C4C4	N2N1 C1	N1N2 C1	N1C1	N1N2	N2C1	C4C4	N2N1 C1	N1N2 C1	C1N1 N2C1	N1N2 C1C6	N2N1 C1C2
AB	1.418	1.258	1.417	9.080	115.1	115.1	1.435	1.249	1.435	6.314	123.0	123.0	8.8	50.7	50.7
	1.418	1.259	1.418	9.091	115.4	115.4	1.436	1.252	1.436	6.297	123.0	123.0	9.1	50.8	50.8
HOAB	1.417	1.260	1.411	9.079	115.1	115.3	1.434	1.251	1.431	6.391	123.1	123.6	9.4	42.2	53.9
	1.418	1.261	1.409	9.090	115.2	115.8	1.435	1.254	1.429	6.377	123.1	123.7	9.8	41.8	53.8
FHOAB	1.409	1.260	1.417	9.081	115.5	114.8	1.429	1.251	1.434	6.403	123.7	123.2	9.3	55.1	40.8
	1.407	1.261	1.417	9.092	115.9	115.0	1.427	1.254	1.435	6.400	123.9	123.1	9.6	55.4	39.7
CH ₃ HOAB	1.411	1.260	1.418	9.071	115.3	115.1	1.432	1.252	1.434	6.345	123.5	123.1	9.2	53.7	42.2
	1.410	1.261	1.418	9.082	115.7	115.3	1.429	1.255	1.435	6.333	123.7	123.1	9.7	53.2	41.8
CH ₃ OHOAB	1.411	1.260	1.417	9.070	115.3	115.1	1.432	1.252	1.435	6.287	123.3	123.0	9.0	51.5	44.6
	1.409	1.262	1.418	9.080	115.9	115.2	1.429	1.255	1.436	6.332	123.7	123.1	9.5	52.7	41.6
CF ₃ HOAB	1.408	1.260	1.418	9.066	115.5	114.7	1.428	1.251	1.431	6.379	123.5	123.2	9.3	57.1	57.1
	1.406	1.262	1.418	9.072	115.9	114.9	1.425	1.254	1.433	6.380	123.7	123.2	9.8	40.3	39.2
C ₆ H ₅ HOAB	1.411	1.259	1.418	9.072	115.3	115.0	1.434	1.252	1.436	6.148	122.8	122.5	8.0	48.1	48.1
	1.409	1.261	1.418	9.082	115.8	115.2	1.431	1.255	1.436	6.206	123.2	122.7	8.7	48.6	45.6
CH ₂ CH ₂ HOAB	1.418	1.258	1.416	9.101	115.1	115.2	1.435	1.250	1.434	6.327	123.0	123.0	9.0	49.2	51.2
	1.418	1.259	1.416	9.111	115.4	115.5	1.436	1.252	1.433	6.316	122.9	123.0	9.3	48.6	51.9
MY	1.417	1.263	1.403	9.121	114.9	115.7	1.432	1.255	1.423	6.487	123.2	124.2	10.0	35.8	56.5
	1.416	1.268	1.397	9.137	115.0	116.4	1.433	1.262	1.413	6.542	123.1	125.2	10.4	29.7	58.9
DO3	1.397	1.265	1.413	9.060	115.9	114.4	1.418	1.254	1.422	6.493	124.0	124.1	11.0	59.1	32.2
	1.386	1.273	1.408	9.065	116.6	114.3	1.406	1.261	1.418	6.574	124.7	124.5	12.8	59.2	26.6
AAB	1.417	1.262	1.406	9.101	114.9	115.6	1.433	1.253	1.427	6.458	123.2	124.0	9.7	38.0	55.6
	1.417	1.266	1.399	9.119	115.1	116.4	1.434	1.259	1.419	6.497	123.1	123.7	10.3	33.3	57.4
SO ₂ NH ₂ AB	1.401	1.263	1.416	9.069	115.8	114.5	1.421	1.254	1.427	6.455	124.2	123.5	9.8	59.3	33.1
	1.392	1.269	1.414	9.077	116.5	114.5	1.411	1.260	1.427	6.517	124.9	123.6	10.9	60.1	29.1
ADAB	1.408	1.264	1.406	9.143	115.3	115.5	1.430	1.256	1.427	6.510	123.5	123.7	11.2	42.8	45.8
	1.407	1.269	1.402	9.165	115.7	116.1	1.427	1.263	1.421	6.564	123.7	124.3	12.4	38.7	44.8
DR ₁	1.409	1.259	1.419	9.023	115.4	114.9	1.430	1.251	1.436	6.334	123.7	122.9	9.2	55.8	41.6
	1.408	1.261	1.419	9.037	115.8	115.1	1.427	1.254	1.437	6.344	124.0	122.9	9.5	55.3	40.0
F(HO) ₃ AB	1.409	1.259	1.419	9.023	115.4	114.9	1.430	1.251	1.436	6.334	123.7	122.9	9.2	55.8	41.6
	1.408	1.261	1.419	9.037	115.8	115.1	1.427	1.254	1.437	6.344	124.0	122.9	9.5	55.3	40.0
F ₃ HOAB	1.405	1.264	1.403	9.106	114.8	116.1	1.419	1.250	1.439	6.412	123.6	122.2	9.4	62.5	40.8
	1.403	1.266	1.402	9.116	115.2	116.2	1.413	1.255	1.436	6.502	124.7	122.6	9.5	60.8	35.3
HO ₃ AB	1.410	1.276	1.372	9.078	116.7	117.5	1.425	1.260	1.404	6.892	122.9	128.8	11.0	36.2	49.6
	1.410	1.276	1.373	9.079	116.8	117.3	1.428	1.261	1.405	6.833	122.8	128.2	10.6	37.8	49.3

First, it is noteworthy to highlight that the geometry optimization of the molecules under investigation resulted in all the *trans* configurations being planar, as expected, with dihedral angles C1N1N2C1, N1N2C1C6, N2N1C1C2 equal to 180 degrees.

Upon analysis of the N1N2 bond lengths, we observed that the smallest values were found in the AB and CH₂CH₂HOAB molecules. Specifically, the *trans* forms of these molecules exhibited N1N2 bond lengths of 1.258 Å in the gas phase and 1.259 Å in the presence of the water solution model. These bond lengths slightly decreased for *cis* configurations of the molecules to 1.249 Å for the gas phase and 1.252 Å in case of accounting water solution.

Dihedral angles C'1N1N2C1 of *cis* forms of studied molecules range from 8.0 to 11.9 degrees in the gas phase and 8.7 to 14.3 degrees in case of accounting PCM. These minimal and maximal angle values correspond to C₆H₅HOAB and DR₁ respectively.

The C1C6 distances, characterizing relative size of a molecule, are changing in case of *trans* conformation from 9.023 to 9.143 Å in the gas phase and from 9.037 to 9.165 Å in case of accounting water solution in calculations. These values exhibited by F(HO)₃AB and ADAB respectively. For the *cis* conformation C1C6 distances range from 6.148 to 6.892 Å in the gas phase and from 6.206 to 6.833 Å case of accounting PCM in calculations. Corresponding to these extreme cases molecules are C₆H₅HOAB and HO₃AB.

Energy

The difference in Gibbs free energies between *trans* and *cis* configurations ΔG and corresponding equilibrium constants K of studied molecules are given in Table 3.

Table 3

Calculated Gibbs free energy differences ΔG (kJ/mole) and equilibrium constants K between *trans* and *cis* configurations of the most stable conformations of the molecules studied obtained from B3LYP-D3 6-31++G(d, p) calculations in the gas phase and water solvent

Molecule	ΔG	K	Molecule	ΔG	K
AB	-55.55	5.39×10^9	DO3	-57.43	1.15×10^{10}
	-52.45	1.54×10^9		-51.69	1.14×10^9
HOAB	-57.61	1.24×10^{10}	AAB	58.44	1.73×10^{10}
	-49.65	4.98×10^8		-51.52	1.06×10^9
FHOAB	-58.88	2.07×10^{10}	SO ₂ NH ₂ AB	-55.31	4.91×10^9
	-52.96	1.90×10^9		-49.99	5.74×10^8
CH ₃ HOAB	-57.23	1.06×10^{10}	ADAB	-61.58	6.14×10^{10}
	-50.80	7.93×10^8		-57.65	1.26×10^{10}
CH ₃ OHOAB	-56.51	7.95×10^9	DR1	-55.94	6.31×10^9
	-49.37	4.45×10^8		-51.20	9.32×10^8
CF ₃ HOAB	-59.49	2.65×10^{10}	F(HO) ₃ AB	-58.43	1.72×10^{10}
	-50.23	6.30×10^8		-50.44	6.86×10^8
C ₆ H ₅ HOAB	-53.09	2.00×10^9	F ₅ HOAB	-44.30	5.77×10^7
	-45.58	9.66×10^7		-32.41	4.76×10^5
CH ₂ CH ₂ HOAB	-55.41	5.10×10^9	HO ₃ AB	-92.39	1.54×10^{16}
	-59.99	3.23×10^{10}		-85.41	9.20×10^{14}
MY	-57.40	1.14×10^{10}			
	-51.32	9.78×10^8			

The equilibrium constants were obtained using the formula:

$$K = \exp(-\Delta G / RT), \quad (1)$$

in which the ΔG is the difference in the Gibbs energies between *trans* and *cis* configurations, T is the room temperature equal to 298.15 K and R is the gas constant.

As expected, the *trans* configurations of all molecules have been found to be more stable than the *cis* configurations, with a stability difference ranging from 44.30 to 92.39 kJ/mol. This is evident from the values of the equilibrium constants, which show a significant difference in magnitude ranging from 5.77×10^7 to 1.54×10^{16} . The solvent effect is observed as decrease in Gibbs free energy differences and equilibrium constants with ΔG ranging between 32.41 and 85.41 kJ/mol and K between 4.76×10^5 and 9.20×10^{14} , correspondingly.

Based on our calculations, it has been determined that the molecules C₆H₅HOAB and F₅HOAB exhibit the smallest values of Gibbs free energy differences and equilibrium constants. Conversely, CH₂CH₂HOAB and HO₃AB exhibit the highest values of these parameters.

Electronic properties

It is well known that the dipole moment of molecules is determined by the formula:

$$p = p_0 + \alpha E + \frac{1}{2} \beta E E + \dots, \quad (2)$$

in which p_0 is the dipole moment without electric field, α is the second-order tensor of the polarizability and β is the first term in infinite series of hyperpolarizabilities. The polarizability tensor has been diagonalized and afterwards the mean and anisotropic polarizabilities have been obtained using the following formulas:

$$\alpha_{mean} = \frac{1}{3}(\alpha_{xx} + \alpha_{yy} + \alpha_{zz}), \quad (3)$$

$$\alpha_{anis} = \sqrt{\frac{(\alpha_{xx} - \alpha_{yy})^2 + (\alpha_{yy} - \alpha_{zz})^2 + (\alpha_{xx} - \alpha_{zz})^2}{2}}, \quad (4)$$

in which α_{xx} , α_{yy} , α_{zz} are the diagonal elements of the polarizability matrix.

All the computed values for dipole moments their differences between the *trans* and *cis* configurations of the most stable conformations of the molecules under investigation are summarized in Table 4, besides, corresponding mean and anisotropic polarizabilities are listed in Table 5. As expected, the calculations accounting a water solvent yielded larger values compared to those obtained in the gas phase, as water serves as a more polarized medium.

Table 4

Calculated dipole moments μ (Debye), their differences between the *trans* and *cis* configurations of the most stable conformations of the studied molecules obtained from B3LYP-D3 6-31++G(d, p) calculations in the gas phase and water solvent

Molecule	μ_{trans}	μ_{cis}	$\Delta\mu$	Molecule	μ_{trans}	μ_{cis}	$\Delta\mu$
AB	0.00	3.45	3.45	DO3	10.34	7.41	-2.93
	0.00	4.72	4.72		15.61	10.57	-5.04
HOAB	1.65	3.37	1.75	AAB	3.10	5.16	2.06
	2.28	4.76	2.48		5.51	7.70	2.19
FHOAB	2.04	2.51	0.46	SO ₂ NH ₂ AB	8.03	3.47	-4.55
	2.73	3.54	0.81		12.25	4.99	-7.25
CH ₃ HOAB	1.13	3.67	2.54	ADAB	1.35	6.24	4.89
	1.60	5.23	3.63		2.41	9.00	6.59
CH ₃ OHOAB	2.84	2.51	0.46	DR1	9.99	7.21	-2.79
	4.05	5.49	1.43		15.36	10.49	-4.87
CF ₃ HOAB	4.97	3.05	-1.92	F(HO) ₃ AB	1.53	3.81	2.28
	6.28	4.20	-2.07		2.03	5.35	3.32
C ₆ H ₅ HOAB	1.56	4.30	2.75	F ₅ HOAB	4.27	4.50	0.23
	2.17	6.08	3.92		5.10	5.97	0.87
CH ₂ CH ₂ HOAB	1.53	2.48	0.95	HO ₃ AB	2.06	2.34	0.28
	1.92	5.38	3.46		2.88	3.22	0.34
MY	4.28	6.38	2.10				
	6.71	9.58	2.87				

As part of our endeavor to create materials with the ability to switch their wettability under light exposure, we are particularly interested in molecules that exhibit a substantial difference in dipole moments between their *trans* and *cis* forms. The presence of a non-zero dipole moment indicates a polar molecule. When the magnitude of this dipole moment decreases, the dipole-dipole interaction between the molecule and water molecules also diminishes. Consequently, this reduction in interaction leads to a less hydrophilic state in terms of wettability.

Table 5

Calculated mean and anisotropic polarizabilities α , and their differences between the *trans* and *cis* configurations of the most stable conformations of the studied molecules obtained from B3LYP-D3 6-31++G(d, p) calculations in the gas phase and water solvent

Molecule	α_{trans}^{mean}	α_{trans}^{anis}	α_{cis}^{mean}	α_{cis}^{anis}	$\Delta\alpha^{mean}$	$\Delta\alpha^{anis}$
AB	183.13	202.86	157.90	79.61	25.22	123.25
	255.20	279.02	221.89	102.05	33.31	176.98
HOAB	194.94	231.47	166.95	95.83	27.99	135.63
	274.31	326.19	235.82	125.87	38.49	200.32
FHOAB	195.56	233.55	166.80	93.94	28.76	139.61
	274.34	330.21	234.56	124.91	39.78	205.30
CH ₃ HOAB	209.76	240.00	178.98	87.34	30.79	152.66
	332.76	292.85	253.00	119.62	39.85	213.15
CH ₃ OHOAB	214.88	233.15	182.13	80.16	32.75	152.99
	301.28	331.79	259.11	117.96	42.17	213.83

Continuation of Table 5

Molecule	α_{trans}^{mean}	α_{trans}^{anis}	α_{cis}^{mean}	α_{cis}^{anis}	$\Delta\alpha^{mean}$	$\Delta\alpha^{anis}$
CF ₃ HOAB	213.58	256.98	181.45	97.03	32.13	159.95
	295.52	350.02	252.94	125.42	42.58	224.60
C ₆ H ₅ HOAB	278.39	295.65	235.08	107.25	43.30	188.40
	384.30	385.50	338.41	157.26	45.89	228.23
CH ₂ CH ₂ HOAB	220.39	244.29	190.94	99.29	29.45	145.00
	300.78	315.35	262.30	113.86	38.48	201.50
MY	247.59	311.68	209.27	132.92	38.32	178.76
	364.42	483.67	306.23	204.87	58.19	278.80
DO3	251.40	359.38	207.66	138.99	43.73	220.39
	417.03	693.03	319.65	233.22	97.38	459.81
AAB	209.33	261.61	177.46	108.02	31.87	153.60
	311.10	416.70	258.48	160.95	52.62	255.75
SO ₂ NH ₂ AB	258.47	326.97	217.91	130.69	40.57	196.28
	378.18	499.48	313.64	179.70	64.54	319.78
ADAB	272.01	365.74	225.31	143.98	46.69	221.75
	404.38	573.73	335.62	227.97	68.77	345.76
DR1	328.69	446.52	274.75	179.75	53.94	266.76
	534.16	845.84	418.08	300.55	116.08	545.29
F(HO) ₃ AB	206.37	242.27	176.38	95.62	29.99	146.66
	287.45	334.48	247.43	126.17	40.02	208.31
F ₅ HOAB	198.14	236.05	169.21	92.11	28.92	143.94
	280.14	354.14	237.49	135.39	42.65	218.75
HO ₃ AB	211.78	257.44	181.57	131.85	30.22	125.59
	300.51	368.79	259.57	174.61	40.95	194.18

The *trans* configuration of AB displayed the smallest dipole moment, measuring 0 Debye, which is consistent with its symmetrical molecular structure. Among the azobenzene derivatives, CH₃HOAB and ADAB exhibited the smallest dipole moments of 1.13 and 1.35 Debye, respectively, in the gas phase. In the water solvent model, these values increased to 1.60 and 2.41 Debye. It is noteworthy that these relatively small dipole moments can be attributed to the compensating effects of the substituted functional groups.

Nevertheless, the ADAB molecule exhibited the most substantial difference in dipole moments between *cis-trans* configurations, surpassing that of AB. This difference amounted to 4.89 Debye in the gas phase and 6.59 when considering water solvent in calculations, compared to 3.45 and 4.72 Debye for AB. Notably, CH₃HOAB and C₆H₅HOAB molecules can be also taken into account as the ones switching wettability from more to less hydrophilic states, with $\Delta\mu$ values for *cis-trans* configurations equal to 2.54 and 2.75 Debye, respectively, increasing to 3.63 and 3.92 Debye in the water solvent model.

It is crucial to highlight instances of negative differences in dipole moments for DO3, DR1, and SO₂NH₂AB. This suggests that the *cis-trans* transition may conversely result in a more hydrophilic state. Particularly noteworthy is the case of SO₂NH₂AB, exhibiting the highest negative difference in dipole moments compared to AB, with $-\Delta\mu$ values of 4.55 and 7.25 in the gas phase and water solvent model calculations, respectively.

Spectroscopic methods offer a means to determine the components of the polarizability matrix. However, obtaining such data can be challenging due to the demanding experimental procedures, particularly for molecules with low or no symmetry. This is where molecular modeling calculations can prove invaluable in fulfilling this objective.

According to our computations, molecules exhibiting the lowest mean polarizability differences include HOAB, F₅HOAB and HO₃AB, with respective values of 27.99, 28.76 and 30.22 au in the gas phase, and 38.49, 39.78 and 40.95 au when considering water solvent in calculations. These values contrast with AB, which registers at 25.22 and 33.31 au, respectively. The corresponding anisotropic polarizability differences for these molecules are 135.63, 139.61, and 125.59 au in the gas phase, and 200.32, 205.30, and 194.18 au when water solvent is considered, compared to AB with values of 123.25 and 176.98 au.

Conversely, molecules with the highest mean polarizability differences include DO3, DR1 and ADAB, exhibiting values of 43.73, 53.94 and 46.69 au in the gas phase, and 97.38, 116.08 and 68.77 au when con-

sidering water solvent. The corresponding anisotropic polarizability differences for these molecules are 220.39, 266.76, and 221.75 au in the gas phase, and 459.81, 545.29, and 345.76 au when accounting for water solvent in calculations.

Molecular properties

In the present work we have obtained the energy of the highest occupied molecular orbital (HOMO) and the energy of the lowest unoccupied molecular orbital (LUMO) as the frontier orbitals of chemical compounds play a vital role in determining their reactivity [22]. It is noteworthy that molecules with a higher HOMO value possess the ability to donate electrons to acceptor molecules with low energy and empty molecular orbitals. Table 6 showcases the calculated HOMO and LUMO energies for studied azobenzene derivatives. Notably, the *trans* and *cis* configurations of the ADAB molecule exhibit the highest HOMO and LUMO values.

Table 6

Calculated molecular properties of *trans* and *cis* configurations of the studied molecules obtained from B3LYP-D3 6-31++G(d, p) calculations in the gas phase and water solvent. Values are in eV

Molecule	<i>trans</i>						<i>cis</i>					
	HOMO	LUMO	Δ LUMO –HOMO	μ	η, τ	χ	HOMO	LUMO	Δ LUMO –HOMO	μ	η, τ	χ
AB	–6.46	–2.54	3.93	–4.50	1.96	4.50	–6.06	–2.29	3.77	–4.18	1.89	4.18
	–6.60	–2.73	3.87	–4.66	1.94	4.66	–6.27	–2.48	3.79	–4.37	1.89	4.37
HOAB	–6.11	–2.39	3.72	–4.25	1.86	4.25	–5.86	–2.19	3.68	–4.02	1.84	4.02
	–6.23	–2.60	3.63	–4.41	1.81	4.41	–6.04	–2.40	3.64	–4.22	1.82	4.22
FHOAB	–6.27	–2.59	3.68	–4.43	1.84	4.43	–6.04	–2.36	3.68	–4.20	1.84	4.20
	–6.31	–2.72	3.59	–4.51	1.79	4.51	–6.14	–2.50	3.65	–4.32	1.82	4.32
CH ₃ HOAB	–6.05	–2.33	3.72	–4.19	1.86	4.19	–5.81	–2.14	3.68	–3.98	1.84	3.98
	–6.19	–2.57	3.62	–4.38	1.81	4.38	–6.01	–2.38	3.63	–4.19	1.82	4.19
CH ₃ OHOAB	–6.00	–2.38	3.61	–4.12	1.81	4.19	–5.86	–2.21	3.65	–4.03	1.82	4.03
	–6.14	–2.61	3.54	–4.31	1.77	4.38	–6.02	–2.41	3.60	–4.22	1.80	4.22
CF ₃ HOAB	–6.14	–2.61	3.54	–4.31	1.77	4.38	–6.02	–2.41	3.60	–4.22	1.80	4.22
	–6.38	–2.83	3.55	–4.60	1.78	4.60	–6.21	–2.58	3.64	–4.40	1.82	4.40
C ₆ H ₅ HOAB	–6.09	–2.40	3.68	–4.25	1.84	4.25	–5.90	–2.24	3.66	–4.07	1.83	4.07
	–6.21	–2.62	3.59	–4.41	1.80	4.41	–6.04	–2.44	3.60	–4.24	1.80	4.24
CH ₂ CH ₂ HOAB	–6.37	–2.51	3.86	–4.44	1.93	4.44	–6.02	–2.27	3.74	–4.14	1.87	4.14
	–6.50	–2.70	3.80	–4.60	1.90	4.60	–6.18	–2.45	3.74	–4.32	1.87	4.32
MY	–5.38	–2.09	3.29	–3.73	1.65	3.73	–5.33	–1.90	3.44	–3.62	1.72	3.62
	–5.46	–2.41	3.05	–3.93	1.52	3.93	–5.46	–2.21	3.26	–3.83	1.63	3.83
DO3	–6.13	–3.12	3.01	–4.62	1.50	4.62	–6.06	–2.96	3.11	–4.51	1.55	4.51
	–5.90	–3.34	2.56	–4.62	1.28	4.62	–5.90	–3.17	2.73	–4.54	1.37	4.54
AAB	–5.68	–2.19	3.48	–3.93	1.74	3.93	–5.56	–2.00	3.56	–3.78	1.78	3.78
	–5.66	–2.43	3.23	–4.04	1.62	4.04	–5.71	–2.27	3.44	–3.99	1.72	3.99
SO ₂ NH ₂ AB	–5.97	–2.63	3.34	–4.30	1.67	4.30	–5.87	–2.36	3.50	–4.12	1.75	4.12
	–5.87	–2.77	3.10	–4.32	1.55	4.32	–5.86	–2.50	3.36	–4.18	1.68	4.18
ADAB	–5.02	–1.80	3.22	–3.41	1.61	3.41	–5.01	–1.72	1.53	–0.95	0.77	0.95
	–5.17	–2.19	2.99	–3.68	1.49	3.68	–5.17	–2.12	1.93	–1.16	0.97	1.16
DR1	–5.91	–3.09	2.81	–4.50	1.41	4.50	–5.72	–2.88	2.84	–4.30	1.42	4.30
	–5.69	–3.32	2.37	–4.51	1.19	4.51	–5.63	–3.15	2.48	–4.39	1.24	4.39
F(HO) ₃ AB	–6.15	–2.46	3.70	–4.31	1.85	4.31	–5.95	–2.25	3.70	–4.10	1.85	4.10
	–6.23	–2.64	3.59	–4.43	1.79	4.43	–6.07	–2.44	3.63	–4.26	1.82	4.26
F ₅ HOAB	–6.58	–2.94	3.64	–4.76	1.82	4.76	–6.55	–2.79	3.76	–4.67	1.88	4.67
	–6.45	–2.97	3.48	–4.71	1.74	4.71	–6.47	–2.81	3.66	–4.64	1.83	4.64
HO ₃ AB	–6.16	–2.72	3.44	–4.44	1.72	4.44	–6.03	–2.55	3.48	–4.29	1.74	4.29
	–6.19	–2.75	3.44	–4.47	1.72	4.47	–6.13	–2.64	3.49	–4.38	1.74	4.38

In accordance with Ref. [23] there is a linear correlation between an ionization potential (IP), an electron affinity (EA) and frontier orbitals: HOMO is associated with IP, LUMO can be equated with EA. To

explore the connection between chemical quantities and molecular properties, chemical potential μ , absolute hardness η , the first electronic excitation energy τ and electronegativity χ were evaluated using following formulas [22, 23]:

$$\eta = (E_{LUMO} - E_{HOMO}) / 2, \quad (5)$$

$$\chi = -(E_{LUMO} + E_{HOMO}) / 2, \quad (6)$$

$$\mu = (E_{LUMO} + E_{HOMO}) / 2, \quad (7)$$

$$\tau = \eta, \quad (8)$$

The results of our calculations are collected in Table 6. According to chemical potential values, that are smaller for *trans* configurations of all molecules, than for *cis*, molecules are tending to transit from *cis* to *trans* configuration, that is in accordance with Gibbs free energy results, showing the *trans* isomerization is more stable.

The concept of hardness in the context of molecular systems is closely linked to reactivity. Specifically, a system with a higher value of absolute hardness η tends to exhibit lower reactivity compared to a system with a lower value [22]. Our findings indicate that the molecules AB and CH₂CH₂HOAB display relatively lower reactivity, suggesting that they are less prone to undergo chemical reactions. On the other hand, the molecules DO3, DR1, and ADAB demonstrate higher reactivity, indicating that they are more likely to engage in chemical transformations.

We found that the inclusion of the water solution model led to a decrease in the energy levels of HOMO and LUMO, as well as a decrease in the energy gap between them (Δ LUMO-HOMO). Therefore, we observed that the chemical potential and absolute hardness values also decreased compared to calculations performed in the gas phase. These findings suggest that the presence of a water solution in the calculations enhances the reactivity of the molecules under study. By considering the water solution model, there is a greater propensity for chemical reactions to occur. This highlights the importance of considering solvent effects when assessing the reactivity of molecules, as the water solution model can significantly influence their electronic properties and overall reactivity.

Conclusion

The current research presented DFT calculations for molecules from azobenzene family. Specifically, we investigated 17 molecules using an innovative approach that incorporates DFT-D3 dispersion corrections, enhancing the accuracy of our results. Furthermore, we considered the effects of a water solvent by employing the polarizable continuum model (PCM), a technique that has not been applied in prior evaluations of these molecules.

Overall, adding the solvent model (water in our case) increases dipole moments for most molecules, with a stronger effect on highly polar compounds like SO₂NH₂AB, DO3, and DR1. In contrast, fluorinated molecules and some alkyl-substituted derivatives show relatively small changes, indicating that their dipole moments are less affected by solvation. The solvent generally enhances the contrast between *trans* and *cis* dipole moments, making the difference more pronounced in most cases.

The dipole moment difference between the *trans* and *cis* configurations was found to be lower in all considered molecules compared to azobenzene, except for ADAB. In the gas phase, ADAB exhibited a dipole moments difference of 4.89 Debye, whereas calculations including PCM yielded a difference of 6.89 Debye.

The relative difference in the dipole moment between the *trans* and *cis* configurations was found to be lower than for azobenzene for all considered molecules except for ADAB, for which the difference was obtained equal to 4.89 Debye in the gas phase and 6.89 Debye in calculations including PCM. Hence, materials incorporating this azobenzene derivative can be regarded as photoswitchable materials capable of transitioning between more and less hydrophilic states by transforming from the *cis* to *trans* configurations. This ability to switch wettability makes these materials promising candidates for various applications.

Moreover, ADAB molecule exhibited the largest mean and anisotropic polarizabilities, as well as the highest HOMO and LUMO energies. Also, ADAB molecules have shown to be the most reactive.

The highest negative difference in the dipole moments between *cis* and *trans* configurations was found for SO₂NH₂AB molecule. In the gas phase, this difference amounted to 4.55 Debye, while in the water solvent model it increased to 7.25 Debye. This finding suggests that this molecule holds promise for applica-

tions where the wettability of a surface needs to be altered under light irradiation, transitioning from a less hydrophilic state to a more hydrophilic state. Such materials could prove valuable in various fields requiring controllable surface properties.

These remarkable characteristics make the ADAB and $\text{SO}_2\text{NH}_2\text{AB}$ molecules an intriguing subject for further exploration and potential applications.

Г. Адырбекова, П. Саидахметов, Р. Бурганова, И. Пиянзина,
Г. Байман, Г. Баубекова, Д. Таюрский

Тығыздықтың функционалдық теориясы шеңберінде сулануды өзгерту үшін азобензол туындыларын әлеуетті материалдар ретінде зерттеу

Зерттеуде тығыздықтың функционалдық теориясы (ТФТ) ылғалдылықты өзгертетін материалдар ретінде олардың әлеуетін бағалай отырып, 16 туынды азобензолдың қасиеттерін талдау үшін қолданылады. К. Ичимураның (2001) азобензолмен модификацияланған беттің сулануы туралы баяндамасынан шабыттана отырып, біз азобензолдың әртүрлі туындыларының *цис* және *транс*-конфигурациялары арасындағы молекулалық диполь моменттерінің өзгеруінен туындаған фотоизомеризацияның әсерін зерттедік. Бұл процесс бастапқы азобензол молекуласында полярлы емес молекуланы гидрофильді *цис* түріне айналдырады. Беттік қабаттың сулануын бақылау өнеркәсіптік, медициналық, микробиология, электроника және материалтану сияқты әртүрлі салаларда орасан зор әлеуетке ие. Осы бақылауды пайдалана отырып, біз инновациялық материалдарды жасау, функционалдылық пен тиімділікті арттыру әлеуетін аша аламыз. Бұл өнімнің өнімділігін жақсартуға, адгезияны жақсартуға және сұйықтықтарды өңдеу кезінде дәлдікке қол жеткізуге мүмкіндік береді. Дисперсиялық түзетілген DFT-D3 гибриді функционалды B3LYP және 6-31++G(d, p) базалық жиынтығын пайдаланып, зерттелген барлық молекулалардың құрылымдық, электронды және молекулалық аспектілері зерттелді, беттік қабаттың икемділігін басқаруға арналған перспективалы азот типті құрылымдар ұсынылды. Әлеуетті үміткер ретінде азобензолдың екі туындысы ұсынылған, олар *цис-транс* фотоизомерленуі кезінде бірі гидрофильділіктің жоғарылау бағытында, екіншісі қарама-қарсы бағытта түрлендірулерді көрсетеді.

Кілт сөздер: азобензол туындысы, ылғалдылыққа ауысу, фотоизомеризация, диполь моменттері, *cis-trans* конфигурациялары, DFT, B3LYP функционалдық, 6-31++G(d, p) базалық жинағы, фотоөткізгіш материалдар, гидрофильділік

Г. Адырбекова, П. Саидахметов, Р. Бурганова, И. Пиянзина,
Г. Байман, Г. Баубекова, Д. Таюрский

Исследование производных азобензола в рамках теории функционала плотности как потенциальные материалы для переключения смачиваемости

В этом исследовании теория функционала плотности (DFT) используется для анализа свойств 16 производных азобензола, оценивая их потенциал в качестве материалов, изменяющих смачиваемость. Вдохновленные докладом К. Ичимуры (2001) о смачиваемости поверхности, модифицированной азобензолом, мы изучаем влияние фотоизомеризации, вызванной изменением молекулярных дипольных моментов между *цис*- и *транс*-конфигурациями различных производных азобензола. В исходной молекуле азобензола этот процесс преобразует неполярную молекулу в более гидрофильную *цис*-форму. Контроль смачиваемости поверхности имеет большое значение в различных областях, таких как промышленность, медицина, микробиология, электроника и материаловедение. Используя этот контроль, мы можем раскрыть потенциал для создания инновационных материалов, повышения функциональности и эффективности. Он позволяет улучшить эксплуатационные характеристики продукта, улучшить адгезию и достичь точности при обращении с жидкостями. Нами изучены структурные, электронные и молекулярные аспекты всех исследованных молекул с помощью гибридного функционала B3LYP с дисперсионной коррекцией DFT-D3 и базисного набора 6-31++G(d, p), представив перспективные структуры азотистого типа для манипулирования смачиваемостью поверхности. Два производных азобензола выступают в качестве потенциальных кандидатов, демонстрируя трансформации в процессе *цис-транс* фотоизомеризации — одна в сторону увеличения гидрофильности, другая — в противоположном направлении.

Ключевые слова: производное азобензола, переключение смачиваемости, фотоизомеризация, дипольные моменты, *цис-транс* конфигурации, DFT, функционал B3LYP, базовый набор 6-31++G(d, p), фотопереключаемые материалы, гидрофильность

References

- 1 Feng, C.L., Zhang, Y.J., Jin, J., Song, Y.L., Xie, L.Y., Qu, G.R., Jiang, L., & Zhu, D.B. (2001). Reversible wettability of photoresponsive fluorine-containing azobenzene polymer in Langmuir Blodgett films. *Langmuir*, 17(15), 4593–4597. <https://doi.org/10.1021/la010071r>
- 2 Miyauchi, M., Nakajima, A., Watanabe, T., & Hashimoto, K. (2002). Photocatalysis and photoinduced hydrophilicity of various metal oxide thin films. *Chemistry of Materials*, 14(6), 2812–2816. <https://doi.org/10.1021/cm020076p>
- 3 Ambrogio, M.W., Thomas, C.R., Zhao, Y.-L., Zink, J.I., & Stoddart, J.F. (2011). Mechanized silica nanoparticles: a new frontier in theranostic nanomedicine. *Accounts of chemical research*, 44(10), 903–913. <https://doi.org/10.1021/ar200018x>
- 4 Yu, X., Wang, Z., Jiang, Y., Shi, F., & Zhang, X. (2005). Reversible phresponsive surface: From superhydrophobicity to superhydrophilicity. *Advanced Materials*, 17(10), 1289–1293. <https://doi.org/10.1002/adma.200401646>
- 5 Minko, S., Muller, M., Motornov, M., Nitschke, M., Grundke, K., & Stamm, M. (2003). Two-level structured self-adaptive surfaces with reversibly tunable properties. *Journal of the American Chemical Society*, 125(13), 3896–3900. <https://doi.org/10.1021/ja0279693>
- 6 Wang, S., Song, Y., & Jiang, L. (2007). Photoresponsive surfaces with controllable wettability. *Journal of Photochemistry and Photobiology C: Photochemistry Reviews*, 8(1), 18–29. <https://doi.org/10.1016/j.jphotochemrev.2007.03.001>
- 7 Ichimura, K., Oh, S.-K., & Nakagawa, M. (2000). Light-driven motion of liquids on a photoresponsive surface. *Science*, 288(5471), 1624–1626. <https://doi.org/10.1126/science.288.5471.1624>
- 8 Von Seggern, N., Oehlsen, N., Moudrakovski, I., & Stegbauer, L. (2023). Photo-modulation of the mechanical properties and photo-actuation of chitosan-based thin films modified with an azobenzene-derivative. *Small*, 2308939. <https://doi.org/10.1002/sml.202308939>
- 9 Bricen˜o-Ahumada, Z., Tapia-Burgos, J.A., D'íaz-Leyva, P., Cadena-Aguilar, A., Garcia-Hernandez, F., & Kozina, A. (2023). Synthesis and cis-trans kinetics of an azobenzene-based molecular switch for light-responsive silica surfaces. *Journal of Molecular Liquids*, 390 (Part A), 122900. <https://doi.org/10.1016/j.molliq.2023.122900>
- 10 Sever, M., & Young, M.A. (2023). Isomerization kinetics of hydroxy-substituted azobenzenes using a modified commercial flash photolysis spectrometer. *Journal of Chemical Education*, 100(7), 2762–2769. <https://doi.org/10.1021/acs.jchemed.3c00200>
- 11 Aleotti, F., Petropoulos, V., Van Overeem, H., Pettini, M., Mancinelli, M., Pecorari, D., Maiuri, M., Medri, R., Mazzanti, A., & Preda, F., et al (2023). Engineering azobenzene derivatives to control the photoisomerization process. *The Journal of Physical Chemistry A*, 127(49), 10435–10449. <https://doi.org/10.1021/acs.jpca.3c06108>
- 12 Sıdır, İ., Gülseven Sıdır, Y., Berber, H., & Fausto, R. (2025). Solvatochromism and cis-trans isomerism in azobenzene-4-sulfonyl chloride. *Photochemical & Photobiological Sciences*, 1–15. <https://doi.org/10.1007/s43630-025-00684-0>
- 13 Sıdır, İ., Sıdır, Y.G., Berber, H., & Fausto, R. (2022). Solvato-, thermo- and photochromism in a new diazo diaromatic dye: 2-(p-tolyldiazenyl)naphthalen-1-amine. *Journal of Molecular Structure*, 1267, 133595. <https://doi.org/10.1016/j.molstruc.2022.133595>
- 14 Sıdır, İ., Kara, Y.E., Sıdır, Y.G., Berber, H., & Fausto, R. (2024). Reversal in solvatochromism, photochromism and thermochromism in a new bis-azo dye based on naphthalen-1-amine. *Journal of Photochemistry and Photobiology A: Chemistry*, 446, 115138. <https://doi.org/10.1016/j.jphotochem.2023.115138>
- 15 Ramírez-Rave, S., Ortega-Valdovinos, L.R., González-Castro, A.P., Yatsimirsky, A.K. (2024). Solvent and Temperature Dependencies of the Rates of Thermal Cis-to-Trans Isomerization of Tetra-(ortho) substituted 4-Aminoazobenzenes Containing 2,6-Dimethoxy Groups. *The Journal of Physical Chemistry B*, 128(31), 7639–7652. <https://doi.org/10.1021/acs.jpcc.4c02951>
- 16 Birla, H., Mir, S.H., Yadav, K., Halbritter, T., Heckel, A., Singh, J.K., & Gopakumar, T.G. (2023). Tuning the Switching Probability of Azobenzene Derivatives on Graphite Surface through Chemical Functions. *The Journal of Physical Chemistry C*, 127(34), 17039–17050. <https://doi.org/10.1021/acs.jpcc.3c02334>
- 17 Saito, N., Itoyama, S., Takahashi, R., Takahashi, Y., & Kondo, Y. (2021). Synthesis and surface activity of photoresponsive hybrid surfactants containing both fluorocarbon and hydrocarbon chains. *Journal of Colloid and Interface Science*, 582, 638–646. <https://doi.org/10.1016/j.jcis.2020.08.054>
- 18 Frisch, M.J., Trucks, G.W., Schlegel, H.B., Scuseria, G.E., Robb, M.A., Cheeseman, J.R., Scalmani, G., Barone, V., Petersson, G.A., Nakatsuji, H., Li, X., Caricato, M., Marenich, A.V., Bloino, J., Janesko, B.G., Gomperts, R., Mennucci, B., Hratchian, H.P., Ortiz, J.V., Izmaylov, A.F., Sonnenberg, J.L., Williams-Young, D., Ding, F., Lipparini, F., Egidi, F., Goings, J., Peng, B., Petrone, A., Henderson, T., Ranasinghe, D., Zakrzewski, V.G., Gao, J., Rega, N., Zheng, G., Liang, W., Hada, M., Ehara, M., Toyota, K., Fukuda, R., Hasegawa, J., Ishida, M., Nakajima, T., Honda, Y., Kitao, O., Nakai, H., Vreven, T., Throssell, K., Montgomery, J.A., Jr Peralta, J.E., Ogliaro, F., Bearpark, M.J., Heyd, J.J., Brothers, E.N., Kudin, K.N., Staroverov, V.N., Keith, T.A., Kobayashi, R., Normand, J., Raghavachari, K., Rendell, A.P., Burant, J.C., Iyengar, S.S., Tomasi, J., Cossi, M., Millam, J.M., Klene, M., Adamo, C., Cammi, R., Ochterski, J.W., Martin, R.L., Morokuma, K., Farkas, O., Foresman, J.B., & Fox, D.J. (2016). Gaussian 16 Revision C.01 Gaussian Inc. Wallingford CT.
- 19 Schlegel, H.B. (1982). Optimization of equilibrium geometries and transition structures. *Journal of Computational Chemistry*, 3(2), 214–218. <https://doi.org/10.1002/jcc.540030212>
- 20 Minisini, B., Fayet, G., Tsobnang, F., & Bardeau, J.F. (2007). Density functional theory characterization of 4-hydroxyazobenzene. *Journal of molecular modeling*, 13(12), 1227–1235. <https://doi.org/10.1007/s00894-007-0244-1>
- 21 Piyanzina, I., Minisini, B., Tayurskii, D., & Bardeau, F. (2015). *Journal of molecular modeling*, 21(34). DOI 10.1007/s00894-014-2540-x.

22 Mendoza-Huizar, L.H., & Rios-Reyes, C.H. (2011). Chemical reactivity of atrazine employing the fukui function. *Journal of the Mexican Chemical Society*, 55(3), 142–147. <https://doi.org/10.29356/jmcs.v55i3.812>

23 Zhan, C-G., Nichols, J.A., & Dixon, D.A. (2003). Ionization potential, electron affinity, electronegativity, hardness, and electron excitation energy: Molecular properties from density functional theory orbital energies. *The Journal of Physical Chemistry A*, 107(20), 4184–4195. <https://doi.org/10.1021/jp0225774>

Information about the authors

Adyrbekova, Gulmira — Associate professor (Chemistry), M. Auezov South Kazakhstan University, Shymkent, Kazakhstan; e-mail: adyrbekova.gulmira@mail.ru; ORCID ID: <https://orcid.org/0000-0003-4411-7713>

Saidakhmetov, Pulat (*corresponding author*) — Candidate of Science (Physics), Assistant professor, Department of Physics, M. Auezov South Kazakhstan University, Shymkent, Kazakhstan; e-mail: timpf_ukgu@mail.ru; ORCID ID: <https://orcid.org/0000-0002-9146-047X>

Burganova, Regina — Institute of Physics, Kazan Federal University, Kremlyovskaya St. 18, Kazan, 420008, Tatarstan, Russia; e-mail: bur.regina@gmail.com; ORCID ID: <https://orcid.org/0000-0002-5985-265X>

Irina, Piyanzina — PhD senior research fellow, Institute of Physics, Kazan Federal University, Kremlyovskaya St. 18, Kazan, 420008, Tatarstan, Russia; e-mail: i.piyanzina@gmail.com; ORCID ID: <https://orcid.org/0000-0003-4251-9196>

Baiman, Gulzagira — Senior Lecturer, Department of Physics, M. Auezov South Kazakhstan University, Shymkent, Kazakhstan; e-mail: bgb_zht@mail.ru; ORCID ID: <https://orcid.org/0000-0003-4250-842X>

Baubekova, Gulnara — Senior Lecturer, Department of Physics, M. Auezov South Kazakhstan University, Shymkent, Kazakhstan; e-mail: baubekova83@mail.ru; ORCID ID: <https://orcid.org/0009-0006-5638-0470>

Tayurskii, Dmitrii — Doctor of Science (Physics and mathematics), Professor, Vice-rector, Kazan Federal University, Kremlyovskaya St. 18, Kazan, Russia; e-mail: Dmitry.Tayurskii@kpfu.ru; ORCID ID: <https://orcid.org/0000-0001-6106-7581>

T.E. Seisembekova^{1✉}, A.K. Aimukhanov¹, A.K. Zeinidenov¹, A.M. Alexeev², D.R. Abeuov¹¹Karaganda Buketov University, Scientific Center for Nanotechnology
and Functional Nanomaterials, Karaganda, Kazakhstan;
²Kazan Federal University, Kazan, Russia

The effect of MoSe₂ nanoparticles on the properties ZnO electron transport layer of organic solar cell

This study investigates the impact of MoSe₂ nanoparticle doping on the structural, optical, and electrical properties of the ZnO electron transport layer (ETL), as well as its effect on the efficiency of organic solar cells (OSCs). ZnO:MoSe₂ composites were synthesized using the sol-gel method, and their morphology was analyzed by transmission electron microscopy (TEM) and scanning electron microscopy (SEM). Optical studies revealed an increase in the bandgap width and enhanced defect-related emission, indicating improved charge carrier dynamics. Electrical measurements confirmed increased conductivity and reduced charge recombination with the addition of MoSe₂. Organic solar cells based on ZnO:MoSe₂ demonstrated enhanced photovoltaic performance compared to pure ZnO devices. The optimal device was achieved at MoSe₂ concentration of 8 %, where the short-circuit current density (J_{sc}) increased from 7.25 mA/cm² to 10.02 mA/cm², the fill factor (FF) improved from 0.37 to 0.52, and the power conversion efficiency (PCE) rose from 0.7 % to 3.3 %. These results confirm the potential of ZnO:MoSe₂ nanocomposites for high-performance optoelectronic and photovoltaic devices.

Keywords: ZnO, MoSe₂, composite film, surface morphology, optical and impedance spectroscopy

✉ *Corresponding author:* Seisembekova Togzhan, tosh_0809@mail.ru

Introduction

Enhancing the performance of photovoltaic devices can be achieved by incorporating 2D materials, which exhibit unique optical and electronic properties. Due to their ease of fabrication and processing, environmental friendliness, stability, and chemical compatibility with other materials in composites, 2D materials are widely used in photovoltaics as efficient transport layers. Among these 2D structures, transition metal dichalcogenides (TMDs) stand out due to their high charge carrier mobility ($10\text{--}10^3\text{ cm}^2\cdot\text{V}^{-1}\cdot\text{s}^{-1}$), transparency in the visible spectrum, and direct bandgap at the monolayer level. Integrating such structures into organic solar cells enables tuning of the bandgap, physical and chemical properties, and formation of van der Waals heterojunctions with other materials used in solar cells. These advantages make TMDs promising candidates for composite photovoltaic devices [1–5].

The 2D TMDs such as MoS₂, MoSe₂, and WSe₂ offer the possibility of tuning the bandgap and chemical properties and creating various van der Waals heterostructures with other materials. Due to their unique monolayer structure, the unshared electron pairs of S and Se atoms can facilitate fast charge transport, thereby increasing charge carrier mobility [6, 7].

However, using MoSe₂ nanoparticles alone does not form a continuous layered structure. Thus, we incorporated them into a ZnO layer synthesized via the sol-gel method to create a suitable composite electron transport layer for high-performance photovoltaic devices. The effect of ZnO doped with 2D TMD nanoparticles on the morphological, optical, and electrical transport properties remains insufficiently studied.

In this study, nanocomposite structures of ZnO doped with MoSe₂ were fabricated. The resulting ZnO:MoSe₂ thin films were used as electron transport layers (ETL) in organic solar cells (OSCs). The influence of MoSe₂ content, morphology, and nanocomposite ETL structure on charge transport and photovoltaic properties was thoroughly investigated. Few studies have been published on the fabrication of solar cells based on ZnO:MoSe₂ nanocomposite films. This work demonstrates that adding MoSe₂ nanoparticles to the ZnO-based ETL significantly improves solar cell efficiency.

Experimental

The ZnO precursor solution was prepared by dissolving 98.7 mg of zinc acetate ($\text{Zn}(\text{CH}_3\text{COO})_2$, 99.9 % purity, Sigma-Aldrich) in 1 ml of isopropanol (99.9 % purity, Sigma-Aldrich). To enhance the solubility of zinc acetate in isopropanol, 75 μl of monoethanolamine was added to the solution. The final solution was stirred at 60 °C for 2 hours and then left at room temperature for 24 hours.

MoSe_2 nanoparticles were obtained by ablation using a solid-state Nd:YAG laser (SOLAR LQ 529, $\lambda = 532$ nm, $E = 193$ mJ, $\tau = 20$ ns) in isopropanol. The concentration of MoSe_2 powder was 0.5 % of the total alcohol volume. Ablation times ranged from 10 to 30 minutes. To create ZnO: MoSe_2 nanocomposite films, nanoparticles were added to the ZnO solution in various concentrations from 2 % to 10 %. The nanoparticle concentration in the solution was calculated based on the density of the material according to the formula:

$$C_{NP} = \frac{C_{\text{MoSe}_2}}{m_{NP} \cdot N_A} = \frac{C_{\text{MoSe}_2}}{\rho_{\text{MoSe}_2} \cdot V_{NP} \cdot N_A} = \frac{\frac{m_{\text{MoSe}_2}}{V_{sol} M_{\text{MoSe}_2}}}{\rho_{\text{MoSe}_2} \cdot \frac{4\pi r^3}{3} \cdot N_A} \quad (\text{mol/l}), \quad (1)$$

where: C_{NP} — nanoparticle concentration; C_{MoSe_2} — concentration of the substance in solution before laser ablation of the substance MoSe_2 ; m_{NP} — average nanoparticle mass; N_A — Avogadro's number; ρ_{MoSe_2} — the density of matter is MoSe_2 ; V_{NP} — the volume of an average nanoparticle; m_{MoSe_2} — weight of the substance MoSe_2 ; V_{sol} — volume of solvent used in laser ablation; M_{MoSe_2} — molar mass of a substance MoSe_2 ; r — the radius of the average nanoparticle.

The ZnO: MoSe_2 nanocomposite films were deposited on substrates by spin coating at 4000 rpm. The films were annealed at 150 °C for 10 minutes to ensure complete solvent evaporation.

Results and discussion

Figure 1 shows the SEM images of pure ZnO and ZnO: MoSe_2 nanocomposite films deposited on a glass substrate. The nanocomposite structures exhibit a uniform distribution of nanoparticles across the ZnO surface, indicating high synthesis quality and sample homogeneity. The average nanoparticle size ranges from 30 nm to 80 nm.

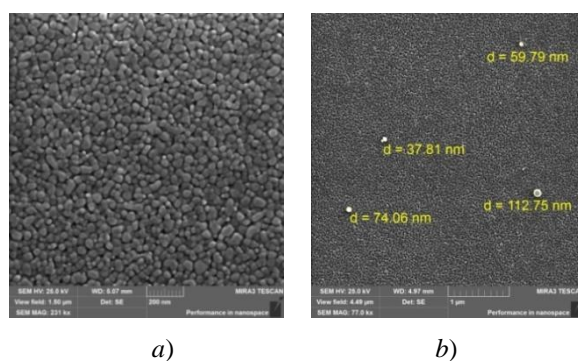


Figure 1. SEM images of surface morphology (a) ZnO and (b) ZnO: MoSe_2 nanocomposite film

Morphological analysis revealed that the grain structure of pure ZnO differs significantly from that of the doped composites. In pure ZnO, the grains exhibit a well-defined crystalline structure, while in the doped samples, the ZnO grains become smaller. Smaller grains and increased grain boundary density enhance light scattering, increasing its path length and absorption probability, thereby improving photogeneration efficiency. Doping with MoSe_2 nanoparticles increases the number of nucleation sites, enhancing the distribution of active sites and improving electron and hole generation.

The quantitative content of MoSe_2 nanoparticles in ZnO was determined using EDX analysis (Fig. 2). The composite film contains elements such as Mo, Se, Zn, and O. As the nanoparticle concentration increases, the corresponding element concentrations also rise.

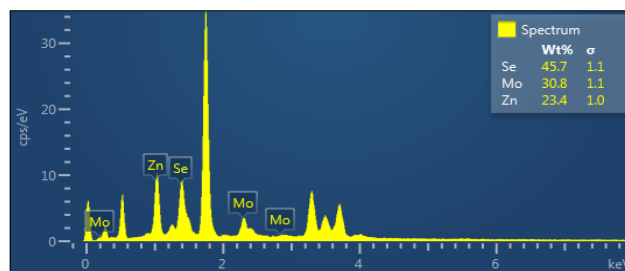
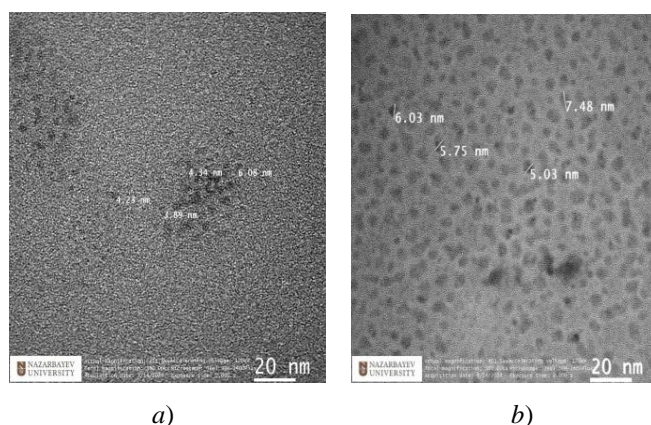
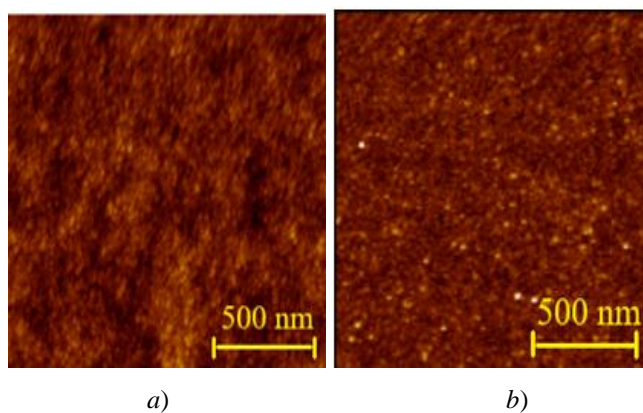
Figure 2. EDX analysis of nanoparticles MoSe₂

Figure 3 presents TEM images of ZnO:MoSe₂ nanocomposite films, revealing that the incorporation of MoSe₂ nanoparticles improves the ZnO film's morphology and topology. The nanoparticles are well-distributed and possess good monodispersity with sizes ranging from 3 to 6 nm.

Figure 3. TEM images of (a) pure ZnO and (b) ZnO:MoSe₂ nanocomposite films

The microstructure, morphology, and distribution of MoSe₂ nanoparticles in ZnO nanocomposite films have been analyzed by transmission electron microscopy (TEM). Figure 3 (a and b) shows TEM images of pure ZnO and nanocomposite ZnO films doped with MoSe₂ nanoparticles with a concentration of 8 %. Figure 3a shows an image of pure ZnO, which have a spherical shape, which is also confirmed by the results of the SEM analysis. Figure 3b shows that nanocomposite films of ZnO doped with MoSe₂ nanoparticles have a particle size in the range of 3-6 nm and have good monodispersity.

Figure 4 shows an AFM topographic image of ETL ZnO nanocomposite films doped with MoSe₂ nanoparticles. As can be seen from the figure, the MoSe₂ nanoparticles reduce the surface roughness.

Figure 4. AFM images of (a) pure ZnO and (b) ZnO:MoSe₂ nanocomposite films

AFM topographic images (Fig. 4) demonstrate that adding MoSe₂ nanoparticles reduces surface roughness (Ra). The Ra decreases from 2.8 nm to 0.8 nm with an 8 % MoSe₂ concentration, indicating

improved surface uniformity. However, at 10 % concentration, Ra significantly increases to 5.2 nm due to nanoparticle aggregation caused by Van der Waals forces [8].

Surface roughness reduction enhances molecular contact between the ZnO film and the active layer, improving interfacial dipole formation and reducing charge recombination.

The absorption spectra of ZnO and ZnO:MoSe₂ nanocomposite films are shown in Figure 5. As the nanoparticle concentration increases, the absorption intensity rises due to film thickness changes. Using Tauc plots, it was determined that the optical bandgap decreases from 3.24 eV to 3.07 eV as the MoSe₂ concentration increases up to 8 %, indicating improved crystallinity and reduced defect density.

At 10 % concentration, the bandgap widens to 3.26 eV due to increased structural defects and non-radiative recombination. These changes can be explained by an increase in the number of structural defects and nonradiative recombination that occur at high concentrations of nanoparticles. According to the study [9], such defects and recombination have a negative effect on the band gap. In addition, the possible formation of dichalcogenide clusters leads to phase separation and deterioration of the optical properties of the composite. Also, a high concentration of impurities can significantly change the ZnO crystal lattice, which further reduces the band gap [9].

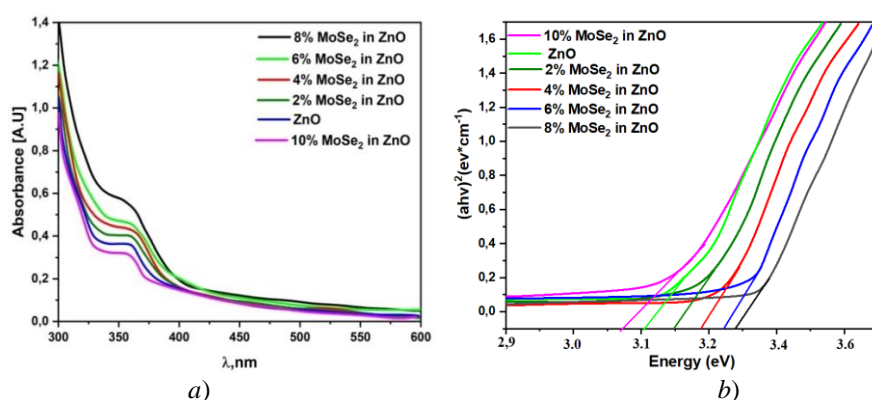


Figure 5. (a) Absorption spectra and (b) Tauc plots of ZnO:MoSe₂ nanocomposite films

The introduction of MoSe₂ nanoparticles can lead to an increase in the absorption coefficient of the composite, which causes enhanced absorption in the visible and near-infrared ranges [10]. It can also have an effect on the intensity and position of the ZnO luminescence bands.

The photoluminescence spectra of nanocomposite films were measured using an LQ529B laser as an excitation source with a wavelength of $\lambda = 325$ nm and an angle of incidence of 45° relative to the normal to the sample. The spectra were recorded using an Avantes AvaSpec-ULS2048CL-EVO spectrometer.

Figure 6 shows the change in the intensity of the photoluminescent (PL) peak at a concentration of 8 % of 2D TMDs nanoparticles obtained at room temperature (300 K).

It can be seen from the figure that the obtained samples show luminescence in the visible region. For all samples of nanocomposite films, a narrow band in the visible region of the spectrum in the range of 370–400 nm is observed in the photoluminescence spectra, which has a high luminescence intensity.

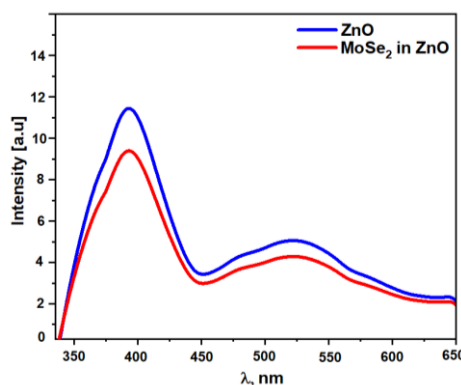


Figure 6. Photoluminescence (PL) spectra of nanocomposite films of ZnO doped with MoSe₂ nanoparticles

Visible radiation, known as green luminescence (PL) ZnO, was observed in all photoluminescence (PL) spectra, with a maximum at a wavelength of about 540 nm. The cause of EVIL is considered to be radiative transitions caused by deep energy levels of intrinsic defects, in particular oxygen vacancies.

Due to trap radiation or surface recombination, it appeared near 560 nm. Very few oxygen defects were present in the ZnO layers [11]. Therefore, we assumed that the effect of oxygen defects in the ZnO layers on the overall performance of the device would be negligible.

The photoluminescence intensity of a ZnO film containing a small number of dichalcogenide nanoparticles apparently decreased with increasing nanoparticle content, MoSe₂ nanoparticles with a concentration of 8 % are the lowest, which leads to better electron transfer to the FTO. Reducing the trap content in ETL solar cell devices would reduce the likelihood of interphase carrier recombination, and increase the J_{sc} and FF, thereby increasing the PCE of the device.

To study in detail the effect of MoSe₂ nanoparticles on the kinetics of electron transport and recombination in Oss, the OSCs impedance spectra were measured. The fitting and analysis of the spectrum parameters were carried out using the EIS-analyzer software package. Using this software, the values of the capacitance C and the values of R_1 and R_2 were calculated. The analysis of the impedance measurement results was carried out according to the diffusion-recombination model [12].

Further, Figure 7 shows the impedance spectra for nanocomposite ZnO films doped with MoSe₂ nanoparticles. According to the results of the study, the resistance of R_1 and R_2 for MoSe₂ nanoparticles also shows a significant decrease with an increase in the concentration of MoSe₂ nanoparticles to 8 %. As can be seen from Table 1, an increase in the concentration of MoSe₂ nanoparticles also leads to a decrease in recombination resistance.

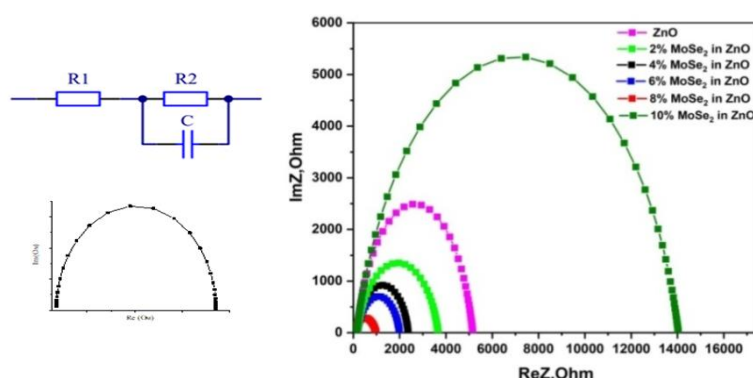


Figure 7. Effect of dichalcogenide nanoparticles on ZnO film impedance spectra

Table 1

The effect of MoSe₂ nanoparticles on the electrical transport characteristics of the ZnO film

Sample	R_1 , Ohm	R_2 , Ohm	C , 10^{-4} F	τ_D , c	Deff , $(\text{cm}^2 \cdot \text{s}^{-1})$	μ_s , $(\text{cm}^2 \cdot \text{V}^{-1} \cdot \text{s}^{-1})$
ZnO	131	5816	1.04	0.013	$2.2 \cdot 10^{-9}$	$0.8 \cdot 10^{-9}$
10 μl (2 %) MoSe ₂ in ZnO	188	3446	2.3	0.043	$6.7 \cdot 10^{-10}$	$2.6 \cdot 10^{-8}$
20 μl (4 %) MoSe ₂ in ZnO	143	2239	2.8	0.040	$7.2 \cdot 10^{-10}$	$2.8 \cdot 10^{-8}$
30 μl (6 %) MoSe ₂ in ZnO	137	1810	3.3	0.045	$6.4 \cdot 10^{-10}$	$2.5 \cdot 10^{-8}$
40 μl (8 %) MoSe ₂ in ZnO	89	954	5.4	0.048	$6.0 \cdot 10^{-10}$	$2.3 \cdot 10^{-8}$
50 μl (10 %) MoSe ₂ in ZnO	146	13892	1.0	0.014	$1.9 \cdot 10^{-10}$	$0.7 \cdot 10^{-8}$

The analysis of the obtained data revealed a critical nanoparticle concentration (8 %) in the film at which the electrical transport properties of the ZnO:MoSe₂ composite film exhibit optimal performance. At this concentration, the film resistance and the charge transfer resistance at the ZnO/electrode interface decrease by 2 and 3.6 times, respectively, while the effective charge carrier mobility increases by 2.8 times.

It follows from the fitting data of the impedance spectra that τ has a maximum value for ZnO films. ZnO:MoSe₂ with a nanoparticle concentration of 8 %. The impedance analysis data is correlated with the VAC data. OSCs with ZnO:MoSe₂ 8 % of nanoparticles form ETL films with improved conductivity and less structural defects. A sharp deterioration in the photovoltaic parameters of OSCs with a ZnO concentration of

over 8 % of the MoSe₂ nanoparticle may be due to a violation of the integrity of the film, which causes holes and voids to form in the film, through which current leakage occurs.

In order to determine the effect of MoSe₂ nanoparticles on electronic transport, a polymer solar cell with an inverted structure was assembled in a polymer solar cell. Upon photoexcitation of the photoactive P3HT:IC60MA layer, an electron-hole pair is formed, which then forms at the ZnO interface ZnO:MoSe₂/P3HT:IC60MA and P3HT:IC60MA/PEDOT:PSS decay into free charge carriers. Electrons are injected into the ETL layer of ZnO:MoSe₂ and the hole in the HTML layer is PEDOT:PSS.

Further, nanocomposite films of ZnO doped with MoSe₂ nanoparticles were used as electronic selective electrodes for organic solar cells based on the photoactive layer P3HT:IC60MA. The voltage curves of the obtained organic cells are shown in Figure 8.

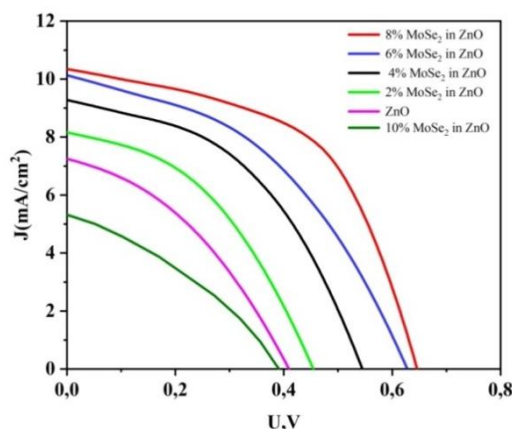


Figure 8. Volt-ampere characteristics of an organic solar cell of the structure FTO/ZnO:MoSe₂/P3HT:IC60MA/Ag

Table 2 shows the photovoltaic parameters of OSCs calculated on the basis of the VAC. As can be seen from Figure 8 and Table 2, the BAX parameters depend on the concentration of MoSe₂ nanoparticles. As the concentration of MoSe₂ increases to 8 %, the parameters of the VAC increase. A further increase in the MoSe₂ concentration leads to a decrease in the values of the VAC parameters. The data obtained correlate with the results of the morphology of the surface of composite films.

Table 2 shows the photovoltaic parameters of organic solar cells. All organic cells with MoSe₂ nanoparticles in the composition of ZnO showed improved values of J_{sc} and PCE compared to the ZnO based cell. Among them, the most optimal device was one in which the concentration of MoSe₂ nanoparticles was 8 %. J_{sc} increased from 7.25 mA/cm² to 10.02 mA/cm², FF increased from 0.37 to 10.52, and PCE increased from 0.7 to 3.3 %.

Table 2

Volt-ampere characteristics of organic solar cells

Sample	U _{oc} (V)	J _{sc} (mA/cm ²)	U _{max} (V)	J _{max} (mA/cm ²)	FF	PCE %
ZnO	0.27±0.01	7.25±0.05	0.27±0.01	4.07±0.05	0.37±0.01	0.7±0.05
10 µl (2 %) MoSe ₂ in ZnO	0.45±0.01	8.19±0.05	0.31±0.01	4.76±0.05	0.40±0.01	1.4±0.05
20 µl (4 %) MoSe ₂ in ZnO	0.54±0.01	9.29±0.05	0.38±0.01	5.78±0.05	0.43±0.01	2.1±0.05
30 µl (6 %) MoSe ₂ in ZnO	0.62±0.01	10.1±0.05	0.42±0.01	5.78±0.05	0.42±0.01	2.6±0.05
40 µl (8 %) MoSe ₂ in ZnO	0.64±0.01	10.2±0.05	0.49±0.01	7.02±0.05	0.52±0.01	3.3±0.05
50 µl (10 %) MoSe ₂ in ZnO	0.21±0.01	5.31±0.05	0.21±0.01	3.25±0.05	0.33±0.01	0.3±0.05

The incorporation of MoSe₂ nanoparticles into ZnO significantly improves the morphological, optical, and electrical properties of the ETL in OSCs. The optimal performance was observed at an 8 % MoSe₂ concentration, where surface roughness was minimized, and conductivity was enhanced, resulting in a power conversion efficiency of 3.3 %. Further increasing the concentration to 10 % led to performance degradation due to nanoparticle aggregation and increased defects. These findings highlight the potential of ZnO:MoSe₂ nanocomposites for advanced photovoltaic applications.

Conclusions

The effect of MoSe₂ nanoparticles on the electron transport properties of the ZnO layer in polymer solar cells was studied. At the critical concentration of 8 % MoSe₂ nanoparticles in the ZnO:MoSe₂ nanocomposite films, the recombination rate at the ZnO:MoSe₂/photoactive layer interface decreases, while the transport of injected electrons improves. As a result, the power conversion efficiency (PCE) of the polymer solar cell with the FTO/ZnO:MoSe₂/P3HT:IC60MA/MoOx/Ag structure reached 3.3 %. The higher efficiency of the PSC with the ZnO:MoSe₂ electron transport layer containing diselenide nanoparticles compared to disulfide nanoparticles is attributed to the relative alignment of their conduction band positions.

Funding

This research is funded by the Science Committee of the Ministry of Science and Higher Education of the Republic of Kazakhstan (Grant No. AP19679109).

References

- 1 Cheng, R., Li, D., Zhou, H. et al. (2014). Electroluminescence and Photocurrent Generation from Atomically Sharp WSe₂/MoS₂ Heterojunction p-n Diodes. *Nano Lett.*, 14(10), 5590–5597. DOI: 10.1021/nl502075n.
- 2 Lee, C.-H., Lee, G.-H., van der Zande, A.M. et al. (2014). Atomically thin p-n junctions with van der Waals heterointerfaces. *Nat. Nanotechnol.*, 9(9), 676–681. doi: 10.1038/nnano.2014.150.
- 3 Deng, Y., Luo, Z., Conrad, N.J., et al. (2014). Black Phosphorus–Monolayer MoS₂ van der Waals Heterojunction p-n Diode. *ACS Nano*, 8(8), 8292–8299. doi:10.1021/nn5027388.
- 4 Buscema, M., Groenendijk, D.J., Steele, G.A. et al. (2014). Photovoltaic effect in few-layer black phosphorus PN junctions defined by local electrostatic gating. *Nat. Commun.*, 5(1), 4651-1-4651-28. doi: 10.1038/ncomms5651.
- 5 Lin, Y., Adilbekova, B., Firdaus, Y. et al. (2019). 17 % Efficient Organic Solar Cells Based on Liquid Exfoliated WS₂ as a Replacement for PEDOT:PSS. *Adv. Mater.*, 31(46), 1902965-1-1902965-36. doi: 10.1002/adma.201902965.
- 6 Huang, Y.-J., Chen, H.-C., Lin, H.-K. et al. (2018). Doping ZnO electron transport layers with MoS₂ nanosheets enhances the efficiency of polymer solar cells. *ACS Applied Materials & Interfaces*, 10(23), 20196–20204. doi: 10.1021/acsami.8b06413
- 7 Chen, Y. Zeng, Herz, A., & Borchers, C. (2014). Inhibition of grain coarsening in nanocrystalline Fe-C alloys by interaction between carbon and grain boundaries. *Advanced Materials Research*, 904, 184–188. doi.org/10.4028/www.scientific.net/AMR.904.184
- 8 Jo, J., Pouliot, J.R., & Wynands, D. et al. (2013). Enhanced efficiency of single and tandem organic solar cells incorporating a diketopyrrolopyrrole-based low-bandgap polymer by utilizing combined ZnO/polyelectrolyte electron-transport layers. *Advanced Materials*, 25(34), 4783–4788. doi. 10.1002/adma.201301288
- 9 Cui, J. (2012). Zinc oxide nanowires. *Materialis Charact*, 64, 43–52. doi.org/10.1016/j.matchar.2011.11.017
- 10 Chiua, W.S., Khiew, P.S., & Clokea, M. et al. (2010). Photocatalytic study of two-dimensional ZnO nanopellets in the decomposition of methylene blue. *Chem. Eng. J.*, 158, 345–352. doi:10.1016/j.cej.2010.01.052
- 11 Xie, Q., Dai, Z., & Liang, J. et al. (2005). Synthesis of ZnO three-dimensional architectures and their optical properties. *Solid State Commun*, 136, 304–307. doi:10.1016/j.ssc.2005.07.023
- 12 Omarbekova, G.I., & Aimukhanov, A.K. (2023). Effect of the thickness and surface interface of In₂O₃ films on the transport and recombination of charges in a polimer solar cell. *Bulletin of the University of Karaganda – Physics*, 2(110), 17–24. doi: 10.31489/2023PH2/17-24.

Т.Е. Сейсембекова, А.К. Аймуханов, А.К. Зейниденов, А.М. Алексеев, Д.Р. Абеуов

MoSe₂ нанобөлшектерінің органикалық күн элементтерінің ZnO электрон тасымалдаушы қабатының қасиеттеріне әсері

Мақалада MoSe₂ нанобөлшектерімен допирленген ZnO электрон-тасымалдаушы қабатының құрылымдық, оптикалық және электрлік қасиеттеріне, сондай-ақ органикалық күн элементтерінің тиімділігіне әсері зерттелді. ZnO:MoSe₂ композиттері золь-гель әдісімен синтезделіп, олардың морфологиясы ТЕМ және СЭМ микроскопиясы арқылы талданды. Оптикалық зерттеулер тыйым салынған аймақтың ені кеңейіп, ақаулық сәулеленудің күшейгенін көрсетті, бұл заряд тасымалдаушылардың динамикасының жақсарғанын білдіреді. Электрфизикалық өлшеулер MoSe₂ енгізу арқылы өткізгіштіктің артуы мен зарядтардың рекомбинациясының төмендеуін растады. ZnO:MoSe₂ негізіндегі органикалық күн элементтері таза ZnO негізіндегі құрылғылармен салыстырғанда жоғары фотоэлектрлік сипаттамалар көрсетті. MoSe₂ концентрациясы 8 % болған

құрылғы ең оңтайлы деп танылды, мұнда қысқа тұйықталу тогының тығыздығы (J_{sc}) 7,25 мА/см²-ден 10,02 мА/см²-ге дейін, толтыру коэффициенті (FF) 0,37-ден 0,52-ге дейін, ал энергияны түрлендіру тиімділігі (PCE) 0,7 %-дан 3,3 %-ға дейін артты. Алынған нәтижелер ZnO:MoSe₂ нанокөміршіктерінің жоғары тиімді оптоэлектрондық және фотогальваникалық құрылғыларда қолдануға тиімді екенін растайды.

Кілт сөздер: ZnO, MoSe₂, композициялық пленка, беттік морфология, оптикалық және импеданс спектроскопиясы

T.E. Сейсембекова, А.К. Аймуханов, А.К. Зейниденов, А.М. Алексеев, Д.Р. Абеуов

Влияние наночастиц MoSe₂ на свойства электронотранспортного слоя ZnO органического солнечного элемента

В статье исследовано влияние допирования наночастицами MoSe₂ на структурные, оптические и электрические свойства электронно-транспортного слоя ZnO, а также на эффективность органических солнечных элементов. Композиты ZnO:MoSe₂ были синтезированы методом золь-гель, их морфология проанализирована с использованием ТЕМ и СЭМ микроскопии. Оптические исследования показали увеличение ширины запрещенной зоны и усиление дефектной эмиссии, что свидетельствует об улучшенной динамике носителей заряда. Электрофизические измерения подтвердили увеличение проводимости и снижение рекомбинации зарядов при введении MoSe₂. Органические солнечные элементы на основе ZnO:MoSe₂ продемонстрировали повышенные фотоэлектрические характеристики по сравнению с устройствами на основе чистого ZnO. Наиболее оптимальным оказалось устройство с концентрацией MoSe₂ 8 %, где плотность тока короткого замыкания (J_{sc}) увеличилась с 7,25 мА/см² до 10,02 мА/см², коэффициент заполнения (FF) с 0,37 до 0,52, а эффективность преобразования энергии (PCE) с 0,7 % до 3,3 %. Полученные результаты подтверждают перспективность нанокөміршіктерін ZnO:MoSe₂ для применения в высокоэффективных оптоэлектронных и фотогальванических устройствах.

Ключевые слова: ZnO, MoSe₂, композицияльная пленка, морфология поверхности, оптическая и импедансная спектроскопия

Information about the authors

Seisembekova, Togzhan (*corresponding author*) — Master, Department of Physics and Nanotechnology, Karaganda Buketov University, Karaganda, Kazakhstan; e-mail: tosh_0809@mail.ru; ORCID ID <https://orcid.org/0000-0002-1497-0759>

Aimukhanov, Aitbek — Candidate of Physical and Mathematical Sciences, Associate professor, Professor of the Department of Radiophysics and Electronics, Leading Researcher, , Scientific Center for Nanotechnology and Functional Nanomaterials, Karaganda Buketov University, Karaganda, Kazakhstan; e-mail: a_k_aitbek@mail.ru; ORCID ID <https://orcid.org/0000-0002-4384-5164>. Scopus Author ID-35321945000

Zeinidenov, Assylbek — PhD, Associate professor, Dean of the Physical-Technical Faculty, Leading Researcher, Scientific Center for Nanotechnology and Functional Nanomaterials, Karaganda Buketov University, Karaganda, Kazakhstan; e-mail: asyl-zeinidenov@mail.ru; ORCID ID <https://orcid.org/0000-0001-9780-5072>. Scopus Author ID-56386144000

Alexeev, Alexandr — Candidate of Physical and Mathematical Sciences, eKazan Federal University, Kazan, Russia; e-mail: alalrus@mail.ru; Researcher ID — A-8526-2012; ORCID ID <https://orcid.org/0000-0002-2800-6047>

Abeuov, Dosmukhammed — Junior researcher, Scientific Center for Nanotechnology and Functional Nanomaterials, Karaganda Buketov University, Karaganda, Kazakhstan; e-mail: Dsk-02@mail.ru; ORCID ID <https://orcid.org/0009-0003-1434-6328>


Article

UDC 621.3.038.624

 <https://doi.org/10.31489/2025PH2/27-34>

Received: 21.01.2025

Accepted: 01.04.2025

B.D. Igamov¹, A.I. Kamardin¹, D.Kh. Nabiev², G.T. Imanova^{3,4},
I.R. Bekpulatov², I.Kh. Turapov⁵, N.E. Norbutaev⁶

¹Scientific and Technical Center with a Design Bureau and Pilot Production,
Academy of Sciences of the Republic of Uzbekistan 100125;

²Karshi State University 180119, Karshi, Uzbekistan;

³Institute of Radiation Problems, Ministry of Science and Education Republic of Azerbaijan,
9 B. Vahabzade str., AZ1143, Baku, Azerbaijan;

⁴Khazar University, Department of Physics and Electronics,
41 Mahsati Str., AZ1096, Baku, Azerbaijan;


⁵Renaissance university of education, Tashkent, Uzbekistan;

⁶Gulistan State University, Gulistan, Uzbekistan

Study of Mn₄Si₇ Silicide Alloys Produced Under Different Conditions Using an X-ray Diffractometer

Mn₄Si₇ silicide crystals obtained by hot isostatic pressing (HIP) and diffusion methods were studied. As a result of the research, 11 peaks were identified in the Mn₄Si₇ crystal obtained by the HIP method, and 14 peaks in the Mn₄Si₇ crystal obtained by the diffusion method. The crystal size of Mn₄Si₇ silicide (D_{HIP}) was established from $8.8 \cdot 10^{-9}$ m to $3.6 \cdot 10^{-8}$ m, (D_{Diff}) from $6.2 \cdot 10^{-10}$ m to $9.1 \cdot 10^{-8}$ m. It has been established that the lattice tension between the atoms of the Mn₄Si₇ silicide crystal (ϵ_{HIP}) varies from 0.01 to 0.41, (ϵ_{Diff}) from 0.31 to 3.71. The dislocation density on the crystal surface (δ_{HIP}) turned out to be from $3.5 \cdot 10^{10}$ to $3.2 \cdot 10^{12}$, (δ_{Diff}) from $1 \cdot 10^{11}$ to $3.2 \cdot 10^{14}$. The degree of crystallization of Mn₄Si₇ silicide obtained by the (HIP) method is 7.02 %, the degree of amorphousness is 92.98 %. It has been established that the Mn₄Si₇ silicide obtained by the diffusion method has a degree of crystallization of 9.3 % and a degree of amorphousness of 90.7 %. (COD-1530134) (d). It has been established that the degree of crystallization of high-manganese silicide Mn₄Si₇ is low, and the degree of amorphousness is high due to the fact that Mn and Si are bound in a non-stoichiometric state.

Keywords: diffusion, crystallization, nonstoichiometric, dislocation density, lattice tension, amorphous, agglomeration

 Corresponding author: Imanova G.T., gunel_imanova55@mail.ru

Introduction

Currently, the demand for electricity is growing every day, so a number of scientists are conducting research on the production of silicide materials with thermoelectric properties by various methods. As a result of the introduction of Mn atoms in the vapor phase into silicon atoms by the diffusion method, a liquid solution is formed, and after solidification, a high-manganese silicide is formed [1, 2]. In addition to the diffusion method, there are other methods, in which it is possible to form not only high manganese silicide, but also other semiconductor structures in the state of a thin film [3–12]. The diffusion coefficient $D(T)$ on the manganese-silicon surface is determined by (1) below.

$$D(T) = D_0 \exp(-E_m/kT), \quad (1)$$

where $D(T)$ is the solubility of manganese in silicon. $D(T) = 5 \cdot 10^{22} \cdot \exp [(6.94 - 2.78) / kT] \text{ cm}^{-3}$ and diffusion $D_0 = (6.9 \pm 2.2) \cdot 10^{-4} \text{ cm}^2 \cdot \text{s}^{-1}$, activation energy $E_m = (0.63 \pm 0.03) \text{ eV}$, $D(T)$ diffusion coefficient from 10^{-6} to $3 \cdot 10^{-5} \text{ cm}^2/\text{s}$ [3]. Mn_4Si_7 – Si film growth mechanism varies depending on the crystallization temperature [11]. A coating of manganese silicide Mn_4Si_7 was obtained in an ampoule at high temperature [13]. It was found that the distribution of Mn diffusion in Si sharply reduces the concentration of manganese at a depth of 15–20 microns [14]. Using high-energy photoelectron spectroscopy and synchrotron radiation, it was discovered that the growth of a manganese film on the Si(111)7×7 surface after the deposition of $\sim 6 \text{ \AA}$ Mn leads to the formation of a manganese silicide film when a thin coating is applied, annealed at temperatures up to $600 \text{ }^\circ\text{C}$ [15]. An increase in the germanium concentration to 1 % in Mn_4Si_7 leads to the destruction of layered deposits and significant changes in thermoelectric properties [16]. The composition of $\text{Si}_{(1-x)}\text{Mn}_x$ coatings grown using a pulsed laser must be chemically homogeneous [17]. In $(\text{MnSi}_{1.71-1.75})$ nickel diffusion is reduced, the use of chromium for diffusion is effective [18]. The quality factor of $\text{Mn}_x\text{Si}_{1-x}/\text{Si}$ in the temperature range $T = 300\text{--}600 \text{ K}$ is $ZT = 0.59 \pm 0.06$ [19–23]. Our work examines the preparation of high-manganese silicides Mn_4Si_7 by the diffusion method and the study of the resulting samples using an X-ray diffractometer (XRD-6100) SHIMADZU.

Experimental

As a result of the interdiffusion of Mn atoms with Si atoms at high temperature, a thin coating of high-manganese silicide Mn_4Si_7 was formed. The P_{Mn} calculation of the mass of manganese used to form Mn_4Si_7 during the diffusion process [1] is found from (2) below.

$$P_{\text{Mn}} = G \cdot t \cdot S. \quad (2)$$

Here G — evaporation rate ($\text{mg}/(\text{cm}^2 \cdot \text{s})$), S — evaporation surface (cm^2), t — evaporation time (minutes). Taking this ratio into account, the mass of manganese consumed for evaporation was calculated ($P_{\text{Mn}} = mg$). Growth temperature of fine Mn_4Si_7 coating was chosen to be $1100 \text{ }^\circ\text{C}$. The growth rate of a thin Mn_4Si_7 layer is determined by Mn and Si diffusion (Fig. 1A). As a result of experiments, it was established that on a Si surface with a size of 1 cm^2 and a thickness of 0.5 cm , a thin layer of Mn_4Si_7 is formed, the thickness of which depends on temperature. HIP (hot isostatic pressing) was carried out under isostatic pressure at a temperature of $1100 \text{ }^\circ\text{C}$ in an argon atmosphere [2] (Fig. 1B).

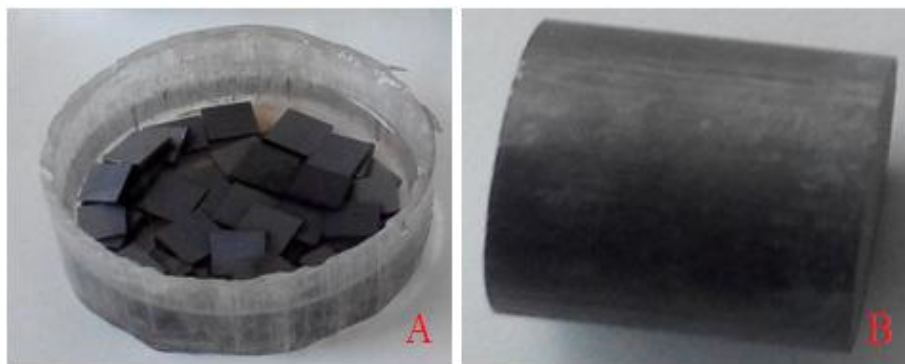
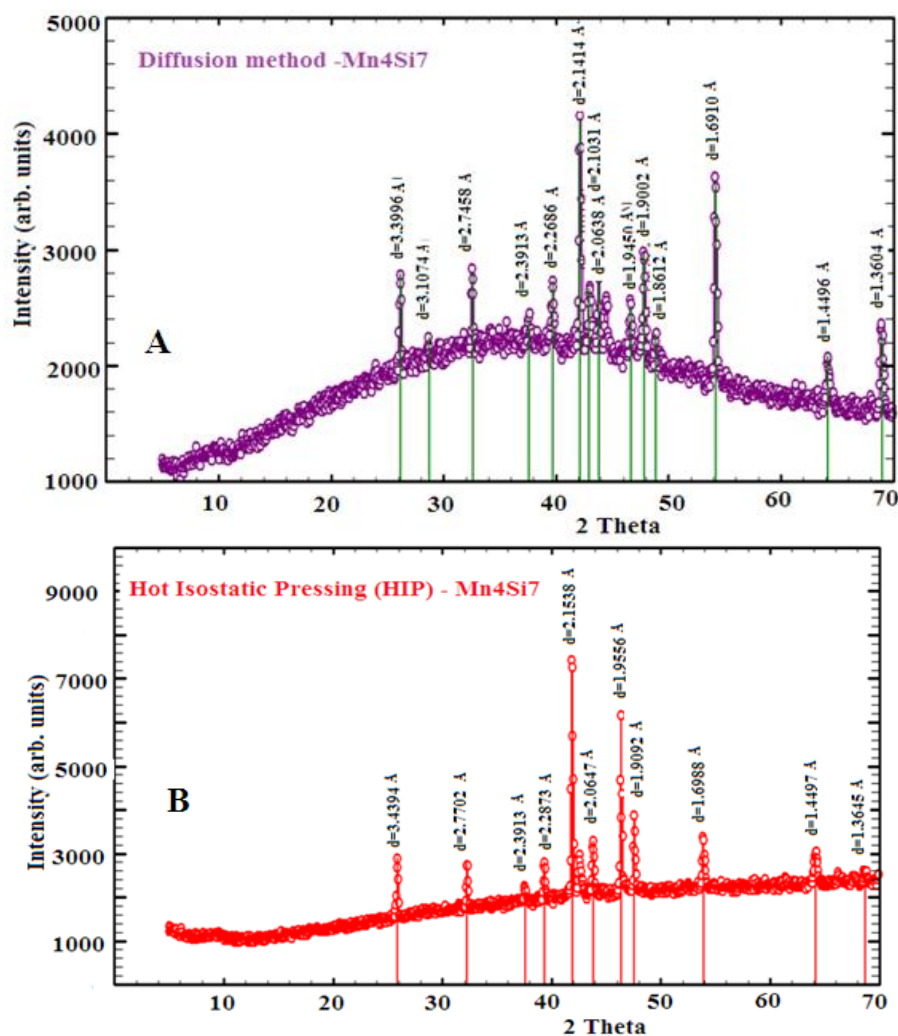


Figure 1. Mn_4Si_7 crystals obtained by diffusion and HIP methods

Results and Discussion

As a result of studying Mn_4Si_7 silicide crystals obtained by diffusion and (HIP) hot isostatic pressing on an X-ray diffractometer (XRD-6100) SHIMADZU, peaks corresponding to Mn_4Si_7 silicide crystals (COD-1530134) were found in the database [21]. 14 peaks from the Mn_4Si_7 silicide crystal obtained by the diffusion method (Fig. 2A) and 11 peaks from the Mn_4Si_7 silicide obtained by the hot isostatic pressing (HIP) method (Fig. 2B) were defined. The results obtained using an X-ray diffractometer may be due to the effect of mutual agglomeration Mn and Si atoms at high temperature.



A — obtained by the diffusion method; B — obtained by the hot isostatic pressing (HIP)

Figure 2. X-ray diffraction analysis

The difference in interatomic distance (Δd) of Mn₄Si₇ obtained by diffusion method is small from 0.01 Å to 0.14 Å compared to the interatomic distance (d) reported in the database (COD-1530134). The difference in interatomic distances (Δd) of Mn₄Si₇ obtained by hot isostatic pressing was found to be in the range from 0.01 Å to 0.05 Å (Table). This is apparently due to the influence of agglomeration and non-stoichiometric bonds at high temperatures, which can lead to an expansion or reduction of the distance between the atoms of the silicide Mn₄Si₇ (d) [20].

Table

The difference in interatomic distances of Mn₄Si₇ obtained by hot isostatic pressing and obtained by the diffusion method

COD-1530134 (d) Å	Diff (d) Å	Diff (Δd) Å	HIP (d) Å	HIP (Δd) Å
3.42	3.39	−0.03	3.43	+0.01
3.24	3.10	−0.14		
2.76	2.74	−0.02	2.77	+0.01
2.44	2.39	−0.05	2.39	+0.05
2.27	2.26	−0.01	2.28	+0.01
2.15	2.14	−0.01	2.15	
1.94	1.94		1.95	+0.01
1.85	1.86	+0.01		

Based on X-ray diffraction analysis of Mn_4Si_7 silicide samples, the size of Mn_4Si_7 crystals was determined using the Scherrer equation [10] (3).

$$D = \frac{K\lambda}{\beta \cos \theta} \quad (3)$$

Here $K=0.9$ is a constant depending on the shape of the crystallites, the angle at the center of the Θ -peak, $\lambda = 0.15406$ (nm) is the X-ray wavelength. In the β -half, the peak width of the diffraction profile is determined by calculating the maximum height of the D-size of the crystallites, which is influenced by their small size. FWHM or β_{hkl} (full width at half maximum) respectively is a mathematical way of defining a peak. This method is used to generate “peaks” which can be used to calculate the resolution of the mass spectrometer determining the spectrum being analyzed. $\beta_{hkl} = \beta_t + \beta_a$ β_t — linewidth obtained from the external dimension of the crystal (4), β_a is the line broadening due to interatomic lattice tension (5) [11].

$$\beta_t = \frac{k\lambda}{L_c \cos(\theta)}; \quad (4)$$

$$\beta_a = 4\varepsilon \tan(\theta). \quad (5)$$

This line broadening can be used to measure crystal size and lattice voltage. The size (D) of crystals of high-manganese silicide Mn_4Si_7 obtained by the diffusion method ranges from $6.2 \cdot 10^{-10}$ m to $9.1 \cdot 10^{-8}$ m. (HIP) The size (D) of Mn_4Si_7 silicide crystals obtained by hot isostatic pressing has been established to be from $8.8 \cdot 10^{-9}$ m to $3.6 \cdot 10^{-8}$ m.

It has been established that the size of Mn_4Si_7 crystals obtained by the (HIP) method is approximately 3 times smaller than that of Mn_4Si_7 silicide crystals obtained by the diffusion method. Lattice deformation or strain between Mn and Si atoms during crystal formation occurs due to high temperature and agglomeration (6).

$$\varepsilon = \frac{\beta_{hkl}}{4 \cdot \tan \theta} \quad (6)$$

Here (ε) lattice strain [3] between the atoms of Mn_4Si_7 silicide crystals obtained by the diffusion method varies from 0.31 to 3.71. It was found that the lattice strain (ε) between the atoms of Mn_4Si_7 silicide crystals obtained by hot isostatic pressing (HIP) varies from 0.01 to 0.41 (Fig. 3).

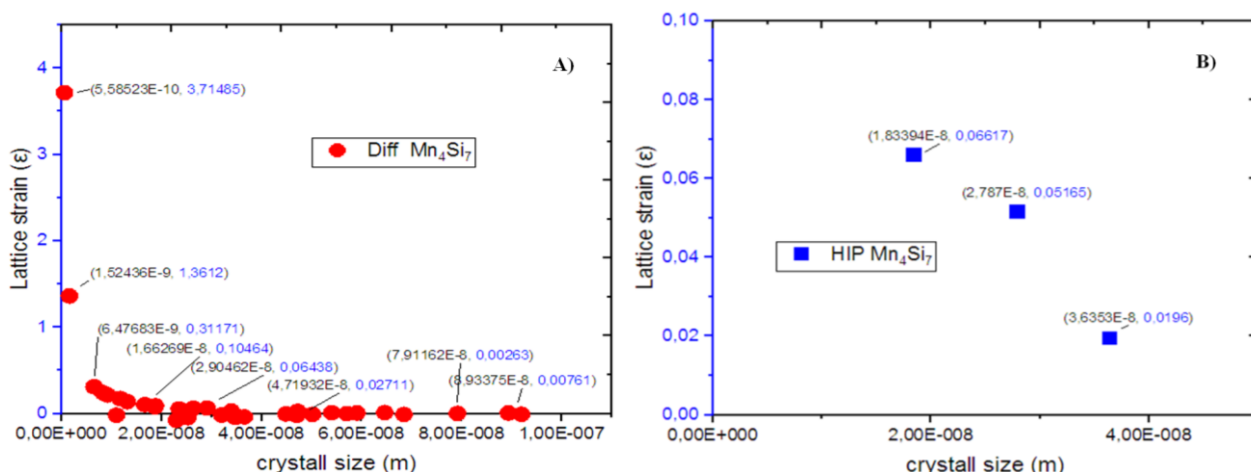


Figure 3. Dependence of Mn_4Si_7 crystal size on lattice strain obtained by the diffusion (A) and obtained by hot isostatic pressing method (B)

By comparing the results obtained in cases where high temperature alone was not sufficient to minimize lattice deformation, it was found that lattice deformation was greatest for silicides prepared by the diffusion method. It has been established that for silicides produced together with high temperature and high pressure, lattice deformation is 15–20 times less. Lattice dislocations arise as a result of the formation of crystals of high-manganese silicide Mn_4Si_7 , which have different sizes during formation and deformation in the crystal

lattice. Types of dislocations include edge and screw dislocations. The density of dislocations is determined (7) [4].

$$\delta = \frac{1}{D^2}. \quad (7)$$

The dislocation can be moved by the sliding method and the diffusion method; Dislocations perpendicular to the displacement vector move by diffusion, causing growth or compression of the plane as a result of expulsion by diffusion. The dislocation density (δ) on the surface of high-manganese silicide Mn₄Si₇ obtained by the diffusion method ranges from $1 \cdot 10^{11}$ to $3.2 \cdot 10^{14}$. It has been established that the dislocation density of Mn₄Si₇ silicide (δ), obtained by the (HIP) method, ranges from $3.5 \cdot 10^{10}$ to $3.2 \cdot 10^{12}$ (Fig. 4).

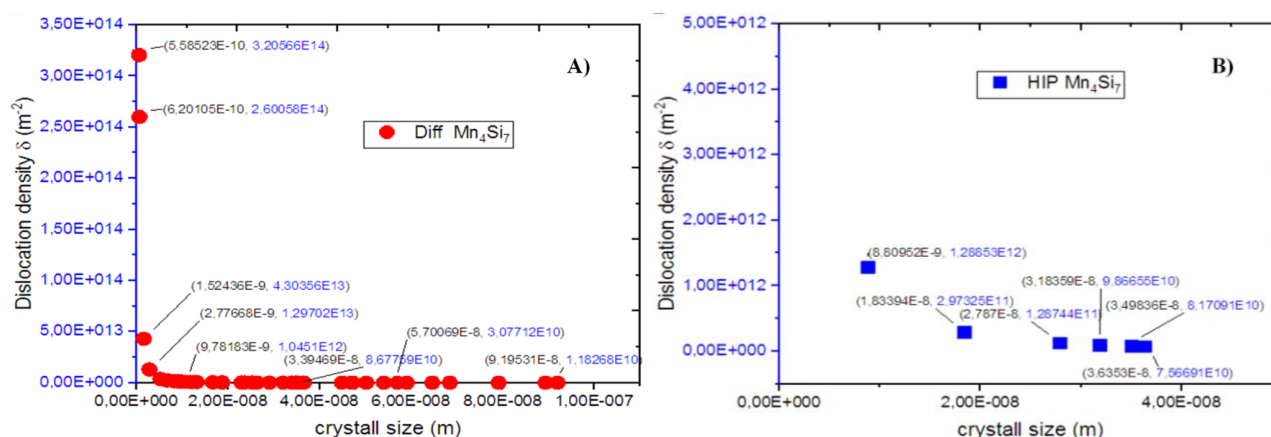


Figure 4. Established that the dislocation density of Mn₄Si₇ silicide, obtained by the diffusion method (A) and obtained by the (HIP) method (B)

The degree of crystallinity of the Mn₄Si₇ was calculated using the program (*Match-3!*). Calculations showed that the degree of crystallization of Mn₄Si₇ obtained by the diffusion method is 9.3 %, the degree of amorphism is 90.7 %, the degree of crystallization of Mn₄Si₇ obtained by the (HIP) method is 7.02 %, degree of amorphism 92.98 %. Mn₄Si₇ has five positions for Mn atoms and four for Si atoms as indicated by (mp-680339), which is the reason for its high degree of amorphism. 1) Mn³⁺ is bonded to ten Si+1.71 atoms. Mn–Si bond distances range from 2.27–2.71 Å.

Mn³⁺ is bonded to eight Si+1.71- atoms in an 8-coordinate geometry. Mn–Si bond distances range from 2.27–2.56 Å. Mn³⁺ is bonded to eight Si+1.71- atoms in an 8-coordinate geometry. Mn–Si bond distances range from 2.28–2.52 Å. Mn³⁺ is bonded to eight Si+1.71- atoms in an 8-coordinate geometry. There are four shorter (2.36 Å) and four longer (2.38 Å) Mn–Si bonds. 5) Mn³⁺ is bonded to eight Si+1.71- atoms in an 8-coordinate geometry. There is a spread of Mn–Si bond distances within the range of 2.32–2.44 Å. For Si there are four equivalent states Si+1.71.

In the Si+1.71- state, Si+1.71- is bonded to five Mn³⁺ atoms in a 4-coordinate geometry. In the Si+1.71- state, Si+1.71- is bonded to four Mn³⁺ atoms in a 4-coordinate geometry. In the Si+1.71- state, Si+1.71- is bonded to five Mn³⁺ atoms in a 5-coordinate geometry. In the Si+1.71- state, Si+1.71- is bonded to five Mn³⁺ atoms in a 5-coordinate geometry. According to the data obtained, Mn₄Si₇ silicides are formed using non-stoichiometric Mn and Si bonds. Based on this, the Mn₄Si₇, obtained by the diffusion and (HIP) method, has a high degree of amorphism and a low degree of crystallization, therefore the Mn₄Si₇ silicide alloy has a generally polycrystalline structure. Consequently, Mn₄Si₇ polycrystals are isotropic due to the random orientation of individual crystals and have the characteristics of an amorphous material [8]. This is shown by X-ray diffraction analysis (XRD-6100) (Fig. 5).

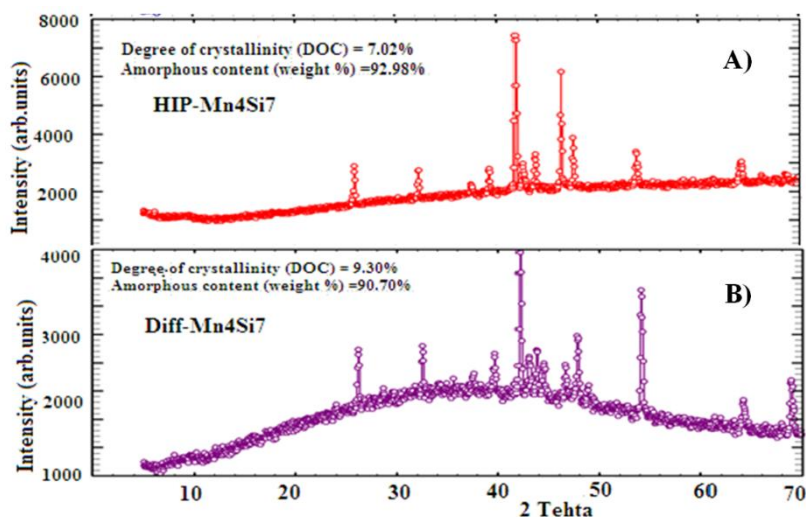


Figure 5. Degree of crystallization of silicide Mn_4Si_7 obtained by the (HIP) method (A) and obtained by the diffusion method (B)

Crystallization requires the interaction of Mn and Si particles and the formation of crystalline bridges between the particles as a result of agglomeration at high temperature. After this process, a stable particle or agglomerate is formed. Due to the formation of Mn_4Si_7 silicides using non-stoichiometric bonds, they exhibit electrophysical properties characteristic of semiconductors.

Conclusions

A study of Mn_4Si_7 silicide crystals obtained by (HIP) and diffusion methods showed that there are 11 peaks of Mn_4Si_7 obtained by the (HIP) method and 14 peaks of Mn_4Si_7 obtained by the diffusion method. It has been established that the size of Mn_4Si_7 silicide crystals (D_{HIP}) is from $8.8 \cdot 10^{-9}$ m to $3.6 \cdot 10^{-8}$ m, (D_{Diff}) from $6.2 \cdot 10^{-10}$ m to $9.1 \cdot 10^{-8}$ m. It has been determined that lattice tension between the atoms of the Mn_4Si_7 silicide crystal (ϵ_{HIP}) varies from 0.01 to 0.41, (ϵ_{Diff}) from 0.31 to 3.71. The dislocation density on the crystal surface (δ_{HIP}) turned out to be in the range from $3.5 \cdot 10^{10}$ to $3.2 \cdot 10^{12}$, (δ_{Diff}) from $1 \cdot 10^{11}$ to $3.2 \cdot 10^{14}$. The degree of crystallization of Mn_4Si_7 silicide obtained by the (HIP) method is 7.02 %, degree of amorphy — 92.98 %. (COD-1530134) Compared with the interatomic distance (d) in Mn_4Si_7 silicide obtained by diffusion method, the interatomic distance difference (Δd) is shorter from 0.01 Å to 0.14 Å. (HIP) Interatomic distance difference (Δd) of Mn_4Si_7 , obtained by hot isostatic pressing was found to be in the range from 0.01 Å to 0.05 Å. It has been established that the degree of crystallization of high-manganese silicide Mn_4Si_7 is low, and the degree of amorphy is high due to the fact that Mn and Si are bound in a non-stoichiometric state.

References

- 1 Markov, V.F. (2014). *Materials of modern electronics*. Ministry of Education and Science Rus. Federation, p. 272.
- 2 Bekpulatov, I.R., Imanova, G.T., Kamilov, T.S., Igamov, B.D., & Turapov, I.K. (2022). Formation of n -type CoSi monosilicide film which can be used in instrumentation. *International Journal of Modern Physics B.*, 2350164. DOI: 10.1142/S0217979223501643
- 3 Umirzakov, B.E., Bekpulatov, I.R., Turapov, I.Kh., & Igamov, B.D. (2022). Effect of Deposition of Submonolayer Cs Coatings on the Density of Electronic States and Energy Band Parameters of $\text{CoSi}_2/\text{Si}(111)$. *Journal of Nano- and Electronic Physics*, 14(2), 02026. DOI: 10.21272/jnep.14(2).02026
- 4 Normurodov, M.T., Bekpulatov, I.R., Normurodov, D.A., & Tursunmetova, Z.A. (2021). Formation and Electronic Structure of Barium-Monosilicide- and Barium-Disilicide Films. *Journal of Surface Investigation*, 15, S211–S215. DOI: 10.1134/S1027451022020318
- 5 Isakhanov, Z.A., Umirzakov, Y.E., Ruzibaeva, M.K., & Donaev, S.B. (2015). Effect of the O_2^+ -ion bombardment on the TiN composition and structure. *Technical Physics*, 60(2), 313–315. DOI: 10.1134/S1063784215020097
- 6 Umirzakov, B.E., Donaev, S.B., & Mustafaeva, N.M. (2019). Electronic and Optical Properties of GaAlAs/GaAs Thin Films. *Technical Physics*, 64(10), 1506–1508. DOI: 10.1134/S1063784219100220
- 7 Donaev, S.B., Umirzakov, B.E., & Mustafaeva, N.M. (2019). Emissivity of Laser-Activated Pd–Ba Alloy. *Technical Physics*, 64(10), 1541–1543. DOI: 10.1134/S1063784219100074

- 8 Weissmuller, J. (1996). Synthesis and Processing of Nanocrystalline Powder / TMS.
- 9 Hicks, L.D. & Dresselhaus, M.S. (1993). Effect of quantum-well structures on the thermoelectric figure of merit. *Physical Review B*, 47, 12727–12731.
- 10 Allon, I. (2008). Enhanced thermoelectric performance of rough silicon nanowires. *NAT*, 451(7175), 163–167.
- 11 Burkov, A.T., & Novikov, S.V. (2012). J. Schumann Nanocrystallization of Amorphous M-Si Thin Film Composites (M=Cr, Mn) and Their Thermoelectric Properties. *AIP Conference Proceedings, 9th European Conference on Thermoelectric*, 1449, 219–222.
- 12 Novikov, S.V., Burkov, A.T., & Schumann, J. (2013). Enhancement of thermoelectric properties in nanocrystalline M-Si thin film composites (M = Cr, Mn). *Journal of Alloys and Compounds*, 557, 239–243.
- 13 Orekhov, A.S., & Klechkovskaya, V.V. (2017). Establishment of the relationship between the microstructure and thermoelectric properties of crystals of higher manganese silicide, doped with germanium. *Physics and technology of semiconductors*, 51(7), 925–928.
- 14 Adachi, K., Ito, K., Zhang, L.T., & Yamaguchi, M. (2003). Thermoelectric properties of CoSi thin films. *Material Science Forum*, 426, 3445–3450. Trans Tech Publications Ltd.
- 15 Maex, K. (2003). Properties of Metal Silicides. *INSPEC*. Stevenage.
- 16 Yoneyama, T., & Okada, A. (2013). Formation of polycrystalline BaSi₂ films by radio-frequency magnetron sputtering for thin-film solar cell applications. *Thin Solid Films*, 534, 116–119. DOI: 10.1016/j.tsf.2013.02.003
- 17 Dubov, V.L. (2008). Formation, structure, optical and photoelectric properties of textured BaSi₂ films on Si(111) and heterostructures based on them. *Dissertation*, 124, 67–70. Blagoveshchensk.
- 18 Egerton, R.F. (2008). Electron energy-loss spectroscopy in the TEM. *Reports on Progress in Physics*, 72(1), 016502.
- 19 Pani, M., & Palenzona, A. (2008). The phase diagram of the Ba-Si system. *Journal of Alloys and Compounds*, 454(1-2), L1-L2.
- 20 Miyazaki, Y., Igarashi D., Hayashi, K., & Kajitani, T. (2008). Modulated crystal structure of chimney-ladder higher manganese silicides MnSi γ ($\gamma \sim 1.74$). *Physical Review B—Condensed Matter and Materials Physics*, 78(21), 214104.
- 21 Kajitani, T. (2010). Electron Density Distribution in Mn_4Si_7 . *Journal of Electronic Materials*, 39, 1482–1487.
- 22 Migas, D.B. (2008). Ab initio study of the band structures of different phases of higher manganese silicides. *Physical Review B—Condensed Matter and Materials Physics*, 77(7), 075205.
- 23 Kamilov, T.S., Rysbaev, A.S., Klechkovskaya, V.V., Orekhov, A.S., Igamov, B.D., & Bekpulatov, I.R. (2019). The Influence of Structural Defects in Silicon on the Formation of Photosensitive $\text{Mn}_4\text{Si}_7\text{-Si(Mn)-Mn}_4\text{Si}_7$ and $\text{Mn}_4\text{Si}_7\text{-Si(Mn)-M}$ Heterostructures. *Applied Solar Energy*, 55, 380–384.

Б.Д. Игамов, А.И. Камардин, Д.Х. Нәбиев, Г.Т. Иманова,
И.Р. Бекпулатов, И.Х. Тұрапов, Н.Е. Норбұтаев

Рентгендік дифрактометр арқылы түрлі жағдайларда өндірілген Mn_4Si_7 силициддің қорытпаларын зерттеу

Ыстық изостатикалық пресеу (ЫИП) және диффузиялық әдістермен алынған Mn_4Si_7 силицид кристалдары зерттелді. Зерттеу нәтижесінде ЫИП әдісімен алынған Mn_4Si_7 кристалында 11 шың, диффузиялық әдіспен алынған Mn_4Si_7 кристалында 14 шың анықталды. Mn_4Si_7 силицидінің (D_{HIP}) кристалдық өлшемі $8,8 \cdot 10^{-9}$ м-ден $3,6 \cdot 10^{-8}$ м-ге дейін, (D_{diff}) $6,2 \cdot 10^{-10}$ м-ден $9,1 \cdot 10^{-8}$ м-ге дейін белгіленді. Mn_4Si_7 силицид кристалының (ε_{HIP}) атомдары арасындағы тордың кернеуі 0,01-ден 0,41-ге дейін, ($\varepsilon_{\text{diff}}$) 0,31-ден 3,71-ге дейін өзгертіні айқындалды. Кристалл бетіндегі дислокация тығыздығы (δ_{HIP}) $3,5 \cdot 10^{10}$ -нан $3,2 \cdot 10^{12}$ -ге дейін, (δ_{diff}) $1 \cdot 10^{11}$ -ден $3,2 \cdot 10^{14}$ -ке дейін болды. (ЫИП) әдісімен алынған Mn_4Si_7 силицидінің кристалдану дәрежесі 7,02 %, аморфия дәрежесі 92,98 %. Диффузия әдісімен алынған Mn_4Si_7 силицидінің кристалдану дәрежесі 9,3 % және аморфизм дәрежесі 90,7 % болатыны анықталды. (КОД-1530134) (ж.). Mn_4Si_7 жоғары марганец силицидінің кристалдану дәрежесі төмен және Mn және Si стехиометриялық емес күйде байланысқандықтан аморфтылық дәрежесі жоғары екені айқындалды.

Кілт сөздер: диффузия, кристалдану, стехиометриялық емес, дислокация тығыздығы, тордың керілуі, аморфты, агломерация

Б.Д. Игамов, А.И. Камардин, Д.Х. Набиев, Г.Т. Иманова,
И.Р. Бекпулатов, И.Х. Турапов, Н.Е. Норбутаев

Исследование сплавов силицида Mn_4Si_7 , полученных в различных условиях, с помощью рентгеновского дифрактометра

Исследованы кристаллы силицида Mn_4Si_7 , полученные методами горячего изостатического прессования (ГИП) и диффузии. В результате исследования в кристалле Mn_4Si_7 , полученном методом ГИП, обнаружено 11 пиков, а в кристалле Mn_4Si_7 , полученном методом диффузии, — 14 пиков. Определен размер кристаллов силицида Mn_4Si_7 (D_{HIP}) от $8,8 \cdot 10^{-9}$ м до $3,6 \cdot 10^{-8}$ м, (D_{Diff}) от $6,2 \cdot 10^{-10}$ м до $9,1 \cdot 10^{-8}$ м. Установлено, что решеточное напряжение между атомами кристалла силицида Mn_4Si_7 (ϵ_{HIP}) изменяется от 0,01 до 0,41, (ϵ_{Diff}) — от 0,31 до 3,71. Плотность дислокаций на поверхности кристалла (δ_{HIP}) составляла от $3,5 \cdot 10^{10}$ до $3,2 \cdot 10^{12}$, а (δ_{Diff}) — от $1 \cdot 10^{11}$ до $3,2 \cdot 10^{14}$. Степень кристаллизации силицида Mn_4Si_7 , полученного методом (ГИП), составляет 7,02 %, а степень аморфности — 92,98 %. Установлено, что степень кристаллизации силицида Mn_4Si_7 , полученного диффузионным методом, составила 9,3 %, а степень аморфности — 90,7 %. (КОД-1530134) (r). Установлено, что степень кристаллизации высокомарганцевого силицида Mn_4Si_7 низкая, а степень аморфности высокая из-за того, что Mn и Si связаны в нестехиометрическом соотношении.

Ключевые слова: диффузия, кристаллизация, нестехиометрический, плотность дислокаций, деформация решетки, аморфный, агломерация

Information about the authors

Igamov, Bakhrom — Professor, Leading Researcher, Scientific and Technical Center with a Design Bureau and Pilot Production of the Academy of Sciences of the Republic of Uzbekistan, Tashkent, Uzbekistan; e-mail igamov@mail.ru

Kamardin, Aliksey — Professor, Leading Researcher, Scientific and Technical Center with a Design Bureau and Pilot Production of the Academy of Sciences of the Republic of Uzbekistan, Tashkent, Uzbekistan; e-mail kamardin89@mail.ru

Nabiev, Dilmurod — Professor, Rector, Karshi State University, Karshi, Uzbekistan; e-mail inaboev0@mail.ru

Imanova, Gunel (*corresponding author*) — PhD in physics, Associate professor, Leading Researcher, Ministry of Science and Education of the Republic of Azerbaijan, Institute of Radiation Problems, Baku, Azerbaijan; e-mail gunel_imanova55@mail.ru

Bekpulatov, Ilkhom — Dr., Associate professor, Leading Researcher, Karshi State University, Karshi, Uzbekistan; e-mail ilkhom90@mail.ru

Turapov, Ilkhom — PhD, Associate professor, Leading Researcher, Renaissance university of education, Tashkent, Uzbekistan; e-mail turppov@mail.ru

Norbutaev, Nodir — PhD, Associate professor, Leading Researcher, Gulistan State University, Gulistan, Uzbekistan; e-mail nurbattd@mail.ru

Zh.Zh. Akhatova¹, B.R. Ilyassov¹✉, G.S. Seisenbayeva¹,
D.S. Kambar¹, A.K. Aimukhanov², L.S. Aldasheva¹, A.V. Zavgorodniy¹

¹Astana IT University, Mangilik El 55/11, Block C1, 010000 Astana, Kazakhstan;

²Karaganda Buketov University, Karaganda, Kazakhstan

Electrochemical rectifying device based on polymer thin films

In this work we study the rectifying behavior of organic electrochemical transistors (OECTs). Despite OECT devices are symmetric devices they display asymmetrical output IV curves at negative and positive drain bias sweep. Here, we show that the asymmetry is introduced by the electrical connections with the drain (or source) potential affecting the distribution of ion density in the channel that tunes the doping/de-doping state of the channel and consequently modulates its conductivity. This effect is profoundly noticeable on accumulation mode OECT based on Poly(3-hexylthiophene) (P3HT) channel layer. We demonstrate that accumulation mode OECT can operate either as a current rectifier with the positive rectification polarity or as a current rectifier with the negative rectification polarity by simple changing connection of the gate electrode either directly to the source or to the drain, respectively. The underline mechanism of the current rectification and hystereses in IV curves of OECT based rectifier are discussed. At the forward V_{ds} sweep, the doping of the drain region occurs due to the injection of anions driven by positive ΔV . During the forward scan, the channel begins in a highly conductive state, resulting in higher forward current. In contrast, during the backward scan, the channel is more resistive, leading to lower current. Besides the capacitive hysteresis caused by ion inertia, the intrinsic capacitive hysteresis associated with electronic charging/discharging and polarization due to lateral ion movement also contributes to the observed hysteresis.

Keywords: organic electrochemical transistor, electrochemical transistor rectifier, electrochemical transistor diode, asymmetric IV curve, inductive hysteresis, ionic-electronic conductor, P3HT layer

✉ *Corresponding author:* Ilyassov Baurzhan, baurzhan.ilyassov@astanait.edu.kz

Introduction

Electrochemical rectifiers based on organic thin films represent a new class of functional devices that harness the interplay between ionic and electronic transport mechanisms to achieve nonlinear current-voltage (I–V) behavior [1–4]. These devices differ fundamentally from conventional semiconductor diodes, which rely on charge carrier separation at p-n junctions to produce rectification [5]. Instead, electrochemical rectifiers operate through the modulation of the charge carrier density in a semiconducting polymer by ionic species from an electrolyte. This process, known as electrochemical doping and de-doping, provides a unique platform for constructing low-voltage, flexible, and biocompatible electronic components using soft materials [6–10].

The emergence of organic mixed ionic-electronic conductors (OMIECs) has significantly expanded the scope of organic electronics. These materials support simultaneous ionic and electronic conduction [11], enabling new types of devices that bridge the gap between traditional electronics and electrochemical systems. Among OMIECs, poly(3-hexylthiophene) (P3HT) is one of the most widely studied due to its ease of processing, structural tunability, and well-characterized optoelectronic properties [12–14]. While P3HT has been primarily used in organic field-effect transistors (OFETs) [15], photovoltaic cells [16–18], and sensors [19], its electrochemical properties have gained increasing attention, particularly in the context of organic electrochemical transistors (OECTs) [20–22]. In OECTs, the application of a gate voltage causes ion penetration into the polymer bulk, modulating its conductivity via bulk electrochemical doping [23]. This mode of operation makes OECTs highly sensitive to ionic environments, thus ideal for applications in biosensing and neuromorphic computing.

Interestingly, the OECT architecture can be reconfigured into a two-terminal rectifying element by electrically connecting the gate to either the source or drain electrode [4]. In such configurations, the gate potential becomes fixed with respect to one terminal, and the drain potential effectively governs the electrochemical state of the channel. This results in asymmetric doping/de-doping dynamics along the channel length,

leading to I-V characteristics that exhibit diode-like rectification. The rectifying behavior in these organic electrochemical systems is not due to Schottky barriers or built-in potentials, but rather to the spatially non-uniform ionic modulation of conductivity driven by electrochemical gradients. This sets them apart from traditional diodes and brings their operation closer to that of nanofluidic diodes [24], ionic memristors [25], and artificial synapses.

Understanding the rectification mechanisms in these soft electronic devices is essential for unlocking their potential in logic circuits, bioelectronics, and energy conversion. However, despite recent interest, systematic investigations of electrochemical rectification in polymer-based devices remain limited. There is still a lack of clarity on how factors such as device geometry, material morphology, gate connection scheme, and bias polarity influence the degree of rectification. Moreover, the role of ionic dynamics in shaping the time-dependent response of such devices — including hysteresis and inductive effects — is not fully understood. These factors are critical for designing stable and efficient rectifiers that can operate under practical conditions.

In this work, we report the fabrication and in-depth characterization of an electrochemical rectifying device based on an amorphous thin film of P3HT, configured in an OECT-like architecture. Using interdigitated indium tin oxide (ITO) electrodes on glass and a planar electrolyte interface, we construct a geometry that allows us to study the asymmetric modulation of channel conductivity. We demonstrate that when the gate is connected to the source or drain, the device exhibits strong diode-like I-V curves with rectification ratios exceeding an order of magnitude at zero gate bias. This two-terminal configuration simplifies the device operation and opens the door to integration with passive circuit elements. Our recent work [4] presents a comprehensive analytical model that captures the key physical mechanisms governing the operation of organic electrochemical rectifiers, forming the theoretical basis for the present study.

We further investigate the origin of the rectification by combining current-voltage measurements with impedance spectroscopy and cyclic voltammetry, we identify the contributions of ionic motion and charge redistribution to the observed asymmetry and hysteresis in the I-V curves. We also observe the emergence of inductive features in impedance spectra at low frequencies, consistent with previously reported chemical inductance in other mixed-conductor systems such as halide perovskites [26–28]. Our results reveal that the dynamic electrochemical behavior of the channel is highly sensitive to both the direction and rate of voltage sweeps, reflecting the inherent ion-electron coupling and slow ionic response.

The findings presented in this study offer new insights into the operation of electrochemical rectifiers and provide a foundation for the rational design of next-generation devices based on organic semiconductors and electrolytes. By harnessing electrochemical rectification in OMIEC materials, it becomes possible to construct soft, printable diodes and memory elements that operate efficiently in aqueous or physiological environments, paving the way for their application in wearable electronics, implantable devices, and neuromorphic circuits.

Experimental

Organic electrochemical rectifiers with the architecture of OECT is fabricated using P3HT as the active material in the channel. P3HT (LT-S909) was purchased from Luminescence Technology Corp. As source-drain electrodes interdigitated pre-patterned ITO glass substrates from Ossila (S161: Width \times Length: 30 mm \times 50 μ m) were used. P3HT solution was prepared by dissolving 25 mg of polymer in 1 ml chlorobenzene in a glovebox with an inert atmosphere. The solution was stirred during 3 hours at 45 °C before spin-coating. ITO patterned source-drain substrates were rigorously cleaned. First, substrates were sonicated in DI water with a detergent for 10 mins, and then were rinsed three times by DI water, followed by a sonication in acetone and IPA for 10 mins. Finally, substrates were dried by nitrogen flow and were treated by UV-ozone (UV Ozone Cleaner with UV intensity is approximately 15 mW/cm² at 185 nm, L2002A3-EU, Ossila) for 15 minutes in order to remove any residual organics and improve wettability of the substrate surface.

P3HT channel layers were casted by a spin-coating technique. 30 μ L of the P3HT solution at 45 °C were dropped on substrate spinning at rate of 1000 rpm and was kept rotating for 1 minute. As-casted P3HT films were further used without annealing in an amorphous state. According to the works of Ginger and his co-workers, amorphous P3HT based OECTs mostly operate in electrochemical mode [20, 21]. 20 mM KCl aqueous solution was used as electrolyte and Ag wire served as a gate electrode. IV curves were measured by a 2 channel Keithley source meter controlled by a customized LabVIEW program. The impedance spectra were probed by PalmSens4 potentiostat with Impedance Analyzer.

Results and Discussion

Rectification behavior of OEET

The simplified diagram of accumulation mode OEETs is depicted in Figure 1A. The interdigitated ITO on a glass substrate was used as source and drain electrodes. An amorphous P3HT layer, 20 mM KCl aqueous solution and Ag wire were used as a channel, an electrolyte and a gate, respectively. The P3HT based OEET, which is the accumulation mode device, is on turn off state at the absence of the gate bias ($V_{gs} = 0$ V). At $V_{gs} = 0$ V, the P3HT channel has a negligible density of holes and as a result a low conductivity. By applying the negative gate bias relative to the source, the conductivity of the channel can be increased dramatically. Under an appropriate negative V_{gs} , anions (Cl^-) from electrolyte are injected into the bulk of P3HT and consequently equivalent amount of holes will be inserted from the source (at $V_{ds} < 0$) in order to electronically compensate for charges of anions. This phenomenon is called an electrochemical doping. Biasing the drain relative to the source generates an electric current in the channel (I_{ds}), the value of which depends on the applied V_{gs} . The more negative V_{gs} results in higher I_{ds} at fixed V_{ds} due to the increased channel conductivity resulted from the electrochemical doping. However, the (de)doping of ions is driven not only by the gate bias but in addition it is affected by the drain (or source) potential interfering the electrochemical doping.

The output curves of P3HT OEET are shown in Figure 1B. The output curves at various gate biases (V_{gs}) were measured at negative and positive drain bias (V_{ds}) polarities relative to the source in order to reveal inherent rectifying feature of OEET. As can be seen from Figure 1B, OEET output curves are asymmetrical, current values at positive V_{ds} sweep is higher in comparison with negative V_{ds} sweep. This asymmetry in the output curve is more profound at $V_{gs} = 0$ V. The rectification ratios at $V_{ds} = \pm 0.3$ V for different gate biases are listed in Table. At $V_{gs} = 0$ V, OEET shows the highest rectification ratio, the current at forward bias ($V_{ds} > 0$) at least one order of magnitude larger in comparison with reversed current ($V_{ds} < 0$). We observe that the more negative gate bias noticeable mitigates this IV asymmetry due to enhanced doping of the channel.

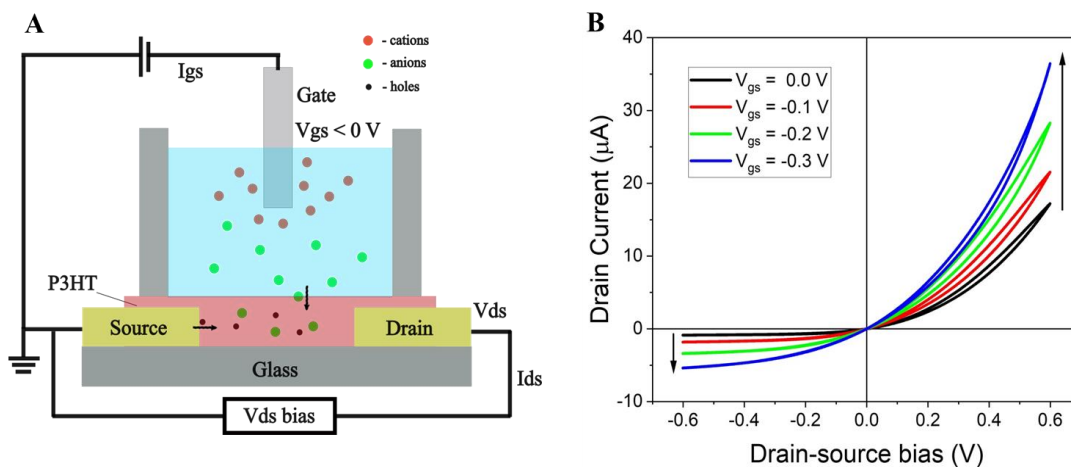


Figure 1. The schematic representation of the P3HT based OEET [4] and its output curves at various gate bias. The output curves were measured at the V_{ds} sweep in both negative and positive values relative to the source

Table

Rectification ratio of the drain current at different gate biases

Gate bias (V_{gs})/V	Current (μA) at V_{ds} : -0.3 V	Current (μA) at V_{ds} : +0.3 V	Rectification ratio
0.0	0.32	4.1	12.8
-0.1	1.6	6.3	3.9
-0.2	2.8	8.4	3.0
-0.3	4.1	10.3	2.5

The rectifying ratio of the OEET is more profound at $V_{gs} = 0$ V, therefore it is straightforward to use OEET as a current rectifier at $V_{gs} = 0$ V, which allow simplifying the OEET into a two terminal device. The simplest approach to maintain V_{gs} at 0 V is to connect it directly to the source electrode, which is a common

technique in MOSFET in order to use a transistor as a diode [29]. However it is worth mentioning that typical MOSFET contains a shunting diode, which passes current when the source and drain are shorted and without the shunting diode MOSFET will have symmetric IV curves. The electrical connection of the OEET with the shorted gate and source and its corresponding IV curve is represented in Figure 2. For comparison IV curves of a pristine amorphous P3HT layer (before adding the electrolyte) and the same device without the gate electrode is also shown. The IV characteristics in Figure 2 and in the following Figures were measured in the range of V_{ds} of -0.4 V to $+0.6$ V. It is due fact that the wider range of V_{ds} caused irreversible change of the channel conductivity.

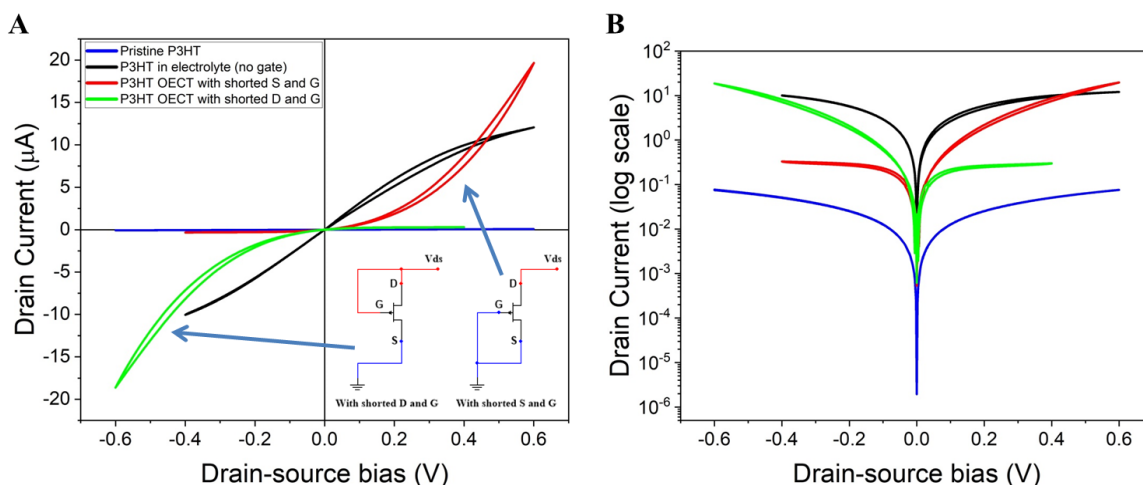
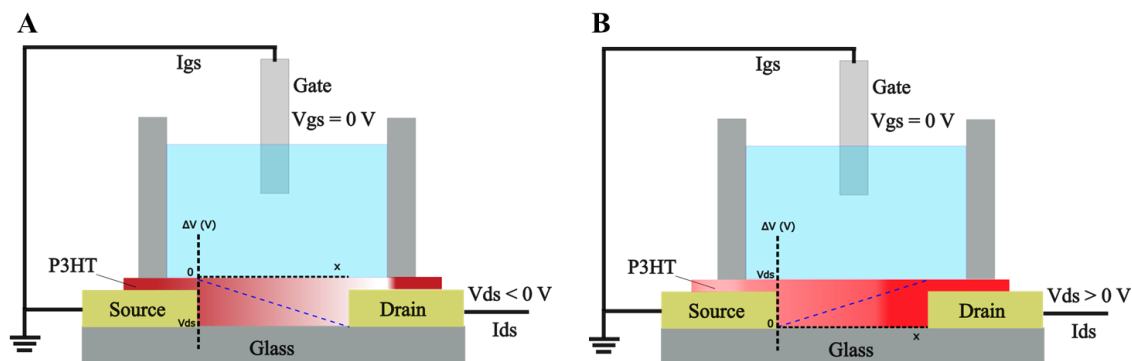


Figure 2. The schematic representation of OEET with shorted gate and source and shorted gate and drain and their IV characteristics (For comparison IV of pristine P3HT and P3HT in electrolyte without gate are also plotted)

The IV curve of the device without gate is almost symmetrical, which highlights the importance of the gate for the current rectification. Without gate electrode, in a perfectly aligned device (where the channel length is much greater than the overlap between the interfaces of electrolyte/channel/electrode), the IV curve of the device would be symmetric [3]. However, in real devices, this interface overlap area is not negligible, and this contact overlap forms an electrochemical double layer causing the electrochemical electrode coupling (EEC), which can cause asymmetric IV curve in OEET devices without a gate [3]. This EEC phenomenon drives inhomogeneous (de)doping of ions and strongly depends on device geometry. In the case when the gate is presented, the rate of (de)doping of ions is governed by the potential difference between the gate and the channel, where the potential of the channel along its length is nonuniform [30–32].

As was seen from Figure 2, OEET with shorted gate and source electrodes reveals diode like IV curve. At the positive V_{ds} , the device is more conductive and at the negative V_{ds} it is highly resistive. We associate this phenomenon with the effect of the drain on doping/de-doping of the channel (Fig. 3). At negative V_{ds} sweep, we detect a low current which is comparable with a current in the pristine P3HT implying that the channel is de-doped (Fig. 3A). Though, this de-doping is not uniform along the channel length and more profound close to the drain. However, at the positive V_{ds} sweep, the device shows a significantly higher current, which indicate about doping of the channel during the scan (Fig. 3B). Similarly, this doping also is not uniform. It is worth mentioning that this highly asymmetrical IV curve of P3HT OEET resembles the IV curve of nanofluidic rectifiers based on nanopores [24, 33]. However, the underline rectifying mechanism is completely different.

One can argue that the enhanced drain current in positive V_{ds} sweep can be the leakage current which can originate between electrolyte/P3HT/drain overlap areas. However, the contribution of the leakage current on I_{ds} can be easily analyzed by comparing I_{ds} with I_g (gate current) due to I_g current is the sum of the channel charging current and the leakage current. Therefore, the origin of this diode-like IV curve of OEET with shorted source and gate is attributed with the effect of the drain potentials on doping/de-doping process.



Blue dotted line shows an overly simplified channel potential (ΔV) along its length relative to the gate. The gradient of the channel color is oversimplified doping state of the channel: in the case of Figure 3A cherry red colored regions are initial low de-doped state, whereas more bleached regions are de-doped state. Oppositely, in the case of Figure 3B, low faintly bleached regions are initial low de-doped state and reddish regions are doped state. The charge carriers are not shown

Figure 3. Simplified diagrams of de-doping (A) and doping (B) of the channel governed by the drain potential

The potential along the length of the channel (ΔV) is not constant (Fig. 3). It is 0 V near the source and either increases or decreases toward the drain, depending on the polarity of the V_{ds} , up to the value of the drain potential near the drain. The source and gate is shorted and the potential difference ΔV ($V_{ch} - V_g$) between the channel region near the source and the gate is 0 V and always fixed to this value. Therefore there is no any ion driving force perpendicular to the channel near the source region, which governs doping/de-doping process. In contrast, the situation is completely different around the channel region near the drain. The drain region potential is changing during the V_{ds} sweep, which causes the change of the magnitude and the direction of the driving force of the doping/ de-doping process at that region. The ΔV is changing and its sign depends on the V_{ds} polarity.

At the negative V_{ds} sweep, the potential of P3HT region from the drain and toward the source is negative relative to the gate and its value increases, which creates ion driving force pattern pushing absorbed anions back to the solution and pulling cations into the channel, therefore causing de-doping of P3HT. At the more negative V_{ds} the state of the de-doping increases and the volume of this depleted region broadens towards the source, which overall contributes to the decrease of the P3HT film conductivity. In contrast, at the positive drain bias sweep, the region around the drain becomes more conductive due to the increase of the anion density caused by positive ΔV . The sweep of V_{ds} to more positive values will further increase the anion density and widen this enriched region toward the source. As result, the conductivity of the film increases.

As it was shown by the previous discussion, the accumulation mode OECT with shorted gate and source electrodes function as a two terminal rectifier with the positive polarity rectification. However, the rectification polarity can be easily reversed by changing the connection of the gate. In Figure 2, an electrical connection of OECT with shorted gate and drain electrodes and its IV curve is shown as well. As the IV curve indicates, the OECT with shorted gate and drain behaves as a rectifier with negative high current. At the positive V_{ds} sweep the current is low and is comparable to the current of the pristine P3HT device. However, at the negative V_{ds} sweep the current is higher by at least one order.

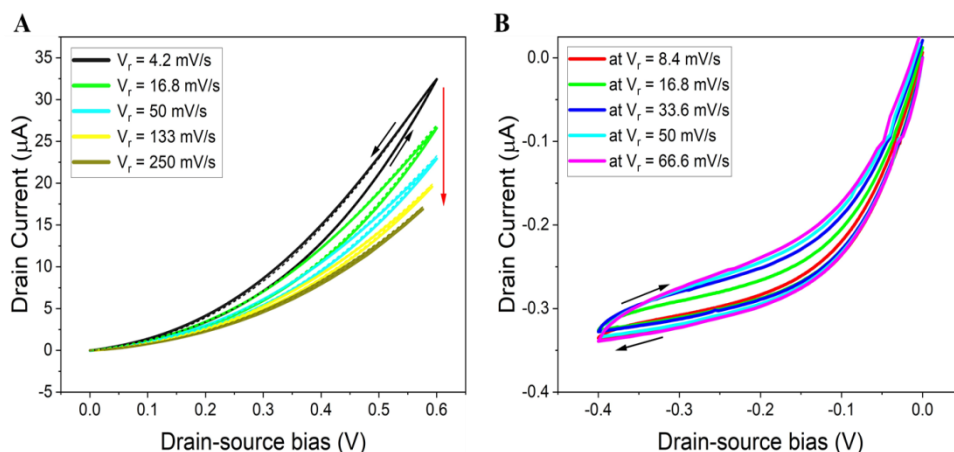
The IV curve of the OECT with shorted gate and drain is almost mirror reflection of the IV curve of the OECT with shorted gate and source. The rectifying mechanism is identical; however the doping/de-doping processes are governed by the source electrode. During V_{ds} sweep, ΔV near the drain region is 0 V (due to $V_{gs} = V_{ds}$) and fixed, whereas at the source region ΔV is changing due to change of gate potential, which is connected to the drain. At positive V_{ds} sweep, $\Delta V < 0$, the gate is more positive relative the source, which causes an intake of cations and pushing anions out. This causes de-doping of the channel region near the source and widening its volume toward the drain, which leads to the decrease of the channel conductivity and lower current at positive V_{ds} sweep. At negative V_{ds} sweep, near the source $\Delta V > 0$, which creates the pattern of ion driving force pushing anions into the channel and extracting cations. Overall, the density of holes increases leading to the growth of channel conductivity and to enhanced I_{ds} .

Hysteresis in IV curves

Electrochemical devices typically have strong hystereses in cyclic voltammetry IV curves. The origin of the hystereses can be various. In this section we will discuss the hystereses originating from sluggish ion response on a potential perturbation. In OECTs, (de)doping rate is limited by ion mobility in the channel, which is significantly smaller in the comparison with the hole mobility. This ion sluggishness usually reveals itself in cyclic voltammetry as hysteresis in various electronic devices involving ion migration due to the applied bias [34–37]. Similarly, in IV curves of OECTs, we observe hystereses, when the current measured at forward scan does not coincide with the current probed at the backward scan. The hysteresis in IV curves of OECTs is inherent phenomenon and in the most cases it is caused by slow response of ions to V_{gs} or V_{ds} change [38, 39].

In Figure 4, cyclic IV curves of the OECT rectifier with shorted gate and source at positive V_{ds} sweep measured at various scan rates (V_r) are depicted. Each IV curves at a fixed scan rate was measured at least two times in order to make sure that observed hystereses are kinetic. We should clarify that these IV curves on Figure 4, technically, is output curves of OECT at $V_{gs} = 0$. However, due to the significant effect of the drain on the channel doping/de-doping process, these IV curves are not measured at the steady-state gate current. During the V_{ds} sweep the gate current changes causing doping and de-doping of the channel. This (de)doping of the channel during the CV measurement causes hystereses.

In cyclic IV curves of the OECT rectifier at positive V_{ds} , we observe inductive hysteresis, which is attributed with the slow response of ions to the change of ΔV . At the forward V_{ds} sweep, the doping of the drain region occurs due to the injection of anions driven by positive ΔV . When the V_{ds} reaches the turning point, the channel has been doped to some extent to a more conductive state and during the backward V_{ds} sweep de-doping takes place, but the channel is in the slightly higher conductive state, which causes the higher backward current and the observed hysteresis. The doping and de-doping of the channel is not fast and is limited by an ion drift diffusion rate.



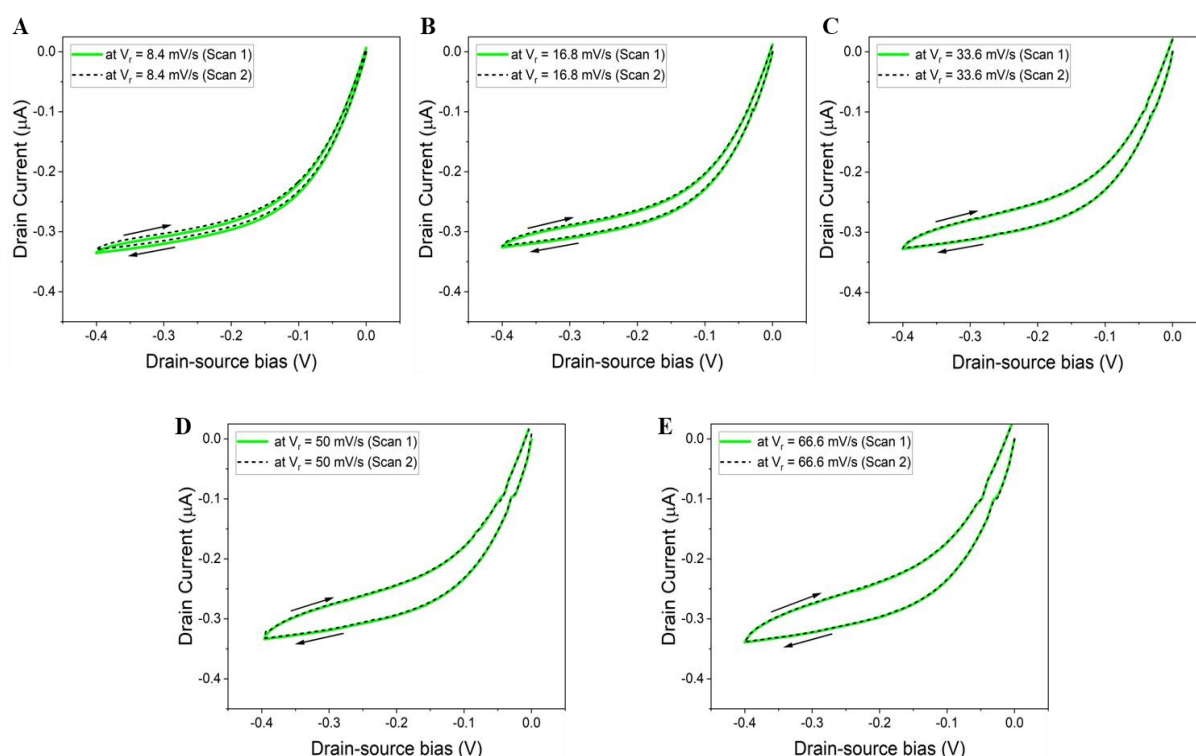
Measurements at each V_r were measured at least two times; second scans were performed after initials with 15 sec delay and they are shown as dotted lines.

For (B) seconds scans are shown in Figure 5

Figure 4. Cyclic voltammetry measurements at positive (A) and negative (B) V_{ds} sweep

The increase of V_{ds} scan rate affects the hysteresis strength and the value of drain current. As can be seen from Figure 4A the hysteresis strength shrinks by increasing V_r and the overall current is decreasing (shown in Figure 4 by a red arrow), which can be explained by the ion slow response to ΔV change. At faster V_r , the channel cannot reach the density of anions that it can do at slower V_r due to ions have less time to dope the channel at the same V_{ds} sweep range and therefore it is less conductive at higher V_r . The collapse of the inductive hysteresis at higher V_r , we attribute with capacitive contribution of the channel. V_{ds} also causes lateral ion movements in the channel, which polarizes the channel [31, 40, 41]. As can be seen from Figure 4, the competition of two types of hystereses results in hysteresis-free IV curve in OECT rectifier at higher positive V_{ds} sweep rate.

The cyclic IV curves of OECT with shorted gate and source at negative V_{ds} sweep also have hystereses. However, in contrast to IV curves in the first quadrant (at positive V_{ds}), the hystereses in IV curves in the third quadrant at negative V_{ds} sweep are purely capacitive (Fig. 4B and 5). Ion slow response to ΔV change can also cause capacitive hysteresis. It depends what occurs at the forward and backward V_{ds} scan: doping and de-doping or vice versa. If it is doping at the forward scan and de-doping at the backward one, the hysteresis is inductive, what we have discussed earlier. Oppositely, at negative V_{ds} sweep during the forward scan it occurs de-doping of the channel, which is more intense near the drain and widens with the decreased intensity toward to the source. Indeed, at negative V_{ds} , the potential difference ΔV is 0 V near the source and growing negatively toward the drain, which causes intake of cations and extraction of anions resulting in the channel depletion (de-doping). At the backward V_{ds} sweep occurs doping due to ΔV value is decreasing and the channel returns to its more conductive state. During the forward scan, the channel starts in a highly conductive state, resulting in a higher forward current. In contrast, during the backward scan, the channel becomes more resistive, leading to a lower current. In addition to the capacitive hysteresis originated from ion inertia, the inherent capacitive hysteresis related with electronic charging/discharging phenomena and polarizing due to the lateral ion shift can also contribute to the observed hysteresis.



CV curves were measured at V_{ds} scan rates (V_r) 8.4 mV/s to 66 mV/s. Measurements at each V_r were measured at least two times; second scans were performed after initials with 15 sec delay and they are shown as dotted lines

Figure 5. Cyclic voltammetry measurements at negative V_{ds} sweep

Additionally, as can be seen from Figure 5 more clearly, with the increase of V_r , the strength of the capacitive hysteresis magnifies. It is also seen from Figure 4B that at the forward scans the current level for each V_r are approximately identical; however the backward currents at higher V_r are noticeably lower in comparison with the backward currents probed at lower V_r . These both trends indicate that at higher V_r other electronic charging/discharging phenomena more profoundly contribute to the hystereses.

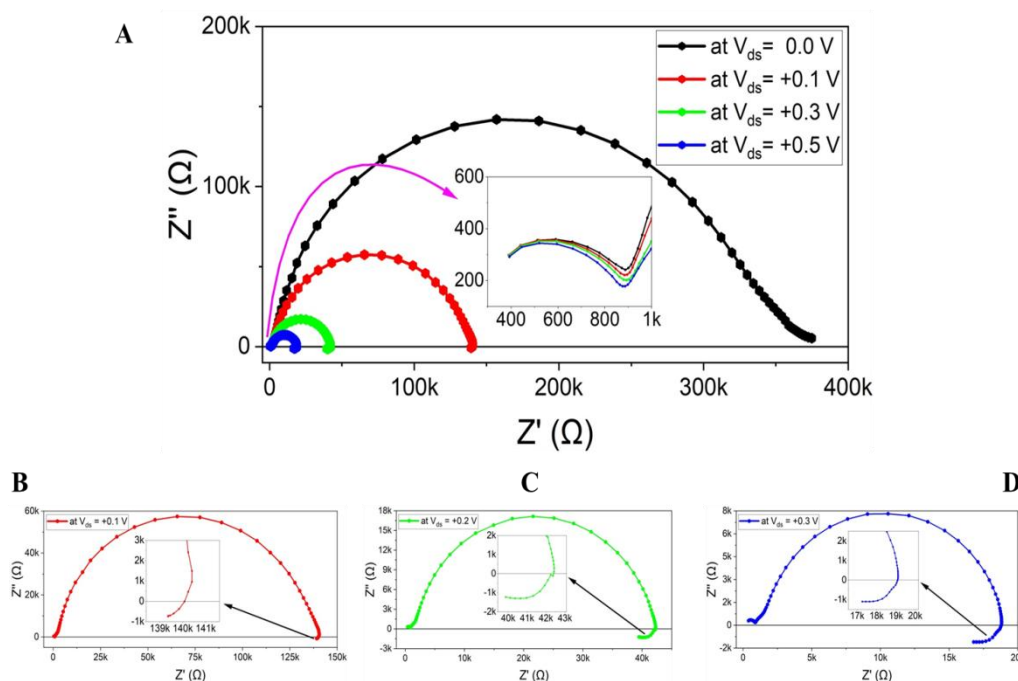
Inductive response in impedance spectra

Inductive hystereses in IV curves also often reported in halide perovskite based devices such as solar cells, photodetectors, LEDs and memristors [34–39]. In many electronic devices, hysteresis is undesired effect due to it complicates the evaluation of device performance and can result to unreliable device operation. Though for some devices such as memristors it is intrinsic property which determines its functionality [42].

As regards OECTs, the usefulness of hysteresis will depend on its application. Therefore a deeper understanding of hysteresis originated from the slow dynamic motion of ions through the electrolyte/channel interface and in the channel itself is important in order to mitigate it or oppositely enhance its strength and reproducibility for specific application.

Impedance spectroscopy technique is one of the useful tools to study charge transfer processes in multi-layered electronic devices [26, 36, 43]. In perovskite based devices, observed inductive hystereses are also detected in impedance spectra (IS) in the form of negative loops at low frequencies [27], which obtained the designation as a chemical inductance [28]. However in OECT, which is a three terminal device, the measurement and analysis of IS not straightforward. Though in the case of OECT with shorted gate and source or shorted gate and drain, the device becomes two terminal and the IS spectra between source and drain can be easily measured. The small AC perturbation applied to the drain will affect both electronic current and additionally ionic current, which with some delay will affect the electronic current.

In Figure 6, the measured IS of the P3HT OECT with shorted gate and source electrodes are shown. IS were measured at the various V_{ds} bias from -0.1 V to $+0.5$ V and at the AC frequency range from 1 MHz to 10 mHz. All measured IS at different V_{ds} compose of three arcs: large arc located in the middle of IS is clearly related with channel resistance and capacitance. We observe that at negative V_{ds} , the middle arc diameter is too large, whereas at positive V_{ds} its value is decreasing (Fig. 6), which is consistent with the IV curve of the device.



A — Impedance spectra measured at V_{ds} bias from 0 V to +0.5 V;
B, C, D — IS at $V_{ds} = +0.1$ V, $V_{ds} = +0.3$ V, and $V_{ds} = +0.5$ V, respectively

Figure 6. Impedance spectra of OECT with shorted gate and source

At high frequencies there is a small arc in all IS, which does not depend on V_{ds} (the inset in Figure 6A). In the IS of pristine P3HT device (without electrolyte) this small arc is absent. However, it is present in the device with electrolyte but without gate, which implies that this arc in the high frequency range presumably represents double layer at the electrolyte/P3HT/electrode interface.

The IS responses at low frequencies are significantly different at both V_{ds} polarities. At negative -0.1 V and 0 V it has mixed diffusion and RC characteristics, whereas at positive V_{ds} , we observe inductive loops curling in negative Z'' toward the origin (Fig. 6B-D). This type of negative loops at low frequencies are common in IS of perovskite based devices associate with slow transients in the current upon ion displacement under bias change [44]. In the same manner, small AC perturbation in OECT causes ion displacement (doping/de-doping) and slow transient of the I_{ds} .

In contrast to the perovskite based devices, in OECT ion drift is two dimensional: (perpendicular) across the channel, which is governed by gate-channel potential difference and (lateral) along the channel, which is determined by potential difference between the drain and the source. The robust electrical equivalent circuit is needed in order to properly fit experimental IS and evaluate charge transport characteristics. The detail analysis of IS of OECTs is beyond the scope of this work and will be addressed in future works. Nevertheless, the observed inductive loop in IS at positive V_{ds} is consistent with inductive hysteresis in OECT output curve, which confirm the concept of last studies showing that slow motion of ions in mixed ionic-electronic devices is universal phenomenon related to the hysteresis in the current-voltage characteristics [43]. A recent effort by J. Bisquert proposed an equivalent circuit for OECTs that incorporates the key features of mixed conduction and transient ionic response [44]. However, this model continues to evolve and requires further refinement and validation across different device configurations and operational regimes.

Conclusions

This work has revealed underestimated rectifying functionality of OECTs. OECTs inherently have asymmetrical output curves caused by the effect of the drain potential. Despite this phenomenon is undesired feature in OECT operation, it can be utilized for the development of organic electrochemical rectifiers (diodes) for printable electronics. The same OECT device can be used as polarity switchable rectifier by changing the connection of the gate electrodes. The origin of rectifying behavior of OECT is proposed based on enormous studies in OECT analysis of IV characteristics. The significant asymmetry in IV curve of OECT with shorted gate and source and shorted gate and drain are related with the enormous effect of the drain (or source) potential, which can modulate doping and de-doping state in the channel. However, detail studies are needed to obtain deep understanding of the rectifying characteristics and to derive solid theoretical model of transient current of OECT based rectifiers. Moreover, it is not clear how the device geometry and channel material properties will affect the rectifying characteristics of OECTs, which require more rigorous studies. Nevertheless, this work reminds overlooked rectifying property of OECTs enabling them found a new application in organic electronics, bioelectronics and neuromorphic computing.

Acknowledgments

We thank the Science Committee of the Ministry of Science and Higher Education of the Republic of Kazakhstan for financial support under the project Grant No. AP19576727. B. Ilyassov expresses his sincere gratitude to Prof. Juan Bisquert and Prof. Antonio Guerrero from INAM, Universitat Jaume I, for providing the valuable opportunity to receive research training at INAM sponsored by Bolashak International Scholarship, focusing on the development and characterization of organic electrochemical transistors (OECTs).

References

- 1 Chen, M., Nilsson, D., Kugler, T., Berggren, M., & Remonen, T. (2002). Electric current rectification by an all-organic electrochemical device. *Applied Physics Letters*, 81(11), 2011–2013. <https://doi.org/10.1063/1.1506785>
- 2 Kim, Y., Kim, G., Ding, B., Jeong, D., Lee, I., Park, S., Kim, B.J., McCulloch, I., Heeney, M., & Yoon, M. (2022). High-Current-Density organic electrochemical diodes enabled by asymmetric active layer design. *Advanced Materials*, 34(7). <https://doi.org/10.1002/adma.202107355>
- 3 Weissbach, A., Cucchi, M., Tseng, H., Leo, K., & Kleemann, H. (2023). Unraveling the electrochemical electrode coupling in integrated organic electrochemical transistors. *Advanced Functional Materials*, 33(46). <https://doi.org/10.1002/adfm.202302205>
- 4 Ilyassov, B., Zavgorodniy, A., Alekseev, A., & Aldasheva, A. (2024b). Rectifying behavior of organic electrochemical transistors. *Physica B Condensed Matter*, 416620. <https://doi.org/10.1016/j.physb.2024.416620>
- 5 Sze, S.M., & Ng, K.K. (2006). *Physics of semiconductor Devices*, 293–296. <https://doi.org/10.1002/0470068329>
- 6 Organic Electrochemical Transistors as an Emerging Platform for Bio-Sensing Applications: A review. *IEEE Sensors Journal*, 21(4), 3977–4006. <https://doi.org/10.1109/jsen.2020.3033283>
- 7 Flexible organic electrochemical transistors for bioelectronics. *Cell Reports Physical Science*, 4(11), 101673. <https://doi.org/10.1016/j.xcrp.2023.101673>
- 8 Feron, K., Lim, R., Sherwood, C.P., Keynes, A., Brichta, A.M., & Dastoor, P.C. (2018). Organic Bioelectronics: Materials and biocompatibility. *International Journal of Molecular Sciences*, 19(8), 2382. <https://doi.org/10.3390/ijms19082382>
- 9 Ohayon, D., & Inal, S. (2020). Organic bioelectronics: from functional materials to Next-Generation devices and power sources. *Advanced Materials*, 32(36). <https://doi.org/10.1002/adma.202001439>

- 10 Torricelli, F., Adrahtas, D.Z., Bao, Z., Berggren, M., Biscarini, F., Bonfiglio, A., Bortolotti, C.A., Frisbie, C.D., Macchia, E., Malliaras, G.G., McCulloch, I., Moser, M., Nguyen, T., Owens, R.M., Salleo, A., Spanu, A., & Torsi, L. (2021). Electrolyte-gated transistors for enhanced performance bioelectronics. *Nature Reviews Methods Primers*, 1(1). <https://doi.org/10.1038/s43586-021-00065-8>
- 11 Paulsen, B.D., Fabiano, S., & Rivnay, J. (2021). Mixed Ionic-Electronic transport in polymers. *Annual Review of Materials Research*, 51(1), 73–99. <https://doi.org/10.1146/annurev-matsci-080619-101319>
- 12 Kleinschmidt, A.T., Root, S.E., & Lipomi, D.J. (2016). Poly(3-hexylthiophene) (P3HT): fruit fly or outlier in organic solar cell research? *Journal of Materials Chemistry A*, 5(23), 11396–11400. <https://doi.org/10.1039/c6ta08317j>
- 13 Ludwigs, S. (2014). P3HT revisited — from molecular scale to solar cell devices. In *Advances in polymer science*, 265, 24–27. <https://doi.org/10.1007/978-3-662-45145-8>
- 14 Agbolaghi, S., & Zenoozi, S. (2017). A comprehensive review on poly(3-alkylthiophene)-based crystalline structures, protocols and electronic applications. *Organic Electronics*, 51, 362–403. <https://doi.org/10.1016/j.orgel.2017.09.038>
- 15 Runfang, H., Yangfan, Y., Leilei, L., Jianlong, J., Qiang, Z., Lifeng, D., Shengbo, S., & Qiang, L. (2022). P3HT-based organic field effect transistor for low-cost, label-free detection of immunoglobulin G. *Journal of Biotechnology*, 359, 75–81. <https://doi.org/10.1016/j.jbiotec.2022.09.022>
- 16 Ghosekar, I.C., & Patil, G.C. (2021). Review on performance analysis of P3HT:PCBM-based bulk heterojunction organic solar cells. *Semiconductor Science and Technology*, 36(4), 045005. <https://doi.org/10.1088/1361-6641/abe21b>
- 17 Rozhkova, X.S., Aimukhanov, A.K., Ilyassov, B.R., Tussupbekova, A.K., Zeinidenov, A.K., Alexeev, A.M., Zhakanova, A.M. (2023). Effect of WS₂ nanoparticles on the current-voltage characteristics of a polymer solar cell. *Bulletin of the University of Karaganda – Physics*, (109) 1, 13–22. <https://doi.org/10.31489/2023PH1/13-22>
- 18 Omarbekova, G.I., Aimukhanov, A.K., Ilyassov, B.R., Alexeev, A.M., Zeinidenov, A.K., & Zhakanova, A.M. (2023). Effect of the thickness and surface interface of In₂O₃ films on the transport and recombination of charges in a polymer solar cell. *Bulletin of the University of Karaganda – Physics*, (110) 2, 17–24. <https://doi.org/10.31489/2023PH2/17-24>
- 19 Cheng, S., Wang, Y., Zhang, R., Wang, H., Sun, C., & Wang, T. (2023). Recent progress in gas sensors based on P3HT Polymer Field-Effect transistors. *Sensors*, 23(19), 8309. <https://doi.org/10.3390/s23198309>
- 20 Giridharagopal, R., Flagg, L.Q., Harrison, J.S., Ziffer, M.E., Onorato, J.W., Luscombe, C.K., & Ginger, D.S. (2017b). Electrochemical strain microscopy probes morphology-induced variations in ion uptake and performance in organic electrochemical transistors. *Nature Materials*, 16(7), 737–742. <https://doi.org/10.1038/nmat4918>
- 21 Flagg, L.Q., Giridharagopal, R., Guo, J., & Ginger, D.S. (2018). Anion-Dependent doping and charge transport in organic electrochemical transistors. *Chemistry of Materials*, 30(15), 5380–5389. <https://doi.org/10.1021/acs.chemmater.8b02220>
- 22 Colucci, R., De Paula Barbosa, H.F., Günther, F., Cavassin, P., & Faria, G.C. (2019). Recent advances in modeling organic electrochemical transistors. *Flexible and Printed Electronics*, 5(1), 013001. <https://doi.org/10.1088/2058-8585/ab601b>
- 23 Rivnay J., Inal S., Salleo A., Owens R. M., Berggren M., & Malliaras G. G. (2018). Organic electrochemical transistors. *Nature Reviews Materials*, 3(2). <https://doi.org/10.1038/natrevmats.2017.86>
- 24 Ramirez, P., Portillo, S., Cervera, J., Bisquert, J., & Mafé, S. (2024). Memristive arrangements of nanofluidic pores. *Phys. Review E*. 109(4), 044803. <https://doi.org/10.1103/PhysRevE.109.044803>
- 25 Xu, G., Zhang, M., Mei, T., Liu, W., Wang, L., & Xiao, K. (2024). Nanofluidic ionic memristors. *ACS Nano*. <https://doi.org/10.1021/acsnano.4c06467>
- 26 Bou, A., & Bisquert, J. (2021). Impedance spectroscopy dynamics of biological neural elements: from memristors to neurons and synapses. *The Journal of Physical Chemistry B*, 125(35), 9934–9949. <https://doi.org/10.1021/acs.jpcc.1c03905>
- 27 Ebadi, F., Taghavinia, N., Mohammadpour, R., Hagfeldt, A., & Tress, W. (2019). Origin of apparent light-enhanced and negative capacitance in perovskite solar cells. *Nature Communications*, 10(1). <https://doi.org/10.1038/s41467-019-09079-z>
- 28 Bisquert, J., & Guerrero, A. (2022). Chemical inductor. *Journal of the American Chemical Society*, 144(13), 5996–6009. <https://doi.org/10.1021/jacs.2c00777>
- 29 Emadi, A., Khaligh, A., Nie, Z., & Lee, Y.J. (2017). Integrated power electronic converters and digital control. In *CRC Press eBooks*. <https://doi.org/10.1201/9781439800706>
- 30 Robinson, N.D., Svensson, P., Nilsson, D., & Berggren, M. (2006b). On the Current Saturation Observed in Electrochemical Polymer Transistors. *Journal of the Electrochemical Society*, 153(3), H39. <https://doi.org/10.1149/1.2172534>
- 31 Kaphle, V., Paudel, P.R., Dahal, D., Krishnan, R.K.R., & Lüssem, B. (2020). Finding the equilibrium of organic electrochemical transistors. *Nature Communications*, 11(1). <https://doi.org/10.1038/s41467-020-16252-2>
- 32 Skowrons, M., Dahal, D., Paudel, P.R., & Lüssem, B. (2023). Depletion type organic electrochemical transistors and the gradual channel approximation. *Advanced Functional Materials*, 34(4), 2303324. <https://doi.org/10.1002/adfm.202303324>
- 33 Ramírez, P., Gómez, V., Cervera, J., Mafé, S., & Bisquert, J. (2023). Synaptical tunability of multipore nanofluidic memristors. *The Journal of Physical Chemistry Letters*, 14(49), 10930–10934. <https://doi.org/10.1021/acs.jpclett.3c02796>
- 34 Muñoz-Díaz, L., Rosa, A. J., Bou, A., Sánchez, R.S., Romero, B., John, R.A., Kovalenko, M.V., Guerrero, A., & Bisquert, J. (2022). Inductive and capacitive hysteresis of halide perovskite solar cells and memristors under illumination. *Frontiers in Energy Research*, 10. <https://doi.org/10.3389/fenrg.2022.914115>
- 35 Bisquert, J., Guerrero, A., & Gonzales, K.C. (2021). Theory of hysteresis in halide perovskites by integration of the equivalent circuit. *ACS Physical Chemistry Au*, 1(1), 25–44. <https://doi.org/10.1021/acspchemau.1c00009>
- 36 Bisquert, J. (2024). Inductive and capacitive hysteresis of Current-Voltage curves: unified structural dynamics in solar energy devices, memristors, ionic transistors, and bioelectronics. *PRX Energy*, 3(1). <https://doi.org/10.1103/prxenergy.3.011001>

- 37 Bisquert, J., Gonzales, K.C., & Guerrero, A. (2023). Transient On/Off photocurrent response of halide perovskite photodetectors. *The Journal of Physical Chemistry C*, 127(43), 21338–21350. <https://doi.org/10.1021/acs.jpcc.3c04672>
- 38 Shameem, R., Bongartz, L.M., Weissbach, A., Kleemann, H., & Leo, K. (2023). Hysteresis in organic electrochemical transistors: relation to the electrochemical properties of the semiconductor. *Applied Sciences*, 13(9), 5754. <https://doi.org/10.3390/app13095754>
- 39 Bisquert, J. (2023). Hysteresis in organic electrochemical transistors: Distinction of capacitive and inductive effects. *The Journal of Physical Chemistry Letters*, 14(49), 10951–10958. <https://doi.org/10.1021/acs.jpclett.3c03062>
- 40 Paudel, P.R., Kaphle, V., Dahal, D., Krishnan, R.K.R., & Lüssem, B. (2020). Tuning the transconductance of organic electrochemical transistors. *Advanced Functional Materials*, 31(3). <https://doi.org/10.1002/adfm.202004939>
- 41 Paudel, P.R., Skowrons, M., Dahal, D., Krishnan, R.K.R., & Lüssem, B. (2022). The transient response of organic electrochemical transistors. *Advanced Theory and Simulations*, 5(5). <https://doi.org/10.1002/adts.202100563>
- 42 Bisquert, J. (2023a). Current-controlled memristors: Resistive switching systems with negative capacitance and inverted hysteresis. *Physical Review Applied*, 20(4). <https://doi.org/10.1103/physrevapplied.20.044022>
- 43 Guerrero, A., Bisquert, J., & Garcia-Belmonte, G. (2021). Impedance Spectroscopy of Metal Halide Perovskite Solar Cells from the Perspective of Equivalent Circuits. *Chemical Reviews*, 121(23), 14430–14484. <https://doi.org/10.1021/acs.chemrev.1c00214>
- 44 Bisquert, J. & Keene, S.T. (2024). Using the transversal admittance to understand organic electrochemical transistors. *Advanced Science*, 12, 2410393, 1–24. <https://doi.org/10.1002/advs.202410393>

Ж.Ж. Ахатова, Б.Р. Ильясов, Г.С. Сейсенбаева, Д.С. Камбар,
А.К. Аймуханов, Л.С. Алдашева, А.В. Завгородний

Полимерлі жұқа қабықшаларға негізделген электрхимиялық түзеткіш құрылғы

Мақалада органикалық электрхимиялық транзисторлардың (ОЕСТs) түзету сипаттамалары зерттелді. ОЕСТ құрылғылары симметриялы құрылғылар болғанына қарамастан, олар ағынның теріс және оң ығысуымен шығыс кернеуінің асимметриялық қисықтарын көрсетеді. Мұнда біз ассимметрияның арнадағы иондар тығыздығының таралуына әсер ететін ағын (немесе көз) потенциалы электрлік қосылыстардан туындайтынын көрсетеміз, бұл арнаның легирлеу/легирлеуді шешу күйін реттейді және осылайша оның өткізгіштігін модуляциялайды. Бұл әсер әсіресе поли(3-гексилтиофен) (РЗНТ) арна қабатына негізделген ОЕСТ жинақтау режимінде байқалады. Жинақтау режиміндегі ОЕСТ оң түзету полярылығы бар ток түзеткіш ретінде немесе басқару электродын тікелей көзге немесе ағынға қосып жай ғана өзгерту арқылы теріс түзету полярылығы бар ток түзеткіш ретінде де жұмыс істей алатынын көрсетілген. ОЕСТ негізіндегі түзеткіштің IV қисықтарындағы токты түзетудің негізгі механизмі және гистерезис талқыланды. ОЕСТ түзеткішінің IV циклдік қисықтарында оң V_{ds} кезінде индуктивті гистерезисті байқаймыз, бұл иондардың ΔV өзгеруіне баяу реакциясымен түсіндіріледі. Тікелей V_{ds} қосылуы кезінде ағынды аймақтың легирленуі оң ΔV туындаған анионды инжекциялау арқылы жүреді. Тікелей сканерлеу кезінде канал жоғары өткізгіштікпен жұмыс істей бастайды, бұл тікелей токтың жоғарылауына әкеледі. Керісінше, кері сканерлеу кезінде канал үлкен кедергіге ие, бұл токтың төмендеуіне әкеледі. Иондық инерциядан туындаған сыйымдылықты гистерезистен басқа байқалатын гистерезис сонымен қатар электронды құрылғыларды зарядтауға/разрядтауға және иондардың бүйірлік қозғалысының поляризациясына байланысты.

Кілт сөздер: органикалық электрхимиялық транзистор, электрхимиялық транзисторлық түзеткіш, электрхимиялық транзисторлық диод, асимметриялық IV қисық, индуктивті гистерезис, иондық-электронды өткізгіш, РЗНТ қабаты

Ж.Ж. Ахатова, Б.Р. Ильясов, Г.С. Сейсенбаева, Д.С. Камбар,
А.К. Аймуханов, Л.С. Алдашева, А.В. Завгородний

Электрохимическое выпрямительное устройство на основе тонких полимерных пленок

В статье изучены характеристики выпрямления органических электрохимических транзисторов (ОЕСТs). Несмотря на то, что устройства ОЕСТs являются симметричными, они демонстрируют асимметричные кривые выходного напряжения при отрицательном и положительном смещении стока. Нами показано, что асимметрия возникает из-за электрических соединений с потенциалом стока (или источника), влияющих на распределение плотности ионов в канале, что настраивает состояние легирования/снятия легирования с канала и, следовательно, модулирует его проводимость. Этот эффект особенно заметен в режиме накопления в ОЕСТ на основе канального слоя из поли(3-гексилтиофена)

(РЗНТ). Мы демонстрируем, что ОЕСТ в режиме накопления может работать либо как выпрямитель тока с положительной полярностью выпрямления, либо как выпрямитель тока с отрицательной полярностью выпрямления путем простого изменения подключения управляющего электрода либо непосредственно к источнику, либо к стоку, соответственно. Обсуждается основной механизм выпрямления тока и гистерезисы в IV кривых выпрямителя на основе ОЕСТ. При прямом сканировании канал начинает работать с высокой проводимостью, что приводит к увеличению прямого тока. Напротив, при обратном сканировании канал обладает большим сопротивлением, что приводит к снижению тока. Помимо емкостного гистерезиса, вызванного инерцией ионов, наблюдаемый гистерезис также обусловлен собственным емкостным гистерезисом, связанным с зарядкой/разрядкой электронных устройств и поляризацией из-за бокового перемещения ионов.

Ключевые слова: органический электрохимический транзистор, электрохимический транзисторный выпрямитель, электрохимический транзисторный диод, асимметричная кривая IV, индуктивный гистерезис, ионно-электронный проводник, слой РЗНТ

Information about the authors

Akhatova, Zhannur — Researcher, Astana IT University, Astana, Kazakhstan; e-mail: Zh.Akhatova@astanait.onmicrosoft.com; ORCID ID: <https://orcid.org/0000-0003-4363-1307>

Ilyassov, Baurzhan (*corresponding author*) — PhD, Associate professor, Astana IT University, Astana, Kazakhstan; e-mail: baurzhan.ilyassov@astanait.edu.kz; ORCID ID: <https://orcid.org/0000-0003-4563-2004>

Seisenbayeva, Gulsaya — Researcher, Astana IT University, Astana, Kazakhstan; e-mail: g.seisenbayeva@astanait.onmicrosoft.com; ORCID ID: <https://orcid.org/0009-0003-7004-4498>

Kambar, Dinara — Researcher, Astana IT University, Astana, Kazakhstan; e-mail: Kambards97@gmail.com; ORCID ID: <https://orcid.org/0000-0003-4742-2000>

Aimukhanov, Aitbek — Professor, Karaganda Buketov University, Karaganda, Kazakhstan; e-mail: aitbekaimukhan@gmail.com; ORCID ID: <https://orcid.org/0000-0002-4384-5164>

Aldasheva, Laura — PhD, Associate professor, Astana IT University, Astana, Kazakhstan; e-mail: Laura.Aldasheva@astanait.edu.kz; ORCID ID: <https://orcid.org/0000-0001-6815-1989>

Zavgorodniy, Alexey — PhD, Astana IT University, Astana, Kazakhstan; e-mail: a.zavgorodniy@astanait.onmicrosoft.com; ORCID ID: <https://orcid.org/0000-0002-3024-7237>

A.E. Goldstein[✉], K.A. Stryapchev*National Research Tomsk Polytechnic University, Tomsk, Russia*

Measurement of ferromagnetic pipe wall thickness by magnetic flux leakage method

The paper considers the use of the magnetic flux leakage method for measuring the wall thickness of ferromagnetic pipes. The method implies longitudinal magnetization of the test pipe section using a short solenoid and measurement of the spatial longitudinal component of the magnetic field strength in the air gap between the solenoid and the test pipe using Hall sensors. A numerical model has been developed to analyze the interaction between the magnetizing field of the short solenoid and the ferromagnetic pipe. The model considers the nonlinear magnetic properties of the test pipe and its geometrical parameters, including the distance between the pipe edge and the measurement plane of magnetic field. The accuracy of the model was validated through physical modeling techniques. A simplified analytical dependence of the longitudinal component of the magnetic field strength on the pipe wall thickness was obtained. A method was proposed to mitigate the impact of the distance from the measurement plane to the pipe edge on wall thickness measurement results. The method entails simultaneous measurement of the magnetic field strength and the distance between the pipe edge and the measurement plane. The method considers the distance between the pipe edge and the measurement plane of the magnetic field strength thereby enabling a 10-fold reduction in the error of the wall thickness measurement induced by the edge effect. The study results can be used for generation, mathematical modeling, and measurement of the magnetic field, including magnetic inspection of steel drill pipes.

Keywords: magnetic testing, magnetic flux leakage method, finite element method, analytical model, Hall sensor

[✉]*Corresponding author:* Goldstein Alexander, algol@tpu.ru

Introduction

Magnetic flux leakage (MFL) has been the most widely used non-destructive testing method for pipes made of ferromagnetic materials [1–4].

According to the MFL method, a pipe section is magnetized along its longitude direction in a constant magnetic field. The main part of the magnetic flux generated by the magnetic field source is closed along the pipe body. A small part of this flux is closed in the air above the pipe, in line with the ratio of magnetic conductivity of the ferromagnetic material and air. The latter is referred to as the magnetic leakage flux.

Given the constant total magnetic flux, a decrease in the pipe cross-sectional area leads to a redistribution of the specified magnetic fluxes: a decrease in the magnetic flux along the pipe body and an increase in the magnetic flux through the air. Consequently, measuring the magnetic flux density in the air (magnetic leakage flux) provides data on the cross-sectional area of a metal object.

In addition, the presence of continuity defects within the pipe leads to the distortion of magnetic field lines, causing a portion of the magnetic flux passing through the metal to leak onto the pipe's surface, thereby forming a local magnetic leakage flux. The disturbance of the magnetic flux depends on dimensions and configuration of the defect, the depth of its location, and its orientation relative to the direction of the magnetizing field.

A comparable technical approach, employed to inspect drill pipes, is testing of steel ropes for the presence of unacceptable reduction in the cross-sectional area and local defects [5, 6].

Problem statement

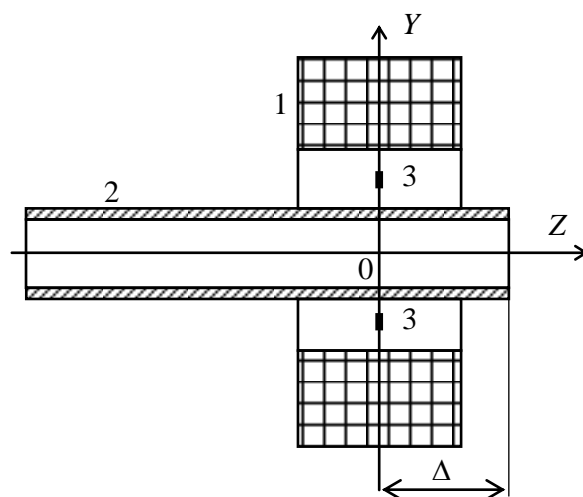
When the MFL method is employed to measure the wall thickness of ferromagnetic pipes, the test object is magnetized by a constant longitudinal magnetic field generated by a short solenoid [7, 8] or by a magnetic system based on permanent magnets [1].

To measure the longitudinal component of the magnetic field strength (hereinafter magnetic field strength), Hall sensors, which are universally employed, are placed in the middle part of the magnetizing de-

vice in the air gap between the magnetizing device and the test object [4]. The number and location of Hall sensors are chosen to overlap the sensitivity zones of adjacent sensors and minimize the impact of test object's transverse displacements on measurement results.

The study attempted to analyze the efficacy of the MFL method for measuring the wall thickness of a ferromagnetic pipe. The study objectives were to develop a numerical model of the interaction between a constant magnetic field generated by a short solenoid and a ferromagnetic pipe, using the finite element method, experimentally verify the developed model, and find simplified analytical expressions to describe the pipe magnetic field and its dependence on the magnetizing device parameters, the pipe wall thickness, and the edge effect.

The geometry of the problem under consideration is depicted schematically in Figure 1.



1 — solenoid; 2 — pipe; 3 — Hall sensor position

Figure 1. Ferromagnetic pipe in the magnetic field of the short solenoid

The test object was a section of the pipe fabricated of 15XM steel. Its outer diameter was 88.9 mm, a wall thickness was 6–12 mm, and a length was 2000 mm. The pipe was magnetized by a solenoid (135 mm in length, 340 mm in outer diameter, 230 mm in inner diameter), with a maximum magnetomotive force $Iw_1 = 8.4$ kA turns, where I denotes the solenoid current and w_1 represents the number of solenoid turns. The pipe and the solenoid were arranged coaxially.

Hall sensors 3 are arranged along the transverse symmetry plane of the solenoid, in the air gap between solenoid 1 and test pipe 2, at an equal distance from the pipe surface. During the pipe wall thickness measurement, at least four Hall sensors are used to minimize the dependence of the measurement result on transverse displacements of the test pipe. The sensors are positioned with an angular shift of 90° relative to the transverse symmetry plane.

During measurement, the test pipe moves in the longitudinal direction Z relative to the solenoid and Hall sensors. During its displacement, the longitudinal component of the magnetic field strength and the distance Δ between the pipe edge and the transverse symmetry plane of the solenoid are measured. The averaged value of the magnetic field measurement by Hall sensors is used as the value of the magnetic field strength H .

A change in the pipe cross-sectional area causes redistribution of magnetic fluxes along the pipe body and through the air. Measuring the magnetic field strength provides data on the cross-sectional area of the metal object, which is linearly related to the pipe wall thickness, T .

Numerical modeling results

A numerical model of interaction between the constant magnetic field generated by the short solenoid and the pipe was developed using the finite element method (FEM).

The benefits of FEM for modeling magnetic fields include arbitrary shape of the inspected area and its capacity to address asymmetric problems by taking into account the heterogeneity of material parameters and the media [9–12].

The model was constructed via the COMSOL Multiphysics software, using the MAGNETIC FIELDS module. The integrated tools of the software were used to construct a 3-D model pipe-inductor, with specified magnetic characteristics of the pipe and the parameters of the inductor, as well as the magnetization mode.

It was assumed in the modeling that the outer boundary of the study area is cylindrical in shape (Fig. 2). The magnetic properties of 15XM steel were set based on a basic magnetization curve experimentally obtained in accordance with GOST 8.377-80 [13].

Figure 3 shows equipotential lines and color spectrum indicating the distribution of magnetic induction B along the longitudinal axis of the pipe at a distance of 20 mm from its surface during interaction with the magnetic field of the solenoid with $Iw_1 = 8.4$ kA turns at a pipe wall thickness of 9.8 mm, which was obtained by numerical modeling. In this case, symmetrical positioning of the pipe relative to the transverse symmetry plane of the solenoid was considered.

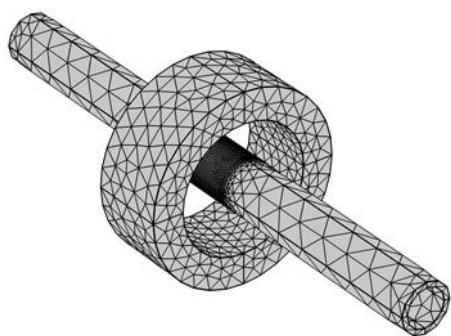


Figure 2. Calculation model after grid superimposition

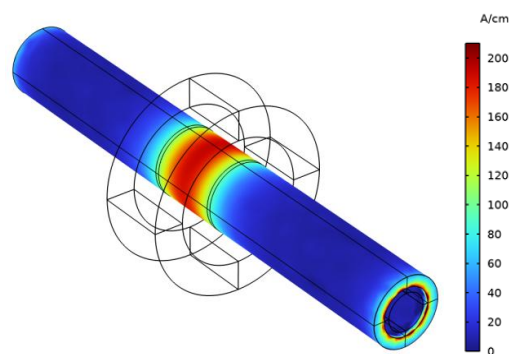


Figure 3. Magnetic induction distribution along the pipe length at a distance of 20 mm from its surface

The analysis of the magnetic field strength distribution along the longitudinal axis $H(Z)$ revealed its inhomogeneous character. A relatively homogeneous magnetic field is observed in the transverse symmetry plane of the solenoid. It extends in the longitudinal direction at a distance comparable to the longitudinal size of the solenoid. In this case, the value of the magnetic field strength H depends on the value of the magnetomotive force Iw_1 , geometrical parameters of the solenoid, magnetic properties of the pipe material, and the pipe wall thickness T .

Figure 4 shows the dependence of the magnetic field strength H in the transverse symmetry plane of the solenoid at a distance of 20 mm from the pipe surface on the value Iw_1 at a wall thickness of 9 mm (solid line) obtained based on the results of numerical simulation. The discrepancy between the calculated and experimental results (circle symbols) does not exceed 3 %, which is acceptable for most practical tasks.

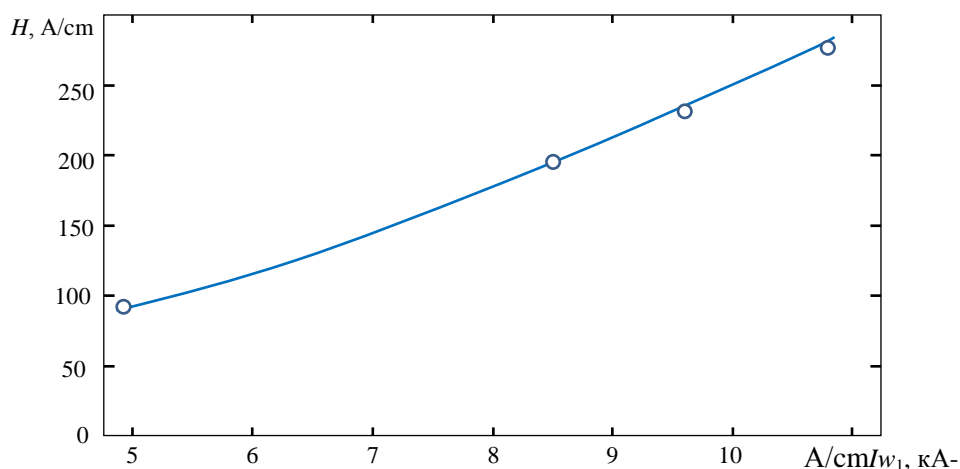


Figure 4. Dependence of the magnetic field strength in the transverse symmetry plane of the solenoid at a distance of 20 mm from the pipe surface on the value of Iw_1

Figure 5 shows the dependence of the magnetic field strength H on the pipe wall thickness T at a fixed value of the magnetomotive force $Iw_1 = 8.4$ kA-turns.

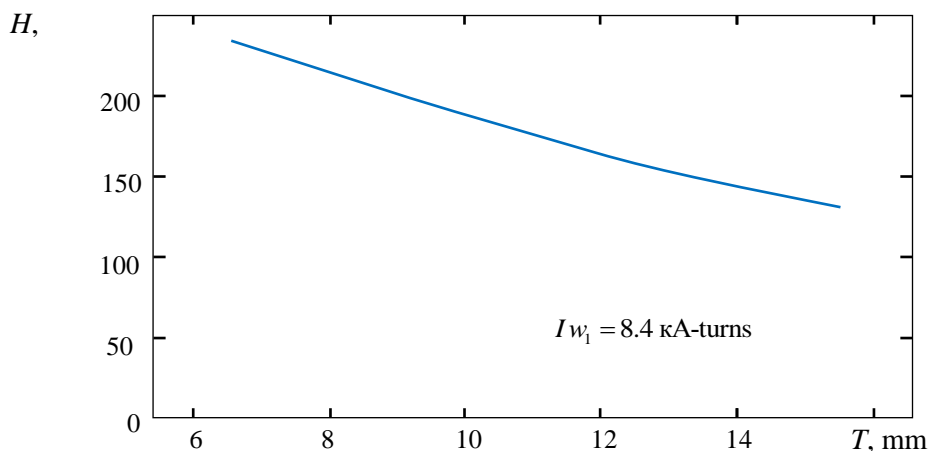


Figure 5. Dependence of the magnetic field strength on the pipe wall thickness

The analysis of this dependence reveals that the direct transformation function $H(T)$ remains constant within the specified range of test parameters $T = (6...12)$ mm. This indicates that the value of T can be determined based on the value of the measured magnetic field strength H . The dependence presented in Figure 5 can be approximated with high accuracy by a polynomial of the third degree:

$$H(T) = 381.003 - 27.145T + 0.932T^2 - 0.016T^3.$$

The inverse transformation function $T(H)$ can also be approximated with high accuracy by a polynomial of the third degree:

$$T(H) = 33.179 - 0.185H + 3.955 \times 10^{-4}H^2 - 3.628 \times 10^{-7}H^3.$$

The magnetic field strength H in the gap depends not only on the pipe wall thickness T , but to a large extent on the distance from the plane (transverse symmetry plane of the solenoid) to the pipe edge.

Figure 6 shows the dependence of the longitudinal spatial component of the magnetic field strength H on the distance Δ between the pipe edge and the transverse symmetry plane of the solenoid.

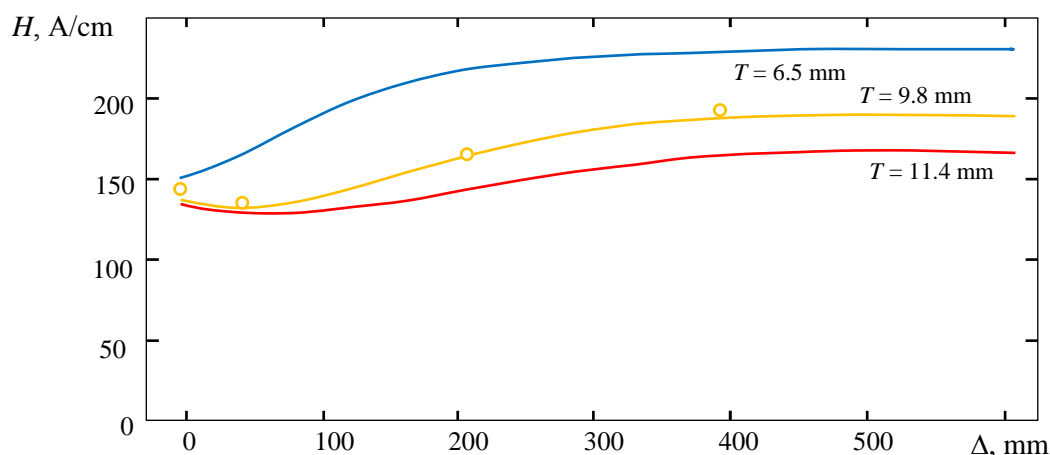


Figure 6. Dependence of the magnetic field strength on the distance from the transverse symmetry plane of the solenoid to the pipe end at different values of T

The analysis of this dependence shows that at the pipe length $L \geq 1.5$ m the magnetic field strength H remains constant in the middle part of the pipe with the constant wall thickness T . When approaching the

pipe edge, the magnetic field strength H decreases significantly. The edge effect is due to the change in the spatial distribution of the magnetic flux when the pipe edge is located close to the magnetized pipe section.

This effect can be mitigated by measuring the magnetic field strength H , as well as the distance Δ between the pipe edge and the transverse symmetry plane of the solenoid. A conventional distance sensor or a distance sensor as part of an electromechanical actuator that moves the test object can be used for measurement. Data on the linear displacement of the test object enable the correction of the wall thickness measurement results that accounts for the edge effect.

Figure 6 (circle symbols) illustrates the experimental dependence of the magnetic field strength on the distance between the pipe end and the transverse symmetry plane of the solenoid at $T = 9.8$ mm. The discrepancy between the calculated and experimental results does not exceed 3.5 %, which indicates that the experimental data correspond to the results of numerical modeling, which is acceptable for most practical tasks.

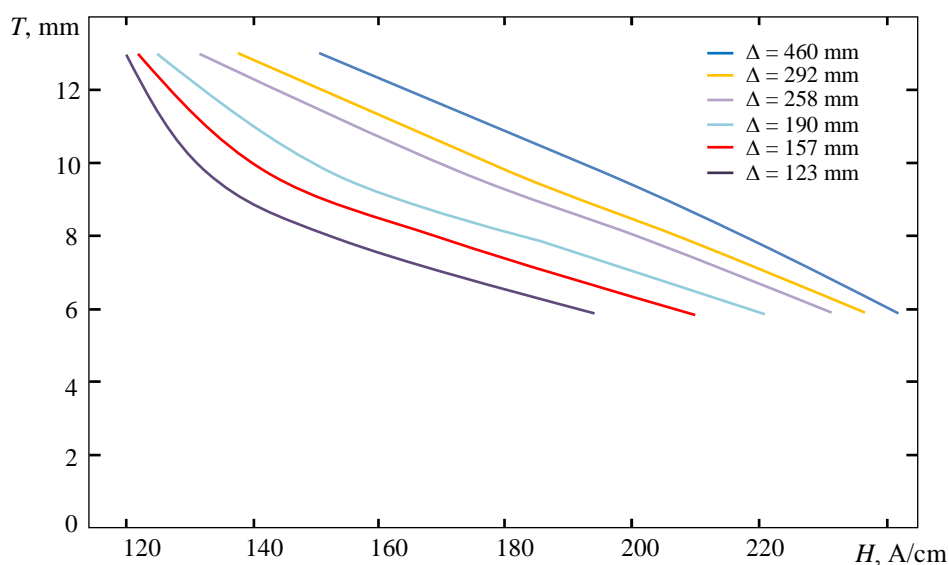


Figure 7. Functions of the inverse transformation of the value of the longitudinal spatial component of the magnetic field strength H into the thickness T of the pipe wall for different distances Δ between the end of the pipe and the transverse plane of symmetry of the solenoid

Figure 7 shows a set of functions of the inverse transformation of the longitudinal spatial component of the magnetic field strength H into the pipe wall thickness T for different distances Δ between the pipe edge and the transverse symmetry plane of the solenoid. A group of pipe specimens with different wall thickness T is used to determine these functions. The magnetic field strength H is measured for fixed values of the distance Δ between the pipe edge and the transverse symmetry plane of the solenoid. Functions $T(H)$ with acceptable accuracy can be obtained by standard approximation of the experimental data by third degree polynomials. For measurement, the value of the test parameter $T(H)$ is calculated for a specific distance Δ .

Conclusion

The effectiveness of the proposed method for measuring ferromagnetic pipe wall thickness was confirmed by the results of laboratory tests performed with a prototype used to measure the thickness of the pipe wall with the specified parameters. A total of 7 test pipes with the wall thickness T within the specified range were used to define the transform functions.

The experimental results showed that the change in the magnetic field strength induced by the edge effect can attain 30 % for the specified geometrical parameters of the test object. Without corrections for the edge effect, the relative measurement error of the wall thickness T can reach 40 %. The length of the edge effect zone is about 500 mm for each of the pipe edges.

The proposed method accounts for the distance between the pipe edge and the solenoid plane and enables 10-fold reduction in the wall thickness error from the edge effect. In this case, the length of untested areas of the test object, where the edge effect mitigation is ineffective, is less than 125 mm.

References

- 1 Christie R. Monitoring and Managing Coiled Tubing Integrity / R. Christie, Ch. Liu, R. Stanley, M. Torregrossa, E. Zheng, L. Zsolt // *Oilfield Review*. — 2015. — Vol. 27, No. 1. — P. 48–56.
- 2 Потапов А.И. Электромагнитные и магнитные методы неразрушающего контроля материалов и изделий. Научное справочно-методическое пособие [в 2 т.]: Т. 2: Электромагнитные и магнитные методы дефектоскопии и контроля свойств материалов / А.И. Потапов, В.А. Сясько, П.В. Соломенчук. — СПб.: Нестор-История, 2015. — 440 с.
- 3 Slesarev D.A. Data processing and representation in the MFL method for nondestructive testing / D.A. Slesarev, A.A. Abakumov // *Russian Journal of Nondestructive Testing*. — 2013. — Vol. 49, No. 9. — P. 3–9.
- 4 Шаранова Д.А. Бесконтактные методы выявления питтинговых дефектов стенок металлических изделий / Д.А. Шаранова // *Территория «НЕФТЕГАЗ»*. — 2016. — № 10. — С. 34–40.
- 5 Промышленная безопасность при эксплуатации грузоподъемных кранов: Сборник документов. Серия 10. Выпуск 7. — 2-е изд., испр. — М.: Научно-технический центр «Промышленная безопасность», 2009. — 288 с.
- 6 Slesarev D. Magnetic and electromagnetic testing of suspension cables of bridges and structures / D. Slesarev, A. Semenov // *Lecture Notes in Civil Engineering*. — 2022. — Vol. 200. — P. 805–810.
- 7 Установка неразрушающего контроля бурильных труб магнитным методом в мобильном исполнении «Магпорт-бур 1.2». Руководство по эксплуатации. СПб., 2016. — 20 с.
- 8 The ARTIS-3 Portable EMI Pipe Inspection System. — [Electronic resource]. — Access mode: <https://oem-usa.com/a3port/> (Date of request: 10.02.2025).
- 9 Potapov A.I. Optimization of the parameters of primary measuring transducers that use the MFL technology / A.I. Potapov, V.A. Syas'ko, O.P. Pudovkin // *Russian Journal of Nondestructive Testing*. — 2013. — Vol. 51, No. 8. — P. 64–71.
- 10 Aikeyeva A.A. Modeling electromagnetic systems / A.A. Aikeyeva, B.A. Zhautikov, A.M. Aidarkhanov, A.S. Zhanasbayeva, F.B. Zhautikov, A.S. Belgibayev // *Bulletin of the University of Karaganda – Physics*. — 2014. — No. 3(75). — P. 28–34.
- 11 Goldshtein A.E. Modeling of magnetic fields and signals of a ferromagnetic pipe flaw detector induced by a through hole defect / A.E. Goldshtein, V.Y. Belyankov // *Bulletin of the University of Karaganda – Physics*. — 2020. — No. 4(100). — P. 49–56.
- 12 Dyusembaeva A.N. Optimal choice of the geometric shape rotor blade wind turbine using the numerical method / A.N. Dyusembaeva, N.K. Tanasheva, T.Zh. Tleubergenova, A.R. Bakhtybekova, Zh.B. Kutumova, A.R. Tussuphanova, N.T. Abdirova // *Bulletin of the University of Karaganda – Physics*. — 2020. — No. 2(114). — P. 53–62.
- 13 ГОСТ 8.377-80 «Материалы магнитомягкие. Методика выполнения измерений при определении статических магнитных характеристик» М.: Издательство стандартов, 1980. — 26 с.

А.Е. Гольдштейн, К.А. Стряпчев

Магниттік ағынның шашырау әдісімен ферромагниттік құбыр қабырғасының қалыңдығын магниттік бақылау

Мақалада ферромагниттік құбырлардың қабырғасының қалыңдығын бақылау үшін магнит ағынының шашырау әдісін қолдану қарастырылған, ол бақыланатын құбыр учаскесінің қысқа соленоиды арқылы бойлық магниттелуіне және электромагниттік құбыр мен бақыланатын Холл датчигі арасындағы ауа саңылауындағы магнит өрісінің кернеулігінің бойлық кеңістік құраушысын өлшеуге негізделген. Сынақ объектісінің сызықты емес магниттік қасиеттерін және оның геометриялық параметрлерін, оның ішінде түтіктің жиегі мен магнит өрісінің кернеулігін өлшеу жазықтығы арасындағы қашықтықты ескере отырып, қысқа соленоидтың магниттеу өрісінің ферромагниттік түтікпен өзара әрекеттесуінің сандық моделі әзірленді. Сандық модельдің дұрыстығы физикалық модельдеу нәтижелерімен расталады. Магнит өрісінің кернеулігінің бойлық құрамдас бөлігінің құбыр қабырғасының қалыңдығына оңайлатылған аналитикалық тәуелділігі алынады. Магнит өрісінің кернеу мәнін және өлшеу жазықтығынан құбырдың шетіне дейінгі қашықтықты бірлесіп өлшеуге негізделген өлшеу жазықтығынан құбырдың шетіне дейінгі қашықтық қабырғасының қалыңдығын бақылау нәтижелеріне әсерін азайту әдісі ұсынылған. Ұсынылған бақылау әдісін қолданған кезде, құбырдың жиегі мен магнит өрісінің кернеулігін өлшеу жазықтығы арасындағы қашықтықты ескере отырып, жиек әсеріне байланысты қабырға қалыңдығын өлшеу қателігін шамамен 10 есе азайтуға болады. Мақалада келтірілген нәтижелер магнит өрістерін құру, математикалық модельдеу және өлшеу есептерін шешуде, соның ішінде болат бұрғылау құбырларын магниттік бақылау үшін пайдаланылуы мүмкін.

Кілт сөздер: магниттік бақылау, магнит ағынының ағу әдісі, соңғы элементтер әдісі, аналитикалық модель, Холл датчигі

А.Е. Гольдштейн, К.А. Стряпчев

Магнитный контроль толщины стенки ферромагнитных труб методом рассеяния магнитного потока

Рассмотрено использование метода рассеяния магнитного потока для контроля толщины стенки ферромагнитных труб, основанного на продольном намагничивании с помощью короткого соленоида участка контролируемой трубы и измерении продольной пространственной составляющей напряженности магнитного поля в воздушном промежутке между соленоидом и контролируемой трубой с помощью датчиков Холла. Разработана численная модель взаимодействия намагничивающего поля короткого соленоида с ферромагнитной трубой, учитывающая нелинейные магнитные свойства объекта контроля и его геометрические параметры, в том числе, расстояние между краем трубы и плоскостью измерения напряженности магнитного поля. Корректность численной модели подтверждена результатами физического моделирования. Получена упрощенная аналитическая зависимость продольной составляющей напряженности магнитного поля от толщины стенки трубы. Предложен метод уменьшения влияния на результаты контроля толщины стенки расстояния от плоскости измерения до края трубы, основанный на совместном измерении значения напряженности магнитного поля и расстояния от плоскости измерения до края трубы. При использовании предлагаемого метода контроля благодаря учету расстояния между краем трубы и плоскостью измерения напряженности магнитного поля погрешность измерения толщины стенки, обусловленная краевым эффектом, может быть снижена примерно в 10 раз. Результаты, представленные в статье, могут быть использованы при решении задач создания, математического моделирования и измерения магнитных полей, в том числе для магнитного контроля стальных буровых труб.

Ключевые слова: магнитный контроль, метод рассеяния магнитного потока, метод конечных элементов, аналитическая модель, датчик Холла

References

- 1 Christie, R., Liu, Ch., Stanley, R., Torregrossa, M., Zheng, E., & Zsolt, L. (2015). Monitoring and Managing Coiled Tubing Integrity. *Oilfield Review*, 27(1), 48–56.
- 2 Potapov, A.I., Syasko, V.A., & Solomenchuk, P.V. (2015). *Elektromagnitnye i magnitnye metody nerazrushaiushchego kontrolya materialov i izdelii. Elektromagnitnye i magnitnye metody defektoskopii i kontrolya svoistv materialov [Electromagnetic and magnetic methods of non-destructive testing of materials and products. Electromagnetic and magnetic methods of defectoscopy and control of material properties]*. (Vols 1–2; Vol. 1). St. Petersburg: Nestor-Istoriia [in Russian].
- 3 Slesarev, D.A., & Abakumov, A.A. (2013). Data processing and representation in the MFL method for nondestructive testing. *Russian Journal of Nondestructive Testing*, 49(9), 3–9.
- 4 Sharanova, D.A. (2016). Beskontaktnye metody vyivleniia pittingovykh defektov stenok metallicheskich izdelii [Non-contact methods for detecting pitting defects in the walls of metal products]. *Territoriia «NEFTEGAS» — Territory of «NEFTEGAZ»*, 10, 34–40 [in Russian].
- 5 (2009). *Promyshlennaia bezopasnost pri ekspluatatsii gruzopodemnykh kranov [Industrial safety during operation of overhead cranes]*. Collection of documents. Series 10. Issue 7. Moscow: Nauchno-tekhnicheskii tsentr «Promyshlennaia bezopasnost» [in Russian].
- 6 Slesarev, D., & Semenov, A. (2022). Magnetic and electromagnetic testing of suspension cables of bridges and structures. *Lecture Notes in Civil Engineering*, 200, 805–810.
- 7 (2016). *Ustanovka nerazrushaiushchego kontrolya burilnykh trub magnitnym metodom v mobilnom ispolnenii «Magportabur 1.2». Rukovodstvo po ekspluatatsii [NDT installation for drill pipes by the magnetic method in the mobile version «Magportabur 1.2». Manual]*. St. Petersburg [in Russian].
- 8 (2025). The ARTIS-3 Portable EMI Pipe Inspection System. Retrieved from <https://oem-usa.com/a3port/>
- 9 Potapov, A.I., Syasko, V.A., & Pudovkin, O.P. (2013). Optimization of the parameters of primary measuring transducers that use the MFL technology. *Russian Journal of Nondestructive Testing*, 51(8), 64–71.
- 10 Aikeyeva, A.A., Zhautikov, B.A., Aidarkhanov, A.M., Zhanasbayeva, A.S., Zhautikov, F.B., & Belgibayev, A.S. (2014). Modeling electromagnetic systems. *Bulletin of the University of Karaganda – Physics*, 3(75), 28–34.
- 11 Goldshtein, A.E., & Belyankov, V.Y. (2020). Modeling of magnetic fields and signals of a ferromagnetic pipe flaw detector induced by a through hole defect. *Bulletin of the University of Karaganda – Physics*, 4(100), 49–56.
- 12 Dyusembaeva, A.N., Tanasheva, N.K., Tleubergenova, A.Zh., Bakhtybekova, A.R., Kutumova, Zh.B., Tussuphanova, A.R., & Abdirova, N.T. (2020). Optimal choice of the geometric shape rotor blade wind turbine using the numerical method. *Bulletin of the University of Karaganda – Physics*, 2(114), 53–62.
- 13 (1980). GOST 8.377-80 «Materialy magnitomiagkie. Metodika vypolneniia izmerenii pri opredelenii staticheskikh magnitnykh kharakteristik» [Soft magnetic materials. Methodology for performing measurements when determining static magnetic characteristics]. Moscow: Izdatelstvo standartov [in Russian].

Information about the authors

Goldstein, Alexander (*corresponding author*) — Doctor of Technical Sciences, Professor, National Research Tomsk Polytechnic University, Tomsk, Russia; e-mail: algol@tpu.ru; ORCID ID: <https://orcid.org/0009-0001-7057-7310>

Stryapchev, Kirill — PhD student, National Research Tomsk Polytechnic University, Tomsk, Russia; e-mail: inscrut@yandex.ru; ORCID ID: <https://orcid.org/0009-0007-3935-5721>

Article

UDC 536.8

 <https://doi.org/10.31489/2025PH2/55-66>

Received: 11.11.2024

Accepted: 20.02.2025

K.O. Sabdenov¹, Zh.K. Smagulov^{2✉}, M. Erzada¹, T.A. Zhakatayev¹

¹*L.N. Gumilyov Eurasian National University, Astana, Kazakhstan;*

²*Karaganda Buketov University, Karaganda, Kazakhstan*

Simulation of a Stirling Engine with a Reversible Reaction $\text{CO} + 2\text{H}_2 \leftrightarrow \text{CH}_3\text{OH}$

Using a simple computer model, the properties of a Stirling engine are studied, where the working substance is a chemically reacting gas with a reversible reaction $\text{CO} + 2\text{H}_2 \leftrightarrow \text{CH}_3\text{OH}$. The model takes into account the relaxation time of hydrodynamic processes in the regenerator. In this case, the engine is considered to consist of three main parts: a heater, regenerator and a cooler, this is fundamental difference from the Langlois Justin model proposed in 2006. The pressure in the engine is 20 MPa, the working piston is free. The efficiency is compared for two cases: 1) a reversible chemical reaction occurs in the working gas and 2) the working gas is chemically inert with relatively high and low molar mass. The average power over the oscillation period is several hundred watts, but the maximum power can reach 2 kW. To increase the power of an engine with reversible chemical reaction, it is necessary to increase the volume of the cooler and reduce the volume of the heater. The modeling results are in good agreement with the previously obtained theoretical results of one of the authors (K. Sabdenov, 2023) based on the analysis of the Stirling cycle with reversible chemical reaction.

Keywords: Stirling cycle, free-piston Stirling engine, methanol, reversible chemical reaction, efficiency and power

✉ *Corresponding author:* Smagulov Zhanaidar, smagul@mail.ru

Introduction

The Stirling engine can produce electrical energy from any external heat source, including solar radiation. Therefore, it is considered as a promising means to solve the problem of energy shortages after the depletion of oil and natural gas reserves [1, 2].

In modern engines, the working gas is either chemically inert or can only react in one direction to form a combustion product. But the results of [3, 4] indicate a strong influence of the efficiency of various thermodynamic cycles due to the ongoing reversible chemical reaction in the working gas. If we compare it with a chemically inert gas, then such a reaction can lead to both a decrease and an increase in efficiency. In particular, high efficiency in the Stirling cycle can be obtained under the following conditions:

- at the compression stage, the working gas must have a higher molecular weight than at the expansion stage;
- the gas expansion coefficient must be sufficiently large;
- the maximum T_{\min} (heater) and minimum T_{\max} (cooler) temperatures should not differ significantly; this is due to the condition for the existence of a cycle.

The results of [3, 4] were obtained for ideal and equilibrium cycles, so they need to be confirmed either on real machines or on computer models. To do this, based on a computer model, the operation of a Stirling

engine with a free working piston is studied. Its first mathematical model in the isothermal approximation was proposed in [5] and since then it has become the basis for many theoretical and experimental studies [6–11]. The isothermal approximation means assuming constant heater and cooler temperatures.

Cyclic changes in the dynamic parameters of the Stirling machine should be obtained as a result of solving the model equations expressing the laws of conservation of mass, momentum and energy. But in many theoretical studies, for example, in [7, 9–11], the coordinates of the working piston and displacer are specified in the form of a sinusoidal function. From the model [5] it is difficult to understand the physical mechanisms by which the machine operates and, most likely, it contains unjustified approximations and complications.

Experimental

This study has two objectives:

1) to build a simple model of a Stirling engine with a free piston, at the same time, the new model must take into account the most important physical properties of the engine;

2) using the constructed model of the Stirling engine, check the correctness of the results obtained from the thermodynamic analysis of a cycle with a reversible chemical reaction [3].

The general structure of the Stirling engine is described in detail in [5], therefore, below only the fundamental differences of the proposed device circuit are indicated. It is shown in Figure 1, here the cooler is combined with the volume (compression, 6) V_c , and the heater is combined with the volume (expansion, 7) V_e .

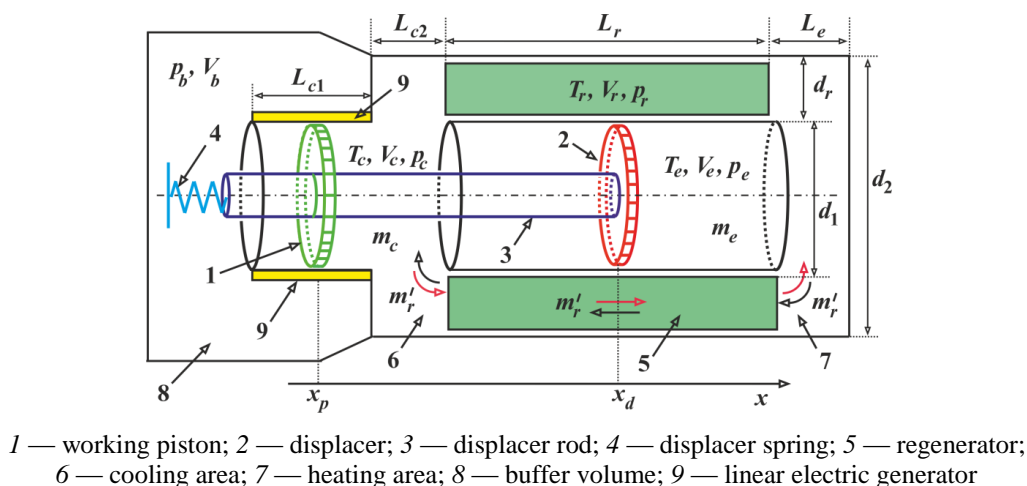


Figure 1. Simplified diagram of the structure of a Stirling engine with a free piston and the direction of the x coordinate

This means that the volumes V_c and V_e are essentially a cooler and a heater. Accordingly, they maintain constant temperatures T_c and T_e . They are taken as the minimum and maximum temperature in the car. The gas masses in each of the indicated volumes are equal to m_c and m_e .

Regenerator 5 continues to be present as an independent and important component of the machine, therefore it is characterized by its physical parameters.

Buffer space 8 with volume V_b and pressure p_b is borrowed from [5].

The working piston 1 moves freely along the rod 3 of the displacer 2, the last two are rigidly connected to each other, and one of the ends of the rod is attached to the spring 4 with a stiffness coefficient k_d . The displacer can move freely inside the cylinder, surrounded by a cylindrical regenerator with length L_r and working space thickness d_r .

As a result of the movement of the working piston, the linear generator 9 generates an electric current, its reverse effect on the operation of the machine is taken into account by the damping coefficient D_p .

A Stirling engine cannot operate without a regenerator; the literature [12, 13] denies this, but points to the very low efficiency of a machine without a regenerator. Thus, although the regenerator is allocated a significant place, it is still not one of the main ones. In fact, in machines “without a regenerator” it is still present in a hidden and primitive form. Since the regenerator plays one of the key roles here, the processes in it need a detailed description. This mainly relates to gas flow.

The regenerator is represented by a narrow and long channel in the space between two coaxial cylinders with diameters d_1 and $d_2 = d_1 + 2d_r$. The average speed of one-dimensional gas motion in it with density ρ_r and in the direction of coordinate x will be denoted by u . Below is the momentum conservation equation for the elementary mass of the regenerator $\Delta m = \rho_r A_r \Delta x$, where the elementary volume in a section of length Δx and cross-sectional area A_r is equal to $A_r \Delta x$. This elementary volume is acted upon by two forces:

- the first of them F_p is associated with the change in pressure in space, $F_p = A_r(p(x + \Delta x) - p(x))$. If there is a local section on the path of gas movement at point $x = x_0$, then this section is characterized by the coefficient of hydraulic resistance K_r . Here the momentum of the flow changes, a force acts on it

$$F_p = \left(p(x + \Delta x) - p(x) + \frac{1}{2} \delta(x - x_0) K_r \rho_r |u| u \Delta x \right) A_r,$$

where $\delta(x - x_0)$ is the Dirac delta function;

- the second force F_r arises as a result of the presence of friction inside the gas, and at the boundary of contact with the solid surface of the channel wall [14]. Friction forces lead to the appearance of tangential stress τ , and $F_{fr} = \tau \Pi \Delta x$.

From hydrodynamics [14], we accept the equality

$$\tau = \text{const} \cdot \zeta \rho_r |u| u,$$

where ζ is the coefficient of hydrodynamic resistance; Π — channel perimeter, $\Pi = 2\pi(d_1 + d_r)$. Thus, we get

$$F_{fr} = \frac{1}{8} \cdot \zeta \rho_r \Pi |u| u \Delta x.$$

The 1/8 factor is explained below. Newton's second law can be written as

$$\Delta m \frac{du}{dt} = -A_r \frac{\partial p}{\partial x} \Delta x - \frac{1}{2} \delta(x - x_0) K_r \rho_r |u| u A_r \Delta x - F_{fr}.$$

Hence, after replacing the total time derivative in the sense of Lagrange with the derivative in the sense of Euler [14],

$$\frac{d}{dt} = \frac{\partial}{\partial t} + u \frac{\partial}{\partial x},$$

and also using the definition of mass Δm and in the limit $\Delta x \rightarrow 0$, the equation is obtained [15]

$$\frac{\partial u}{\partial t} + u \frac{\partial u}{\partial x} = -\frac{1}{\rho_r} \frac{\partial p}{\partial x} - \frac{1}{8} \cdot \frac{\zeta \Pi}{A_r} |u| u - \frac{1}{2} \delta(x - x_0) K_r |u| u. \quad (1)$$

In typical Stirling machines, the thermal expansion of gas is small, the pressure also does not change much, and the compressibility of the gas is insignificant. Therefore, the derivative of density with time is small compared to convective transport. As a result, the mass flow $\rho_r u$ can only be a function of time. This means that the gas in the regenerator moves like a liquid and its speed is only a function of time. Therefore, instead of (1), we can consider the equation

$$\frac{du}{dt} = -\frac{1}{\rho_r} \frac{\partial p}{\partial x} - \frac{1}{8} \cdot \frac{\zeta \Pi}{A_r} |u| u - \frac{1}{2} \delta(x - x_0) K_r |u| u,$$

where the partial derivative with respect to time is replaced by the total derivative, but in the Euler sense. Taking the gas velocity to be weakly dependent along the length of the regenerator, $\partial u / \partial x \approx 0$, by integrating over the length of the regenerator this equation is reduced to the form [15]

$$L_r \frac{du}{dt} = \frac{1}{\rho_r} \Delta p - \frac{1}{8} \zeta \frac{L_r \Pi}{A_r} |u| u - \frac{1}{2} K_r |u| u. \quad (2)$$

The pressure difference Δp is positive if the gas flows from left to right. Now let us explain the origin of the factor 1/8; in the stationary case and flow in a pipe, the well-known Darcy-Weisbach equation should be obtained [16]. In the case of an arbitrary pipe of length L_r and diameter D , the ratio $\Pi / A_r = 4/D$, and then it follows

$$\Delta p = \frac{1}{2} \zeta \rho_r \frac{L_r}{D} |u|u - \frac{1}{2} K_r \rho_r |u|u.$$

This is the Darcy-Weisbach equation for a pipe. For a regenerator (Fig. 1), the ratio of the perimeter to the flow area is $\Pi/A_r = 2/d_r$.

Equation (2) is relaxation, it takes into account the time required for the formation of gas velocity in the regenerator when pressure and friction change.

The model obtained above includes the equations of motion of the displacer, piston and gas in the regenerator. The coordinate of the displacer x_d with mass m_d is measured from the equilibrium position $x_{d,0}$, the initial coordinate of the piston x_p with mass m_p coincides with the coordinate reference point x .

The gas in the buffer volume compresses and expands under adiabatic conditions with index γ . External and initial pressure p_0 .

The equations of motion of the displacer and piston have the form [5]

$$m_d \frac{d^2 x_d}{dt^2} + k_d (x_d - x_{d,0}) = p_b A_{rod} + p_c A_p - p_e A_d, \quad (3)$$

$$m_p \frac{d^2 x_p}{dt^2} + D_p \frac{dx_p}{dt} = (p_b - p_c) A_p. \quad (4)$$

The coefficient D_p characterizes the production of electrical energy by a linear generator. Equations (3) and (4) are supplemented with formulas for determining pressures:

$$p_b = p_0 \left(\frac{V_{b,0}}{V_b} \right)^\gamma, \quad (5)$$

$$p_c = \frac{R_{g,c} T_c}{V_c} m_c, \quad p_e = \frac{R_{g,e} T_e}{V_e} m_e. \quad (6)$$

A change in the chemical composition of the gas leads to a change in the gas constant; the composition of the gas is different in the heater and cooler. Accordingly, two notations $R_{g,c}$ and $R_{g,e}$ are introduced for the gas constant.

The volumes contained here are found using the formulas

$$V_c = V_{c,0} + A_p (x_d - x_{d,0} - x_p), \quad (7)$$

$$V_e = V_{e,0} - A_d (x_d - x_{d,0}), \quad V_b = V_{b,0} + A_{rod} (x_d - x_{d,0}) + A_p x_p.$$

Here $V_{c,0}$, $V_{e,0}$ are the initial volumes of the cooler and heater.

The gas masses in the displacer m_c and heater m_e are determined by solving the equations

$$\frac{dm_c}{dt} = -m'_r, \quad \frac{dm_e}{dt} = m'_r. \quad (8)$$

The gas mass flow rate m'_r in the regenerator is found from equation (2) and this issue is discussed below. The pressure p_r and temperature T_r in the regenerator are taken to be the average values in the heater and cooler:

$$p_r = \frac{p_e + p_c}{2}, \quad T_r = \frac{T_e + T_c}{2}. \quad (9)$$

Equalities (9) mean accepting a linear dependence on the x coordinate of changes in pressure and temperature in the regenerator. Linear dependencies are well fulfilled since the differences $p_c - p_e$ and $T_c - T_e$ are small values, and $d_r/L_r \ll 1$.

Then the gas density in the regenerator ρ_r is determined from the equation of state

$$\rho_r = \frac{p_e + p_c}{(T_e + T_c) R_g}. \quad (10)$$

Equation (10) is necessary to find the mass of gas in the regenerator m_r . Density ρ_r can be more accurately determined by calculating the average density using linear functions $p(x)$ and $T(x)$ and the gas equation

of state for the regenerator [5]. But such averaging, which leads to a complex expression, does not provide noticeable advantages.

In Figure 1, between the regenerator and volumes V_c and V_e , there are local sections of gas flow rotation; they are included in the regenerator and are characterized by the coefficient K_r .

Equation (2) can also be written for mass flow $m'_r(t) = u(t)\rho_r A_r$. Using this definition and taking into account the constancy of density ρ_r , we write the equation for flow velocity,

$$\frac{dm'_r}{dt} = \frac{A_r}{L_r} \Delta p - \frac{1}{2} \frac{K_\Sigma |m'_r|}{m_r} m'_r, \quad (11)$$

$$K_\Sigma = K_r + \frac{L_r}{2d_r} \zeta, \quad m_r = \rho_r L_r A_r = \rho_r V_r, \quad V_r = L_r A_r. \quad (12)$$

According to Figure 1, the positive direction of gas movement corresponds to a positive sign of the pressure drop Δp , so it should be $\Delta p = p_c - p_e$.

Since the regenerator is a porous (mesh) structure made of thin metal wire [12, 13], then in the general case the porosity factor should be added to the determination of the gas volume V_r . Here it is assumed that the porosity is close to unity.

Let us denote by $m_{c,0}$ and $m_{e,0}$ the initial values of the gas masses in the cooler and heater, then from the sum of equations (8) and after integration the equality follows

$$m_c - m_{c,0} = -(m_e - m_{e,0}), \quad (13)$$

$$m_{c,0} = \frac{p_0 V_{c,0}}{R_{g,c} T_c}, \quad m_{e,0} = \frac{p_0 V_{e,0}}{R_{g,e} T_e}.$$

Chemical reactions of the first order take place in volumes V_c and V_e . In the first of them, the chemical transformation (reverse reaction) proceeds according to the scheme $B \rightarrow A$ at a rate k_c , and in the second (direct reaction) according to the scheme $A \rightarrow B$ at a rate k_e . At the same time, a mass of gas enters (or leaves) the indicated volumes at a speed m'_r ; i.e. in each of them there can be two sources of substances of grade A and B. Each of them in an arbitrary volume has a mass m_A and m_B , their sum is always equal to the total mass of the gas in this volume. Substances A and B are characterized by relative mass concentrations g_A and g_B , and

$$g_A + g_B = 1. \quad (14)$$

For simplicity, the chemical transformation inside the regenerator is not taken into account. The simple connection (14) between concentrations allows us to subsequently use equations for only one of them, for example, g_B .

Since the gas mass in the cooler and heater is different, g_B will be determined in different ways. Therefore, below g_B is supplemented with indices indicating its value in V_c and V_e , i.e. $g_{B,c}$ and $g_{B,e}$. Using them, you can determine the gas constants $R_{g,c}$ and $R_{g,e}$ [17]:

$$R_{g,c} = R \left(\frac{g_{B,c}}{\mu_B} + \frac{1 - g_{B,c}}{\mu_A} \right), \quad R_{g,e} = R \left(\frac{g_{B,e}}{\mu_B} + \frac{1 - g_{B,e}}{\mu_A} \right), \quad (15)$$

where R is the universal gas constant; μ_A , μ_B are the molar masses of substances A and B.

In the volume of the regenerator, the rates of forward and reverse chemical reactions are approximately equal. Since there is no change in the composition of the gas in the regenerator, when calculating the mass of gas in the regenerator m_r , the gas constant in it $R_{g,r}$ is determined by the conditions:

$$\text{if } m'_r \geq 0, \text{ then } R_{g,r} = R_{g,c}; \text{ if } m'_r < 0, \text{ then } R_{g,r} = R_{g,e}.$$

Mass m_r is found from the equation of state

$$m_r = \frac{p_r V_r}{R_{g,r} T_r}.$$

The above data is sufficient to determine the parameters of the regenerator.

Consider the volume V_c and the 1st case $m'_r > 0$, then the substance B will decrease due to convective entrainment from this volume and due to a chemical reaction. A simple first order reaction gives a conservation equation for the mass $m_{B,c}$,

$$\frac{dm_{B,c}}{dt} = -g_{B,c}m'_r - m_c k_c g_{B,c}. \quad (16)$$

According to the definition of relative mass concentration,

$$g_{B,c} = \frac{m_{B,c}}{m_c}.$$

Then, taking into account the first equality in (8), equation (16) can be written for $g_{B,c}$:

$$\frac{dg_{B,c}}{dt} = -k_c g_{B,c}. \quad (17)$$

In the 2nd case, $m'_r < 0$ and the content of gas grade B changes both due to a chemical reaction and due to convective transfer from the heater. In volume V_e , the reaction $A \rightarrow B$ takes place. There, its concentration is designated $g_{B,e}$. The mass conservation equation will now take the form

$$\frac{dm_{B,c}}{dt} = -g_{B,e}m'_r - m_c k_c g_{B,c}.$$

After passing here to the concentration $g_{B,c}$, we obtain

$$\frac{dg_{B,c}}{dt} = \frac{g_{B,c} - g_{B,e}}{m_c} m'_r - k_c g_{B,c}. \quad (18)$$

In it, the reaction also has the first order, but now a substance of type B is formed. The derivation of equations for the concentration is carried out according to the same scheme as in the previous example. In the case $m'_r > 0$ for the mass $m_{B,e}$, the following equation is obtained:

$$\frac{dm_{B,e}}{dt} = g_{B,c}m'_r + m_e k_e (1 - g_{B,e}).$$

To pass to the equation for the concentration $g_{B,e}$, we use the second equality in (8) and the definition $g_{B,e} = m_{B,e}/m_e$, as a result, we obtain

$$\frac{dg_{B,e}}{dt} = \frac{g_{B,c} - g_{B,e}}{m_e} m'_r + k_e (1 - g_{B,e}). \quad (19)$$

In the case of $m'_r < 0$, the concentration $g_{B,e}$ is determined from the equation

$$\frac{dg_{B,e}}{dt} = k_e (1 - g_{B,e}). \quad (20)$$

Results and Discussion

Equations (3), (4), (11) and (17)–(20) as well as one of the equations (8) are basic. To these are added auxiliary equalities (5)–(7), (9), (10), (12), (13) and (15).

The reversible reaction of methanol formation $\text{CO} + 2\text{H}_2 \leftrightarrow \text{CH}_3\text{OH}$ is considered [18, 19]. Substance A is a mixture of carbon monoxide and hydrogen with molar mass $\mu_A = 0.0107$ kg/mol; substance B is methanol with molar mass $\mu_B = 0.032$ kg/mol. At low temperature T_c , the decomposition reaction of methanol predominantly occurs according to the scheme $B \rightarrow A$ with the reaction constant k_c ; at high temperature T_e , methanol is formed according to the scheme $A \rightarrow B$ with the reaction constant k_e .

The numerical solution of the equations was carried out by the Runge-Kutta method [20] with second order accuracy and with various time steps to verify the correctness of the results obtained. To obtain reliable results, it is enough to take the integration step equal to 10^{-4} s. Initial conditions:

$$t = 0: \quad x_p = 0, \quad x_d = x_{d,0}, \quad \frac{dx_p}{dt} = 0, \quad \frac{dx_d}{dt} = 1 \text{ m/s}; \quad m'_r = 0, \quad g_{B,c} = 0.15, \quad g_{B,e} = 0.85.$$

Electrical power P_{el} is always positive and equal to

$$P_{el} = D_p \left(\frac{dx_p}{dt} \right)^2.$$

At the initial moment of time, the pressure in all volumes of the engine and outside was the same and equal to p_0 ; the mechanical system is in equilibrium. Then the total power of the engine P_m , or the rate of production of mechanical work, is equal to

$$P_m = \left| (p_c - p_e) \frac{dV_c}{dt} \right| + \left| (p_e - p_0) \frac{dV_e}{dt} \right| = \left| (p_c - p_e) A_p \left(\frac{dx_d}{dt} - \frac{dx_p}{dt} \right) \right| + \left| (p_e - p_0) A_d \frac{dx_d}{dt} \right|.$$

The necessity of the modulus sign is explained by the fact that useful work is performed both during expansion and compression of gas in volumes. Engine efficiency η_{el} was determined by the average power values P_{el} and P_m :

$$\eta_{el} = \frac{\langle P_{el} \rangle}{\langle P_m \rangle}.$$

The results in Figures 2–4 were obtained for the following input parameters:

- general and for buffer volume —

$$p_0 = 20 \text{ MPa}; \gamma = 1.37; V_{b,0} = 2.0 \cdot 10^6 \text{ m}^3 \text{ (the buffer volume is taken very large to exclude it);}$$

- for displacer and working piston —

$$m_d = 3.0, m_p = 3.3 \text{ kg}; k_d = 50 \text{ kg} \cdot \text{s}^{-2};$$

$$d_1 = 0.8, d_{rod} = 0.05, L_e = 0.3 \text{ m}; D_p = 5500 \text{ kg} \cdot \text{s}^{-1};$$

- for heater and cooler —

$$T_c = 293, T_e = 673 \text{ K}; V_{c,0} = 0.94, V_{e,0} = 0.54 \text{ m}^3; x_{d,0} = 1.6 \text{ m};$$

$$k_c = 4.0 \cdot 10^{-2}, k_e = 4.2 \cdot 10^{-2} \text{ s}^{-1}; L_{c1} = 1.0, L_{c2} = 0.5 \text{ m};$$

- for regenerator —

$$L_r = 1.2, d_r = 0.1 \text{ m}; A_r = 0.28 \text{ m}^2; K_r = 0.01, \zeta = 0.12.$$

Work [21] gives a specific (per unit mass of copper catalyst) reaction constant for CO consumption of about $k_{CO} = 10^{-2} \text{ mol}/(\text{kg}_{\text{cat}} \cdot \text{s})$. Here reaction constants of the order of $0.01 \dots 0.1 \text{ s}^{-1}$ are used and in a different dimension. But a correlation can be established between these reaction constants: the gas volumes V_c and V_e are of the order of magnitude 10 mol. Then, taking 10 kg of catalyst (taking into account the high density of copper, such a mass of catalyst occupies a relatively small volume), we obtain $k_{CO} \sim 0.01 \text{ s}^{-1}$, which is comparable to the given value of k_e . The rate of the reverse reaction k_c is assumed to be approximately the same order of magnitude.

The oscillation of the displacer was established after approximately 70 s, its average position did not change (Fig. 2). But the average position of the piston shifts with a weak wave movement to the left along the x coordinate and by the time of 100 s it still has not reached its stationary point.

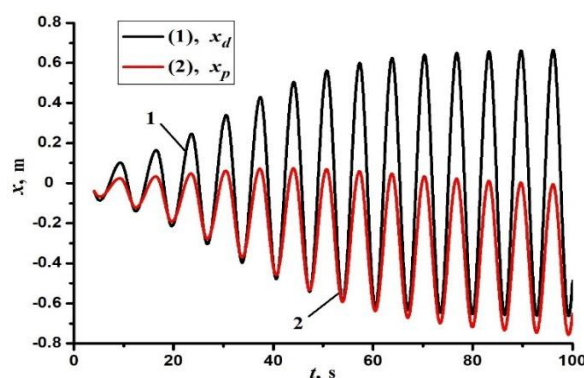


Figure 2. Coordinates of the displacer and piston depending on time

Power averaging (Fig. 3) was carried out over a time interval from 80 to 100 seconds, the results obtained were $\langle P_{el} \rangle = 355.3$, $\langle P_m \rangle = 906$ W; $\eta_{el} = 0.392$. The oscillation frequency is $\nu = 0.16$ Hz.

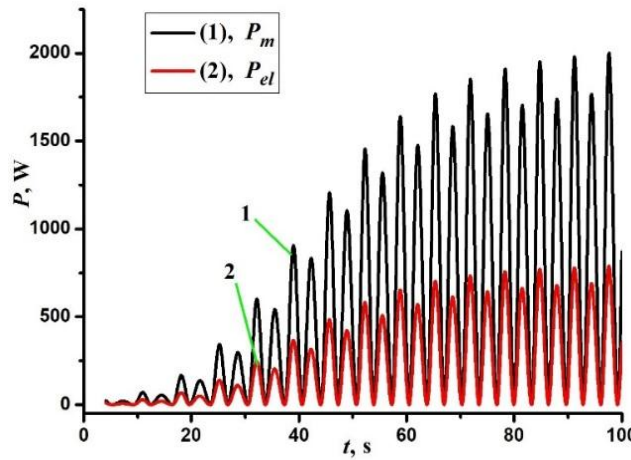


Figure 3. Dependence of powers P_m and P_{el} on time

The efficiency of an ideal Stirling cycle with a reversible chemical reaction η_{St} is characterized by a dimensionless parameter [3]

$$\alpha_{St} = \frac{\mu_B(\gamma_B - 1)}{\mu_A(\gamma_A - 1)},$$

where γ_A , γ_B are the adiabatic exponent of substances A and B. The condition for exceeding η_{St} efficiency of the Carnot cycle with a chemically inert working gas η_0 is given by the inequality

$$\alpha_{St} > \frac{T_{max}}{T_{min}}. \quad (21)$$

The γ_A exponent is easily determined, since detailed experimental data exist for the gases CO and H₂; from them it is easy to determine $\gamma_A = 1.37$. The situation is more complicated with the adiabatic index of methanol γ_B ; its physical properties change in a complex and ambiguous way depending on pressure and temperature [19], since it is located near the critical point. Therefore, in contrast to work [3], we use the formula from the theory of ideal gases [17]

$$\gamma_B = \frac{i + 2}{i},$$

where i is the number of degrees of freedom. From the structure of the methanol molecule it is easy to obtain the estimate $i = 10$, so we can take $\gamma_B = 1.2$. This, together with $\gamma_A = 1.37$, gives the value $\alpha_{St} = 1.76$, and inequality (21) is not satisfied, since $T_{max}/T_{min} = 2.465$ ($T_{max} = T_e$, $T_{min} = T_c$). Accordingly, the efficiency according to the Carnot formula for a chemically inert working gas is equal to $\eta_0 = 1 - T_{min}/T_{max} = 0.565 > \eta_{el}$.

In [3] a formula was proposed for calculating the efficiency of an ideal Stirling cycle η_{St} ; in the notation adopted here it has the form:

$$\eta_{St} = 1 - \frac{T_{min}}{T_{max}} G(\omega), \quad (22)$$

$$G(\omega) = \frac{G_{0,1} + G_1}{G_{0,2} + G_1}, \quad G_1 = \left(1 + \frac{\mu_B - \mu_A}{\mu_A} \frac{\omega}{\omega - 1} \right) \ln \omega,$$

$$G_{0,1} = \frac{1}{\gamma_B - 1} \frac{T_{max}}{T_{min}} - \frac{\mu_B}{\mu_A(\gamma_A - 1)}, \quad G_{0,2} = \frac{1}{\gamma_B - 1} - \frac{\mu_B}{\mu_A(\gamma_A - 1)} \frac{T_{min}}{T_{max}}.$$

Here there is a volume ratio ω on the upper (or lower) isotherm. This parameter ω depends on the engine design, so it can be found from the simulation results.

The cycle being implemented in the engine can be constructed in volume/pressure coordinates, since electrical energy is produced by the cooler, such a cycle is constructed in the variables $V_c/(p_c - p_0)$ in Figure 4 and bears little resemblance to the ideal cycle.

The lines are not closed because the piston has not yet reached the midpoint. But these data are sufficient to estimate the volume ratio $\omega = 1.28$ at points 2 and 1. Then from equation (22) we find $\eta_{st} = 0.354$. This is less than the result obtained above $\eta_{el} = 0.392$ by approximately 10 %, and their difference may be introduced by the difference in the cycles in Figure 4 and ideal cycle, or, the approximate nature of equality (22). The fact is that when obtaining equation (22), a simple assumption was made of a linear dependence of the mass concentration of the product of a chemical reaction on the specific volume [3].

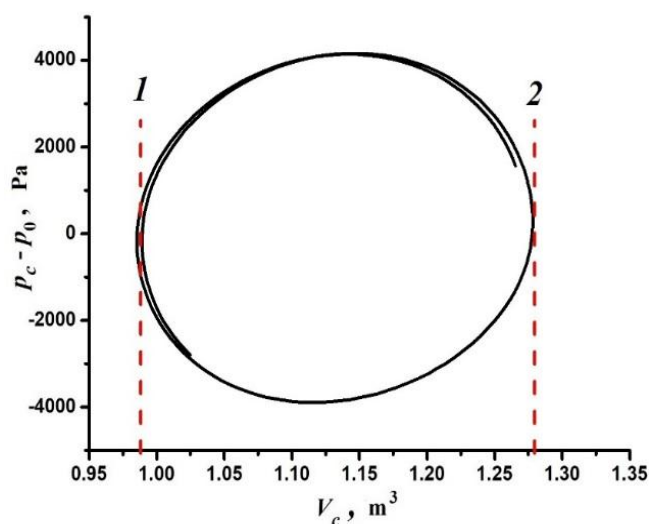


Figure 4. Image of the cycle in the Stirling engine in coordinates $V_c/(p_c - p_0)$, the cycle is built for a time interval from 80 to 100 s

If we take the working gas to be a chemically inert substance with a molar mass of light gas $\mu_A = 0.0107$ kg/mol, then no displacement of the working piston is observed (Fig. 5).

However, all other input parameters remained unchanged. The engine reaches a steady state of operation in approximately 40 s. The frequency and amplitude of oscillations increased noticeably ($\nu = 0.17$ Hz), which explains the almost doubling of power: $\langle P_{el} \rangle = 684.6$, $\langle P_m \rangle = 1739$ W. There was also a very slight increase in electrical efficiency $\eta_{el} = 0.394$.

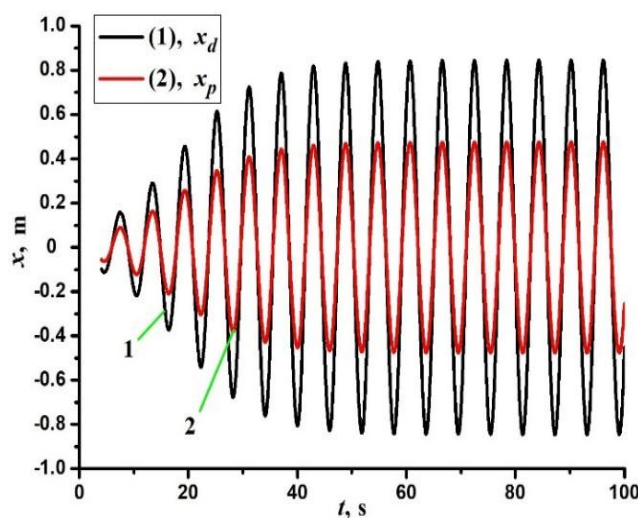


Figure 5. Changes in the coordinates of the displacer and piston over time for a chemically inert working gas

For a chemically inert (relatively heavy) working gas with a molar mass $\mu_B = 0.032$ kg/mol, the working piston does not shift either. But the power and oscillation frequency are significantly reduced: $\langle P_{el} \rangle = 59.64$, $\langle P_m \rangle = 152.3$ W; $\nu = 0.10$ Hz. In addition, the time it takes for the engine to reach a steady state of operation increases; here this time is longer than the calculated time of 100 s.

From equation (22) it follows that efficiency increases with increasing expansion coefficient ω (at constant temperatures). To check this conclusion, the calculation was carried out with a change in the volume of the cooler by changing the length $L_{c,2}$. Below are the results for three options Table:

Table

$L_{c,2}$, m	ω	$\langle P_{el} \rangle$, W	$\langle P_m \rangle$, W	η_{el}	η_{st}
0.25	1.38	346	883	0.392	0.362
0.5	1.28	355	906	0.392	0.354
0.85	1.23	407	1037	0.392	0.350

No change in efficiency is observed, but engine power increases as the expansion coefficient decreases. Moreover, both total and electrical power increases proportionally, and a decrease in ω is achieved by increasing the volume of the cooler.

If you increase the volume of the heater while other parameters remain unchanged, then an increase in the volume of the heater leads to a decrease in power. For example, a calculation with a length $L_{c,2} = 0.5$, but with $L_e = 0.5$ m instead of the previous value $L_e = 0.3$ m gives $\langle P_{el} \rangle = 342$ and $\langle P_m \rangle = 873$ W.

Conclusions

In this study an isothermal model of a Stirling engine with a free piston and working gas, where a reversible chemical reaction occurs, is proposed. If we do not consider the presence of a chemical reaction, the new model differs from the previously proposed Langlois Justin model [5] by taking into account the relaxation time of hydrodynamic processes in the regenerator. Moreover, it consists of three main parts: heater, cooler and regenerator.

Based on the modeling results, the following conclusions were drawn:

- chemical transformation leads to a change in the molar mass of the gas mixture in the cooler and heater, as a result, during engine operation, the equilibrium position of the working piston shifts;
- such a shift occurs to the left if the molar mass of the gas is less than in the heater, if vice versa, then the piston moves to the right. Piston displacement does not occur in the case of gas with constant molar mass;
- the results of calculating the efficiency using the proposed model and the previously obtained formula for an ideal Stirling cycle with a reversible chemical reaction differ by approximately 10 %.

Conflict of interest statement

The authors declare that they have no conflict of interest in relation to this research, whether financial, personal, authorship or otherwise, that could affect the research and its results presented in this paper.

CRedit author statement

Sabdenov K.O.: Conceptualization, Methodology, Writing-Review & Editing; Smagulov, Zh.K.: Conceptualization, Methodology; Erzada, M.: Original Draft, Visualization, Software; Zhakatayev, T.A.: Original Draft, Software.

References

- 1 Minassians, A.D. (2007). Stirling Engines for Low-Temperature Solar-Thermal-Electric Power Generation. *Doctor's thesis*. University of California, Berkeley.
- 2 Taki, O., Rhazi, K.S., & Mejdoub, Y. (2021). A Study of Stirling Engine Efficiency Combined with Solar Energy. *Advanc. Scien., Techn. Engin. Syst. Journ.*, 6, 837–845.
- 3 Sabdenov, K. (2023). The Thermodynamics Cycles with a Reversible Chemical Reaction. *Americ. Journ. Modern Phys*, 12, 14–20.
- 4 Sabdenov, K.O. (2021). The thermodynamic Brayton cycle with a reversible chemical reaction. *Tech. Phys.*, 66, 1275–1283.

- 5 Langlois, J.L.R. (2006). Dynamic computer model of a Stirling space nuclear power system. *Trident Scholar project report*, 345. Annapolis: US Naval Academy.
- 6 Wong, H.M., & Goh, S.Y. (2020). Goh Experimental comparison of sinusoidal motion and non-sinusoidal motion of rise-dwell-fall-dwell in a Stirling engine. *Journ. Mech. Eng., Sci. (JMES)*, 14, 6971–6981.
- 7 Snyman, H., Harms, T., & Strauss, J. (2008). Design analysis methods for Stirling engines. *Journ. Energ. South. Africa*, 19, 4–19.
- 8 Ghozzi, S., & Boukhanouf, R. (2015). Computer Modeling of a Novel Mechanical Arrangement of a Free-Piston Stirling Engine. *Journ. Clean Energ. Techn.*, 3, 140–144. <https://DOI:10.7763/JOCET.2015.V3.184>.
- 9 Kwankaomeng, S., Silpsakoolsook, B., & Savangvong, P. (2014). Investigation on Stability and Performance of a Free-Piston Stirling Engine. *Energy Procedia*, 52, 598–609.
- 10 Farid, Z.M., Faiz, R.M., Rosli, A.B., & Kumaran, K. (2018). Thermodynamic performance prediction of rhombic-drive beta-configuration Stirling engine. *1st International Postgraduate Conference on Mechanical Engineering (IPCME 2018)*, <https://doi:10.1088/1757-899X/469/1/012048>
- 11 Perozziello, C., Grosu, L., & Vaglieco, B.M. (2021). Free-Piston Stirling Engine Technologies and Models: A Review. *Energies*, 14, 7009. <https://doi.org/10.3390/en14217009>
- 12 Walker, G. (1973). *Stirling-cycle machines*. University of Calgary, Canada. Clarendon Press, Oxford.
- 13 Reader, G.T., & Hooper, Ch. (1982). *Stirling engines*. London; N.Y.: E. & F.N. Spon Press.
- 14 Loitsyansky, L.G. (1966). *Fluid and Gas Mechanics*. Oxford, New York, Pergamon Press.
- 15 Sabdenov, K.O. (2024). A Simple Model of Stirling Machine (Engine) with Free Working Piston. *J Eng Phys Thermophy.*, 97, 1034–1041. <https://doi.org/10.1007/s10891-024-02974-3>
- 16 Howell, G.W., & Weathers, T.M. (1974). *Aerospace fluid component*. Designers' handbook. Volume 1. Edwards. California.
- 17 Baehr, H.D. (1973). *Thermodynamik*. Springer-Verlag, Berlin.
- 18 Graaf, G.H., & Winkelmann, J.G.M. (2021). Methanol: association behavior, third-law entropy analysis and determination of the enthalpy of formation. *Fluid Phase Equilibria*, 529, 112851. DOI: <https://doi.org/10.1016/j.fluid.2020.112851>
- 19 Engineering ToolBox, Methanol – Specific Heat. (2018). Retrieved from https://www.engineeringtoolbox.com/methanol-CH3OH-specific-heat-capacity-Cp-Cv-isobaric-isochoric-d_2103.html [Accessed 19 Junes. 2021].
- 20 Hall, G., & Watt, J.M. (1976). *Modern numerical methods for ordinary differential equations*. Oxford. Clarendon Press.
- 21 Kuczynski, M., Brown, W.I., Fonten, H.J., & Westerterp, K.R. (1987). Reaction Kinetics for the Synthesis of Methanol from CO and H₂ on a Cooper Catalyst. *Chem. Eng. Proc.*, 21, 179–191.

К.О. Сабденов, Ж.К. Смагулов, М. Ерзада, Т.А. Жакатаев

Стирлинг қозғалтқышын қайтымды реакциямен CO + 2H₂ ↔ CH₃OH модельдеу

Қарапайым компьютерлік модельдің көмегімен Стирлинг қозғалтқышының қасиеттері зерттелген, мұнда жұмыс заты CO + 2H₂ ↔ CH₃OH қайтымды реакциясы бар химиялық әрекеттесетін газ қоспасы. Мұндай қозғалтқыш алғашқы рет қарастырылуда. Модель регенератордағы гидродинамикалық процестердің релаксация уақытын ескереді. Бұл жағдайда қозғалтқыш үш негізгі бөліктен тұрады: қыздырғыш, регенератор және салқындатқыш камералар, осы жаңа модель 2006 жылы ұсынылған Langlois Justin моделінен екінші түбегейлі айырмашылығымен сипатталады. Қозғалтқыштағы қысым 20 МПа, жұмыс поршені бос. Зерттеуде тиімділік екі жағдайда салыстырылады: 1) қайтымды химиялық реакция жұмыс газында жүреді және 2) жұмыс газы салыстырмалы түрде жоғары және төмен молярлық массасы бар химиялық инертті. Тербеліс кезеңіндегі орташа қуат бірнеше жүз ватт, бірақ максималды қуат 2 кВт-қа жетуі мүмкін. Қайтымды химиялық реакциясы бар қозғалтқыштың қуатын арттыру үшін салқындатқыштың көлемін ұлғайту және жылытқыштың көлемін азайту қажет. Модельдеу нәтижелері авторлардың бірінің бұрын алған теориялық нәтижелерімен жақсы сәйкес келеді (К. Сабденов, 2023) қайтымды химиялық реакциясы бар Стирлинг циклін талдауға негізделген.

Кілт сөздер: Стирлинг циклі, Стирлингтің бос поршенді қозғалтқышы, метанол, қайтымды химиялық реакция, ПӘК және қуат

К.О. Сабденов, Ж.К. Смагулов, М. Ерзада, Т.А. Жакатаев

Моделирование двигателя Стирлинга с обратимой реакцией $\text{CO} + 2\text{H}_2 \leftrightarrow \text{CH}_3\text{OH}$

С помощью простой компьютерной модели впервые изучены свойства двигателя Стирлинга, где рабочим веществом является химически реагирующий газ с обратимой реакцией $\text{CO} + 2\text{H}_2 \leftrightarrow \text{CH}_3\text{OH}$. Модель учитывает время релаксации гидродинамических процессов в регенераторе. В данном случае двигатель считается состоящим из трех основных частей: нагревателя, регенератора и охлаждающей камеры. В этом состоит второе принципиальное отличие от модели Langlois Justin, предложенной в 2006 году. Давление в двигателе составляет 20 МПа, рабочий поршень свободен. Эффективность двигателя сравнивается для двух случаев: 1) в рабочем газе происходит обратимая химическая реакция и 2) рабочий газ химически инертен с относительно высокой и низкой молярной массой. Средняя мощность за период колебаний составляет несколько сотен ватт, но максимальная мощность может достигать 2 кВт. Чтобы увеличить мощность двигателя с обратимой химической реакцией, необходимо увеличить объем охладителя и уменьшить объем нагревателя. Результаты моделирования хорошо согласуются с ранее полученными теоретическими результатами одного из авторов (К. Сабденов, 2024), основанными на анализе цикла Стирлинга с обратимой химической реакцией.

Ключевые слова: цикл Стирлинга, свободнопоршневой двигатель Стирлинга, метанол, обратимая химическая реакция, КПД, мощность

Information about the authors

Sabdenov, Kanysh — Doctor of Mathematical and Physical Sciences, Associate Professor, Department of Electrical Power Engineering, L.N. Gumilyov Eurasian National University, Astana, Kazakhstan; e-mail: sabdenovko@yandex.kz; ORCID ID: <https://orcid.org/0009-0008-4733-6667>

Smagulov, Zhanaidar (*corresponding author*) — Candidate of Physical and Mathematical Sciences, Associate Professor, Department of Radiophysics and Electronics, Karaganda Buketov University, Karaganda, Kazakhstan; e-mail: smagul@mail.ru; ORCID ID: <https://orcid.org/0000-0002-3412-973X>

Erzada, Maira — PhD, Associate Professor, Department of Electrical Power Engineering, L.N. Gumilyov Eurasian National University, Astana, Kazakhstan; e-mail: mayira76@yahoo.co.jp; ORCID ID: <https://orcid.org/0000-0002-3943-651X>

Zhakatayev, Toksan — Doctor of Technical Sciences, Senior lecturer, Department of Electrical Power Engineering, L.N. Gumilyov Eurasian National University, Astana, Kazakhstan; e-mail: Toksanzh@yandex.kz; ORCID ID: <https://orcid.org/0009-0007-4119-2490>

U.K. Zhapbasbayev¹, D.Zh. Bossinov¹, M.A. Pahomov², Z. Sattinova³✉¹Satbayev University, Almaty, Kazakhstan;²Kutateladze Institute of Thermophysics SB RAS, Novosibirsk, Russia;³L.N. Gumilyov Eurasian National University, Astana, Kazakhstan

Modeling of Turbulent Non-Isothermal Flow in a Heating Network Pipe

The article presents a mathematical model of turbulent non-isothermal flow of viscoplastic fluid in a pipe with a sudden expansion of the heat network. Heat exchange of non-isothermal flow of viscoplastic fluid with cold environment leads to an increase in its viscosity and yield strength. Shvedov-Bingham rheological model represents the viscoplastic state of fluid. The Reynolds Stress Model (RSM) turbulence model describes the properties of anisotropy of the velocity components of pulsating motion in a pipe with a sudden expansion. In addition, the ability to predict turbulence anisotropy of the RSM model is used to construct a linear model of turbulent viscosity. Calculation data are obtained for different values of Reynolds and Bingham numbers. The calculation results show that with an increase in the Bingham number, the circulation zone decreases behind the section of the sudden expansion of the pipe. The results of the comparison of the radial profiles of the normalized axial mean and fluctuation velocity with the experimental data along the pipe with sudden expansion are given. The results show the anisotropic property of the axial and radial profiles of the velocity of fluctuation movement, which are in agreement with the data of the DNS (Direct Numerical Simulation) model.

Keywords: sudden expansion pipe, non-isothermal turbulent flow, viscoplastic fluid, RSM model of turbulence, yield strength, heat transfer, recirculation region, fluctuation velocity

✉ *Corresponding author:* Sattinova Zamira, sattinova.kz@gmail.com

Introduction

Sudden expansion of flow is widely used to intensify transfer processes in Newtonian flows (NF) and is encountered in many technical devices, for example, when connecting pipes of different diameters. Knowledge of the flow and heat transfer characteristics in separated flows is important from both fundamental and practical points of view. The flow in a sudden expansion pipe has been frequently used by several authors to test and evaluate turbulence models. Such a flow combines a region of strong nonequilibrium, a recirculation region, after which the flow returns to equilibrium. The sudden expansion pipe has also been the subject of many experimental studies, providing useful information and improving our understanding of turbulence. Of industrial interest is the application in flows associated with turbulence, such as corrosion in the heating network [1]. The separation and reattachment of flows in a sudden expansion pipe were studied experimentally in [2–6]. A numerical study was carried out in [7], where the (k-ε) and algebraic stress models and their modifications to account for the curvature of streamlines were considered. As a result, it was shown that the modified algebraic stress model gives a better agreement with the experimental data [8].

It should be noted that we have not found any experimental or numerical works devoted to heat transfer in turbulent separated non-Newtonian flows, with the exception of [9]. The aim of this work is a numerical study of the flow structure, kinetic energy of turbulence and heat transfer of a non-Newtonian fluid in a pipe with sudden expansion. The novelty of this work is also the consideration of the dependence of viscosity and yield strength on temperature.

1. Mathematical model

1.1 Statement of the Problem

The pipe diameter at the inlet $D_1 = 2R_1 = 0.2 \text{ m}$, and after a sharp expansion $D_2 = 2R_2 = 0.3 \text{ m}$, the step height $H = 0.05 \text{ m}$, $\frac{H}{(2R_1)} = 0.25$, the expansion coefficient $ER = ER = \left(\frac{R_2}{R_1}\right)^2 = 2.25$. The pipe length

$L = 12 m \left(\frac{x}{D_2} = 40 \right)$. The average axial velocity and average temperature at the inlet $U_{m1} = 0.2 - 0.8 \frac{m}{s}$, $T_1 = 303 K$, respectively. The wall temperature is constant and varies within the range $T_w = 273 - 293 K$. The Reynolds number $Re = \frac{U_{m1} D_1}{\nu_{w1}} = (0.7 - 3) \cdot 10^4$, where $\nu_{w1} = \mu_{w1} / \rho$. The Prandtl number of paraffinic oils at the inlet is $Pr = \mu_{w1} C_{p1} / \lambda_{w1} = 42$.

1.2 Basic equations

The basic equations of non-isothermal turbulent motion of a viscoplastic fluid are given in [10, 11]:

$$\nabla \cdot \mathbf{U} = 0 \quad (1)$$

$$\nabla \cdot (\rho \mathbf{U} \mathbf{U}) = -\nabla P + \nabla \cdot (2\mu_{eff} \mathbf{S}) + \nabla \cdot (-\rho \mathbf{u}' \mathbf{u}') + \nabla \cdot 2\mu_{eff}' \mathbf{S}' \quad (2)$$

$$\nabla \cdot (\rho C_p T \mathbf{U}) = \nabla \cdot (\lambda \nabla T) + \nabla \cdot (-\rho C_p \mathbf{u}' t') + \tau : \nabla \mathbf{U} \quad (3)$$

The coefficient of effective molecular viscosity μ_{eff} is found from the expression [12–15]:

$$\mu_{eff} = \begin{cases} \mu_p + \tau_0 |\dot{\gamma}|^{-1}, & |\tau| > \tau_0 \\ \infty, & |\tau| \leq \tau_0 \end{cases} \quad (4)$$

The singular property $|\tau| \leq \tau_0$ of formula (4) can be regularized using the approach [14, 15] and written as:

$$\mu_{eff} = \mu_p + \frac{\tau_0 [1 - \exp(-m|\dot{\gamma}|)]}{|\dot{\gamma}|}, \quad (5)$$

where the regularization parameter is $m = 1000 s$ [16].

The system of basic equations (1–5) is considered together with the RSM model of turbulent stresses, which is written in the form [17, 18]:

$$\begin{aligned} \frac{\partial}{\partial x_j} (\rho U_j u'_i u'_j) &= \rho (P_{ij} + \phi_{ij} - \varepsilon_{ij}) + \frac{\partial}{\partial x_l} \left[\rho \nu_{eff} \delta_{lm} + \rho \frac{C_\mu T_T}{\sigma_k} u'_l u'_m \right] \frac{\partial}{\partial x_m} u'_i u'_j + D_{NNF} \\ \frac{\partial}{\partial x_j} (\rho U_j \varepsilon) &= \frac{1}{T_T} (C_{\varepsilon 1} \tilde{P} - C_{\varepsilon 2} \varepsilon) + \frac{\partial}{\partial x_l} \left[\rho \nu_{eff} \delta_{lm} + \rho \frac{C_\mu T_T}{\sigma_\varepsilon} u'_l u'_m \right] \frac{\partial \varepsilon}{\partial x_m} + \varepsilon_{NNF} \\ \chi - L_T^2 \nabla^2 \chi &= 1 \end{aligned} \quad (6)$$

here, P_{ij} and $\tilde{P} = 0.5 \tilde{P}_{kk}$ are stress production terms, ϕ_{ij} is redistribution term [17], $L_T = m \left(\frac{k^{3/2}}{\varepsilon}, C_\eta \frac{\nu^{3/4}}{\varepsilon^{1/4}} \right)$

and $T_T = \max \left(\frac{k}{\varepsilon}, C_T \sqrt{\frac{\nu}{\varepsilon}} \right)$ are turbulent time and length macroscales, where $2k = u'_i u'_j$ is the turbulent kinetic energy, ε_{ij} is viscous dissipation rate tensor of turbulent stresses, $\varepsilon = 0.5 \varepsilon_{kk}$, and χ is a blending coefficient, and it changes from zero at the wall to unity far from the wall [17]. The constants and model functions of the system of equations (8) are given in [17].

1.3 Boundary conditions

The flow diagram is shown in Figure 1. On the pipe wall before and after expansion:

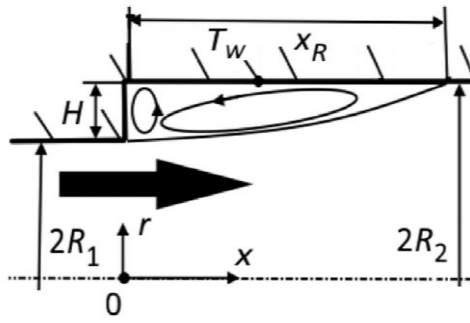


Figure 1. Flow diagram in a pipe with a sudden expansion

$$U = V = u'u' = 0; T = T_w = \text{const}; \varepsilon = 2\nu_w \frac{k}{y^2}; \chi = 0 \quad (7)$$

on the pipe axis:

$$\frac{\partial U}{\partial r} = V = \frac{\partial T}{\partial r} = \frac{\partial u'u'}{\partial r} = \frac{\partial \varepsilon}{\partial r} = \frac{\partial \chi}{\partial r} = 0 \quad (8)$$

Constant values of variables are set at the pipe inlet, and soft boundary conditions are set at the outlet.

2. Numerical realization

The numerical solution is obtained using a control volume method on a staggered grid. The algorithm for solving the system of equations (1)–(6) in the variables “velocity — pressure components” is described in detail in the work [10, 19]. All numerical predictions are performed using the “in-house” code.

The numerical method was verified by comparison with the experimental results [19] of isothermal flow in a pipe with a sharp expansion (Fig. 2). It is known [20] that the generalized model of a Newtonian fluid can describe non-Newtonian flows that thin under shear. The regime parameters, properties of Newtonian and non-Newtonian fluids with xanthan gum (XG) are given in Table. The power-law fluid was an aqueous solution with 0.2 % XG with an index $n = 0.34$ by weight [21] and 0.1 % XG with $n = 0.43$ [19]. The difference in the average axial velocity profiles between the results for NF and NNF is insignificant (Fig. 2a). The average axial velocity profiles for NF and NNF are similar in the experiments [19] and the authors’ calculations. The recirculation length in NNF is 20 % shorter than in NF (Table). The radial velocity profiles of axial pulsations show agreement between the measurements [19] and the authors’ calculations (Fig. 2b).

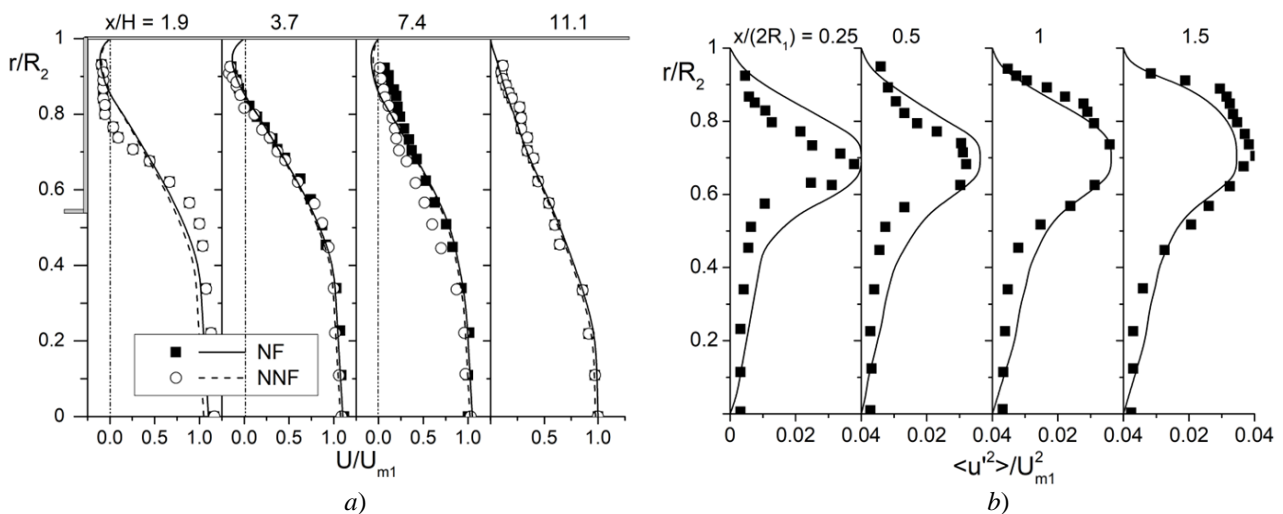


Figure 2. Radial profiles of axial average (a) and fluctuation (b) velocity along a pipe with sudden expansion. Symbols are measurements [18, 20], lines are authors’ calculations

The length of recirculation region. Comparisons with measurements of [18]

Fluid	U_{m1} , m/s	Re_w	x_R/H [14]	Authors' simulations
Water	4.61	1.35×10^5	8.43	9
Water	1.73	5.03×10^4	8.71	9
0.1 % XG	3.04	1.96×10^4	6.93	7.5
0.2 % XG	4.05	1.94×10^4	7.14	7.4
0.2 % XG	5.01	2.72×10^4	6.78	7.3

3. Discussion of calculated data.

Viscoplastic turbulent flow in a pipe without sudden expansion

Figure 3 shows comparisons of the pulsating velocity in the axial and radial directions with the DNS data [22]. The RSM model qualitatively describes the anisotropy of the axial and radial velocity pulsation profiles well (Figs. 3a and 3b). The maximum discrepancy between DNS and RANS of the authors is up to 20 %. The positions of the maximum values and practically coincide with the DNS data [22]. The predictions obtained confirm the possibility of successfully using the RSM model to describe the non-isothermal turbulent flow of a viscoplastic fluid without additional terms in the RSM transfer equations.

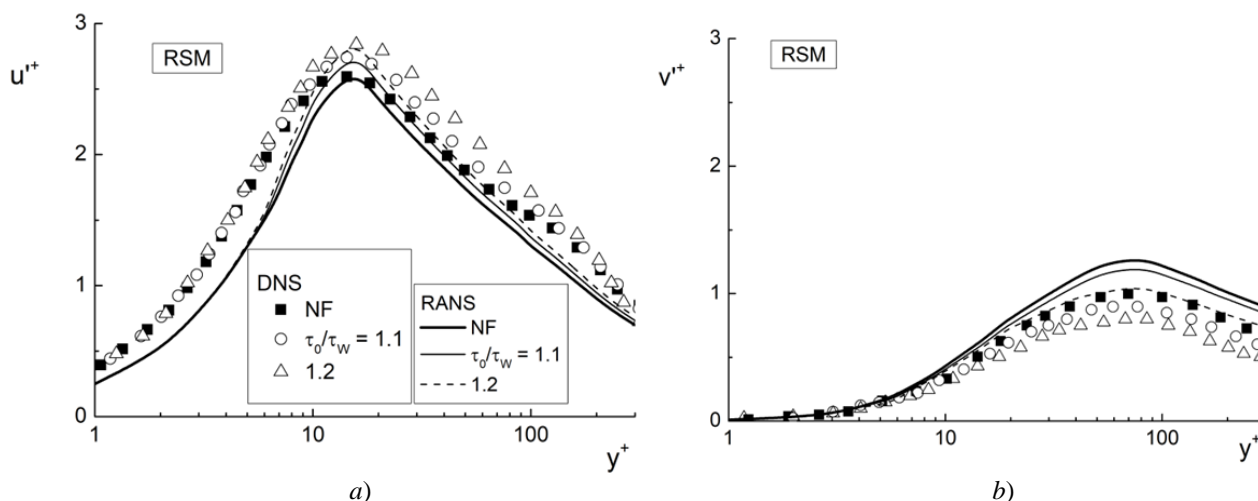


Figure 3. Comparison of the results of calculations of the RSM model of axial (a) and radial (b) velocity fluctuations with the results of DNS [21]

4. Calculated data of turbulent flow of viscoplastic fluid.

Structure of viscoplastic fluid flow

Figure 4 shows the distributions of the recirculation length (a) and maximum values of turbulent kinetic energy (b) of isothermal viscoplastic fluid from Bingham numbers Bm . Here x_R^{NF} and k_{\max}^{NF} are the recirculation length of the flow and the maximum value of turbulent kinetic energy Newtonian fluid (NF), respectively.

The non-Newtonian fluid causes a significant decrease in the length of the recirculation flow zone and the turbulence level (Figs. 4a and 4b). An almost twofold decrease in the length of the recirculation region is shown at $Bm = 17$ compared to the flow of a Newtonian fluid ($Bm = 0$) (Fig. 4a). The decrease in turbulent kinetic energy reaches 60 % at $Bm = 17$ (Fig. 4b). The Reynolds numbers $Re = 0.5 \cdot 10^4$ and $2.0 \cdot 10^4$ do not have a large effect on the length of the recirculation zone, the difference is up to 10 % at $Bm = 17$.

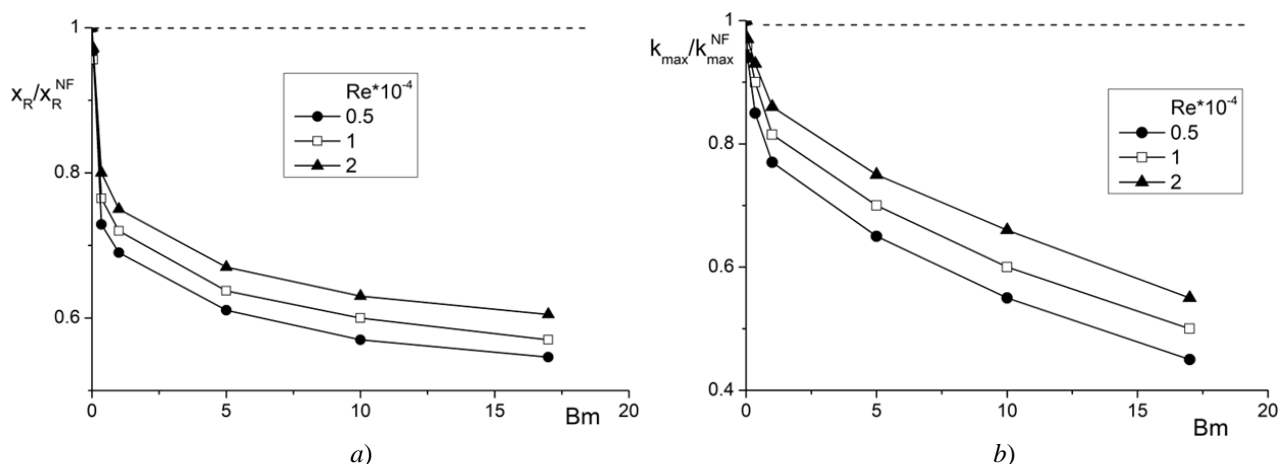


Figure 4. The effect of flow Reynolds and Bingham numbers on distributions of recirculation length (a) and maximal values of turbulent kinetic energy (b)

Figure 5 shows the influence of the Bingham (a) and Reynolds (b) numbers on the maximum average axial value of the reverse flow of an isothermal viscoplastic fluid.

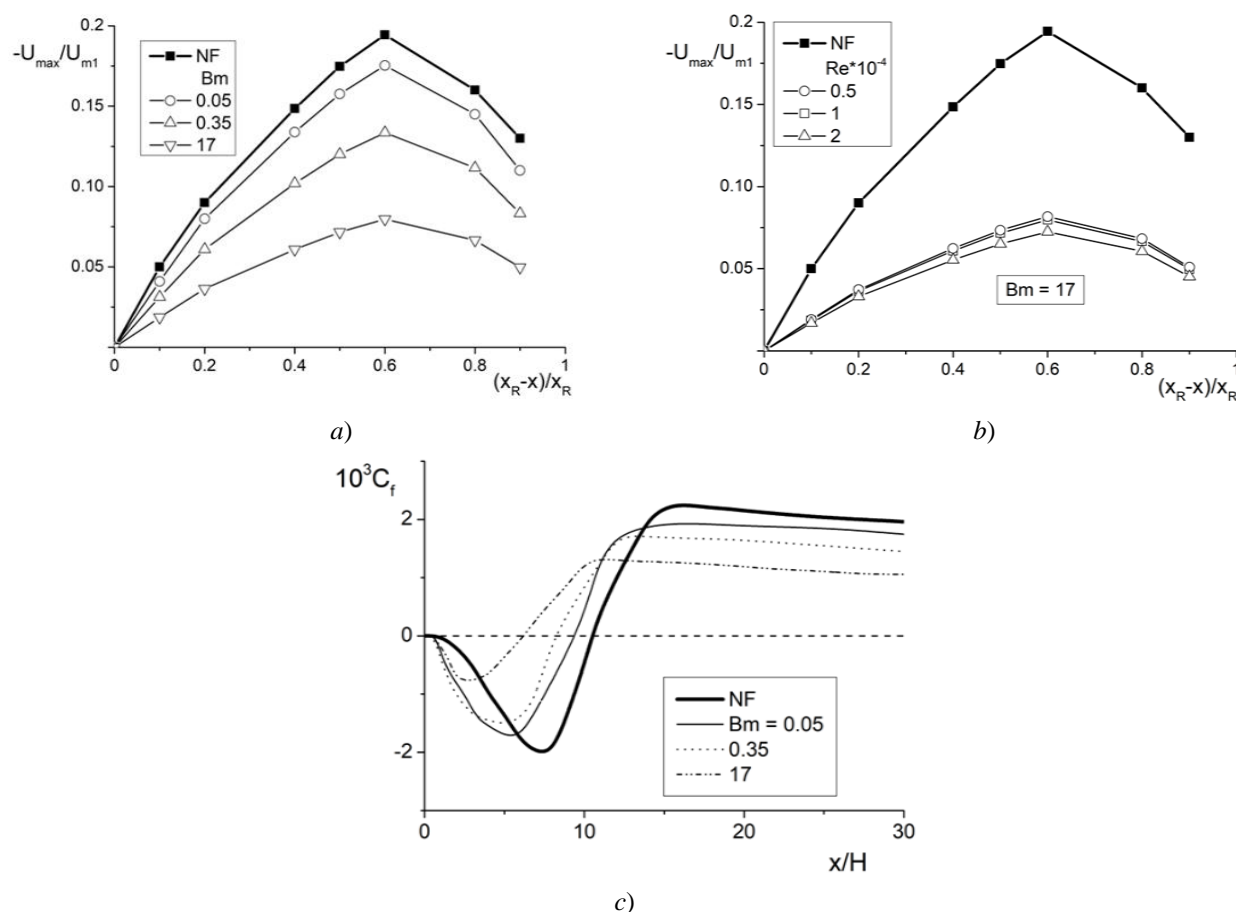


Figure 5. The effect of Bingham (a) and Reynolds (b) numbers on the maximal mean axial magnitude of reverse flow, and wall friction (c) of isothermal SB fluid. (a and c): $Re = 10^4$; (b): $Bm = 17$

For a Newtonian fluid ($Bm = 0$), the maximum negative values of the reverse flow $-U_{max}/U_{m1}$ reach 20 % (Fig. 5a) and correspond to the known data for flow in a pipe with sudden expansion [23, 24]. The calculated data for different Bingham numbers are also presented here, and a sharp decrease in the maximum negative velocity ($-U_{max}/U_{m1} \approx 0.075$) is obtained for $Bm = 17$ (Fig. 5a). It can be noted that for non-

isothermal flows of viscoplastic fluid, the recirculation zone does not have a significant effect on the processes of turbulent transfer of momentum and energy compared to the Newtonian one. Similarly, an increase in the Reynolds number of the flow does not have a significant effect on the dynamics of the reverse flow (Fig. 5b).

The distribution of the wall friction coefficient $C_f / 2 = \tau_w / (\rho U_{m1}^2)$ along the flow is shown in Figure 5c for different Bingham numbers Bm . The flow reattachment point for NF and NNF is located at $C_f = 0$. The value of the wall friction coefficient is negative in the recirculation region for NF and NNF due to the reverse flow (Fig. 5c). Downstream of the reattachment point, an increase in the wall friction coefficient is observed and the values become positive. The wall friction in isothermal flow is greater than for viscoplastic fluid. The location of the minimum point of C_f for NNF shifts upstream by almost 2 times compared to NF due to the manifestation of non-Newtonian behavior.

A comparison of non- and isothermal viscoplastic flow following sudden expansion of a pipe is shown in Figure 6.

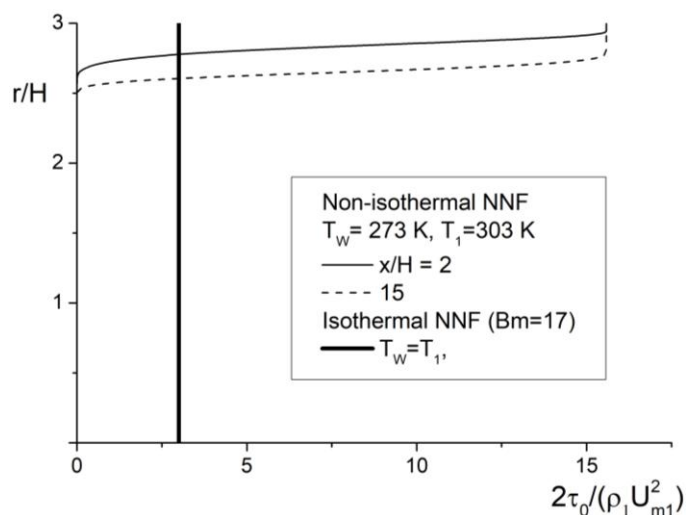


Figure 6. Distributions of yield shear stress τ_0 over the pipe radius for non- (solid and dashed lines) and isothermal (bold line) NNF behind the pipe sudden expansion

Calculation of isothermal flow NNF with a constant value of the Bingham number $Bm = 17$ shows a constant value of the yield strength along the pipe radius (Fig. 6). Calculations of the transition of non-isothermal turbulent flow of paraffinic crude oil show a more complex flow behavior. In the flow core, the yield strength value becomes zero ($\tau_0 \approx 0$) and in this zone the flow is Newtonian (Fig. 6). In the recirculation zone ($x/H = 2$) and near the pipe wall at ($x/H = 15$), the yield strength $\tau_0 \approx 16$ (Fig. 6). Viscoplastic flow of the liquid takes place in this region.

Conclusion

The results of modeling non-isothermal turbulent flow in a pipe with expansion show the correctness of the developed mathematical model. In particular, a comparison of the radial profiles of the normalized axial average and fluctuation velocity with experimental data along a pipe with sudden expansion is carried out. The calculations show the anisotropic property of the axial and radial profiles of the fluctuation motion velocity, which is in agreement with the data of the exact DNS model. Viscoplasticity of a turbulent fluid leads to the following effects: 1) reduction of the length of the recirculation zone and reduction of the kinetic energy of the fluctuation motion; 2) reduction of the maximum negative velocity ($-U_{max}/U_{m1} \approx 0.075$) and reduction of the friction coefficient $C_f / 2 = \tau_w / (\rho U_{m1}^2)$ in the recirculation zone. In general, the recirculation zone of a viscoplastic fluid does not have a significant effect on the processes of turbulent momentum and energy transfer compared to the Newtonian one.

Acknowledgements

This work was supported by the Science Committee of the Ministry of Science and Higher Education of the Republic of Kazakhstan (Grant #BR24992907 for 2024-2026) and the Reynolds stress turbulence model was developed under the state contract with IT SB RAS (121031800217-8).

Funding

This research has been funded by the Science Committee of the Ministry of Science and Higher Education of the Republic of Kazakhstan (Grant #BR24992907 for 2024-2026)

References

- 1 Sedahmed, G.H., Abdo, M.S.E., Amer, M.A., & Abd El-Latif, G. (1999). Effects of drag reducing polymers on the rate of mass transfer-controlled corrosion in pipelines under developing turbulent flow. *Int. Comm. Heat Mass Transfer*, 26, 531–538. [https://doi.org/10.1016/S0735-1933\(99\)00039-1](https://doi.org/10.1016/S0735-1933(99)00039-1)
- 2 Back, L., & Roschke, E. (1972). Shear layer regimes and wave instabilities and reattachment lengths downstream of an abrupt circular sudden expansion. *J. Appl. Mech.*, 94, 677–681. <https://doi.org/10.1115/1.3422772>
- 3 Khezzar, L., Whitelaw, J.H., & Yianneskis, M. (1985). An experimental study of round sudden expansion flows. In: *Proceedings of the Fifth Symposium on turbulent shear flows*, 5–25. Cornell University.
- 4 Driver, D.M., & Seegmiller, H.L. (1983). Features of a reattaching turbulent shear layer in divergent channel flow. *AIAA Journal*, 23, 163.
- 5 Stieglmeier, M., Tropea, C., Weiner, N., & Nitsche, W. (1989). Experimental investigation of the flow through axisymmetric expansions. *J. Fluids Eng.*, 111, 464–471. <https://doi.org/10.1115/1.3243669>
- 6 Founti, M., & Klipfel, A. (1998). Experimental and computational investigations of nearly dense two-phase sudden expansion flows. *Experimental Thermal and Fluid Science*, 17, 27. [https://doi.org/10.1016/S0894-1777\(97\)10046-2](https://doi.org/10.1016/S0894-1777(97)10046-2)
- 7 Sindir, M.S. (1982). A numerical study of turbulence flows in backward-facing step geometries: a comparison of four models of turbulence. *PhD Thesis*. University of California, Davis, California,
- 8 Kim, J., Kline, S.J., & Johnston, J.P. (1978). Investigation of Separation and Reattachment of a Turbulent Shear Layer: Flow Over a Backward Facing Step. *Thermoscience Division*, Report MD-37. Stanford University, Stanford, California.
- 9 Pak, B., Cho, Y.I. & Choi, S.U.S. (1991). A study of turbulent heat transfer in a sudden expansion pipe with drag-reducing viscoelastic fluid. *Int. J. Heat Mass Transfer*, 34, 1195–1208. [https://doi.org/10.1016/0017-9310\(91\)90028-D](https://doi.org/10.1016/0017-9310(91)90028-D)
- 10 Pakhomov, M.A., Zhapbasbayev, U.K., & Bossinov, D.Zh. (2023). Numerical simulation of the transition of a Newtonian to a viscoplastic state in a turbulent flow. *J. King Saud University-Sci.*, 35(2), 102522. <https://doi.org/10.1016/j.jksus.2022.102522>
- 11 Pakhomov, M.A. & Zhapbasbayev, U.K. (2024). Comparative predictions of turbulent non-isothermal flow of a viscoplastic fluid with a yield stress. *Heliyon*, 10 e24062. <https://doi.org/10.1016/j.heliyon.2024.e24062>
- 12 Schwedoff, F.N. (1900). La rigidité des fluides. *Rapports du Congrès International de Physique* 1, 478.
- 13 Bingham, E.C. (1922). *Fluidity and Plasticity*, McGraw-Hill. New York.
- 14 Sattinova, Z., Assilbekov, B., Zhapbasbayev, U., Ramazanov, G., Sagindykova, G. (2024). Evaluation of influence of thermoplastic slurry flow conditions on heat transfer coefficient during beryllium ceramic formation. *Bulletin of the University of Karaganda-Physics*, 2(114), <https://doi.org/10.31489/2024ph2/82-93>
- 15 Wilkinson, W.L. (1960). *Non-Newtonian fluids. Fluid Mechanics, Mixing and Heat Transfer*. Pergamon Press, London
- 16 Papanastasiou, T.C. (1987). Flows of materials with yield. *J. Rheology*, 31(5), 385–404.
- 17 Fadai-Ghotbi, A., Manceau, R., & Boree, J. (2008). Revisiting URANS computations of the backward-facing step flow using second moment closures. Influence of the numeric. *Flow, Turbulence and Combust*, 81(3), 395–410. [10.1007/s10494-008-9140-8](https://doi.org/10.1007/s10494-008-9140-8)
- 18 Pakhomov, M.A., & Zhapbasbayev, U.K. (2024). RANS predictions of turbulent non-isothermal viscoplastic fluid in pipe with sudden expansion. *J. Non-Newtonian Fluid Mech.*, 334, 105329. <https://doi.org/10.1016/j.jnnfm.2024.105329>
- 19 Pereira, A.S., & Pinho, F.T. (2000). Turbulent characteristics of shear-thinning fluids in recirculating flows. *Exp. Fluids*, 28, 266–278.
- 20 Gavrilov, A.A., & Rudyak, V.Y. (2016). Reynolds-averaged modeling of turbulent flows of power-law fluids, *J. Non-Newton. Fluid Mech.*, 227, 45–55. <https://doi.org/10.1016/j.jnnfm.2015.11.006>
- 21 Pereira, A.S., & Pinho, F.T. (2002). The effect of the expansion ratio on a turbulent non-Newtonian recirculating flow. *Exp. Fluids*, 32, 458–471. <https://doi.org/10.1007/s00348-001-0386-3>
- 22 Singh, J., Rudman, M., Blackburn, H.M. (2017). The effect of yield stress on pipe flow turbulence for generalised Newtonian fluids. *J. Non-Newtonian Fluid Mech.*, 249, 53–62. <https://doi.org/10.1016/j.jnnfm.2017.09.007>
- 23 Terekhov, V.I., Bogatko, T.V., Dyachenko, A.Yu., Smulsky, Ya.I., & Yarygina, N.I. (2021). *Heat Transfer in Subsonic Separated Flows*. Springer, Cham.
- 24 Ota, T. (2000). A survey of heat transfer in separated and reattached flows. *Appl. Mech. Rev.*, 53, 219–235. <https://doi.org/10.1115/1.3097351>

У.К. Жапбасбаев, Д.Ж. Босинов, М.А. Пахомов, З.К. Саттинова

Жылу желісі кенеттен кеңейгенде құбырдағы тұтқырпластикалы сұйықтықтың турбулентті ағынын модельдеу

Мақалада жылу желісінің кенеттен кеңеюі бар құбырдағы тұтқырпластикалы сұйықтықтың турбулентті изотермиялық емес ағынының математикалық моделі келтірілген. Тұтқырпластикалы сұйықтықтың изотермиялық емес ағынының суық ортамен жылу алмасуы оның тұтқырлығы мен аққыштығының жоғарылауына әкеледі. Шведов-Бингем реологиялық моделі сұйықтықтың тұтқырпластикалық күйін көрсетеді. RSM турбуленттік моделі кенет кеңеюі бар құбырдағы пульсациялы қозғалыстың жылдамдық компоненттерінің анизотропиясының қасиеттерін сипаттайды, сонымен қатар турбуленттілік анизотропиясын болжау мүмкіндігі турбуленттік тұтқырлықтың сызықтық моделін құру үшін қолданылады. Есептелген деректер Рейнольдс және Бингем сандарының әртүрлі мәндері үшін алынды. Есептеу нәтижелері Бингем санының ұлғаюымен құбырдың кенеттен кеңею кимасының артында циркуляциялық аймақтың кішірейетіндігін көрсетеді. Нормаланған осьтік орташа және флуктуация жылдамдығының радиалды профильдерін кенет кеңеюі бар құбыр бойындағы тәжірибелік мәліметтермен салыстыру нәтижелері берілген. Нәтижелер DNS (Direct Numerical Simulation) моделінің деректерімен сәйкес келетін тербелмелі қозғалыстың осьтік және радиалды жылдамдық профильдерінің анизотропия қасиеттерін көрсетеді.

Кілт сөздер: кенеттен кеңею құбыры, изотермиялық емес турбулентті ағын, тұтқырпластикалы сұйық, RSM турбуленттік моделі, аққыштық шегі, жылу тасымалдау, рециркуляция аймағы, флуктуация жылдамдығы

У.К. Жапбасбаев, Д.Ж. Босинов, М.А. Пахомов, З.К. Саттинова

Моделирование турбулентного течения вязкопластичной жидкости в трубе тепловой сети с резким расширением

В статье приводится математическая модель турбулентного неизоэтермического течения вязкопластичной жидкости в трубе с резким расширением. Теплообмен неизоэтермического потока вязкопластичной жидкости с холодной окружающей средой приводит к повышению ее вязкости и предела текучести. Реологическая модель Шведова-Бингама представляет вязкопластичное состояние жидкости. RSM модель турбулентности описывает свойства анизотропии компонент скорости пульсационного движения в трубе с резким расширением. Расчетные данные получены при различных значениях числа Рейнольдса и Бингама. Результаты расчетов показывают, что с ростом числа Бингама циркуляционная зона сокращается за сечением резкого расширения трубы. Приведены результаты сравнения радиальных профилей нормализованной осевой средней и флуктуационной скорости с опытными данными вдоль трубы с внезапным расширением. Результаты показывают анизотропное свойство осевых и радиальных профилей скорости флуктуационного движения, которые находятся в согласии с данными DNS (Direct Numerical Simulation) модели.

Ключевые слова: труба внезапного расширения, неизоэтермическое турбулентное течение, вязкопластичная жидкость, модель турбулентности RSM, предел текучести, теплопередача, область рециркуляции, скорость флуктуации

Information about the authors

Zhapbasbayev, Uzak — Doctor of Technical Sciences, Professor, Head of the Research and Production Laboratory “Modeling in Energy”, Satbayev University, 22 Satpaev Street, 050013 Almaty, Kazakhstan; e-mail: uzak.zh@mail.ru; ORCID ID: <https://orcid.org/0000-0001-5973-5149>

Bossinov, Daniyar — Master of Science, Research Worker, Satbayev University, 22 Satpaev Street, 050013 Almaty, Kazakhstan; e-mail: dansho.91@mail.ru; ORCID ID: <https://orcid.org/0000-0003-3757-6460>

Pahomov, Maksim — Doctor of Physical and Mathematical Sciences, Major Research Worker, Kutateladze Institute of Thermophysics SB RAS, Novosibirsk, Russia; e-mail: Pakhomov@itp.nsc.ru; ORCID ID: <https://orcid.org/0000-0002-8127-3638>

Sattinova, Zamira (*corresponding author*) — Candidate of Physical and Mathematical Sciences, Associated Professor, L.N. Gumilyov Eurasian National University, 2 Satpayev str., 010008 Astana, Kazakhstan; e-mail: sattinova.kz@gmail.com; ORCID ID: <https://orcid.org/0000-0002-2990-6581>

B.K. Rakhadilov¹, A.B. Kengesbekov^{2,3✉}, N.M. Magazov²,
A.A. Kusainov², L.S. Kairbaeva^{2,3}, Y.S. Molbosynov²

¹“PlasmaScience” LLP, Ust-Kamenogorsk, Kazakhstan;

²D. Serikbayev East Kazakhstan Technical University, Kazakhstan, Ust-Kamenogorsk;

³Institute of Composite Materials/LLP, Ust-Kamenogorsk, Kazakhstan

Study of the Effect of Thermomechanical Treatments on the Property of Beryllium Bronze in Order to Expand Its Application

The article is devoted to the study of the influence of thermomechanical treatments on mechanical and physicochemical properties of beryllium bronze in order to expand its application in modern technologies. This paper studies the influence of different modes of thermomechanical processing on the structure and properties of beryllium bronze. The mechanism of influence of these methods on modification of alloy microstructure, which directly affects its performance characteristics, is described. The obtained results allow expanding the areas of application of beryllium bronze in industry, aircraft construction and other sectors. And also the main conclusions are that the introduction of advanced methods of thermomechanical processing helps not only to improve the physical characteristics of bronze, but also makes it possible to use this material in new areas, such as aerospace and automotive industries. The article is of importance for specialists in the field of materials science and engineering, as it provides new data and recommendations that can improve the processes of production and operation of beryllium bronze products.

Keywords: beryllium bronze, heat treatment, mechanical treatment, thermomechanical treatment, aging, hardening, material microstructure, equal-channel angular pressing (ECAP)

✉Corresponding author: Kengesbekov Aidar, aidar.94.01@mail.ru

Introduction

Beryllium bronze is a unique copper alloy containing 0.5 % to 3 % beryllium and, in some cases, other alloying elements such as cobalt or nickel [1]. This material combines high strength, non-magnetization, wear resistance and corrosion resistance, which makes it in demand in various industries. Due to its heat treatability, beryllium bronze exhibits exceptional mechanical properties, including strengths up to 1400 MPa, which is far superior to other copper alloys [2]. Its thermal conductivity of 107 W/m·K is also 3–5 times higher than that of tool steel, which opens up additional opportunities for its application.

Due to its unique characteristics, beryllium bronze is used in a wide range of applications, from the production of tools for hazardous environments to high-tech components in the aerospace industry [3]. Its non-magnetic nature and its ability to prevent sparks make the material indispensable for the manufacture of tools used in hazardous environments such as coal mines, drilling rigs and grain elevators. In addition, beryllium bronze is used in electronics, production of musical instruments and devices for precise measurements, as well as in the production of springs, contacts and bearings [4]. The main producers of beryllium are the USA, China and Kazakhstan. In total, about 300 tons of beryllium are produced in the world per year.

BrB2 is a tin-free, pressure-treated beryllium bronze. The chemical composition of BrB2 alloy is described in GOST 18175-78 and includes the following components: copper 96.9–98.0 %, beryllium 1.8–2.1 %, nickel 0.2–0.5 % and up to 0.5 % of impurities.

Thermomechanical treatment is an important tool to improve the properties of beryllium bronze [5]. It is an effective tool for optimizing the properties of beryllium bronze. The development of new TMT modes will allow to significantly expand the application area of this unique material, providing an increase in its performance characteristics and durability. The processes of hardening, aging and plastic deformation at high temperatures lead to changes in its microstructure, which in turn affects its mechanical and physical properties [6]. For example, the use of aging allows the formation of ordered phases in the alloy structure, which increases its hardness and tensile strength. This makes beryllium bronze even more adaptable to different operating conditions. Aging is a key stage of heat treatment that contributes to the hardening of beryllium bronze due to the release of fine phases in its structure [6, 7]. This process improves the hardness, strength

properties and wear resistance of the alloy, which is especially important for elements subjected to significant loads. However, further strengthening of properties can be achieved by additional plastic deformation after aging [7]. This combined treatment allows not only to increase the mechanical characteristics but also to improve the isotropy of the material, which expands its capabilities in difficult operating conditions. Hardening is an effective method for changing the microstructure of beryllium bronze, which achieves a more uniform phase distribution and reduces residual stresses [8]. Sharp cooling after heating at high temperatures increases strength and decreases ductility, making the alloy more resistant to stress. Additional plastic deformation after hardening optimizes material properties by combining high hardness with improved wear resistance. This combined treatment is particularly important for high friction and wear applications [9].

Due to its unique combination of mechanical, corrosion and electrical conductive properties, this material is widely used in the aerospace, electronics, power generation and tooling industries. However, the properties of the alloy are significantly influenced by thermomechanical treatments, which can significantly improve its performance characteristics.

ECAP (equal channel angular pressing) is one of the most effective methods of severe plastic deformation (SPD), allowing to create ultrafine grain structure in materials, including beryllium bronze BrB2. This method, as noted in IPD works, provides multiple shear deformation without changing the macroscopic geometry of the specimen, which makes it unique for industrial applications [1]. It has been reported in the literature that grain refinement to submicron or nanometer scale leads to significant improvement in mechanical properties including hardness, strength and yield strength [2].

The purpose of this work is to study the effect of thermomechanical treatments on the properties of beryllium bronze after ECAP and to analyze the changes in the microstructure of the alloy and its mechanical properties, which will allow to optimize the treatment modes to improve the performance characteristics and expand the areas of application of this material.

Materials and methods of experiments

Beryllium bronze alloy containing 97-98 % copper and about 2 % beryllium was used as a material for the study. In addition to the main components, the composition may contain alloying elements such as nickel (up to 0.5 %), iron, silicon and aluminum (up to 0.15 % each), as well as minor impurities. This alloy is characterized by high strength and wear resistance, excellent spring properties, good antifriction characteristics, as well as medium electrical conductivity and thermal conductivity. In addition, beryllium bronze is extremely ductile in the hardened state, which facilitates machining and forming.

To study the influence of thermomechanical treatment, two types of treatment were chosen to study the change in the properties of beryllium bronze. In the first treatment variant, the samples were subjected to hardening at 800 °C and aging process at 320 °C for 2 hours, which allows evaluating the effect of temperature influence on the structure and properties of the material. In the second variant, after the aging process, mechanical treatment was additionally carried out to study the effect of plastic deformation on the material already modified by heat treatment. To study the effect of heat treatment on the properties of the alloy, 9 samples with different treatments were prepared. Table shows the treatment parameters of the samples.

T a b l e

Sample processing parameters

Name of samples	Type of treatment	Processing parameter
No. 1	Without treatment	Initial
No. 2	Heat treatment	800 °C (hardening)
No. 3	Heat treatment	320 °C (aging)
No. 4	Mechanical treatment	ECAP (4 passes)
No. 5	Mechanical treatment	ECAP (3 passes)
No. 6	Mechanical treatment	ECAP (2 passes)
No. 7	Mechanical treatment	ECAP (1 passes)
No. 8	Thermo-mechanical treatment	ECAP (4 passes) + Heat treatment (aging)
No. 9	Thermo-mechanical treatment	ECAP (3 passes) + Heat treatment (aging)

All the selected processing modes are aimed at identifying the optimal conditions to improve the mechanical properties and structural characteristics of beryllium bronze.

The samples were preliminarily ground using 100 to 2000 grit sandpaper and polished using diamond paste. Then, to determine the microstructure, the samples were etched using Kroll's Reagent (100 ml water, 1–3 ml hydrofluoric acid, 2–6 ml nitric acid).

Metallographic analysis methods using Olympus Corporation optical microscopy, OLYMPUS BX53M, (Tokyo, Japan) were used to study the microstructure of beryllium bronze.

X-ray phase analysis. One of the popular methods of studying the structure of metals and alloys is X-ray diffraction analysis (XRD) [10]. The X-ray diffractometer X'PertPRO from "PANalytical" (the Netherlands) using $\text{CuK}\alpha$ radiation was used to study the structure-phase composition of the coatings. The samples were prepared according to standard methods, and the diffractograms of all samples were recorded under the same conditions, which allowed a more accurate comparison of the obtained data. Imaging was carried out at the following parameters: tube voltage $U = 40$ kV; tube current $I = 30$ mA; exposure time 1 s; imaging step 0.02° , and the investigated area of angles 2θ was from 20° to 90° . The diffractograms were interpreted using the High Score program and PDF-4 database, and quantitative analysis was performed using the Powder Cell computer program.

Mechanical properties were studied using hardness and elasticity tests. Different methods were used to measure hardness, such as the Vickers method using a diamond pyramid on a Metolab 502. Measurement parameters: load 0.025 g, dwell time 10 s. Vickers number (HV) is calculated by the formula:

$$HV = \frac{1.854P}{d_2} . \quad (1)$$

Martens method with hardness and modulus of elasticity investigation using a load-discharge curve. The hardness and modulus of elasticity of the coatings were measured using a FISHER SCOPE HM 2000 system (Helmut Fischer GmbH, Sindelfingen, Germany) controlled with WIN-HCUS software version 7.1. This instrument is designed to evaluate microhardness and other mechanical properties of materials in accordance with the requirements of ISO14577. The waiting time is 10 s and the loading time is 1 N. In order to evaluate the cracking resistance of the coating under constant loads, the cracking initiation rate (CIT) parameter was calculated. This parameter characterizes the change in indentation depth over time under constant load and is calculated as the percentage change in indentation depth versus dwell time. The formula for calculating CIT is as follows:

$$CIT = \frac{h(t) - h_0}{h_0} \cdot 100 \% . \quad (2)$$

Tribological tests on the "ball-disk" scheme. Tribological tests for sliding friction were carried out on a TRB^3 tribometer (Switzerland Anton Paar Srl.). The tribological properties of the materials were studied using the standard "ball-disk" technique (ASTM G 99). A 3.0 mm diameter ball made of Si_3N_4 coated steel was used as a counterbody. The tests were carried out at a load of 10 N and a linear velocity of 3 cm/s, with a wear curvature radius of 4 mm and a friction length of 100 m. Tribological characteristics were evaluated on the basis of wear intensity and friction coefficient.

Results of the research

Figure 1 shows microstructural analysis of beryllium bronze BrB2, from the three states, revealed significant changes in the structure of the material in the process of heat treatment. In the initial state (Fig. 1a) the material has a coarse-grained structure with clear boundaries, which indicates its stable state without significant defects. After quenching (Fig. 1b), the microstructure shows pronounced signs of internal stresses and deformation due to the accumulation of defects resulting from rapid cooling. After aging (Fig. 1c), the structure is significantly stabilized: grains are restored, stresses are reduced, and beryllium-rich secondary phases are formed. These changes confirm that the aging process promotes the relaxation of defects, increases the orderliness of the structure and improves the mechanical properties of beryllium bronze BrB2.



a — initial state; *b* — after quenching; *c* — after aging

Figure 1. Microstructure of beryllium bronze BrB2

The results of the analysis (Fig. 2) showed that after quenching (state 2) the structure of beryllium bronze is characterized by a significant level of defects, stresses and reduced crystallite sizes, which is reflected in broad and less intense peaks on the diffractogram. In the aging process (state 3), the separation of beryllium-rich secondary phases is observed, which leads to crystallite growth, a decrease in internal stresses and an increase in the intensity of diffraction peaks. These changes are due to the redistribution of beryllium in the structure, which provides defect relaxation and matrix strengthening. Thus, beryllium bronze BrB2 demonstrates high hardening efficiency due to the formation of an ordered structure and secondary phases during aging, which makes it indispensable in critical applications requiring a combination of strength and resistance to wear.

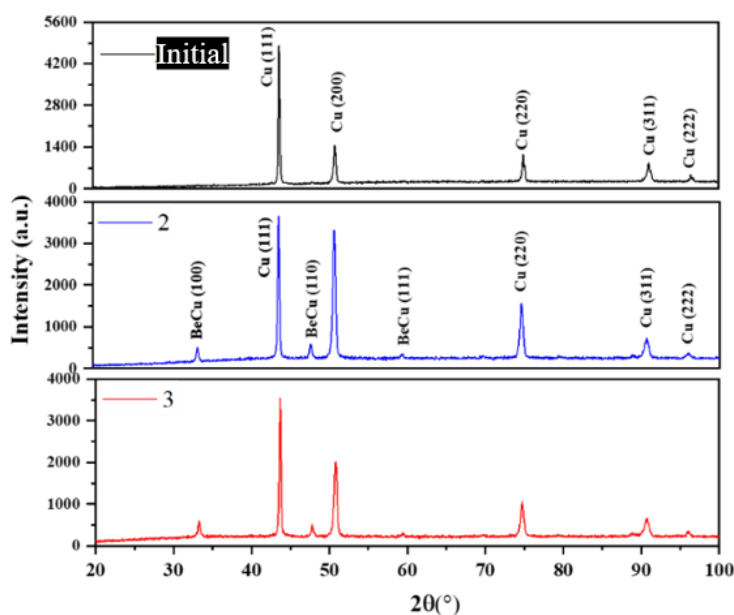


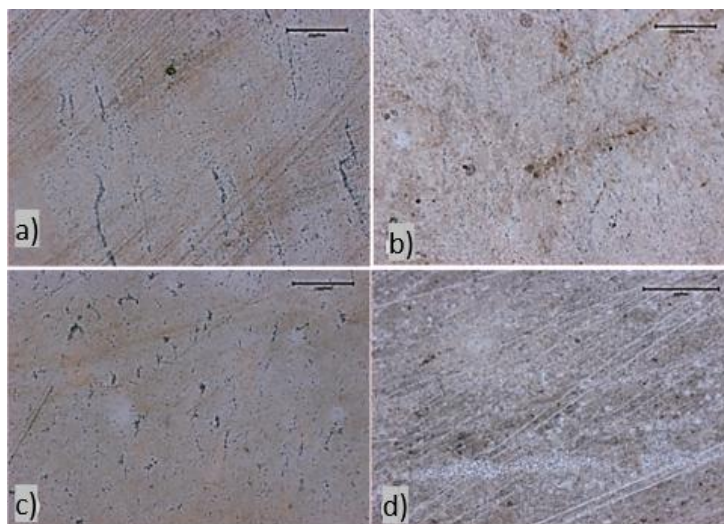
Figure 2. Results of X-ray phase analysis of the studied samples

The conducted studies in Figure 3 showed that after the 1st pass of ECAP, beryllium bronze retains predominantly coarse-grained structure characteristic of the initial stage of plastic deformation, which is consistent with similar data for other materials such as aluminum and copper alloys. At this stage, high-angle grain boundaries begin to form and zones of local accumulation of dislocations begin to nucleate, which is confirmed by studies of deformation processes in metals [4].

After the 2nd pass, active grain refinement and increase in dislocation density are observed, which is associated with intensive shear and stress redistribution in the material. Similar effects have been described in studies based on IPD of aluminum alloys, where after two or three passes the appearance of substructure with low-angle boundaries and initial stabilization of grains were observed [5]. In the case of beryllium bronze, this process leads to an increase in hardness and initial phase stabilization due to the redistribution of beryllium and defects in the structure.

At the third stage (after the 3rd pass), the grains become finer, reaching submicron size, and the structure shows signs of recrystallization. Similar changes are described in the works devoted to copper and its alloys, where the third pass of ECAP promotes the creation of a highly ordered ultrafine — grained structure. For beryllium bronze BrB2, this means that the material acquires optimum properties for mechanical hardening and improved wear resistance.

After the 4th pass, the material structure is fully stabilized, the grains reach nanometer dimensions and defects and internal stresses are virtually absent. This confirms the fundamental theories of IPD, according to which an increase in the number of passes leads to the formation of a stable ultrafine-grained structure with high mechanical characteristics [6]. In addition, for beryllium bronze, improvements in properties such as fatigue limit and corrosion resistance can be expected at this stage, as has been observed for other copper-based alloys.



a — after 1 pass; *b* — after 2 passes; *c* — after 3 passes; *d* — after 4 passes

Figure 3. Microstructure of beryllium bronze BrB2 after ECAP

Thus, in comparison with literature data, the results of ECAP for beryllium bronze BrB2 confirm the general regularities characteristic of materials subjected to severe plastic deformation. The method allows to achieve a unique combination of mechanical and operational properties, making this alloy promising for use in critical structures.

The X-ray diffraction studies of beryllium bronze BrB2 in Figure 4 confirm the influence of ECAP on the evolution of its phase composition and defect structure. After the 1st pass, relatively broad and less intense diffraction peaks are observed, indicating the initial stage of grain refinement and an increase in defect density. This is consistent with literature data, where it is noted that the early stages of severe plastic deformation are accompanied by the formation of a large number of dislocations that begin to localize in the grain structure [11].

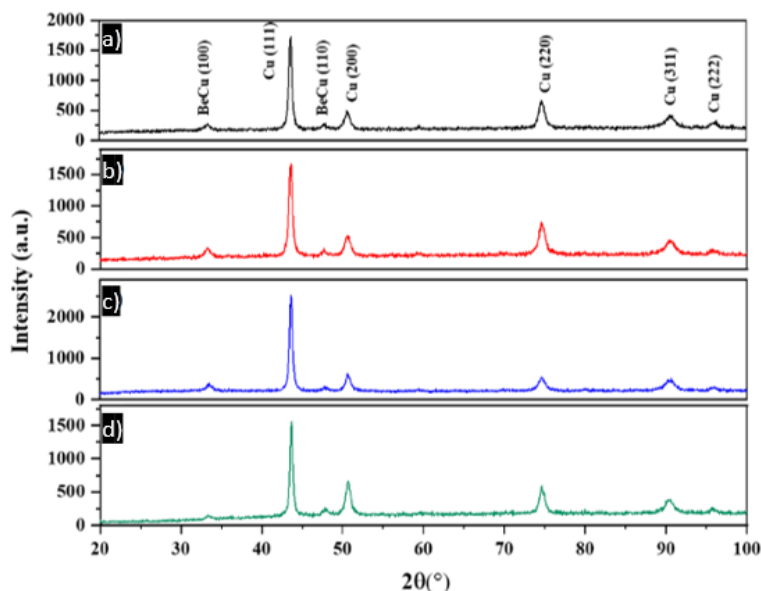
At the 2nd pass the peaks become sharper, indicating active redistribution of stresses in the material and further pulverization of the structure. The appearance of substructures with low-angle boundaries and the first signs of recrystallization allows the material to retain high hardness while maintaining plasticity [12]. Besides, it is confirmed by the change of lattice parameters of beryllium bronze, which can be related to the redistribution of beryllium atoms and local stabilization of the phase composition.

After the 3rd pass of ECAP, further ordering of the structure, peak intensity and reduction of line widths are observed. This indicates significant grain refinement and formation of high-angle grain boundaries characteristic of ultrafine-grained materials. Such changes in the structure are the basis for a significant improvement in the mechanical properties of the material, as noted for copper and aluminum based alloys in similar studies [13].

After the 4th pass, the structure stabilizes: the width of peaks on the X-ray image decreases and their intensity reaches the maximum value. This confirms the completion of recrystallization processes, redistribution of internal stresses and formation of a stable ultrafine-grained structure [14]. Similar results for other

alloys indicate that after 4-5 passes an optimum balance between mechanical properties such as hardness, strength and ductility is achieved [15].

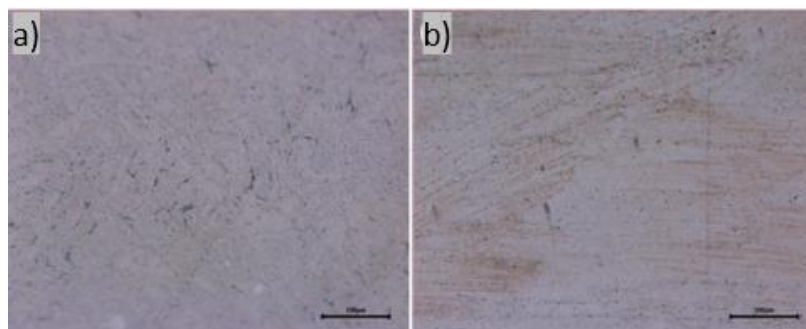
Comparison with literature data shows that BrB2 beryllium bronze exhibits similar trends as other metals subjected to IPD, with the presence of beryllium contributing to the formation of a unique stable structure that enhances the mechanical properties of the alloy. The data obtained during ECAP confirm the promising potential of this method for industrial hardening of beryllium bronze, which makes it suitable for use in critical structures where high strength, hardness and wear resistance are required.



a — after the 1st pass; *b* — after 2 passes; *c* — after 3 passes; *d* — after 4 passes

Figure 4. Radiographs of beryllium bronze BrB2 after ECAP

Figure 5 shows that thermal aging of beryllium bronze BrB2 at 320 °C for 2 hours was carried out on samples that underwent ECAP 1st (*a*) and 2nd (*b*) passes. Microstructural analysis has shown that after aging the sample (*a*), subjected to the 1st pass of ECAP, retains a relatively coarse-grained structure with minimal separations of secondary phases, which is associated with the initial stage of beryllium redistribution and a moderate degree of plastic deformation. Sample (*b*), treated with 2 passes of ECAP, shows more pronounced grain refinement and the presence of secondary phases formed as a result of thermal aging, which is associated with a higher degree of plastic deformation and accumulation of defects after the second pass. These structural changes confirm that thermal aging effectively eliminates defects, redistributes beryllium and improves mechanical properties, especially for samples with more intense pre-plastic deformation. This makes ECAP treatment followed by aging a promising method for increasing the hardness and strength of BrB2 beryllium bronze.



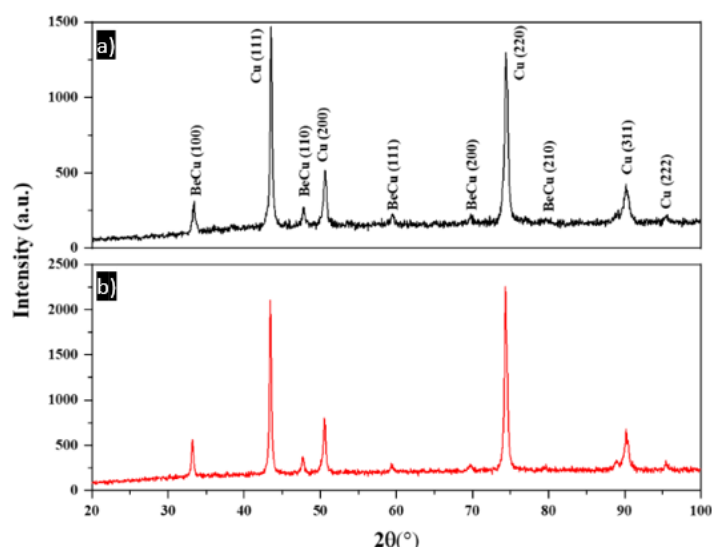
a — sample after 1 ECAP pass; *b* — sample after 2 ECAP passes

Figure 5. Microstructure of beryllium bronze BrB2 after ECAP and thermal aging at 320 °C for 2 hours

The diffractograms of the samples in Figure 6 show significant changes in the width and intensity of the peaks. In the sample after the 1st pass of ECAP (Fig. 6a), the peaks are characterized by moderate width and relatively low intensity, which indicates the presence of a high level of defects in the crystal lattice and the initial stages of beryllium redistribution. Thermal aging promotes the separation of secondary phases, but their fraction remains relatively low, which is confirmed by moderate changes in peak intensities.

The sample that underwent 2 passes of ECAP (Fig. 6b) shows a marked decrease in peak width and a significant increase in peak intensity after aging. This indicates active release of beryllium-rich secondary phases, as well as a significant decrease in the defectivity of the structure. The observed changes reflect the process of stabilization of the ultrafine-grained structure formed as a result of intense plastic deformation.

Thus, the results of XRD confirm that the increase in the number of passes of ECAP promotes more intensive grain refinement and accumulation of defects, which creates preconditions for the formation of hardening phases in the process of thermal aging. This leads to improvement of mechanical properties of beryllium bronze BrB2, including increase of hardness and strength. The most pronounced changes in phase composition and structure ordering are observed after 2 passes of RCMP with subsequent aging, which makes this treatment mode preferable for improving the performance characteristics of the material.



a — sample after the 1st ECAP pass; *b* — sample after 2 ECAP passes

Figure 6. X-ray phase analysis of beryllium bronze BrB2 after ECAP and thermal aging at 320 °C for 2 hours

In Figure 7, the samples numbered 1, 2 and 3 shows the results of hardness measurements before and after heat treatment. The initial hardness of the BrB2 sample is about 150 HV, which corresponds to the standard state of the material before heat treatment. In this state, the bronze has its initial structure, which has not gone through the over-quenching or aging process. After quenching (Fig. 7 No. 2) at 800 °C, a stable alpha phase with a beryllium-supersaturated structure is formed which exhibits higher hardness compared to the initial state. Hardening helps to strengthen the metal by increasing the density of its crystal lattice, which explains the increase in hardness. The diagram shows that the hardness of this sample is significantly increased (about 200 HV), which confirms the effect of hardening. Aging (Fig. 7 No. 3) at 320 °C improves mechanical properties, especially hardness, due to the separation of different phases from the material matrix. In the case of beryllium bronze, aging promotes the formation of small crystals that strengthen the structure, increasing hardness. Although aging takes place at a lower temperature, it also leads to an increase in hardness of about 200 HV, as can be seen in the diagram.

Thus, the increase in hardness after quenching and aging is explained by changes in the microstructure of the material, such as the formation of harder phases and the strengthening of bonds between atoms. Quenching at 800 °C increases hardness, while aging at 320 °C improves mechanical properties due to the formation of stable phases that strengthen the bronze structure.

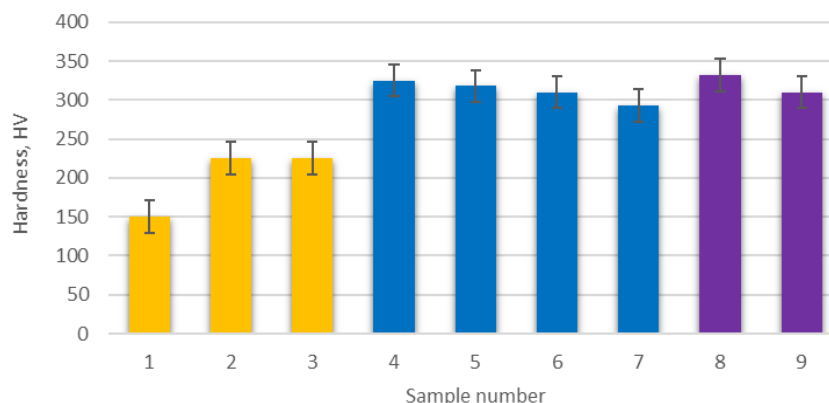


Figure 7. Results of hardness measurement of beryllium bronze BrB2

In Figure 7 from No. 4 to No. 7, the results of hardness measurement after ECAP are shown. The test results show that the hardness of specimen No. 4 is about 320 HV. This is the hardest specimen among the submitted specimens, indicating that the mechanical properties of the material were improved due to the higher number of passes during pressing. Each repeated exposure during the ECAP process improves the structure of the material, increasing its strength and hardness. The hardness of sample No. 5 is about 315 HV. There is a slight decrease in hardness here compared to sample No. 4, which may be due to fewer passes in the pressing process, which does not have the same effect of improving the structure as sample No. 4. The hardness of sample No. 6 is approximately 300 HV. The fewer passes during ECAP, the less pronounced is the improvement in the mechanical properties of the material. This sample has even lower hardness, which may indicate insufficient densification of the material structure. Sample No. 7 has a hardness of about 290 HV, which is the lowest value among the samples presented. The low number of passes during ECAP may not provide a significant improvement in mechanical properties, which is reflected in the lower hardness.

Graphs 8 and 9 in Figure 7 shows comparative data on hardness of two samples of beryllium bronze BrB2 after ECAP and thermal aging at 320 °C for 2 hours. No. 8 sample after 4 passes of ECAP and No. 9 sample after 3 passes of ECAP.

No. 8 specimen was subjected to ECAP with 4 passes and aging at 320 °C. Its hardness is about 330 HV, indicating improved mechanical properties after five passes of pressing as well as aging. This machining process creates a finer-grained structure of the material, which increases its strength and hardness. Sample No. 9 underwent ECAP with 3 passes and was also subjected to aging at 320 °C. Its hardness is lower than that of sample No. 8 and is about 315 HV. This confirms that the number of ECAP passes affects the mechanical properties, and a lower number of passes results in a lower hardness improvement.

Figure 8 shows the results of tribological tests of BrB2 beryllium bronze before and after heat treatment. Graph No. 1 of the sample shows that this sample has a coefficient of friction that varies up to 0.849, with a mean value of 0.734. This means that the source material has moderate friction, but with noticeable fluctuations. These fluctuations may be due to the microstructure of the material, which has not yet been subjected to heat treatments such as quenching or aging.

Graphing for sample No. 2, quenched at 800 °C, the coefficient of friction varies up to 0.936, with an average of 0.771. Quenching at high temperature increased the stability of the material, which is reflected in the slightly higher average friction coefficient value compared to the original sample. Hardening tends to make the material stiffer and stronger, which can lead to an increase in friction.

Graph No. 3 of a sample that underwent aging at 320 °C shows that the coefficient of friction varies up to 0.914, with an average value of 0.764. Aging at a lower temperature increases the hardness and wear resistance of the material, but the average friction coefficient is slightly lower than that of sample No. 2, which may indicate a different type of interaction between the materials during the friction process.

The coefficient of friction of No. 4 sample varies up to 0.855, with a mean value of 0.777 and a standard deviation of 0.031. This sample shows a stable coefficient of friction with noticeable fluctuations, which may be due to the improvement of its structure after five press passes.

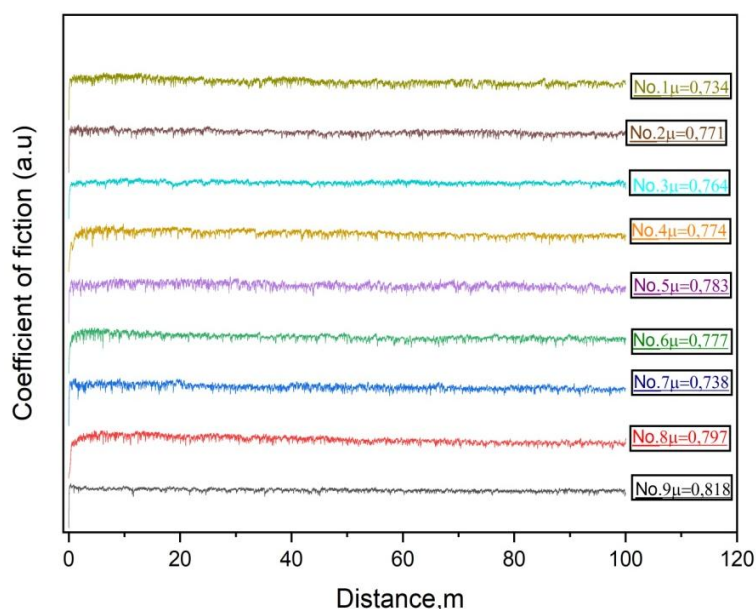
For sample No. 5, the coefficient of friction varies up to 0.896, with a mean of 0.778 and a standard deviation of 0.032. Sample No. 5 has similar values to sample No. 4, but slightly larger variations in the graph. This may indicate the improved mechanical properties associated with ECAP.

The coefficient of friction of sample No. 6 varies up to 0.828, with a mean value of 0.738 and a standard deviation of 0.032. This specimen also shows a stable coefficient of friction, but its value is slightly lower compared to specimens that have undergone more passes, which may indicate less improvement in mechanical properties.

The coefficient of friction for sample No. 7 ranges up to 0.852, with a mean value of 0.738 and a standard deviation of 0.032. This graph is similar to that of sample No. 6, with the same characteristics, indicating stable but not the highest mechanical properties.

The average value of the coefficient of friction for sample No. 8 is 0.797 ± 0.04 . This sample showed moderately high variation in the coefficient of friction, with a relatively stable average value. This confirms the improvement in mechanical properties after ECAP and aging, with the material remaining stable under friction.

For sample No. 9, the average value of coefficient of friction is 0.818 ± 0.053 . This sample exhibits a higher average value of coefficient of friction (0.818) than sample No. 8. The friction coefficient fluctuations also remain stable, with a slightly larger standard deviation [16].



No. 1 — initial state; No. 2 — after hardening; No. 3 — after aging

Figure 8. Results of tribological tests of beryllium bronze BrB2

Thus, ECAP with a higher number of passes (4 and 3) improves the wear resistance and co-friction resistance of the material.

Applications for this work include the manufacture of springs and spring-loaded parts for critical applications, wear-resistant components of various types, and non-sparking tools that are in demand in explosive and aggressive environments. Due to its unique properties, this material is used in electronics, mechanical engineering, aviation and other industries that require a combination of reliability, durability and specific functional characteristics.

Conclusion

The conducted study of the influence of thermomechanical treatment on the properties of beryllium bronze of domestic production allowed obtaining significant results demonstrating the possibilities of improving the mechanical and elastic characteristics of this material. Four main treatment modes were studied: aging, aging followed by plastic deformation, quenching, and quenching followed by plastic deformation. These treatments had a significant effect on the microstructure and mechanical properties of the bronze, including hardness.

Microstructure analysis showed that after thermomechanical treatment, significant changes are observed in the structure of the material: ordered phases are formed, which improve strength properties, and the grain size is reduced, which contributes to increased hardness and wear resistance. The Martens hardness study showed that the maximum hardness was achieved by hardening followed by plastic deformation (sample 4), where the increase was 42.7 % relative to the initial state. Similar trends were observed in Vickers hardness and indentation hardness measurements, where samples subjected to the combined treatment regimes showed the highest values.

Thus, the results of the study show that thermomechanical treatments, especially combined (thermal and subsequent plastic deformation), provide a significant improvement in the mechanical properties of beryllium bronze. These data can be used to optimize machining regimes in industries that require materials with high strength, wear resistance and durability. The obtained results also open perspectives for expansion of application areas of beryllium bronze in critical structures and units operating under conditions of increased mechanical and thermal loads.

Funding

This research has been funded by the Committee of Science of the Ministry of Science and Higher Education of the Republic of Kazakhstan (Grant No. BR24992854).

References

- 1 Zhang, Q., Huo, J.D., Lu, B., & Zhao, B.Y. (2014). Application of Dark Field Model of OM in Quantitative Detection of Strengthen Phase in Beryllium Bronze. *Advanced Materials Research*, 1082, 38–41. <https://doi.org/10.4028/www.scientific.net/AMR.1082.38>
- 2 Baraz, V.R., Estemirova, S.X., & Ishina, E.A. (2020). The Microstructural Peculiarities of Beryllium Bronze after Heat Treatment. *Materials Science Forum*, 989, 172–176. <https://doi.org/10.4028/www.scientific.net/MSF.989.172>
- 3 Saha, B., Nimbalkar, V., Sagar, D.B.A., Rao, M.S.K., & Deshmukh, V.P. (2017). Bronzes for Aerospace Applications. N.E. Prasad, R.J.H. Wanhill (Eds.). *Aerospace Materials and Material Technologies: Indian Institute of Metals Series*, 247–266. Singapore: Springer Singapore. https://link.springer.com/chapter/10.1007/978-981-10-3_11?error=cookies_not_supported&code=2d9d1879-ac4f-4805-bb95-492e5b4632ce
- 4 Lu, R., Han, J., Li, Z., Zhang, C., Liu, J., Liu, C., Lang, Z., & Ma, X. (2023). Study of the Mechanical Properties and Microstructure of Spiral Tubes and Actuators for Controlled Extension Fabricated with Beryllium Bronze Strips. *Materials*, 16(20), 6719. <https://doi.org/10.3390/ma16206719>
- 5 Zisel'man, V.L., Shatalov, R.L., & Aldunin, A.V. (2006). Developing efficient regimes of thermomechanical treatment for obtaining quality strip made of beryllium bronzes. *Metallurgist*, 50(1–2), 102–107. <https://link.springer.com/article/10.1007/s11015-006-0047-0>
- 6 Korshunov, L., Korznikov, A., & Chernenko, N.L. (2011). Effect of the severe plastic deformation and aging temperature on the strengthening, structure, and wear resistance of a beryllium bronze. *The Physics of Metals and Metallography*, 111, 395–402. <https://link.springer.com/article/10.1134/S0031918X10061018>
- 7 Duraev, P.P., Kaplun, Y.A., Pastukhova, Z., & Rakhshadt, A.G. (1985). Combined aging of beryllium bronze. *Metal Science and Heat Treatment*, 27, 634–635. <https://link.springer.com/article/10.1007/BF00699368>
- 8 Ping, D. (2003). Optimization of Deformation Aging Process of Beryllium Bronze. *Heat Treatment of Metals*, 2, 63–64.
- 9 Timofeeva, Z.A., & Zhermunskaia, L.B. (1965). Study of strength and elastic properties of microribbon made from BrB2 beryllium bronze. *Metal Science and Heat Treatment*, 7, 172–175. <https://link.springer.com/article/10.1007/BF00658527>
- 10 Kengesbekov, A.B., Rakhadilov, B.K., Zhurero, L.G., Uazyrkhanova, G.K., & Kambarov, Y.Y. (2022). Formation of TiN coatings by air plasma spraying. *Bulletin of the Karaganda University. "Physics" Series*, 08(4), 22–31.
- 11 Glezer, A.M., Sundeev, R.V., Shalimova, A.V., & Metlov, L.S. (2023). Physics of severe plastic deformation. *Uspekhi Fizicheskikh Nauk — Advances in Physical Sciences*, 193(1), 33–62.
- 12 Zhilyaev, A.P., & Langdon, T.G. (2008). Using high-pressure torsion for metal processing: Fundamentals and applications. *Progress in Materials science*, 53(6), 893–979. <https://doi.org/10.1016/j.pmatsci.2008.03.002>
- 13 Mazzer, E.M., Da Silva, M.R., & Gargarella, P. (2022). Revisiting Cu-based shape memory alloys: Recent developments and new perspectives. *Journal of Materials Research*, 37(1), 162–182. <https://link.springer.com/article/10.1557/s43578-021-00444-7>
- 14 Dyakonov, G., Mironov, S., Yakovleva, T., & Semenova, I. (2020). Thermal Stability and Recrystallization of Titanium Grade 4 with Ultrafine-Grained Structure. In *MATEC Web of Conferences*, 321, 11060. EDP Sciences. <https://doi.org/10.1051/mateconf/202032111060>
- 15 Shi, J., Hou, L., Zuo, J., Zhuang, L., & Zhang, J. (2017). Cryogenic rolling-enhanced mechanical properties and microstructural evolution of 5052 Al-Mg alloy. *Materials Science and Engineering*, A, 701, 274–284. <https://doi.org/10.1016/j.msea.2017.06.087>

16 Khasenov, A.K., Nussupbekov, B.R., Karabekova, D.Zh, Bulkaïrova, G.A., Shashubai, B.U., & Bolatbekova, M.M. (2022). Electric pulse method of processing cullet. *Bulletin of the Karaganda University. "Physics" Series, 1*, 75–80.

Б.К. Рахадиллов, А.Б. Кеңесбеков, Н.М. Магазов,
А.А. Кусайнов, Л.С. Каирбаева, Е.С. Молбосынов

Термомеханикалық өңдеулердің бериллий қоласының қасиеттеріне әсерін оның қолданылуын кеңейту мақсатында зерттеу

Мақала термомеханикалық өңдеулердің бериллий қоласының механикалық және физика-химиялық қасиеттерінің әсерін зерттеуге арналған, яғни қазіргі заманғы технологияларда қолдану аясын кеңейту мақсатында. Қатаю сияқты термомеханикалық өңдеудің әртүрлі әдістері егжей-тегжейлі қарастырылған. Бұл әдістердің қорытпаның микроқұрылымын өзгертуге әсер ету механизмі сипатталған, бұл оның жұмысына тікелей әсер етеді. Алынған нәтижелер бериллий қоласын өнеркәсіпте, авиақұрылыста және басқа да салаларда қолдану салаларын кеңейтуге мүмкіндік береді. Сонымен қатар, негізгі тұжырымдар термомеханикалық өңдеудің озық әдістерін енгізу қоланың физикалық өнімділігін арттыруға ғана емес, бұл материалды аэроғарыш және автомобиль өнеркәсібі сияқты жаңа салаларда қолдануға мүмкіндік беретіндігіне байланысты. Авторлар мақалада материалтану және машина жасау мамандары үшін өте маңызды, өйткені ол бериллий қола бұйымдарын өндіру және пайдалану процестерін жақсартатын жаңа деректер мен ұсыныстарды ұсынған.

Кілт сөздер: БрБ2 бериллий қоласы, термиялық өңдеу, механикалық өңдеу, термомеханикалық өңдеу, тозу, қатаю, материалдың микроқұрылымы, теңарналы бұрыштық престеу (ТАБП)

Б.К. Рахадиллов, А.Б. Кеңесбеков, Н.М. Магазов,
А.А. Кусайнов, Л.С. Каирбаева, Е.С. Молбосынов

Изучение влияния термомеханической обработки на свойства бериллиевой бронзы с целью расширения области ее применения

В статье исследовано влияние различных режимов термомеханической обработки на структуру и свойства бериллиевой бронзы. Описан механизм воздействия этих методов на модификацию микро-структуры сплава, что напрямую влияет на его эксплуатационные характеристики. Основные выводы сводятся к тому, что термомеханическая обработка повышает физические характеристики бронзы. В статье представлены новые данные и рекомендации, которые помогут улучшить процесс производства и эксплуатации изделий из бериллиевой бронзы, расширить области ее применения в промышленности, авиастроении и других отраслях.

Ключевые слова: бериллиевая бронза, термическая обработка, механическая обработка, термомеханическая обработка, старение, закалка, микроструктура материала, равноканальное угловое прессование (РКУП)

Information about the authors

Rakhadilov, Bauyrzhan— PhD, Associate Professor, Director “PlasmaScience” LLP, Ust-Kamenogorsk, Kazakhstan; e-mail: rakhadilovb@mail.ru; ORCID ID: <https://orcid.org/0000-0001-5990-7123>

Kengesbekov, Aidar (*corresponding author*) — Postdoctoral fellow, “PlasmaScience” LLP, Ust-Kamenogorsk, Kazakhstan; e-mail: aidar.94.01@mail.ru; ORCID ID: <https://orcid.org/0000-0002-5630-9467>

Magazov, Nurtoleu— Researcher of the Scientific Center “Protective and Functional Coatings”, Ust-Kamenogorsk, Kazakhstan; e-mail: magazovn@gmail.com; ORCID ID: <https://orcid.org/0000-0002-9941-9199>

Kussainov Arystanbek — Doctoral student, D. Serikbayev East Kazakhstan Technical University, Ust-Kamenogorsk, Kazakhstan; e-mail: arys20055@gmail.com; ORCID ID: <https://orcid.org/0000-0003-4623-4681>

Kairbaeva Limara — Student, D. Serikbayev East Kazakhstan Technical University, Ust-Kamenogorsk, Ust-Kamenogorsk, Kazakhstan; e-mail: limaralkairbaeva52@gmail.com; ORCID ID: <https://orcid.org/0009-0001-6091-1071>

Molbosynov Yermakhan — Student, D. Serikbayev East Kazakhstan Technical University, Ust-Kamenogorsk, Ust-Kamenogorsk, Kazakhstan; e-mail: molbossynov.ye@edu.ektu.kz; ORCID ID: <https://orcid.org/0009-0009-0578-6544>

S. Katsyv¹, V. Kukharchuk¹, V. Madyarov¹, V. Kucheruk^{2✉}, P. Kulakov², M. Hribov³

¹Vinnitsia National Technical University, Vinnitsia, Ukraine;

²Uman National University of Horticulture, Uman, Ukraine;

³National Academy of Internal Affairs, Kyiv, Ukraine

Non-standard analysis in electrical engineering. Ideal DC inductive circuits with infinitesimal parameters of different orders

The analysis of DC circuits with ideal inductive elements using standard methods of theoretical electrical engineering is too difficult or even impossible, because when using them, it is often necessary to reveal type $\frac{0}{0}$

uncertainties. In this regard, the article proposes to use not the usual mathematical analysis, but a non-standard one, in which the frequency of the direct current is taken not as zero, but as an infinitesimal number α . In this case, the reactances of the inductive elements will be equal to αL , and it becomes possible to apply all standard methods of theoretical electrical engineering. The article considers examples of the analysis of ideal DC inductive circuits, with particular attention paid to circuits whose calculation requires the use of infinitesimal numbers for inhomogeneous parameters. In such cases, the order of these numbers is determined based on individual considerations, and this is a non-standard task.

Keywords: infinitesimal number, infinitude, hyperreal number, unconventional number, ideal reactive element

✉ *Corresponding author:* V. Kucheruk, vladimir.kucheruk@gmail.com

Introduction

When solving various scientific and technical problems, it becomes necessary to reveal type $\frac{0}{0}$ uncertainties, but when using classical methods for this purpose, significant difficulties may arise. Therefore, in such cases, the use of ideas and methods of non-standard analysis is promising. Based on the ideas of non-standard analysis, which consist of and are based on the direct use of infinitesimal numbers, Leibniz and Newton created the foundations for the development of differential and integral calculus. In the scientific works of Cauchy and other scientists, infinitesimal numbers were not used; the mathematical apparatus of differential and integral calculus was created on the basis of numerical and functional sequences and limiting relations of quantities, which ensured its axiomatic rigor, but complicated the solution of a certain range of problems [1–5].

Non-standard analysis began to be widely used in the middle of the last century, when a new axiomatics of mathematical analysis was proposed. This axiomatics is based on the set of hyperreal numbers, which, in addition to standard (real) numbers, also contains non-standard numbers (infinitely small numbers, infinitely large numbers, and their combinations with standard numbers) [6, 7]. Methods of non-standard analysis have been actively developing since the end of the last century to the present and are used in various fields of science and technology [8, 9]. The use of non-standard analysis methods in the identification of internal parameters of electric motors, which in many cases cannot be solved by traditional methods, is promising [10–15]. The use of non-standard analysis allows for effective solutions to some problems in calculating electrical circuits [16–18].

Formulation of the problem

The calculation of DC electrical circuits is usually carried out using unified methods based on Ohm and Kirchhoff's laws. There are certain tasks in this field for which the direct use of unified methods is impossible. Such tasks include, for example, the calculation of DC circuits with ideal reactive elements. The complexity of calculations in such circuits is due to the fact that at constant current the resistance of an ideal inductance tends to zero, and the resistance of an ideal capacitance tends to infinity. Typically, to solve such

problems, energy characteristics of inductances and capacitances are used, which significantly complicates the calculation of these circuits, especially for complex circuits. Therefore, it is relevant to use the mathematical apparatus of non-standard analysis, which allows using unified methods for calculating such circuits.

The aim of the article is to identify a class of non-standard electrical engineering problems aimed at analyzing DC electrical circuits that include ideal inductances, and to extend non-standard analysis methods to problems of analyzing electrical circuits with ideal reactive elements. This article considers the non-standard analysis of ideal DC inductive circuits with infinitesimal parameters of different orders.

Research results

Let consider the foundations of the non-standard analysis axiomatics [3, 6, 16–18]. Let denote by R the ordered set of real numbers. The number α is called an infinitesimal number if and only if

$$\forall r \in R (\alpha < r). \quad (1)$$

With infinitesimal numbers, it is possible to perform all algebraic operations (addition, subtraction, multiplication, division, exponentiation, etc.) and apply all theorems (commutativity, associativity, etc.).

Infinitesimal numbers of various orders are used, namely: $\alpha > \alpha^2 > \alpha^3 > \alpha^k$ — infinitesimal numbers of the first, second, third, and k -th order. Together with the real numbers $r \in R$, the infinitesimal numbers form an ordered set of hyperreal numbers *R .

It is customary to call real numbers $r \in R$ standard or Archimedean numbers in contrast to non-standard (non-Archimedean) numbers ${}^*r \in {}^*R$. Every non-standard number contains a standard part

$${}^*r = r \pm \alpha, \quad (2)$$

that is,

$$r = st({}^*r). \quad (3)$$

Thus, an ordinary real number is a standard part of some non-standard number. It is obvious that there can be an infinite number of such numbers. Two standard numbers a and b are equal if and only if

$$a - b = 0. \quad (4)$$

Two non-standard numbers *a and *b are called equivalent, or infinitely close to each other, if and only if

$${}^*a - {}^*b \approx \alpha. \quad (5)$$

The sign \approx means the equivalence of two non-standard numbers.

For standard numbers m and n , let write the following relations that follow from (1–5):

$$\frac{m\alpha}{n\alpha} = \frac{m}{n}, \frac{m\alpha}{n} = \frac{m}{n}\alpha, m\alpha + n \approx n, m\alpha^k + n \approx n, \sin \alpha \approx \alpha, \cos \alpha \approx 1. \quad (6)$$

Let consider several examples of the use of non-standard numbers in mathematical analysis, namely, that is let determine the derivatives of some functions using non-standard analysis methods. For all the following examples of determining the derivatives of mathematical functions, let introduce the substitution $dx = \alpha$.

Let define the derivative of the function $y = x^n$.

$$\begin{aligned} \frac{dy}{dx} &= \frac{(x + \alpha)^n - x^n}{\alpha} = \frac{x^n + \frac{n!}{1!(n-1)!}x^{n-1}\alpha + \frac{n!}{2!(n-2)!}x^{n-2}\alpha^2 + \dots}{\alpha} \\ &= \frac{x^n + \frac{n!}{2!(n-2)!}x^2\alpha^{n-2} + \frac{n!}{1!(n-1)!}x\alpha^{n-1} + \alpha^n - x^n}{\alpha} = \frac{n!}{1!(n-1)!}x^{n-1} + \frac{n!}{2!(n-2)!}x^{n-2}\alpha + \dots \\ &\dots + \frac{n!}{2!(n-2)!}x^2\alpha^{n-3} + \frac{n!}{1!(n-1)!}x\alpha^{n-2} + \alpha^{n-1} \approx nx^{n-1}. \end{aligned} \quad (7)$$

Let define the derivative of the function $y = \frac{1}{x^n}$.

$$\begin{aligned}
\frac{dy}{dx} &= \frac{\frac{1}{(x+\alpha)^n} - \frac{1}{x^n}}{\alpha} = \frac{\frac{1}{x^n + \frac{n!}{1!(n-1)!}x^{n-1}\alpha + \dots + \frac{n!}{1!(n-1)!}x\alpha^{n-1} + \alpha^n} - \frac{1}{x^n}}{\alpha} = \\
&= \frac{x^n - x^n - \frac{n!}{1!(n-1)!}x^{n-1}\alpha - \dots - \frac{n!}{1!(n-1)!}x\alpha^{n-1} - \alpha^n}{\alpha \left(x^{2n} + \frac{n!}{1!(n-1)!}x^{2n-1}\alpha + \dots + \frac{n!}{1!(n-1)!}x^{n+1}\alpha^{n-1} + x^n\alpha^n \right)} = \\
&= \frac{-\frac{n!}{1!(n-1)!}x^{n-1} - \dots - \frac{n!}{1!(n-1)!}x\alpha^{n-2} - \alpha^{n-1}}{x^{2n} + \frac{n!}{1!(n-1)!}x^{2n-1}\alpha + \dots + \frac{n!}{1!(n-1)!}x^{n+1}\alpha^{n-1} + x^n\alpha^n} \approx \frac{-\frac{n!}{1!(n-1)!}x^{n-1}}{x^{2n}} = -\frac{n}{x^{n+1}}.
\end{aligned} \quad (8)$$

Let define the derivative of the function $y = \sqrt{x}$.

$$\frac{dy}{dx} = \frac{\sqrt{x+\alpha} - \sqrt{x}}{\alpha} = \frac{(\sqrt{x+\alpha} - \sqrt{x})(\sqrt{x+\alpha} + \sqrt{x})}{\alpha(\sqrt{x+\alpha} + \sqrt{x})} = \frac{x+\alpha-x}{\alpha(\sqrt{x+\alpha} + \sqrt{x})} = \frac{1}{(\sqrt{x+\alpha} + \sqrt{x})} \approx \frac{1}{2\sqrt{x}}. \quad (9)$$

Let define the derivative of the function $y = \operatorname{tg} x$.

$$\begin{aligned}
\frac{dy}{dx} &= \frac{\frac{\sin(x+\alpha)}{\cos(x+\alpha)} - \frac{\sin x}{\cos x}}{\alpha} = \frac{\frac{\sin x \cos \alpha + \sin \alpha \cos x}{\cos x \cos \alpha - \sin x \sin \alpha} - \frac{\sin x}{\cos x}}{\alpha} = \\
&= \frac{\cos x \sin x \cos \alpha + \sin \alpha \cos^2 x - \sin x \cos x \cos \alpha + \sin^2 x \sin \alpha}{\alpha \cos^2 x \cos \alpha - \alpha \cos x \sin x \sin \alpha} \approx \\
&\approx \frac{\alpha(\cos^2 x + \sin^2 x)}{\alpha \cos^2 x - \alpha^2 \cos x \cdot \sin x} \approx \frac{\cos^2 x + \sin^2 x}{\cos^2 x - \alpha \cos x \cdot \sin x} \approx \frac{1}{\cos^2 x}.
\end{aligned} \quad (10)$$

Let define the derivative of the function $y = \operatorname{ctg} x$.

$$\begin{aligned}
\frac{dy}{dx} &= \frac{\frac{\cos(x+\alpha)}{\sin(x+\alpha)} - \frac{\cos x}{\sin x}}{\alpha} = \frac{\frac{\cos x \cos \alpha - \sin x \sin \alpha}{\sin x \cos \alpha + \sin \alpha \cos x} - \frac{\cos x}{\sin x}}{\alpha} = \\
&= \frac{\sin x \cos x \cos \alpha - \sin^2 x \sin \alpha - \cos x \sin x \cos \alpha - \sin \alpha \cos^2 x}{\alpha \sin^2 x \cos \alpha + \alpha \sin \alpha \cos x \sin x} \approx \\
&\approx \frac{-\alpha(\sin^2 x + \cos^2 x)}{\alpha \sin^2 x + \alpha^2 \cos x \sin x} \approx \frac{-(\sin^2 x + \cos^2 x)}{\sin^2 x + \alpha \cos x \sin x} \approx \frac{-1}{\sin^2 x}.
\end{aligned} \quad (11)$$

Let define the derivative of the function $y = \sec x$. Because $\sec x = \frac{1}{\cos x}$, that

$$\begin{aligned}
\frac{dy}{dx} &= \frac{\frac{1}{\cos(x+\alpha)} - \frac{1}{\cos x}}{\alpha} = \frac{\frac{1}{\cos x \cos \alpha - \sin x \sin \alpha} - \frac{1}{\cos x}}{\alpha} = \\
&= \frac{\cos x - \cos x \cos \alpha + \sin x \sin \alpha}{\alpha \cos^2 x \cos \alpha - \alpha \cos x \sin x \sin \alpha} \approx \frac{\alpha \sin x}{\alpha \cos^2 x - \alpha^2 \cos x \sin x} \approx \frac{\sin x}{\cos^2 x - \alpha \cos x \cdot \sin x} \approx \frac{\sin x}{\cos^2 x}.
\end{aligned} \quad (12)$$

Let define the derivative of the function $y = \operatorname{cosec}(x)$. Because $\operatorname{cosec}(x) = \frac{1}{\sin x}$, that

$$\begin{aligned} \frac{dy}{dx} &= \frac{\frac{1}{\sin(x+\alpha)} - \frac{1}{\sin x}}{\alpha} = \frac{\frac{1}{\sin x \cos \alpha + \sin \alpha \cos x} - \frac{1}{\sin x}}{\alpha} = \\ &= \frac{\sin x - \sin x \cos \alpha - \sin \alpha \cos x}{\alpha \sin^2 x \cos \alpha + \alpha \sin \alpha \cos x \sin x} \approx \frac{-\alpha \cos x}{\alpha \sin^2 x + \alpha^2 \cos x \sin x} \approx -\frac{\cos x}{\sin^2 x}. \end{aligned} \quad (13)$$

Let define the derivative of the function $y = e^x$. Because $e = \lim_{n \rightarrow \infty} \left(1 + \frac{1}{n}\right)^n$, then within the framework of non-standard analysis we can write $e \approx (1 + \alpha)^{\frac{1}{\alpha}}$, $e^x \approx (1 + \alpha)^{\frac{x}{\alpha}}$.

$$\begin{aligned} \frac{dy}{dx} &\approx \frac{(1 + \alpha)^{\frac{x+\alpha}{\alpha}} - (1 + \alpha)^{\frac{x}{\alpha}}}{\alpha} = \frac{(1 + \alpha)^{\frac{x}{\alpha}} (1 + \alpha)^{\frac{\alpha}{\alpha}} - (1 + \alpha)^{\frac{x}{\alpha}}}{\alpha} = \frac{(1 + \alpha)^{\frac{x}{\alpha}} (1 + \alpha)^{\frac{\alpha}{\alpha}} - (1 + \alpha)^{\frac{x}{\alpha}}}{\alpha} = \\ &= \frac{(1 + \alpha)^{\frac{x}{\alpha}} \left[(1 + \alpha)^{\frac{\alpha}{\alpha}} - 1 \right]}{\alpha} = \frac{(1 + \alpha)^{\frac{x}{\alpha}} [1 + \alpha - 1]}{\alpha} = (1 + \alpha)^{\frac{x}{\alpha}} \approx e^x. \end{aligned} \quad (14)$$

Not only the set of real numbers, but also the set of complex numbers can have the same structure. Based on this, taking into account (6), we can write:

$$m\alpha + jn \approx jn, m + jn\alpha \approx m. \quad (15)$$

Next, we will consider how non-standard analysis methods can be used to analyze DC circuits with ideal inductive elements. Before proceeding to the application of the above expressions to solve applied problems, it should be noted that there are no general rules for choosing a parameter that should be equated to an infinitely small or infinitely large number. This choice is made by the researcher depending on the context of the specific task. It should be noted that in the case of the need to replace several heterogeneous parameters in one problem with infinitesimal numbers, determining the relationships between these numbers is in most cases very difficult and sometimes requires additional research.

Next, let consider examples of solving problems using inhomogeneous infinitesimal parameters. Since a DC circuit can be considered as a sinusoidal AC circuit, with an alternating current of zero frequency, the symbolic method can be used to solve such problems, provided that $\omega = \alpha$. Taking $\omega = \alpha$, for the complex resistance of the inductance we can write

$$\underline{Z}_L \approx j\alpha L. \quad (16)$$

Consider the first example, in a DC circuit (Fig. 1), the task is to determine the currents in all branches of the circuit.

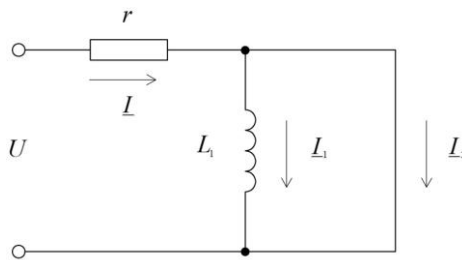


Figure 1. Circuit with shorted ideal inductance

In the circuit shown in Fig. 1, the inductance L_1 is short-circuited. The question arises as to how best to represent a branch that is switched on in parallel with L_1 . If this branch is represented as an ideal resistor R with zero resistance, then two different infinitesimal numbers $\omega \approx \alpha_1$ and $R \approx \alpha_2$ will appear simultaneously in the problem. At the same time, the ratio between α_1 and α_2 is unknown to us, and it is difficult to even estimate this ratio. Therefore, it is appropriate to represent this branch as an ideal inductance \underline{Z}_2 , in which $L_2 \approx \alpha_2$. In this case, the total complex resistance of this branch can be written as

$$\underline{Z} \approx j\alpha_1\alpha_2. \quad (17)$$

The product of two infinitesimal numbers is an infinitesimal number of higher order than each of the factors, so one of the inequalities holds

$$j\alpha_1\alpha_2 \leq jm\alpha_1^2, \quad (18)$$

or

$$j\alpha_1\alpha_2 \leq jm\alpha_2^2. \quad (19)$$

Let's solve the problem for the first inequality (obviously, the result will be similar for the second). The total complex resistance of the circuit is given by the expression

$$\underline{Z}_{ex} \approx r + \frac{(j\alpha_1 L_1)(jm\alpha_1^2)}{j\alpha_1 L_1 + jm\alpha_1^2} = r + \frac{j^2 m \alpha_1^3 L_1}{j\alpha_1 (L_1 + m\alpha_1)} = r + jm\alpha_1^2 \frac{L_1}{(L_1 + m\alpha_1)}, \quad (20)$$

and according to (15)

$$\underline{Z}_{ex} \approx r. \quad (21)$$

Hence $\underline{I} = \frac{U}{r}$, and the voltage on the parallel branches is

$$\underline{U}_L = jm\alpha_1^2 \frac{L_1}{(L_1 + m\alpha_1)} \underline{I} = \frac{U}{r} jm\alpha_1^2 \frac{L_1}{(L_1 + m\alpha_1)}, \quad (22)$$

and after transformations, we get

$$\underline{U}_L = \frac{U}{r} jm\alpha_1^2 \frac{L_1}{(L_1 + m\alpha_1)} \approx \frac{U}{r} jm\alpha_1^2 \frac{L_1}{L_1} = \frac{U}{r} jm\alpha_1^2. \quad (23)$$

Then the current in the branch with inductance is determined by the expression

$$\underline{I}_1 = \frac{\underline{U}_L}{j\alpha_1 L_1} = \frac{U}{r} \frac{jm\alpha_1^2}{j\alpha_1 L_1} = \frac{U}{r} \frac{m}{L_1} \alpha_1 \approx 0, \quad (24)$$

and in the parallel branch

$$\underline{I}_2 = \frac{\underline{U}_L}{jm\alpha_1^2} = \frac{U}{r} \frac{jm\alpha_1^2}{jm\alpha_1^2} = \frac{U}{r}. \quad (25)$$

More interesting is the case when, in a circuit with ideal inductances, the active resistances of the coils are infinitesimal numbers of different orders. Consider the second example, the DC circuit, which is shown on the Figure 2.

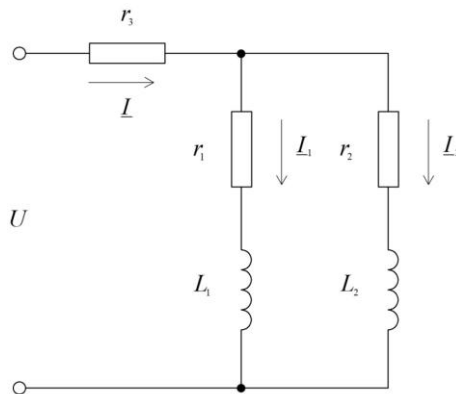


Figure 2. Circuit with ideal inductances in which the active resistances of the coils are infinitesimal numbers of different orders

The electric circuit shown in Figure 2 will be considered a circuit with ideal inductances if the resistances r_1, r_2 are infinitely small numbers, i.e. $r_1 \approx \alpha_1, r_2 \approx \alpha_2$. This problem, it is necessary to consider three different infinitesimal numbers $\omega \approx \alpha, r_1 \approx \alpha_1, r_2 \approx \alpha_2$, the order ratio of which is unknown in advance.

Let consider possible variants of the relations between these different infinitesimal numbers. In this case, it makes sense to assume that the resistances r_1, r_2 , are infinitesimal numbers of the same order. There are a total of three subsequent variants of the above relationships.

Variant 1. The order of the direct current frequency ω is equal to the order of the resistances r_1, r_2 , i.e.

$$\alpha \approx \alpha_1 \approx \alpha_2. \quad (26)$$

Variant 2. The order of the direct current frequency ω is greater than the order of the resistances r_1, r_2 , i.e.

$$\alpha < (\alpha_1 \approx \alpha_2). \quad (27)$$

Variant 3. The order of the direct current frequency ω is less than the order of the resistances r_1, r_2 , i.e.

$$\alpha > (\alpha_1 \approx \alpha_2). \quad (28)$$

Let determine the currents in the branches of the circuit for each of the above variants. Let consider the first variant. In general form, we can write

$$\alpha_1 \approx m\alpha, \alpha_2 \approx n\alpha, \quad (29)$$

where m, n — arbitrary standard numbers (in particular 1).

Then for the impedances of the circuit branches (Fig. 2) we can write

$$\underline{Z}_1 = r_1 + j\omega L_1 = \alpha_1 + j\alpha L_1 = m\alpha + j\alpha L_1 = \alpha(m + jL_1), \quad (30)$$

$$\underline{Z}_2 = r_2 + j\omega L_2 = \alpha_2 + j\alpha L_2 = n\alpha + j\alpha L_2 = \alpha(n + jL_2), \quad (31)$$

$$\underline{Z}_3 = r_3. \quad (32)$$

The impedance of the entire circuit (Fig. 2) is given by the expression

$$\underline{Z}_{ex} = \underline{Z}_3 + \frac{\underline{Z}_1 \underline{Z}_2}{\underline{Z}_1 + \underline{Z}_2} = r_3 + \frac{\alpha(m + jL_1)\alpha(n + jL_2)}{\alpha(m + jL_1) + \alpha(n + jL_2)} = r_3 + \frac{\alpha(m + jL_1)(n + jL_2)}{m + n + j(L_1 + L_2)} \approx r_3. \quad (33)$$

Hence $\underline{I} = \frac{U}{r_3}$, and the voltage on the parallel branches \underline{Z}_1 and \underline{Z}_2

$$\underline{U}_Z = \underline{I} \frac{\alpha(m + jL_1)(n + jL_2)}{m + n + j(L_1 + L_2)} = \frac{U}{r} \frac{\alpha(m + jL_1)(n + jL_2)}{m + n + j(L_1 + L_2)}, \quad (34)$$

and the currents in the branches

$$\underline{I}_1 = \frac{\underline{U}_Z}{\underline{Z}_1} = \frac{\frac{U}{r} \frac{\alpha(m + jL_1)(n + jL_2)}{m + n + j(L_1 + L_2)}}{\alpha(m + jL_1)} = \frac{U(n + jL_2)}{r[m + n + j(L_1 + L_2)]}, \quad (35)$$

$$\underline{I}_2 = \frac{\underline{U}_Z}{\underline{Z}_2} = \frac{\frac{U}{r} \frac{\alpha(m + jL_1)(n + jL_2)}{m + n + j(L_1 + L_2)}}{\alpha(n + jL_2)} = \frac{U(m + jL_1)}{r[m + n + j(L_1 + L_2)]}. \quad (36)$$

As follows from expressions (35) and (36), in the first variant, despite the constant voltage, the currents in the inductances are complex quantities.

Let consider the second variant. In general form, we can write

$$\alpha \approx m\alpha_1^k, \alpha_2 \approx n\alpha_1, \quad (37)$$

where m, n — arbitrary standard numbers (in particular 1).

Then for the impedances of the circuit branches (Fig. 2), we can write

$$\underline{Z}_1 = r_1 + j\omega L_1 = \alpha_1 + j\alpha L_1 = \alpha_1 + jm\alpha_1^k L_1, \quad (38)$$

$$\underline{Z}_2 = r_2 + j\omega L_2 = \alpha_2 + j\alpha L_2 = n\alpha_1 + jm\alpha_1^k L_2, \quad (39)$$

$$\underline{Z}_3 = r_3. \quad (40)$$

The impedance of the entire circuit (Fig. 2) is given by the expression

$$\begin{aligned} \underline{Z}_{\text{ex}} &= \underline{Z}_3 + \frac{\underline{Z}_1 \underline{Z}_2}{\underline{Z}_1 + \underline{Z}_2} = r_3 + \frac{(\alpha_1 + jm\alpha_1^k L_1)(n\alpha_1 + jm\alpha_1^k L_2)}{\alpha_1 + jm\alpha_1^k L_1 + n\alpha_1 + jm\alpha_1^k L_2} = r_3 + \frac{(\alpha_1 + jm\alpha_1^k L_1)(n + jm\alpha_1^{k-1} L_2)}{1 + jm\alpha_1^{k-1} L_1 + n + jm\alpha_1^{k-1} L_2} = \\ &= r_3 + \frac{(\alpha_1 + jm\alpha_1^k L_1)(n + jm\alpha_1^{k-1} L_2)}{n + 1 + jm\alpha_1^{k-1} (L_1 + L_2)} \approx r_3. \end{aligned} \quad (41)$$

Hence $\underline{I} = \frac{U}{r_3}$, and the voltage on the parallel branches \underline{Z}_1 and \underline{Z}_2

$$\underline{U}_Z = \underline{I} \frac{(\alpha_1 + jm\alpha_1^k L_1)(n + jm\alpha_1^{k-1} L_2)}{n + 1 + jm\alpha_1^{k-1} (L_1 + L_2)} = \frac{U}{r} \frac{(\alpha_1 + jm\alpha_1^k L_1)(n + jm\alpha_1^{k-1} L_2)}{n + 1 + jm\alpha_1^{k-1} (L_1 + L_2)}, \quad (42)$$

and the currents in the branches

$$\underline{I}_1 = \frac{\underline{U}_Z}{\underline{Z}_1} = \frac{\frac{U}{r} \frac{(\alpha_1 + jm\alpha_1^k L_1)(n + jm\alpha_1^{k-1} L_2)}{n + 1 + jm\alpha_1^{k-1} (L_1 + L_2)}}{(\alpha_1 + jm\alpha_1^k L_1)} = \frac{U(n + jm\alpha_1^{k-1} L_2)}{r[n + 1 + jm\alpha_1^{k-1} (L_1 + L_2)]} \approx \frac{Un}{r(n + 1)}, \quad (43)$$

$$\underline{I}_2 = \frac{\underline{U}_Z}{\underline{Z}_2} = \frac{\frac{U}{r} \frac{(\alpha_1 + jm\alpha_1^k L_1)(n + jm\alpha_1^{k-1} L_2)}{n + 1 + jm\alpha_1^{k-1} (L_1 + L_2)}}{n\alpha_1 + jm\alpha_1^k L_2} = \frac{U}{r} \frac{(1 + jm\alpha_1^{k-1} L_1)}{n + 1 + jm\alpha_1^{k-1} (L_1 + L_2)} \approx \frac{U}{r(n + 1)}. \quad (44)$$

As follows from expressions (43) and (44), in the second variant, the currents in the inductances do not depend on the values of the inductances themselves.

Let consider the third variant. In general form, we can write

$$\alpha_1 \approx m\alpha^k, \quad \alpha_2 \approx n\alpha^k, \quad (45)$$

where m, n — arbitrary standard numbers (in particular 1).

Then for the impedances of the circuit branches (Fig. 2) we can write

$$\underline{Z}_1 = r_1 + j\omega L_1 = \alpha_1 + j\alpha L_1 = m\alpha^k + j\alpha L_1 = \alpha(m\alpha^{k-1} + jL_1), \quad (46)$$

$$\underline{Z}_2 = r_2 + j\omega L_2 = \alpha_2 + j\alpha L_2 = n\alpha^k + j\alpha L_2 = \alpha(n\alpha^{k-1} + jL_2), \quad (47)$$

$$\underline{Z}_3 = r_3. \quad (48)$$

The impedance of the entire circuit (Fig. 2) is given by the expression

$$\underline{Z}_{\text{ex}} = \underline{Z}_3 + \frac{\underline{Z}_1 \underline{Z}_2}{\underline{Z}_1 + \underline{Z}_2} = r_3 + \frac{\alpha(m\alpha^{k-1} + jL_1)\alpha(n\alpha^{k-1} + jL_2)}{\alpha(m\alpha^{k-1} + jL_1) + \alpha(n\alpha^{k-1} + jL_2)} = r_3 + \frac{\alpha(m\alpha^{k-1} + jL_1)(n\alpha^{k-1} + jL_2)}{(m + n)\alpha^{k-1} + j(L_1 + L_2)} \approx r_3. \quad (49)$$

Hence $\underline{I} = \frac{U}{r_3}$, and the voltage on the parallel branches \underline{Z}_1 and \underline{Z}_2

$$\underline{U}_Z = \underline{I} \frac{\alpha(m\alpha^{k-1} + jL_1)(n\alpha^{k-1} + jL_2)}{(m + n)\alpha^{k-1} + j(L_1 + L_2)} = \frac{U}{r} \frac{\alpha(m\alpha^{k-1} + jL_1)(n\alpha^{k-1} + jL_2)}{(m + n)\alpha^{k-1} + j(L_1 + L_2)}, \quad (50)$$

and the currents in the branches

$$I_1 = \frac{U_Z}{Z_1} = \frac{U \frac{\alpha(m\alpha^{k-1} + jL_1)(n\alpha^{k-1} + jL_2)}{(m+n)\alpha^{k-1} + j(L_1 + L_2)}}{\alpha(m\alpha^{k-1} + jL_1)} = \frac{U(n\alpha^{k-1} + jL_2)}{r[(m+n)\alpha^{k-1} + j(L_1 + L_2)]} \approx \frac{UL_2}{r(L_1 + L_2)}, \quad (51)$$

$$I_2 = \frac{U_Z}{Z_2} = \frac{U \frac{\alpha(m\alpha^{k-1} + jL_1)(n\alpha^{k-1} + jL_2)}{(m+n)\alpha^{k-1} + j(L_1 + L_2)}}{\alpha(n\alpha^{k-1} + jL_2)} = \frac{U(m\alpha^{k-1} + jL_1)}{r[(m+n)\alpha^{k-1} + j(L_1 + L_2)]} \approx \frac{UL_1}{r(L_1 + L_2)}. \quad (52)$$

As follows from expressions (43) and (44), in the third variant, the currents in the inductances depend only on the values of the inductances themselves. It is this variant that conceptually corresponds to the applied problems of the theory of electrical circuits.

Conclusions

1. The authors first identified the class of non-standard electrical engineering problems aimed at the analysis of DC electrical circuits that include ideal inductances. It has been proven that solving a selected class of problems using standard methods of theoretical electrical engineering is very difficult, or sometimes impossible.

2. In order to solve the identified problems, it is proposed to use non-standard analysis methods for analyzing DC electric circuits with ideal inductances. The advantages of implementing such an approach are confirmed by examples of calculations of electrical circuits with inductances and inhomogeneous infinitesimal parameters.

3. To expand the scope of use of non-standard analysis methods, it is recommended to outline similar tasks in those branches of science and technology in which limit transitions and differential calculus are used, and in which the solution of the corresponding tasks by standard methods is significantly limited or impossible.

References

- 1 Sanchez-Ortiz, Jorge, Omar, U. Lopez-Cresencio, Francisco, J. Ariza-Hernandez, & Martin, P. (2021). Cauchy Problem for a Stochastic Fractional Differential Equation with Caputo-Itô Derivative. *Mathematics*, 9, 1–10.
- 2 Vedmitskiy, Y.G., Kukharchuk, V.V., Hraniak, V.F., Vishtak, I.V., Kacejko, P., & Abenov, A. (2018). Newton binomial in the generalized Cauchy problem as exemplified by electrical systems. *Proc. SPIE 10808, Photonics Applications in Astronomy, Communications, Industry, and High Energy Physics Experiments*, 108082M.
- 3 Donaldson, J.A. (1977). The abstract Cauchy problem. *Journal of Differential Equations*, 25, 3, 400–409.
- 4 De Laubenfels, R. (1991). Entire solutions of the abstract Cauchy problem. *Semigroup Forum*, 42, 83–105.
- 5 Zhen, Wang, & Ding, Xiaqi. (1997). Uniqueness of generalized solution for the Cauchy problem of transportation equations. *Acta Mathematica Scientia*, 17(3), 341–352.
- 6 Robinson, A. (1996). *Non-Standard Analysis*. Princeton: Princeton University Press, 308 p.
- 7 Jensen, A. (1972). A computer oriented approach to “nonstandard analysis”. *Studies in Logic and the Foundations of Mathematics*, 69, 281–289.
- 8 Bell, J. (1998). *A Primer of Infinitesimal Analysis*. Cambridge University Press, 140 p.
- 9 Lutz, R., & Goze, M. (1981). *Nonstandard Analysis. A Practical Guide with Applications*. Berlin: Springer-Verlag, 261 p.
- 10 Aree, P. (2016). Analytical approach to determine speed-torque curve of induction motor from manufacturer data. *Procedia Computer Science*, 86, 293–296.
- 11 IEEE Standard Test Procedure for Polyphase Induction Motors and Generators. IEEE Std 112–2004 from 12th May 2004 (Revision of IEEE Std 112–1996). New York: American National Standard Institute.
- 12 Kojooan-Jafari, H., Monjo, L., Corcoles, F., Pedra, J. (2014). Parameter Estimation of Wound-Rotor Induction Motors from Transient Measurements. *IEEE Transactions on Energy Conversion*, 29, 300–308.
- 13 Kucheruk, V.Yu., Kurytnik, I.P., Oshanov, Ye.Z., Kulakov, P.I., Semenov, A.A., Karabekova, D.Zh., & Khassenov, A.K. (2019). Computer-measuring system of the induction motor’s dynamical torque-speed characteristics. *Bulletin of the University of Karaganda – Physics*, 2(94), 92–100.
- 14 Pfingsten, G., & Hameyer, K. (2017). Highly efficient approach to the simulation of variable-speed induction motor drives. *Science Measurement & Technology IET*, 11, 793–801.

- 15 Volodymyr, A. Podzharenko, & Pavlo, I. Kulakov "Photoelectric angle converter", Proc. SPIE 4425, Selected Papers from the International Conference on Optoelectronic Information Technologies, (12 June 2001). <https://doi.org/10.1117/12.429768>
- 16 Katsyv, S., Kukharchuk, V., Madyarov, V., Holodiuk, V., Kucheruk, V., Kulakov, P., & Hribov, M. (2022). Non-standard analysis in electrical engineering. Transient analysis in second-order electrical circuits with violation of switching laws. *Bulletin of the University of Karaganda – Physics*, 4, 56–64.
- 17 Katsyv, S., Kukharchuk, V., Kucheruk, V., Kulakov, P., & Gribov, M. (2023). Nonstandard analysis in electrical engineering. The analysis of the direct current circles with ideal reactive elements. *Bulletin of the University of Karaganda – Physics*, 1(109), 31–39.
- 18 Kukharchuk, V.V., Pavlov, S.V., Katsyv, S.Sh., Koval, A.M., Holodiuk, V.S., Lysyi, M.V., Kotyra, A., Mamyrbaev, O., & Kalabayeva, A. (2021). Transient analysis in 1st order electrical circuits in violation of commutation laws. *Przegląd Elektrotechniczny*, 9, 26–30.

С. Кацыв, В. Кухарчук, В. Мадьяров, В. Кучерук, П. Кулаков, М. Грибов

Электртехникадағы стандартты емес талдау. Әр түрлі ретті шексіз кіші параметрлері бар тұрақты токтың идеалды индуктивті тізбектері

Теориялық электртехниканың стандартты әдістерін қолдана отырып, идеалды индуктивті элементтері бар тұрақты ток DC тізбектерін талдау өте күрделі немесе тіпті мүмкін емес болуы мүмкін, өйткені оларды пайдалану кезінде көбінесе $\frac{0}{0}$ типтік белгісіздіктерді анықтау қажет. Осыған байланысты мақалада тұрақты ток жиілігі нөлге тең емес, α шексіз аз сан ретінде қабылданатын стандартты емес талдауды қолдану ұсынылған. Бұл жағдайда индуктивті элементтердің реактивтері αL тең болады және теориялық электртехниканың барлық стандартты әдістерін қолдануға болады. Мақалада тұрақты токтың идеалды индуктивті тізбектерін DC талдау мысалдары қарастырылған, олардың есебі гетерогенді параметрлер үшін шексіз аз сандарды қолдануды қажет ететін тізбектерге ерекше назар аударылған. Мұндай жағдайларда бұл сандардың орналасу реті жеке ойлар негізінде анықталады және бұл стандартты емес тапсырма.

Кілт сөздер: шексіз аз сан, шексіздік, гиперреал сандар, дәстүрлі емес сандар, идеалды реактивті элемент

С. Кацыв, В. Кухарчук, В. Мадьяров, В. Кучерук, П. Кулаков, М. Грибов

Нестандартный анализ в электротехнике. Идеальные индуктивные цепи постоянного тока с бесконечно малыми параметрами разного порядка

Анализ цепей DC постоянного тока с идеальными индуктивными элементами с использованием стандартных методов теоретической электротехники слишком сложен или даже невозможен, поскольку при их использовании часто возникает необходимость выявления неопределенностей типа $\frac{0}{0}$. В связи с этим в статье предлагается использовать не обычный математический анализ, а нестандартный, при котором частота постоянного тока берется не за ноль, а за бесконечно малое число α . В этом случае реактивные сопротивления индуктивных элементов будут равны αL , и становится возможным применять все стандартные методы теоретической электротехники. В статье рассматриваются примеры анализа идеальных индуктивных цепей DC постоянного тока, при этом особое внимание уделяется цепям, расчет которых требует использования бесконечно малых чисел для неоднородных параметров. В таких случаях порядок расположения этих чисел определяется исходя из индивидуальных соображений, и это нестандартная задача.

Ключевые слова: бесконечно малое число, бесконечность, гиперреальные числа, нетрадиционное число, идеальный реактивный элемент

Information about the authors

Katsyv, Samuil — Candidate of Technical Sciences, Associate professor of the Department of Computerized Electromechanical Systems and Complexes, Vinnytsia National Technical University, Ukraine; e-mail: katsyvsam@ukr.net; ORCID ID: <https://orcid.org/0000-0003-1375-5229>

Kukharchuk, Vasyl (*corresponding author*) — Doctor of Technical Sciences, Professor of the Department of Computerized Electromechanical Systems and Complexes, Vinnytsia National Technical University, Ukraine; e-mail: BKuch@ukr.net; ORCID ID: <https://orcid.org/0000-0001-9920-2726>

Madyarov, Viacheslav — Candidate of Technical Sciences, Professor of the Department of Computerized Electromechanical Systems and Complexes, Vinnytsia National Technical University, Ukraine; e-mail: madiarov@vntu.edu.ua; ORCID ID: <https://orcid.org/0000-0001-5116-6017>

Kucheruk, Volodymyr — Professor, Doctor of Science (Engineering), Professor of the Department of Information Technologies, Uman National University, Ukraine; e-mail: vladimir.kucheruk@gmail.com; ORCID ID: <https://orcid.org/0000-0002-6422-7779>

Kulakov, Pavlo — Doctor of Technical Sciences, Professor of the Department of Information Technologies, Uman National University, Ukraine; e-mail: kulakovpi@gmail.com; ORCID ID: <https://orcid.org/0000-0002-0167-2218>

Hribov, Mykhailo — Doctor of Law, Professor of the Department of Investigative Activities, the National Academy of Internal Affairs, Ukraine; e-mail: griboff007@gmail.com; ORCID ID: <https://orcid.org/0000-0003-2437-5598>

N.K. Tanasheva^{1,2}, L.L. Minkov³, A.R. Bakhtybekova^{1,2},
Sh.S. Kyzdarbekova^{1,2}, A.A. Potapova^{1,2}, N.K. Botpaev^{1,2}

¹Karaganda Buketov University, Karaganda, Kazakhstan;

²Scientific Center "Alternative Energy", Karaganda, Kazakhstan;

³Tomsk State University, Tomsk, Russia

Aerodynamic optimization of Magnus wind turbine blades using an active deflector

In this work, the optimization of wind turbines is considered by introducing a cylindrical blade with an active deflector. The use of metal (aluminum) deflector, compared with plastic (polypropylene), significantly increased the aerodynamic efficiency of the blade. It is shown that the aluminum deflector reduces the drag force by 18–20 % and increases the lifting force by 2.7 times. The maximum lifting force reached 2.16 N at a wind speed of 15 m/s with an aluminum deflector. In addition, the blade with an aluminum deflector achieved a higher rotation speed — up to 1100 rpm, which is 10 % higher compared to the blade with a polypropylene deflector. The improved performance is due to the high rigidity and minimal deformation of the aluminum material under the influence of air flow. The use of an active aluminum deflector eliminates the need for additional triggers, simplifying the design and reducing operating costs. The results obtained indicate that the use of an active aluminum deflector increases the efficiency of Magnus wind turbines and contributes to the development of renewable energy technologies.

Keywords: cylindrical blade, active deflector, wind turbines, self-starting rotation, aerodynamic characteristics, aluminum deflector, lifting force, drag force, Magnus effect, wind speed, rotation speed, optimization of wind turbine

 *Corresponding author:* Bakhtybekova Asem, asem.alibekova@inbox.ru

Introduction

As global energy demand increases, humanity is facing serious problems related to climate change and environmental degradation. The development and use of renewable energy sources are a necessary solution to ensure global energy security and sustainable development [1]. Among the technologies for generating electricity from renewable sources, wind energy stands out due to its advantages, such as short construction time and low operating costs. According to the Global Wind Energy Council, by the end of 2020, the total installed capacity of the global wind energy industry reached 743 GW [2]. Forecasts show that by 2027, the annual increase in installed capacity may increase significantly, supporting the transition to a more sustainable and environmentally friendly energy future [3–6].

Special attention in this area is paid to various types of wind turbines and the improvement of their designs [7]. Traditionally, wind turbines are divided into horizontal-axial [8] and vertical-axial installations [9]. Horizontal-axial turbines are the most common and efficient at stable wind directions and high wind speeds. However, their large dimensions and the need for complex orientation systems limit their use in urbanized areas [10]. Vertical-axial turbines, on the contrary, are capable of operating efficiently in variable wind directions and have a more compact design, which makes them attractive for use in urban environments and in limited areas. However, their efficiency is often lower, which encourages further research to optimize their aerodynamic characteristics.

One of the innovative directions in the development of wind energy is the use of Magnus wind turbines. These installations use the Magnus effect, based on the interaction of a rotating cylinder with an air flow to generate lift. As a result, such turbines are able to provide efficient operation at low wind speeds and in conditions of turbulence [11, 12].

However, despite the promise of Magnus wind turbines, their widespread use is hampered by a number of technical problems and disadvantages. Recent studies [13–16] indicate the main limitations, such as insufficient lifting force at very low wind speeds, the need for an external drive to initiate rotation of cylindrical

blades, which complicates the design and increases operating costs, as well as the complexity of construction and maintenance due to an increase in the number of moving parts.

In a number of papers [11, 12, 15], it was noted that Magnus wind turbines demonstrate reduced efficiency under certain wind conditions and require additional design optimization. For example, researchers have reported the need to use additional triggers to initiate blade rotation [17], which increases the complexity of the system and operating costs.

To solve these problems, it is proposed to introduce an active deflector on a cylindrical blade. A deflector is a device that optimizes airflow to increase thrust and improve the efficiency of a wind turbine (Fig. 1). It interacts with the incoming airflow, creating an additional moment that promotes self-starting rotation of the blade without the need for an electric drive. This simplifies the design, reduces operating costs and increases turbine efficiency by increasing lift and reducing drag.

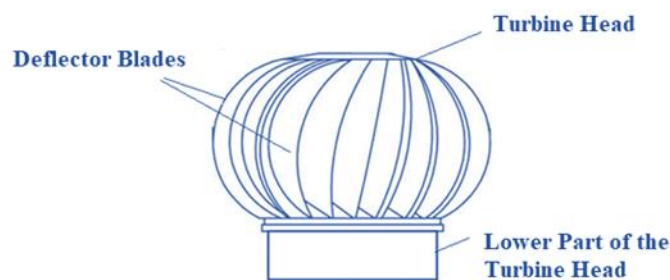


Figure 1. Deflector

The deflector consists of the following main elements: the turbine head, which includes a system of rotating blades; deflector blades located around the head and guiding the airflow to increase aerodynamic efficiency; and the lower part of the turbine head, which serves to connect the structure to the support base, ensuring its stability and functionality.

The principle of operation of the deflector is based on the effect of the incoming air flow on the blades of the active head of the device, which creates a centrifugal force and drives the cylindrical tube. This eliminates the need to use additional triggers. The key advantages of the deflector are simplicity, lightness and cost-effectiveness. The turbine head, structurally resembling a multi-blade vertical-axis rotor, is rigidly connected to the cylinder and spins it due to wind force, increasing the lifting force and aerodynamic efficiency of the installation. For reliable operation in various climatic conditions, deflectors must have strength, durability, wear resistance and low weight; the use of aluminum in the structure allows to reduce weight and increase corrosion resistance.

The purpose of this work is to increase the efficiency of Magnus wind turbines by developing and experimentally studying a cylindrical blade with an active deflector made of aluminum. The novelty of the work lies in the use of an active deflector, which provides self-starting rotation of the blade without the use of additional starting mechanisms, as well as in a comparative analysis of the aerodynamic characteristics of blades with deflectors made of different materials to determine the optimal solution.

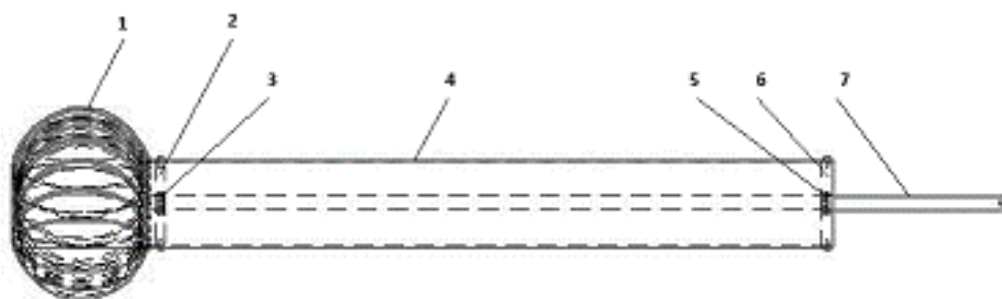
Experimental methodology

As part of the study, a combined blade was developed, made in the form of a cylinder with a deflector. Experimental studies were conducted in the laboratory “Aerodynamic measurements” of the Scientific Center “Alternative Energy” of the Karaganda Buketov University. The object of the study was installed in the working area of the T-1-M wind tunnel, where experimental measurements were performed.

The experimental sample of a cylindrical blade consists of a cylinder equipped with a deflector. The deflector lobes open under the influence of air flow, which ensures the independent start of rotation of the cylindrical blade without the need for additional starting mechanisms (Fig. 2). The cylindrical blade under study consists of a rotating cylinder (4) and an active rotary deflector (1) mounted on an iron rod (7), which is attached to a radial disk (not shown) of the horizontal axis of the wind turbine. Bearings (3, 5) are installed at both ends of the rotating pipe using mounting discs (2, 6). The principle of operation of the blade is as follows: due to the rotational action of the deflector (1), under the influence of an incoming air flow, the cylin-

drical pipe (4) begins to rotate through the bearings (3), without using an electric drive. At the same time, a lifting force is created due to the Magnus effect, which triggers the rotation of the blade and, ultimately, drives the wind wheel of the installation.

This design of the deflector allows for autonomous rotation of the entire blade without the use of additional sources for the trigger mechanism. The deflector is made in the shape of a ball with 24 separate lobes, which are attached on one side to a cylindrical pipe, and on the other to a round base using bolts.



1 — active deflector; 2, 6 — bearing mounting discs; 3, 5 — bearings;
4 — rotating pipe; 7 — iron pipe for mounting the blade

Figure 2. Diagram of a laboratory sample of a cylinder with an active rotary deflector element

Geometric parameters of a cylindrical blade with a deflector in Table 1.

Table 1

Parameters of a cylindrical blade with a deflector

Parameter	Value	Unit of measurement
Deflector radius (R_1)	0.05	m
Radius of the cylinder (R_2)	0.025	m
Cylinder length (L)	0.205	m
Deflector area (S_1)	0.00785	m ²
Cylinder area (S_2)	0.01025	m ²
Total cross-sectional area (s_1)	0.0181	m ²
Kinematic viscosity (ν)	0.0000149	m ² /s
Density (ρ)	1.21	kg/m ³

To conduct a comparative analysis of the efficiency of the blade, a laboratory mock-up of a cylindrical blade with an active deflector made of metal (aluminum) and plastic (polypropylene) was made (Figs 3 and 4).



Figure 3. Experimental layout of a cylindrical blade with a metal active deflector (made of aluminum)



Figure 4. Experimental layout of a cylindrical blade with a plastic active deflector (made of polypropylene)

Table 2 presents a comparative analysis of the main characteristics of aluminum and polypropylene used in the manufacture of an active deflector [18].

Table 2

Comparative characteristics of aluminum and polypropylene for an active deflector

Characteristic	Aluminum	Polypropylene
Density, kg/m ³	2700	900
The thickness of the material in the deflector, mm	0.2	0,5
Tensile strength, MPa	70–700 (depending on the alloy)	20–40
Modulus of elasticity, GPa	69	1,5–2
Stiffness and deformation under load	High rigidity, minimal deformation	Low rigidity, prone to deformation
Aerodynamic properties	Lowdrag, highlift	High drag, lowlift
Weight at the same size	Heavier due to higher density, offset by a smaller thickness	Lighter, but requires more thickness for durability

As part of the study, experimental models of a cylindrical blade with an active deflector made of aluminum and polypropylene were made for comparative analysis.

According to the standard [19], an analysis of measurement uncertainty was carried out (1–4). In our case, the values of the drag force and lift (Y) were not measured directly, but were calculated using N other values X_1, X_2, X_3 and X_N according to the functional dependence (1):

$$Y = f(X_1, X_2, X_3 \dots X_N). \quad (1)$$

For each input parameter X_i , participating in the model, the estimate is made taking into account its value x_i and the standard uncertainty $u(x_i)$. The estimate of the input quantities ($x_1, x_2 \dots x_n$) is their mathematical expectation, and the standard uncertainty $u(x_i)$ is the standard deviation.

The methods for estimating standard uncertainties depend on the available information about the value of X_i and can be performed according to type A or type B. The standard uncertainty of type A is calculated using the formula (2):

$$U_A = \left(F \sqrt{\frac{\sum_{i=1}^n (F_i - \bar{F})^2}{n(n-1)}} \right), \quad (2)$$

where, F_i — measurement of the value; n — number of measurements; \bar{F} — the arithmetic mean, calculated as

$$\bar{F} = \frac{\sum_{i=1}^n F_i}{n}.$$

The standard uncertainty of type B is estimated based on non-statistical information using the formula (3):

$$U_B = (F) = \frac{\Delta F}{\sqrt{3}}, \quad (3)$$

where, $\pm \Delta F$ are the limits of the permissible error of the device.

The total standard uncertainty is determined by the following expression (4):

$$u_c = \sqrt{\sum_{i=1}^n k_i u_i^2}, \quad (4)$$

where, u_i is the standard uncertainty of the i -th factor; k_i is the sensitivity coefficient or weighting factor for this factor; n is the total number of uncertainty factors.

This approach allows you to take into account all possible sources of errors and provides a reliable assessment of measurement accuracy.

In engineering practice, the formula (5) is widely used to calculate the lift coefficient:

$$C_y = \frac{\Delta F_y}{\rho \cdot \frac{u^2}{2} \cdot S} \text{ or } C_y = \frac{2F_y}{\rho u^2 \cdot S}. \quad (5)$$

The following expression was used to calculate the drag coefficient (6):

$$C_x = \frac{\Delta F_x}{\rho \cdot \frac{u^2}{2} \cdot S} \text{ or } C_x = \frac{2F_x}{\rho u^2 \cdot S}, \quad (6)$$

where, ΔF_x — the drag force, [N]; ΔF_y — lifting force, [N]; ρ — the air density, [kg/m³]; u — the air flow velocity, [m/s]; S — the area of the midsection, [m²].

To determine the Reynolds number characterizing the ratio of inertial forces to viscosity forces, the formula was used (7):

$$\text{Re} = \frac{U \cdot D}{\nu}, \quad (7)$$

where D is the characteristic linear size of the stream lined body; ν is the kinematic coefficient of viscosity.

Results and Discussion

Aerodynamic laboratory experiments were carried out to study aerodynamic forces depending on the flow velocity (3–15 m/s). The dependence of the drag force on the wind speed for two samples of blades is shown in Figure 5. Figure 6 shows how wind speed affects the lifting force of the blade.

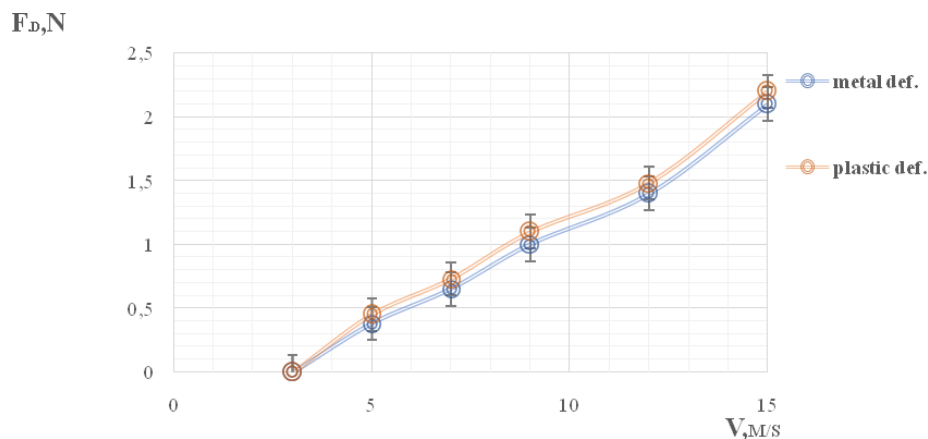


Figure 5. Comparison of the values of the drag forces of the blades with deflectors made of various materials

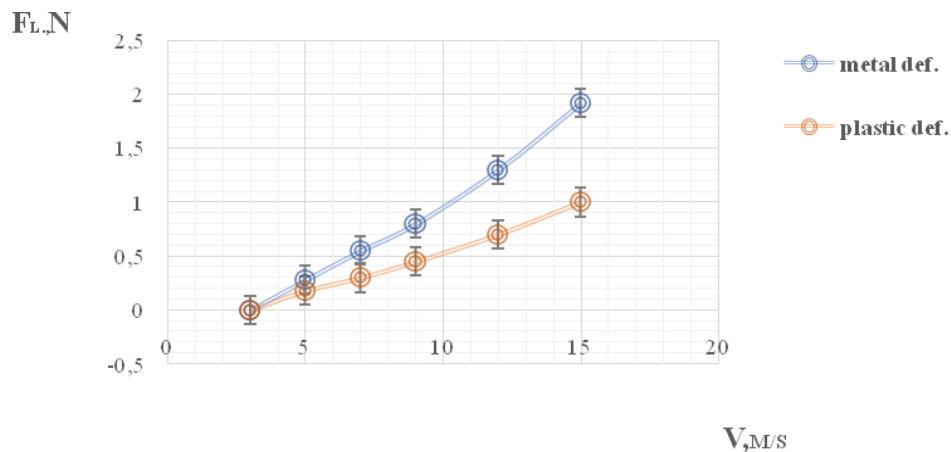


Figure 6. Comparison of the values of the lifting forces of the blades with deflectors made of various materials

As can be seen from the drawings, the blade sample with a metal deflector has the best aerodynamic performance. The drag force of the sample with a metal deflector is almost 18–20 % lower than that of the sample with a plastic deflector, while the maximum drag force was about 2.21 N at a wind speed of 15 m/s. The explanation for this is the difference in the thickness of the materials used for the deflector, i.e., the thickness of the metal is about 0.2 mm, while the thickness of the plastic is 0.5 mm, which is almost 2 times higher. It is known that the thinner the material, the lower the drag.

In the speed range of 2–14 m/s, the lifting force for a metal deflector exceeds that for a plastic deflector. The lift value of a blade with a metal deflector is 2.7 times higher than that of a blade with a plastic deflector. The maximum lifting force of the blade with a metal deflector was 2.16 N. The data indicate a higher aerodynamic efficiency of the metal deflector, which may be due to its geometric stability at high speeds.

An analysis of measurement uncertainty (formulas 1–4) was carried out in order to find the true measurement value, and measurement errors were calculated (Tables 3–6).

Table 3

Results of calculating the uncertainty of the drag of a metal layout

V, m/s	Arithmetic mean.	Uncert. A	Uncert. B	Total uncertainty	Standard deviation	Confidence interval	Error rate
5	0.40	±0.01	±0.02	±0.02	0.02	0.02	7.13
7	0.57	±0.02	±0.03	±0.03	0.02	0.02	6.98
9	0.99	±0.01	±0.05	±0.05	0.03	0.03	7.10
12	1.41	±0.01	±0.06	±0.06	0.04	0.05	7.08
15	2.09	±0.01	±0.10	±0.10	0.07	0.08	7.11

Table 4

Results of calculating the uncertainty of the lifting force of a metal layout

V, m/s	Arithmetic mean.	Uncert. A	Uncert. B	Total uncertainty	Standard deviation	Confidence interval	Error rate
5	0.27	±0.01	±0.01	±0.01	0.03	0.03	7.04
7	0.55	±0.02	±0.03	±0.03	0.03	0.03	6.96
9	0.79	±0.02	±0.04	±0.04	0.02	0.02	7.07
12	1.29	±0.01	±0.06	±0.06	0.03	0.03	7.10
15	1.90	±0.01	±0.09	±0.09	0.03	0.03	7.13

Table 5

Results of calculating the uncertainty of the drag of a plastic layout

V, m/s	Arithmetic mean.	Uncert. A	Uncert. B	Total uncertainty	Standard deviation	Confidence interval	Error rate
5	0.45	±0.01	±0.01	±0.01	0.03	0.03	7.13
7	0.73	±0.02	±0.01	±0.01	0.03	0.03	7.10
9	1.10	±0.02	±0.02	±0.02	0.03	0.03	6.98
12	1.48	±0.01	±0.04	±0.04	0.03	0.04	7.05
15	2.20	±0.02	±0.05	±0.05	0.04	0.05	6.98

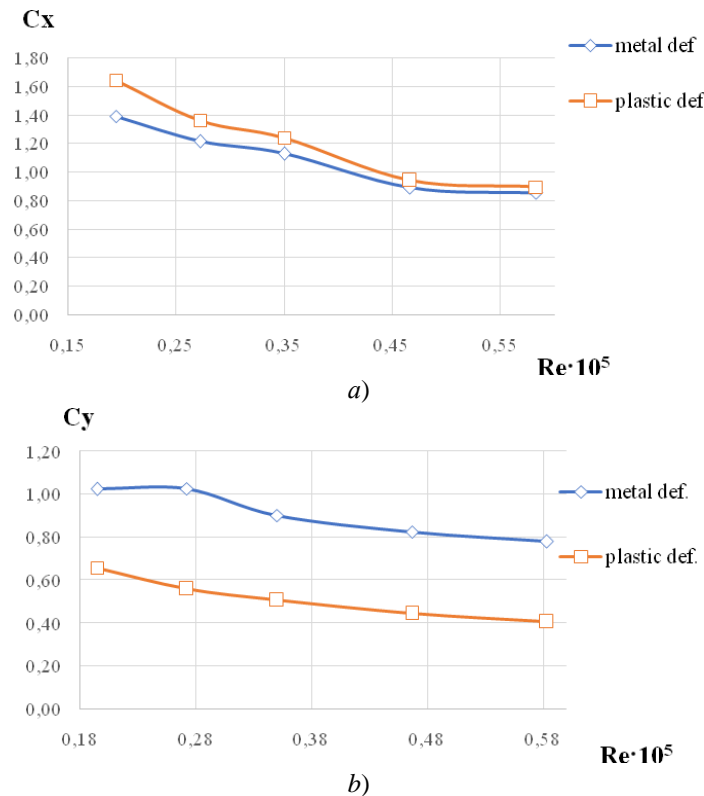
Table 6

Results of calculating the uncertainty of the lifting force of a plastic layout

V, m/s	Arithmetic mean.	Uncert. A	Uncert. B	Total uncertainty	Standard deviation	Confidence interval	Error rate
5	0.19	±0.02	±0.01	±0.01	0.03	0.04	7.01
7	0.26	±0.01	±0.01	±0.02	0.03	0.04	7.05
9	0.44	±0.02	±0.02	±0.02	0.03	0.03	6.98
12	0.72	±0.01	±0.03	±0.03	0.02	0.02	7.13
15	0.99	±0.00	±0.05	±0.05	0.03	0.03	6.97

As can be seen from Figures 5 and 6, the uncertainty for both drag and lift is shown in the form of vertical stripes, but they are omitted in the following figures for clarity. Tables 3–6 show that the error was about 7 %, which indicates the high accuracy of the experimental studies.

Figures 7(a) and 7(b) below show the dependencies of the aerodynamic coefficients on the Reynolds number.



a — coefficient of drag force; b — coefficient of lift

Figure 7. Dependence of aerodynamic coefficients on the Reynolds number

The drag coefficient of a blade with a metal deflector is on average 15 % less than that of a blade with a plastic deflector, which indicates lower aerodynamic losses in a metal deflector. The maximum coefficient value for a plastic deflector was 1.6 at $Re = 0.15 \cdot 10^5$, while for a metal deflector it reached only 1.4 under the same conditions. When comparing the obtained results of the drag coefficient with data from other authors, it was found that a cylinder with a metal deflector has a drag coefficient 37–40 % higher than that of conventional cylinders [17], but 35–36 % less than that of cylinders with a plate [20]. Conventional cylinders with a maximum Reynolds number have a drag coefficient of about 1 and do not create significant lift, whereas cylinders with a plate have a coefficient of about 1.9 due to turbulence caused by their geometric features.

The lift coefficient of a metal deflector is on average 1.7 times higher than that of a plastic one. The maximum value for a metal deflector was 1.1 at $Re = 0.18 \cdot 10^5$, whereas for a plastic deflector it was only 0.65. These data confirm the higher aerodynamic efficiency of the metal deflector, which is probably due to its rigidity and stable shape when exposed to air flow. Comparing the results with a cylinder with a rough surface [14], a cylinder with a rough surface demonstrates a 31 % higher lift coefficient on average than a cylinder with a metal deflector at the same air flow rates. However, as the air flow velocity increases, the lift coefficient of a cylinder with a rough surface gradually decreases, reaching a value of 0.23 at a speed of 15 m/s, whereas a cylinder with a metal deflector has more stable dynamics and a value of 0.29 at the same speed, which is 15 % higher. This indicates a more uniform aerodynamic efficiency of deflector cylinders, which can be an advantage when used in conditions of variable air flow velocities, where lift stability is important.

Figure 8 shows the effect of wind speed on the number of revolutions.

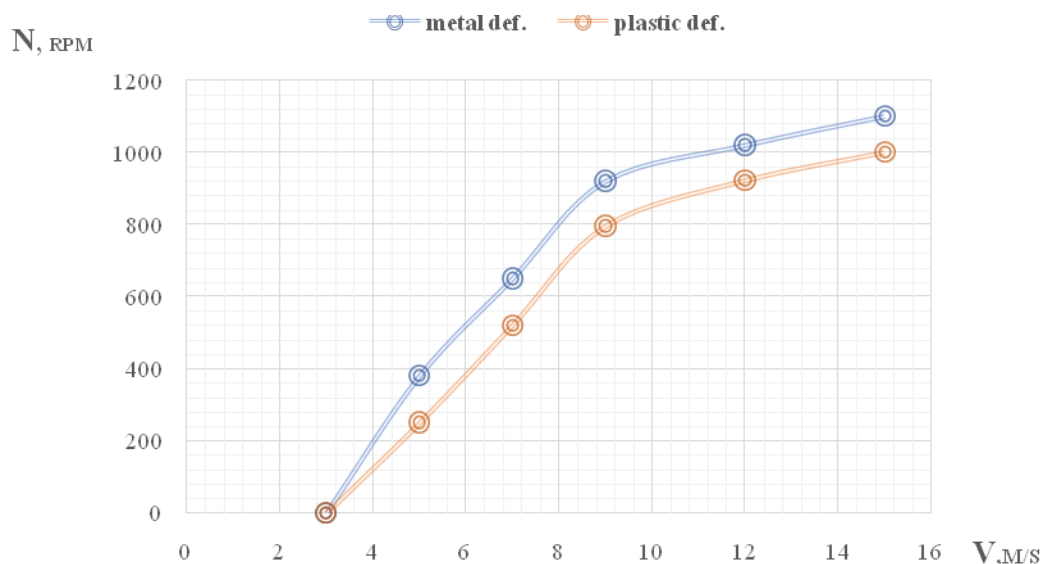


Figure 8. The effect of wind speed on the number of blade rotations

During the comparative analysis, it was determined that the blade with a metal deflector has a higher rotation speed, which at $v = 15$ m/s is $N = 1100$ rpm, which is 10 % higher than the rotation speed of blades with a plastic deflector. This indicates that the metal deflector contributes to a more efficient use of wind energy. The rigidity of the aluminum deflector allows you to maintain stable aerodynamic quality, which is especially important at high wind speeds, when the plastic can be subject to significant deformation.

From the conducted studies, it is shown that a cylindrical blade with an aluminum deflector, being poorly deformable, rigid and retaining a given shape, has relatively higher aerodynamic parameters.

Conclusion

This article discusses the problem of optimizing wind turbines by introducing a cylindrical blade equipped with an active deflector. The characteristic features of this design are analyzed; special attention is paid to its ability to initiate rotation without additional triggers due to the interaction of the deflector with the air flow. The conducted research has established that the introduction of a cylindrical blade with an active aluminum deflector significantly increases the efficiency of wind turbines. The use of an aluminum deflector reduces the drag force by 18–20 % and increases the lifting force by 2.7 times compared to the polypropylene analog. The maximum lifting force reached 2.16 N at a wind speed of 15 m/s, and the blade rotation speed increased to 1100 rpm, which is 10 % higher than that of a blade with a polypropylene deflector.

The improved aerodynamic characteristics are due to the high rigidity and minimal deformation of the aluminum material, which ensures more effective interaction with the air flow. The use of an active aluminum deflector allows you to eliminate additional triggers, simplifying the design and reducing operating costs.

The results obtained confirm the prospects of using active aluminum deflectors in the design of Magnus wind turbines to increase their efficiency and develop renewable energy technologies.

Funding

This research was funded by a grant from Science Committee of the Ministry of Science and Higher Education of the Republic of Kazakhstan (AP23483857 “Development and creation of a new design prototype wind turbine with a complex geometric shape of the blades”).

References

- 1 Liu, Z., Cheng, X., Peng, X., Wang, P., Zhao, X., Liu, J., ... & Qu, R. (2024). A review of common-mode voltage suppression methods in wind power generation. *Renewable and Sustainable Energy Reviews*, 203, 114773. <https://doi.org/10.1016/j.rser.2024.114773>
- 2 Global Wind Energy Council. Retrieved from <https://gwec.net/>

- 3 Hassan, Q., Viktor, P., Al-Musawi, T.J., Ali, B.M., Algburi, S., Alzoubi, H.M., ... & Jaszczur, M. (2024). The renewable energy role in the global energy Transformations. *Renewable Energy Focus*, 48, 100545. <https://doi.org/10.1016/j.ref.2024.100545>
- 4 Nwokediegwu, Z.Q.S., Ibekwe, K.I., Ilojiyanya, V.I., Etukudoh, E.A., & Ayorinde, O.B. (2024). Renewable energy technologies in engineering: A review of current developments and future prospects. *Engineering Science & Technology Journal*, 5(2), 367–384. <https://doi.org/10.51594/estj.v5i2.800>
- 5 Rusilowati, U., Ngemba, H.R., Anugrah, R.W., Fitriani, A., & Astuti, E.D. (2024). Leveraging ai for superior efficiency in energy use and development of renewable resources such as solar energy, wind, and bioenergy. *International Transactions on Artificial Intelligence*, 2(2), 114–120. <https://doi.org/10.33050/italic.v2i2.537>
- 6 Bošnjaković, M., Katinić, M., Santa, R., & Marić, D. (2022). Wind turbine technology trends. *Applied Sciences*, 12(17), 8653. <https://doi.org/10.3390/app12178653>
- 7 Tanasheva, N.K., Bakhtybekova, A.R., Shuyushbayeva, N.N., Dyusembaeva, A.N., Burkov, M.A., & Nurkenov, S.A. (2024). Experimental study of aerodynamic coefficients of a combined blade. *Bulletin of the Karaganda University. "Physics" Series*, 29, 1(113), 92–98. <https://doi.org/10.31489/2024ph1/92-98>
- 8 Roy, S., Das, B., & Biswas, A. (2023). A comprehensive review of the application of bio-inspired tubercles on the horizontal axis wind turbine blade. *International Journal of Environmental Science and Technology*, 20(4), 4695–4722. <https://doi.org/10.1007/s13762-021-03784-3>
- 9 Dyusembaeva, A., Tanasheva, N., Tussybayeva, A., Bakhtybekova, A., Kutumova, Z., Kyzdarbekova, S., & Mukhamedrakhim, A. (2024). Numerical Simulation to Investigate the Effect of Adding a Fixed Blade to a Magnus Wind Turbine. *Energies*, 17(16), 4054. <https://doi.org/10.3390/en17164054>
- 10 Tleubergenova, A.Zh., Dyusembayeva, A.N., Tanasheva, N.K., Bakhtybekova, A.R., Kutumova, Zh.B., & Mukhamedrakhim, A.R. (2024). Experimental studies of the performance efficiency of a wind turbine with combined blades. *Eurasian Physical Technical Journal*, 21(2 (48)), 31–37. <https://doi.org/10.31489/2024No2/31-37>
- 11 Babayeva, M., Abdullin, A., Polyakov, N., & Konstantin, G. (2020, January). Comparative analysis of modeling of a Magnus effect-based wind energy system. In *2020 IEEE Conference of Russian Young Researchers in Electrical and Electronic Engineering (EIConRus)* (pp. 602–605). IEEE. <https://doi.org/10.1109/EIConRus49466.2020.9039233>
- 12 Bianchini, A., Bangga, G., Baring-Gould, I., Croce, A., Cruz, J.I., Damiani, R., ... & Orrell, A. (2022). Current status and grand challenges for small wind turbine technology. *Wind Energy Science*, 7(5), 2003–2037. <https://doi.org/10.5194/wes-7-2003-2022>
- 13 Lukin, A., Perepelkina, S., Demidova, G., Lukichev, D., Rassölkin, A., Vaimann, T., & Kallaste, A. (2020, October). Generative Design in Development of Mechanical Components for Magnus Effect-Based Wind Turbine. In *2020 XI International Conference on Electrical Power Drive Systems (ICEPDS)* (pp. 1–5). IEEE. <https://doi.org/10.1109/ICEPDS47235.2020.9249344>
- 14 Tanasheva, N.K., Bakhtybekova, A.R., Minkov, L.L., Bolegenova, S.A., Shuyushbaeva, N.N., Tleubergenova, A.Z., & Toktarbaev, B.A. (2021). Influence of a rough surface on the aerodynamic characteristics of a rotating cylinder. *Bulletin of the Karaganda University. "Physics Series"*, 103(3), 52–59. <https://doi.org/10.31489/2021ph3/52-59>
- 15 Mdouki, R. (2020). Parametric study of Magnus wind turbine with spiral fins using Bem approach. *Journal of Applied Fluid Mechanics*, 14(3), 887–895. <https://doi.org/10.47176/jafm.14.03.31789>
- 16 Liu, J., Lin, H., & Zhang, J. (2019). Review on the technical perspectives and commercial viability of vertical axis wind turbines. *Ocean Engineering*, 182, 608–626. <https://doi.org/10.1016/j.oceaneng.2019.04.086>
- 17 Pezzotti, S., Mora, V. N., Andrés, A. S., & Franchini, S. (2020). Experimental study of the Magnus effect in cylindrical bodies with 4, 6, 8 and 10 sides. *Journal of Wind Engineering and Industrial Aerodynamics*, 197, 104065. <https://doi.org/10.1016/j.jweia.2019.104065>
- 18 Chavooshi, A., & Madhoushi, M. (2013). Mechanical and physical properties of aluminum powder/MDF dust/polypropylene composites. *Construction and Building Materials*, 44, 214–220. <https://doi.org/10.1016/j.conbuildmat.2013.02.079>
- 19 Dieck, R.H. (2007). *Measurement uncertainty: methods and applications*. ISA.
- 20 Liu, P. (2022). *Aerodynamics*. Springer. <https://doi.org/10.1007/978-981-19-4586-1>

Н.К. Танашева, Л.Л. Миньков, А.Р. Бахтыбекова,
Ш.С. Кыздарбекова, А.А. Потапова, Н.К. Ботпаев

Магнус желтурбинасының қалақшаларына белсенді дефлекторды пайдаланып, аэродинамикалық оңтайландыру

Жұмыста цилиндрлік қалақшалы белсенді дефлекторымен енгізу арқылы желтурбиналарын оңтайландыру қарастырылған. Пластикпен (полипропилен) салыстырғанда, металл (алюминий) дефлекторын қолдану қалақшаның аэродинамикалық тиімділігін едәуір арттырады. Алюминий дефлекторы кедергі күшін 18–20 %-ға төмендетіп, көтеру күшін 2,7 есеге арттыратыны көрсетілді. Максималды көтеру күші 15 м/с жел жылдамдығында алюминий дефлекторымен 2,16 Н-ға жетті. Сонымен қатар, алюминий дефлекторымен қалақша жоғары айналу жылдамдығына жетті, яғни 1100 айн/мин дейін, бұл дегеніміз полипропилен дефлекторы бар қалақшамен салыстырғанда 10 %

жоғары. Жақсартылған көрсеткіштер алюминий материалдың жоғары қаттылығы мен ауа ағынының әсерінен минималды деформациясына байланысты. Белсенді алюминий дефлекторын қолдану қосымша электр қозғалтқыштарының қажеттілігін жояды, құрылымды жеңілдетіп, пайдалану шығындарын төмендетеді. Алынған нәтижелер белсенді алюминий дефлекторын қолдану Магнус жел турбиналарының тиімділігін арттыратынын және жаңартылатын энергия технологияларын дамытуға ықпал ететінін көрсетеді.

Кілт сөздер: цилиндрлік қалақша, белсенді дефлектор, жел турбиналары, өздігінен іске қосылатын айналу, аэродинамикалық сипаттамалар, алюминий дефлекторы, көтеру күші, маңдайлық кедергі күші, Магнус әсері, жел жылдамдығы, айналу жылдамдығы, жел турбинасын оңтайландыру

Н.К. Танашева, Л.Л. Миньков, А.Р. Бахтыбекова,
Ш.С. Кыздарбекова, А.А. Потапова, Н.К. Ботпаев

Аэродинамическая оптимизация лопастей ветровых турбин Магнуса с использованием активного дефлектора

В данной работе рассматривается оптимизация ветряных турбин путем введения цилиндрической лопасти с активным дефлектором. Использование металлического (алюминиевого) дефлектора, по сравнению с пластиковым (полипропиленовым), значительно повысило аэродинамическую эффективность лопасти. Показано, что алюминиевый дефлектор снижает силу сопротивления на 18–20 % и увеличивает подъемную силу в 2,7 раза. Максимальная подъемная сила достигла 2,16 Н при скорости ветра 15 м/с с алюминиевым дефлектором. Кроме того, лопасть с алюминиевым дефлектором достигла более высокой скорости вращения — до 1100 об/мин, что на 10 % выше по сравнению с лопастью с полипропиленовым дефлектором. Улучшение характеристик обусловлено высокой жесткостью и минимальной деформацией алюминиевого материала под воздействием воздушного потока. Использование активного алюминиевого дефлектора устраняет необходимость в дополнительных электродвигателях, упрощая конструкцию и снижая эксплуатационные расходы. Полученные результаты свидетельствуют о том, что использование активного алюминиевого дефлектора повышает эффективность ветровых турбин Магнуса и способствует развитию технологий возобновляемой энергетики.

Ключевые слова: цилиндрическая лопасть, активный дефлектор, ветряные турбины, самозапускающееся вращение, аэродинамические характеристики, алюминиевый дефлектор, подъемная сила, сила лобового сопротивления, эффект Магнуса, скорость ветра, скорость вращения, оптимизация ветряной турбины

Information about the authors

Tanasheva, Nazgul — PhD doctor, Associate professor, Karaganda Buketov University, Karaganda, Kazakhstan; e-mail: nazgulya_tans@mail.ru; ORCID ID: <https://orcid.org/0000-0002-6558-5383>

Minkov, Leonid — Doctor of Physical and Mathematical Sciences, Professor, Tomsk State University, Tomsk, Russia; e-mail: lminkov@ftf.tsu.ru; ORCID ID: <https://orcid.org/0000-0001-6776-6375>

Bakhtybekova, Asem (*corresponding author*) — PhD, Researcher, Karaganda Buketov University, Karaganda, Kazakhstan; e-mail: asem.alibekova@inbox.ru; ORCID ID: <https://orcid.org/0000-0002-2018-8966>

Kyzdarbekova, Sholpan — Doctoral student, Karaganda Buketov University, Karaganda, Kazakhstan; e-mail: sholp1@mail.ru; ORCID ID: <https://orcid.org/0009-0000-9985-4636>

Potapova, Arina — Student, Karaganda Buketov University, Karaganda, Kazakhstan; e-mail: arina_no_way@mail.ru

Botpaev, Nurlan — Engineer, Karaganda Buketov University, Karaganda, Kazakhstan; e-mail: botpaev.nurlan@mail.ru